ABSTRACT

Title of Dissertation: VLSI DESIGN OF HEART MODEL

Li Wang, Doctor of Philosophy, 2007

Dissertation directed by: Professor Robert W. Newcomb
Department of Electrical and Computer Engineering

Heart disease is a leading cause of death in the United States and abroad. Research interests arise in understanding the nature of the dynamics of the heart and seeking methods to control and suppress arrhythmias. Simulation of the heart electrical activity is a useful approach to study the heart because it yields some quantities of interest that cannot practically be obtained in any other way. However, the complexity of the human heart leads to complicated mathematical models, and consequently, modeling arrhythmias of a whole heart with computers is extremely data intensive and computational challenging.

In this dissertation, we introduce an analog VLSI design that simulates cardiac electrical activities. The selected cardiac model is based on the Beeler-Reuter equations and the continuous core-conductor model. The Beeler-Reuter equations formulate the membrane ionic kinetics of ventricular cells, and the core-conductor model describes the electrical signal conduction on cardiac tissues. We discuss

the design flows of mapping equations into circuits and present a set of circuit blocks of basic mathematical function units. The transistor circuits for realizing the ionic model of a single cell is introduced, and capacitors are used to calculate time directives. A method of shifting the initial conditions of differential equations to zero is discussed for saving the circuit which sets up the initial voltages of the capacitors. We also introduce a method of implementing reaction-diffusion systems using non-linear RC networks, and present the circuit which simulates the reaction-diffusion process, i.e. the electrical propagation, of the heart.

Error analysis is carried out for the circuit-realized Beeler-Reuter model by comparing the simulated functions with the equation calculated values. The PSpice simulation results show that the circuit created action potential is satisfactory. The important reentry phenomena, the primary mechanism underlying fibrillation, is presented, and an anatomical reentry in the 1-dimensional model and a functional reentry (spiral wave) in the 2-dimensional model are successfully simulated in circuits.

The presented methods of implementing equations with analog VLSI circuit contribute to the fundamentals for a novel technique of obtaining numerical solutions and potential fast application-specified analog computational devices if the circuits are fabricated on chips. Unlike computing with digital computers, which is mainly a serial process and needs to discretize the space and the time domain for finding numerical solutions of the discretization points one by one, computation with analog VLSI relies on the physics of the electrical devices and takes advantage of the integration properties of capacitors and, hence, computing in analog circuit hardware is a parallel process and can be real-time, that is, the calculation time is the time simulated by equations.

VLSI DESIGN OF HEART MODEL

by

Li Wang

Dissertation submitted to the Faculty of the Graduate School of the
University of Maryland, College Park in partial fulfillment
of the requirements for the degree of
Doctor of Philosophy
2007

Advisory Committee:

Professor Robert W. Newcomb, Chairman
Professor Pamela Abshire
Professor William E. Kirwan
Professor Martin Peckerar
Professor Gang Qu

©Copyright by

Li Wang

2007

DEDICATION

To the people who can be potentially benefited by this dissertation.

ACKNOWLEDGEMENTS

I would like to thank the following people who made this work a reality. First, I would like to thank my advisor, Professor Newcomb, for his constant and patient guidance. He was always on campus hard-working on Sunday, and this made it possible for me to discuss with him frequently and get quick suggestions when I full-time worked off the campus. Professor Newcomb often read my dissertation in his fully occupied schedule by scarifying his personal time at home and gave me immediate helpful feedback. His valuable knowledge in the academic field and his dedicated attitude to science not only made my graduate study very fruitful but also gave me a life-model for my future career.

I would also like to thank my committee members, Dr. Abshire, Dr. Peckerar, and Dr. Qu, for kindly consenting to join the defense and review this dissertation; special thanks to Dr. Kirwan for managing to be on the committee from his extremely heavy business for the University. I would also like to thank Ms. Xinhua He, who gave me helpful discussions, and Ms. Yu Jiang, Ms. Koranan Limpaphayom, and Ms. Yingying Zhao for contributing a friendly and pleasant working environment in the Microelectronics Lab.

Finally, I would like to thank my families - my parents and sister, and special thanks to my husband, Zhu Han, for having been always by my side when I had difficulties, giving me great encouragement, and supporting me throughout these years.

TABLE OF CONTENTS

LIST OF TABLES

LIST OF FIGURES

Chapter 1

Introduction

1.1 Modeling Heart Electrical Activity

The heart is one of the most essential organs in our body. The heart working together with the blood vessels transports blood in the body and maintains the circulation of our life. In this system the heart works as a reliable rhythmic pump and as a blood reservoir. The heartbeat is so critical to our life and any interruption in the heartbeat for more than a few minutes can cause circulatory collapse and death. Heart disease is a leading cause of death in the United States and abroad. In 2002, a total of 696,947 people died of heart disease in the United States[1], accounting for 29% of all U.S. deaths. In 2005, heart disease is projected to have cost $393 billion, including health care services, medications, and lost productivity. Therefore, great research interests have arisen around people in investigating the factors that cause and sustain these life-threatening conditions.

The pumping mechanical activity is driven by electrical activity of the heart. The study of cardiac electrical excitation is a necessary and important step for understanding the heart's electrophysiology and its mechanical deformation to as-

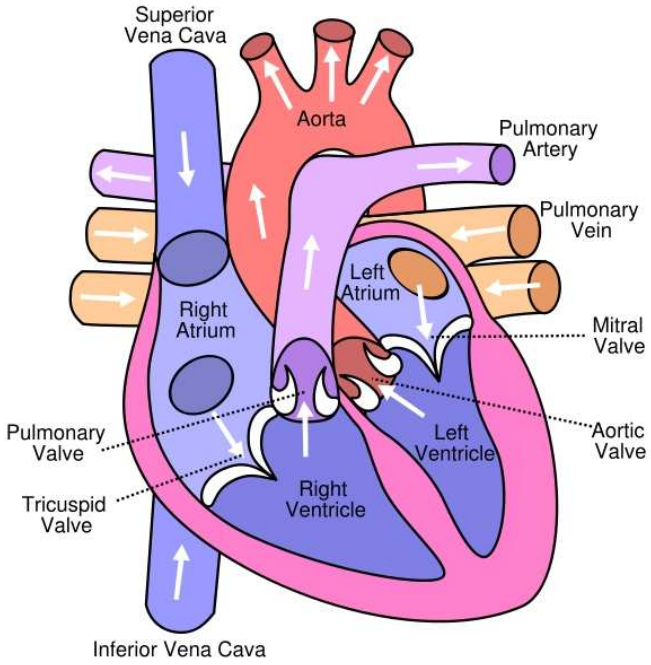

Figure 1.1: Cross section of the heart [3].

sist investigating the methodologies of controlling and suppressing heart disease. Shown in Figure 1.1 is a cross section of a heart. The heart is separated into two similar structures, the right and left halves, which represents two functionally different parts in the blood circulation system [2](pp. 98). The right half collects the deoxygenated blood from the body and pumps it to the lungs. The left half receives the oxygenated blood from the lungs and delivers it to the body. The halves can be further divided into an upper and lower part, called atria and ventricles respectively. The atria and ventricles are composed of walls surrounding a cavity, which is normally filled with blood. The walls consist primarily of a muscle structure, the myocardium [1]. The contraction of the myocardium causes the blood flow. The electrophysiology is tightly coupled with the pump function of the heart

[1]Myocardium is the muscular wall of the heart[4].

by controlling the development of tension. The origin of the electrical activity of the heart are the cardiac cells, which show electrical excitability like nerve cells. The electrical excitation of a cardiac cell is tightly coupled with its mechanical contraction. The electrical excitation is propagated from a cell to neighboring cells via gap junctions by intercellular transport of ions.

The study on live models for cardiac electrophysiology, though fruitful and necessary, have only provided partial insights into the mechanisms of arrhythmia formation and termination [5]. One reason for this is that all quantities of interest cannot be measured in vivo. An experimental investigation can be limited by coarse resolutions, hard data collection during the critical time following shocks, easy damage to tissue, and difficult optical mapping for cells not on the surface. To integrate and interpret the measurements, computational modeling of the system can contribute greatly to our understanding of the heart. The simulation of the heart yields information that cannot practically be obtained in any other way, and makes it possible to predict prior unknown behavior through complex phenomena. The simulation of the heart allows us to gain knowledge of the mechanisms of heart failure, to simplify the development and validation of heart drugs and medical devices, and to explore the side effects of a product. Modeling of the heart is an interdisciplinary research activity that includes the areas of anatomy, electrophysiology, excitation propagation, force development and mechanics as well as the coupling of these areas [5]. In this dissertation, we focus on modeling the electrophysiology of the heart. We introduce a novel methodology of simulation which utilizes analog VLSI circuits to model electrical activities of the heart. Compared to running simulation of a heart model on digital computers, the introduced method can be implemented on analog hardware which is able to obtain simulation

results fast. We present a set of circuits components that are useful for implementing basic mathematical expressions in membrane ionic models, and perform the PSpice simulation for the VLSI circuits which realize the Beeler-Reuter equations.

1.2 Review of Mathematical Models for Cardiac Cell Electrical Activity

A large number of mathematical models have been constructed to describe the electrophysiological behavior of cardiac cells. External electrical stimulus to a cardiac cell may lead to a changing membrane potential, known as an *action potential*. The models that describe action potentials and the ion transport across the cell membrane are also referred to as *ionic models*. In the following an overview of cardiac electrophysiological models are presented. The principles and the advances of the models are discussed.

Most ionic models of cardiac cells are based on the Hodgkin-Huxley formalism [6], which first reported a quantitative description of the active and passive electrical behavior of the axon membrane of giant squids [7]. The model was built in 1952, a work that resulted in a Noble Prize for the authors. It described the electrophysiology of the axon membrane using a RC (Resistor-Capacitor) circuit, in which the resistor is significantly nonlinear. The nonlinearities can be attributed to the behavior of ionic channels [5]. Hodgkin and Huxley separated the membrane current into three types of ionic current components: sodium ion flow I_{Na}, potassium ion flow I_k and a small "leakage current" I_l. The currents were characterized as the product of conductances and the differences of the driving forces for ions, namely chemical gradient and electrical gradient. The conductances for I_{Na} and I_k

are time- and voltage-dependent, and modeled by using gating variables, which are formulated by first-order ODEs (Ordinary Differential Equations), and make the whole model a system of degree-four differential equations, i.e. a time-dependent membrane potential and three gate variables. The Hodgkin and Huxley model described the way in which ionic currents vary with membrane potential and time. Its structure forms a basis for almost all models of excitable membrane behavior.

The FitzHugh-Nagumo model reduces the Hodgkin-Huxley model from degree-four differential equations to degree-two, for which phase plane analysis applies. The FitzHugh-Nagumo model [8][9] was a modification of the van der Pol equation . The Van der Pol equation was intended to represent the *qualitative* rather than the *quantative* properties of a wide class of excitable-oscillatory systems using simple algebraic form [10]. The resulted BVP model (B. van der Pol model) has two variables of state, representing excitability and refractoriness, and its properties can therefore be visualized on a phase plane. For example, Glaze utilized BVP model to perform simulations for heart in [11]. The FitzHugh-Nagumo model used a single mathematical processes to represent multiple channel properties and did not target to model the accuracy and complexity of cellular processes. It preserved the essential behavior of the membrane and is still used, due to its low computational cost, as the excitability component in some models of cardiac action potential propagation [12].

In 1962, Noble published the formulation applicable to Purkinje fibers of the heart [13]. It is one of the first mathematical models of a cardiac cell. The Purkinje fibers differ from squid nerve in that depolarization decreases the potassium permeability of the membrane. During large depolarization, this decrease is transient and the potassium permeability increases slowly during the passage of the

depolarizing current. By modifying the Hodgkin-Huxley equations to take account of this behavior in potassium current, Noble described the long lasting action and pacemaker potentials of the Purkinje fibers of the heart. A novel quality of this model was the decomposition of the sodium and potassium currents as well as the reconstruction of the pace-maker property for the cardiac cells. The Noble model adopted all the gating variables from Hodgkin-Huxley, and was also a degree-four differential system.

The next significant cardiac membrane model following Noble's is the McAllister-Noble-Tsien model published in 1975 [14]. By 1962, the theory of long-lasting action potentials had developed much further than the experimental work and it did not seem fruitful to explore further theoretical modifications due to the lack of the quantitative information of the ionic currents as complete as that provided by Hodgkin and Huxley in the case of squid nerve. The McAllister-Noble-Tsien model, which was based on a wide range of experimental results for cardiac muscle obtained using the voltage clamp technique, was not constructed until sufficient experimental information was accumulated, about 10 years after the technique was first successfully applied to cardiac membranes in 1964. The model formulated the electrical activity of cardiac Purkinje fibers. In this model, the total ionic current is broken down into nine discrete individual ionic fluxes. There are eleven gating variables, among which nine are time-dependent and described by first-order differential equations, and this makes the McAllister-Noble-Tsien model a degree-ten ODE system.

The Beeler-Reuter model, published in 1977, is a pioneering effort to describe the cardiac ventricular active potential [15]. This work incorporated the majority of the experimental data of ventricular myocardial action potentials by using the

voltage clamp method. The total ionic flux is divided into only four individual ionic currents in the Beeler-Reuter model: a time-independent outward potassium current, a inward sodium current, which is primarily responsible for the rapid upstroke of the action potential, a slow inward calcium current, and a outward time-dependent potassium current. The main contribution of the Beeler-Reuter model is that it includes the intracellular calcium ion concentration, which plays a dominant role in the creation of the myocardial action potential plateau. The model contains eight coupled, first order, non-linear differential equations, which are for the membrane potential, the intracellular calcium ion concentration, and six gating variables for the various membrane conductances.

The experimental data used in the Beeler-Reuter model was subject to limitations in available voltage clamp techniques and their application to multicellular preparations of cardiac muscle [16]. These limitations were overcome with the single-cell and single-channel recording techniques developed in the 1980s. The Luo-Rudy I model [17], a system of degree-nine ODEs, was based on the data derived from the new measurement techniques. The Luo-Rudy I model was published in 1991, and described the electrophysiology of guinea pig ventricular cells. It is a significant update of the Beeler-Reuter mammalian ventricular model. The model reformulated the fast inward sodium current and the outward potassium currents, and investigated the phenomena dominated by these currents. The slow inward current developed in the Beeler-Reuter model, which is to support the plateau of the action potential, was retained.

The Luo-Rudy I model was further developed in 1994 to become the Luo-Rudy II model [18]. The phase-II model reformulated the slow calcium current, and incorporated a more thorough description of the processes which regulate

the intracellular calcium ion concentration and the movement of calcium ions. This model is also based on experimental data of guinea pig ventricular cells from single-cell and single-channel experiments. It provides a framework for future development of models of the excitation-contraction coupling process in cardiac cells. The model consists of eleven types of membrane currents and four types of calcium currents that move to and from sarcoplasmic reticulum. There are six gating variables and seven species of ion concentration formulated using differential equations, which make the Luo-Rudy II model a system of degree-fourteen ODEs.

Reviews of more cardiac cell ionic models are available in [5][12][19]. While the experimental methods are becoming more sophisticated to obtain data for constructing more accurate ionic models that take into account more ion flow mechanisms, we adopt Beeler-Reuter's ventricular cell model in our work for simulating the action potential. The advantage lies in its less complex formulation, and hence less simulation and hardware cost, while still keeping the description of the basics of membrane ionic flows between the intra- and extracellular media.

1.3 Motivation for VLSI Implementation of Heart Model

Computer simulation of cardiac tissues is extremely computationally intensive. Combining the equations for transmembrane ion flows and binding processes produces a virtual cell as a complex nonlinear system of differential equations. We can take a relatively simple electrophysiology model, say, Beeler-Reuter as an example. The model describes a system of eight coupled, first order, non-linear differential equations, which are for the membrane potential, the intracellular calcium ion

concentration, and six activation or inactivation parameters for the various membrane conductances. Considering a sheet of 2-dimensional cardiac tissue of 1 cm^2, assuming each cell is 100 $\mu m \times$ 100 μm in size, there are totally 10^4 cells in this tissue and hence there are 8×10^4 coupled differential equations to represent the virtual model. Furthermore, the demand of high spatial discretization and small time-step sizes needed by the computational accuracy in turn requires the use of huge memories and very fast processors. An approximate way to quantifying the computational load is to estimate the number of floating point operations that would be necessary to compute one heartbeat [20]. Suppose a heartbeat takes about 1 s, and the time step of the computation is 0.01 ms and the space step is 100 μm, then it would require some 10^{14} floating point operations to simulate the cardiac electrical activity. This would take at least 30 hours of run-time on a 1GHz processor.

To handle the simulation request of huge memory and high computational speed, many researchers have explored computing parallelism as the solver. In the work presented in [21], the author, Pavarino, ran the simulation of the cardiac reaction-diffusion system on two platforms. One platform employed an IBM SP RS/6000 with Power 4 processors. The other consisted of an HP SuperDome 64000 with PA8700 processors. The work simulated a complete cardiac cycle (excitation-recovery) in a slab of cardiac tissue of size $4 \times 4 \times 0.5$ cm^3 and mesh $400 \times 400 \times 50$ using the Luo-Rudy I model as the membrane model and the Monodomain model as the cardiac reaction-diffusion model. An adaptive algorithm was applied on the time steps. To complete the simulation, the HP platform with 32 processors took 20 hours, and the IBM SP4 machine with 64 processors took about 2.5 hours.

However the performance does not scale up linearly as the number of parallel

processors increases. Pormann [22] presented the results of computational speed-up vs. the number of parallel computing nodes. A cluster of 180 dual-CPU nodes was used to do the investigation. Each node contained two 200 MHz Power3 CPUs and 1 GB of memory. The results showed that to calculate 1.0 ms of electrical activity of a 290×290×290 grid, with 0.001 ms in time-step, it takes 5386 seconds (1.5 hours) using 1 CPU. The speed-up degraded with the increase of node number. For a cluster of 32 CPUs, instead of achieving 32 times faster in speed, there was only a speed-up of 21.97 due to the overhead of the communications between the CPUs.

In this dissertation, we present an alternate but novel approach to simulate cardiac electrophysiology using analog VLSI circuits. As stated in the previous sections, the complexity of the heart leads to tremendous complexity in computer simulations. The complexity arises from the nonlinearities caused by the extremely highly coupled differential equations. In order to solve the nonlinear system, time is finely discretized and the three dimensions are well meshed. Computation is carried out for each time step and spatial grid. The introduced analog VLSI of the heart model can be made on chips which serve as processing devices. Computation with analog hardware has the advantage of obtaining fast solutions for time-based differential systems due to the differential nature of capacitor components, i.e. the derivative of a capacitor's voltage with respect to time is proportional to its current. By using analog VLSI hardware, the simulation of the heart model can be performed with great speed-up. In the situations that people are attacked by heart diseases, time is very critical to save lives. The VLSI implementation of the simulation allows the fast analysis of fatal heart behavior and, thus, may allow for obtaining real-time cure.

Compared to running simulation on digital computers, the simulation using analog VLSI may require smaller hardware so that it is easy to carry it out. Digital circuits operate based on the mathematics of Boolean logic. Their transistors work as switches, and each wire represents a single bit with a value of either 0 or 1. Analog circuits operate with continuous signals. Their primitives of computation arise from the physics of the devices. One wire represents many bits, and hence the amount of computation per a single transistor is usually higher than for digital circuits. For example, an 8-bit current multiplier can be implemented with 8 transistors in analog circuits, whereas, digital implementation takes approximately 3000 transistors [23]. The area usage and power consumption demanded by an analog system for a computation is also more efficient than a digital system in general, because more wiring and communication overhead is required in digital circuits due to the greater number of transistors [23]. Therefore, using analog VLSI to perform the simulations for a heart model can lead to lower power dissipation, and less area and devices than using the general-purpose CPUs or other dedicated digital systems.

In this dissertation, we introduce a methodology of simulating cardiac electrophysiology using analog VLSI circuits. We consider one of the most used detailed membrane models in the literature, the Beeler-Reuter model, introduced in Section 1.2. The Beeler-Reuter model mathematically reconstructs the action potential of a mammalian ventricular cell. There are four ion currents and six gating variables described in this model. More details are provided in the next chapter. It is worth mentioning that though the introduced work targets the ventricular model developed by Beeler-Reuter, the proposed methodology of VLSI implementation can be applied to any other cell model and can be used for implementing almost any

time-based differential system.

1.4 Contributions

In this work, we investigate how to design an analog VLSI system to simulate a cardiac electrical activity model which is usually done using high-performance computers. We present the design methodology and the circuit components of implementing the mathematical model using VLSI. The ventricular myocardium model of Beeler-Reuter is realized with VLSI circuits to demonstrate the feasibility of simulating complex numerical models using analog circuits.

The main contributions of this work are:

- A design of an analog VLSI circuit that simulates the Beeler-Reuter's cardiac electrophysiology model.
- An RC circuit architecture that calculates reaction-diffusion equations, and the application of the RC circuit architecture to model the electrical propagation process on the heart.
- A method to transform the original formulas to mathematical expressions that are suitable to realize by VLSI circuits.
- Schemes for quantitatively scaling the equations to adapt to the computational circuits which are restricted by device parameters and working regions.
- An approach to change the initial conditions of differential equation systems to zero to save the elaborate hardware necessary to set the initial voltages of integration capacitors.

- A set of transistor circuit blocks that are useful for implementing basic mathematical expressions, especially the equations in membrane ionic models.

- A methodology for implementing time-based differential equations, numerical models, and general reaction-diffusion systems using analog VLSI circuits with special reference to differential equations describing the heart.

1.5 Organization of Dissertation

The dissertation is organized in five chapters.

Chapter 2 introduces the basics of cardiac electrophysiology related to this work. It starts with presenting cellular physiology. A general description of cell membrane is given, followed by the introduction of cardiac action potential and its ionic mechanism. The formulation of the membrane ionic models is presented next. Finally the ventricular myocardium model developed by Beeler-Reuter is discussed in detail.

Chapter 3 first introduces the design flow of implementing the mathematical formulas using analog VLSI circuits. The transformation of mathematical expressions to forms that are feasible for circuit implementation is discussed. Then, the scaling of the equation parameters and the shifting of initial conditions are presented, followed by the introduction of a set of transistor circuit blocks used for realizing basic mathematical functions and specialized for implementing the cardiac model. An analog VLSI design of the Beeler-Reuter model is given next. The circuits for realizing four ionic currents and the action potential are introduced and the implementation accuracies of the circuits are discussed.

Chapter 4 provides the circuit simulation of the electrical propagation in cardiac

tissues. It starts with presenting the core-conductor model of the cardiac propagation process, which is described by a reaction-diffusion equation. The method of mapping a generalized reaction-diffusion system to an RC circuit is introduced next. Then, the PSpice simulation of a transistor circuit for modeling a segment of a 1-dimensional cardiac fiber is discussed. The reentry phenomena and the spiral wave simulated by the introduced RC network are presented finally.

Chapter 5 concludes our work in this dissertation, and provides a discussion of the future works at the end.

Chapter 2

Heart Electrophysiology and Its Mathematical Models

2.1 Introduction

The contraction of the heart is controlled by the cardiac electrical conduction system. This system generates electrical impulses, known as action potentials, and conducts them rapidly throughout the heart, stimulating the heart to contract and pump blood. The creation of the electrical impulses is tightly related to the ionic mechanisms of the cardiac cells.

Each cell in our body is surrounded by a thin membrane [24](pp. 3). A cell membrane, also known as a plasma membrane or plasmalemma, is a selectively permeable bilayer, which mediates the diffusion of ions and molecules into and out of the cell and establishes different ion concentrations between the intra and extracellular space. The established ion concentration gradient also leads to an electrical potential difference, called the membrane potential, across the cell membrane due to the charge of ions. The membrane potential is conventionally expressed as the

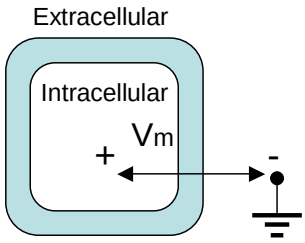

Figure 2.1: Membrane potential V_m is the intracellular electrical potential with respect to the extracellular media.

potential in the cell minus that on the exterior of the cell, and the extracellular potential is taken as the ground, as illustrated in Figure 2.1. The membrane potential is usually electrically negative when a cell is resting, i.e. when a cell does not conduct any electrical signals. The membrane potential can be perturbed by passing a positive current pulse from the exterior into the interior to charge a cell and make it *depolarized*. Depolarization refers to the change in the membrane potential to a more positive value [25][26](pp. 31). The larger the stimulating current that passes into the cell, the larger is the change in the membrane potential. When the applied current exceeds a certain strength, a threshold membrane potential is reached, and this triggers the cell to fire an *action potential*, which is a much larger response than the responses created from less stimulating currents.

The action potential created by a cardiac cell is described by models based on the Hodgkin-Huxley formulation, and the Beeler-Reuter model is one of them, with the latter being the one used in our work to simulate the cardiac action potential with VLSI. The Beeler-Reuter model can be summarized with Figure 2.2, which shows the dependence of the variables in the mathematical presentation. As we will present in the last part of this chapter, the Beeler-Reuter model describes four membrane ionic currents, six gating variables, and a varying calcium concentration,

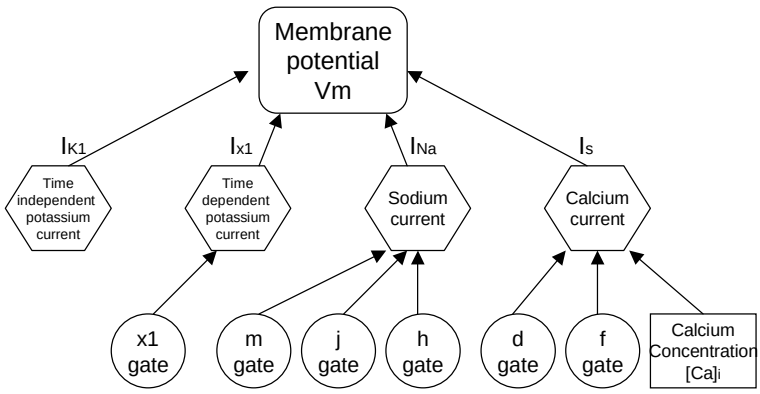

Figure 2.2: Variable dependence in the Beeler-Reuter model.

and formulates a nonlinear system of degree-eight, first order differential equations.

In the rest of the chapter, we will first introduce the cellular electrophysiology, and explain membranes, ionic currents across membranes, and the cardiac action potential. The mathematical models of ionic membranes are presented next. The Hodgkin-Huxley model and the Beeler-Reuter model are described in detail finally.

2.2 Cellular Electrophysiology

2.2.1 Cell Membrane

A cellular membrane is a lipid bilayer, which separates a cell from its extracellular environment [24](pp. 3). It serves as a permeable barrier that permits the selective passage of molecules across the membrane at a controlled rate. This selective permeability allows a cell to maintain an interior composition different from the extracellular media.

The direction of net ion movement across the membrane depends on both the chemical force caused by the concentration difference and the electrical force caused

by the electrical potential difference. For a given type of ion A, the ion tends to diffuse down the concentration gradient. Also, ion A tends to move from the side with a higher electrical potential to the side with a lower electrical potential. When the chemical and the electrical forces are equal in magnitude and opposite in direction, no net movement of the ion occurs through the membrane, and the ion is said to be in *electrochemical equilibrium*. The membrane potential that is required to produce an electrical force that counterbalances the concentration force is called the *equilibrium potential* or equivalently, the *Nernst potential* [26](pp. 22), and can be calculated with the *Nernst equation*:

$$E_A = \frac{RT}{zF} \ln \left(\frac{[A]_e}{[A]_i} \right), \tag{2.1}$$

where E_A is the equilibrium potential of ion A, R is the ideal gas constant (8.3 $\frac{J}{mol \cdot K}$), T is the absolute temperature in degrees K, z is the valence of the ion, F is Faraday's number, i.e., the charge of 1 *mol* of electrons (96,500 C/mol), $[A]_e$ is the extracellular concentration of ion A, and $[A]_i$ is the intracellular concentration of the ion. The polarity of the equilibrium potential is related to the direction of a chemical force. A positive equilibrium potential indicates that the force caused by the concentration gradient tends to make the ion flowing into the cell, and a negative sign indicates the concentration force drives the ionic current out of the cell. The magnitude of the equilibrium potential represents the strength of the chemical force.

Ions in a cell are usually impacted by the same electrical potential, i.e., the membrane potential, whereas different types of ions have various chemical potentials due to different ion concentrations. Hence in most tissue, ions are not in electrochemical equilibrium. Table 2.1 shows the typical ion concentrations of a cardiac muscle cell, and the corresponding equilibrium potentials [24](pp. 3). For

Table 2.1: Typical ion concentrations and equilibrium potentials in cardiac cell [24].

	Intracellular Concentration (mM)	Extracellular Concentration (mM)	Equilibrium Potential (mV)
Sodium(Na^+)	10	145	+71
Potassium(K^+)	140	4	-95
Calcium(Ca^{2+})	0.0001	1.5	+128

Na^+ and Ca^{2+}, the diffusion caused by the concentration gradient is inward, since their intracellular concentrations are much less than the extracellular media. In opposite, K^+ tends to move outward in the effect of its concentration gradient. A ventricular cardiac cell normally has an action potential that ranges from approximately -90 to 40 mV [27]. When the action potential of a ventricle is negative, the electrical force is in the same direction as the concentration force of Na^+ and Ca^{2+}, and this causes a net inward movement of Na^+ and Ca^{2+}. The chemical force on K^+, though in the opposite direction of the electrical force, has a larger magnitude, known by comparing the magnitude of K^+ equilibrium potential, 95 mV, with the maximal absolute value of the membrane potential, 90 mV. Consequently, K^+ shows a tendency of inward movement. When the action potential is positive, the direction of the ionic currents can be deduced in a similar way. As a result, the Na^+ and Ca^{2+} flows are always inward and the K^+ flow is always outward during the period of a ventricular action potential.

2.2.2 Ionic Mechanism of Action Potential

The permeability of the membrane is mediated through *ion channels* that act as pathways for the passage of charged molecules. Ion channels are specialized proteins embedded in the membrane that allow only desired ions to cross the membrane [28][29]. Most ion channels are gated and are capable of flipping between a conducting (open) and non-conducting (closed) state. The transition of the state is a random event [25],and hence it is not possible to predict whether a given channel is open or closed. However, the laws of probability allow people to make certain predictions of the average behavior of a channel. The probability of being open can be estimated by calculating the fraction of time a channel spends in the open state during a period of time. The open probability can be regulated by chemical or electrical signals, temperature, or mechanical force [30].

The ionic currents that occur through protein ion channels make possible the important electrical activities based on the voltage changes of the membrane potential. The rapid movement of ions via ion channels sometimes can create electrical currents that are large enough to produce rapid changes in the membrane potential. The rapidly changed membrane potentials are termed *action potentials*, and can be created by a stimulating current that exceeds a certain strength. An inward current pulse applied to a cell membrane causes the membrane potential to depolarize, and the size of the depolarization depends on the magnitude of the stimulus. When the current pulse reaches above a certain value to make the membrane potential exceed a *threshold*, the cell fires an action potential, a much larger response with a different shape compared to the potential changes resulted from a smaller stimulus. This is illustrated in Figure 2.3. Figure 2.3(a) shows four stimulating pulses with different amplitudes. Figure 2.3(b) shows four time courses of chang-

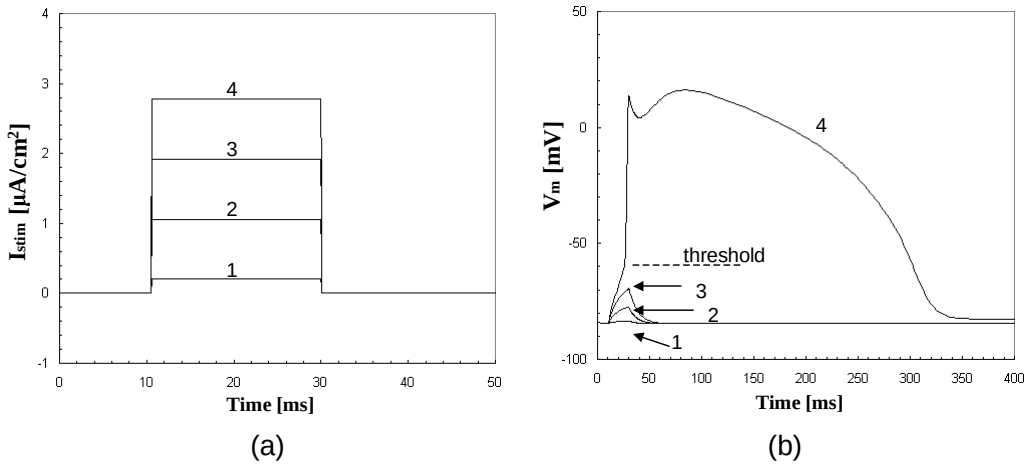

Figure 2.3: Responses of membrane potential to various stimulus. (a)Four stimulating currents with different strength. (b)Corresponding membrane potentials in response of the stimulus. An action potential is created when the membrane potential is charged by the 4th stimulus to pass a threshold.

ing membrane potentials, each of which represents the response to the stimulus of the same number in Figure 2.3(a). Among the stimulus, the number 4 current impulse is the only one that is able to charge the membrane potential to reach the threshold at around 60 mV and make an action potential.

A cardiac action potential pulse is the electrical activity of a individual cardiac muscle cell. The cardiac action potential voltage differs in different portions in the heart [31](chapter 6). This differentiation of the action potentials allows the difference in the electrical characteristics and functions of the varied types of cardiac cells. The numerical simulation models of the myocardial action potential have been reported for a few different locations on the heart: sinoatrial node, Purkinje fiber, atrial myocardium and ventricular myocardium [14]-[18] [32]-[35].

Figure 2.4 shows a waveform of the action potential in a ventricular cell. The

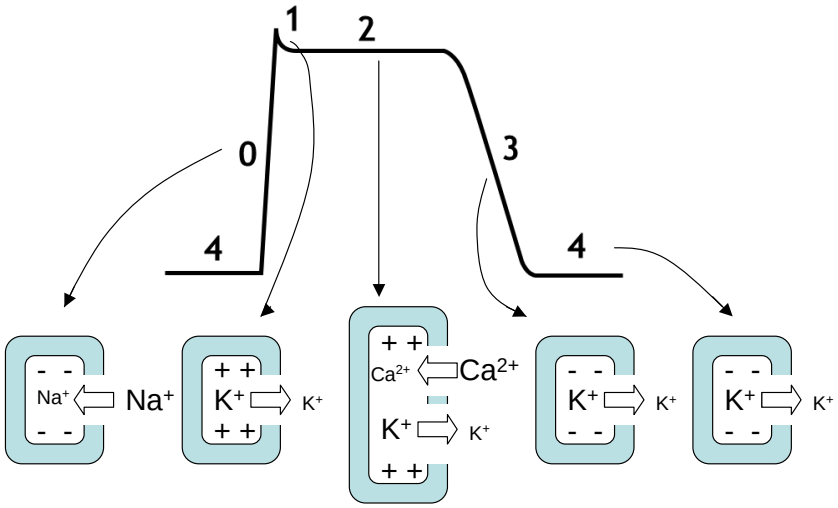

Figure 2.4: Phases of ventricular action potential and active ionic currents in each phase. (0)upstroke, (1)early re-polarization, (2)plateau, (3)late re-polarization, (4)rest.

ventricular action potential has 5 phases [36][37][38], established due to the fast changes in membrane permeability to certain ions, mainly to sodium, potassium, and calcium, resulting from the opening and closing of the ion channels. Figure 2.4 summarizes the ionic channel currents that occur during each phase of the ventricular action potential. The net movement direction of the ions depends on the polarity of the intercellular potential with respect to the exterior, denoted with "-" and "+" inside the cells in the figure, as well as the concentration differences between the interior and exterior of the cell, indicated with different sizes of the fonts for the ion names. The arrows represent the directions of the ion flows.

Phase 0 is the rapid depolarization phase. It arises from the sudden opening of the sodium channels and the subsequent rapid influx of the sodium current. The rapid opening of the *activation gate* is responsible for the large and abrupt increase in the sodium conductance in the membrane. The activation gate refers

to the gates that tend to open when the membrane potential becomes less negative. The sodium continues entering the cell when the channels are open and this eventually reverse the polarity of the membrane potential. The inward sodium flux finally stops and phase 0 is terminated due to the closure of the other type of sodium gates, called *inactivation gates*, which are defined as the gates that tend to close when the membrane potential becomes less negative. Phase 0 is followed by a slight repolarization period, called phase 1. The repolarization results from the outflow of potassium. After the repolarization, a plateau stage follows, known as phase 2. At this stage, the calcium channels start to open and this allows an influx of positive charge, Ca^{2+}, under the influence of the inward electrochemical potential for calcium. The inward flow of calcium and the outward flow of potassium currents roughly cancel each other. The membrane potential then reaches the steady plateau. After the plateau, the calcium channels close, and the potassium current dominates and repolarizes the cell back to the resting potential, and this makes up phase 3. In phase 4, the membrane potential stays in a constant level of approximately -85 mV, a little more positive than the equilibrium potential of potassium (refer to Table 2.1). Hence, the chemical force that favors the out flow of potassium exceeds very slightly the electrical force that favors the influx of potassium. Consequently there is a tiny outward potassium current during the resting state of phase 4.

The ionic concentrations, which largely influence the membrane potential, are maintained by the *active transport* [5](pp. 161) [26](pp. 14) [39](chapter 15). The active transport is also protein-mediated. In addition, this process allows ions to move through membranes against an electrochemical potential, and hence it requires energy. The concentration gradient of Na^+ and K^+ are maintained by a

Na^+/K^+ pump, an active transport that moves three Na^+ ions out of and two K^+ ions into the cell with the consumption of an APT(Adenosine Triphosphate - a type of chemical energy within cells) ([39](chapter 15). The Ca^+ pump helps maintain the concentration gradient of Ca^+. There are two types of Ca^+ pump involved. One type transports Ca^+ out of the cell. The other type transports intercellular Ca^+ into the *sarcoplasmic reticulum*(SR), an intercellular structure that stores Ca^+ ions. The release of Ca^+ ions stored in a SR are triggered by raised intracellular calcium resulting from transmembrane calcium influx [40].

2.3 Mathematical Description of Cardiac Electrophysiology

The development of experimental technologies necessitates the detailed understanding of the electrical behavior of a cellular membrane. The experiments include the measurement of the voltages across membranes in different spatial positions, current flows, ion concentrations and opening states of single ion channels [5] (pp.157). The commonly used measurement method is the voltage clamp technique, in which two electrodes are inserted into a cell to "clamp" voltage to a fixed value and the current needed to maintain a desired voltage is measured. The quantities obtained by the experiments are partly used to create mathematical models of different levels of abstraction. The models allow the numerical simulation of the electrophysiological behavior of cells, and assist the reconstruction of the measured data and the further discovery of unknown phenomena.

In this section, We first introduce the voltage clam technique, and present the mathematical formulation of the membrane models. The Hodgkin-Huxley model

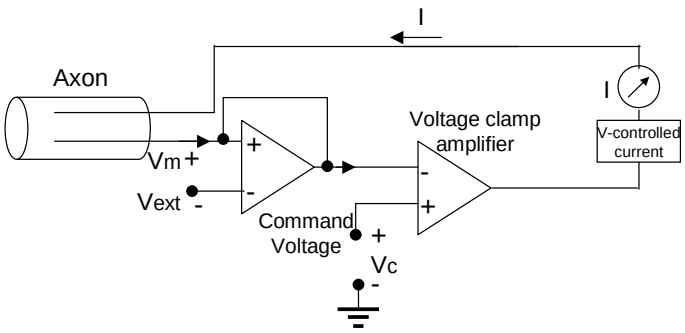

Figure 2.5: Measurement of ionic current using voltage clamp technique.

for squid axon and the ventricular myocardium model developed by Beeler-Reuter are described next.

2.3.1 Voltage Clamp

The voltage clamp allows the measurement of ionic currents under the influence of the membrane potential [41]. As shown in Figure 2.5, the voltage clamp technique involves two electrodes that are placed inside a cell. One electrode, used to measure the intercellular potential V_m, is connected to an amplifier. The other side of the amplifier is connected to the exterior of the cell to take the extracellular potential V_{ext}. The measured potential feeds into a voltage clamp amplifier to compare with a voltage to be maintained by the membrane potential, called a command voltage V_c. The output of the voltage clamp amplifier, i.e. the amplified value of the difference between V_m and V_c, controls a feedback current flowing into the cell to make these two potentials the same. The feedback current I, which is injected into the membrane through the other electrode, is then the mirror image of the current generated by the cell membrane at the command voltage, that is, when $V_m = V_c$. In order to measure currents of individual ions, other experimental procedures can

be also involved, such as ion substitution, channel blockers, and specific clamp protocols [41][42].

A wealth of new knowledge concerning ion channels resulted from the invention of the patch clamp method, a refined version of the voltage clamp. In this technique, a glass pipette with a tip diameter of about 1 or 2 μm [2](pp. 42) is used to form an exterior contact with a tiny area of a membrane. The contact is made very tight, by applying a small suction, such that all the ions that flow through the opening channels in the sealed patch of membrane flow into the pipette. If there is only one ion channel in the patch, the resulting electrical current, measured with an ultrasensitive electronic amplifier, is due to the opening and closing of the single channel, and the measured value transits randomly between zero and a certain non-zero value. The patch clamp method allows the study of a single ion channel and gains further insight into the electrophysiology of membranes.

2.3.2 Ionic Membrane Models

Cell Membrane as Capacitor Circuit

The electrical behavior of a cell membrane can be approximated by a circuit with a capacitor connected in parallel to current sources as illustrated in Figure 2.6(a) [7]. From the equivalent circuit, the membrane current can be expressed mathematically as the following equation:

$$I_{ext} = C_m \frac{dV_m}{dt} + I_{ion}, \tag{2.2}$$

$$I_{ion} = \sum_{i=1}^{N} I_i, \tag{2.3}$$

where I_{ext} is the membrane current (inwards current positive); I_{ion} is the total ionic current (outwards current positive); V_m is the membrane potential; C_m is the

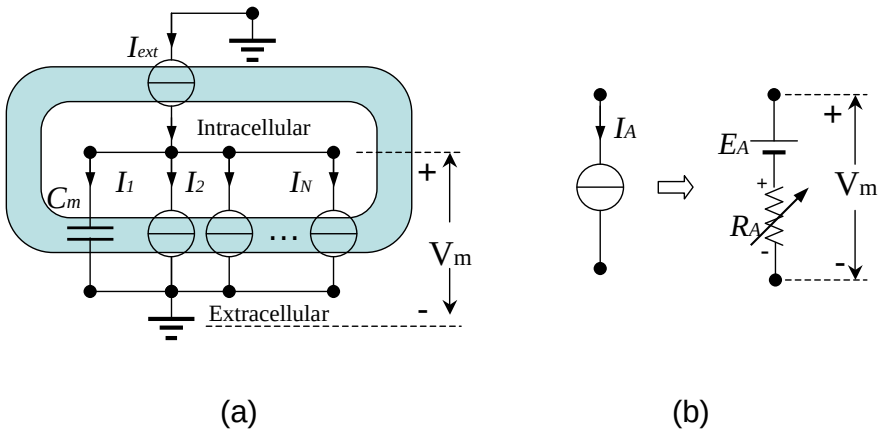

Figure 2.6: Equivalent circuits for Hodgkin-Huxley type of membrane models. (a)Membrane is approximated by a circuit with a capacitor and ionic currents. (b)Each ionic current represents a type of ionic flow and can be modeled as a nonlinear resistor connected with a Nernst potential. $R_A = 1/(\overline{g_A} y)$.

membrane capacitance; and t is time. I_{ion} characterizes the total transmembrane currents caused by different ion flows. The component I_{ext} represents the external influence applied on the cell. If all the ionic currents flow into the membrane capacitor, i.e. $I_{ext} = 0$, equation (2.2) and (2.3) simulate the electrical activity of an isolated cell. The permeability of the membrane for each type of ion varies along the changes of the membrane potential, and reversely, the varying ionic currents are attributed to the changing of the membrane potential. Next, we will discuss the mathematical model for transmembrane ionic currents.

Mathematical Models of Ionic Channels

Almost all the ionic models of biological cells are inspired by the Hodgkin-Huxley equations, which formulate in detail the ionic flows between the intracellular and extracellular media. As suggested by Hodgkin and Huxley [7][42], the ionic perme-

ability of the membrane can be expressed in terms of ionic conductances, whose values are determined by the number of opening channels, and thus can be modulated by the membrane potentials. The flow of ion is dependent on the conductances of the ion channels, and is also influenced by the ion concentration gradient and the difference of the potential across the membrane. Therefore, an ionic current can be expressed in terms of Ohm's law:

$$I_A = \overline{g_A} \cdot y \cdot (V_m - E_A), \tag{2.4}$$

where I_A is the current associated to the ion A (mA/cm^2); $\overline{g_A}$ is the maximal conductance of the corresponding ion channel (mS/cm^2); y is a dimensionless variable which represents the proportion of the ion channel in an open state ($0 < y < 1$); V_m is the membrane potential (mV); and E_A is the equilibrium potential of ion A (mV), expressed by equation (2.1). Like in the Ohm's law, an ionic current is expressed as a voltage multiplied by a conductance. This can be illustrated by Figure 2.6(b), in which R_A is the equivalent conductance of the ion channel and is described as the inverse of the product of $\overline{g_A}$ and y. The voltage across R_A is $V_m - E_A$. The sign of the calculated result from equation (2.4) indicates the direction of the ionic current. A positive sign represents an outward flow, and a negative sign represents an inward flow.

Ion channels can be governed by more than one gate [43]. A channel is only fully open when all the gating variables reach the maximum values. Therefore, y can be modeled as a product of serial gates:

$$y = y_1 y_2 ... y_M, \tag{2.5}$$

where y_i ($i = 1 \sim M$) is the open proportion of the ith gate. The behavior of the gates can present different properties, with some having more opening probability

at higher V_m, called activation gates, and the others having more opening probability at lower V_m, called inactivation gates. A current flow is totally inhibited if any one of the gates is fully closed.

The gating variable is controlled by a voltage-dependent gating mechanism for most channels. The open or closed state of the gate is determined by the membrane potential, but most of the gates do not respond instantaneously to the voltage. The time-dependence of the gating variables is conveniently modeled by a first order differential equation, as shown in the following, and its rate of change depends on two coefficients, namely a gate opening rate and a gate closing rate:

$$\frac{dy_i}{dt} = \alpha_i(1 - y_i) - \beta_i y_i, \tag{2.6}$$

where α_i is the opening rate coefficient of the ith gate and β_i is the closing rate coefficient. For the voltage-dependent gating channels, these rates are controlled by the membrane potential. In order to obtain the functions connecting α_i and β_i with the membrane potential, experimental measurements have been carried out and data processing is performed, as presented in the following.

When a cell is in the resting state, y_i has a resting value given by:

$$y_{i0} = \frac{\alpha_{i0}}{(\alpha_{i0} + \beta_{i0})}. \tag{2.7}$$

The "0" in the variable names in the above equation denotes that these are the values associated with the resting state. When the membrane potential is changed suddenly, say, to V'_m, α_i and β_i instantly take up the values related to the new potential. Therefore, the changes of y_i along the time can be expressed by the analytical solution of equation (2.6), given in the following:

$$y_i = y_{i\infty} - (y_{i\infty} - y_{i0})e^{(-\frac{t}{\tau_i})}, \tag{2.8}$$

where the time constant is:

$$\tau_i = 1/(\alpha'_i + \beta'_i), \tag{2.9}$$

and the final value is:

$$y_{i\infty} = \alpha'_i/(\alpha'_i + \beta'_i). \tag{2.10}$$

α'_i and β'_i are the opening and closing rates associated with the new membrane potential V'_m.

The time course of y_i can be measured by recording the membrane currents using the voltage clamp technique [42], and setting the command voltage to a step function jumping from the resting membrane potential to V'_m. The values of τ_i and $y_{i\infty}$ can be obtained by drawing a smooth curve from the equation (2.8) to fit the experimental data points. α'_i and β'_i can then be calculated from the following relations which are derived from equation (2.9) and (2.10):

$$\alpha'_i = \frac{y_{i\infty}}{\tau_i}, \tag{2.11}$$

$$\beta'_i = \frac{(1 - y_{i\infty})}{\tau_i}. \tag{2.12}$$

By changing the value of V'_m, we can finally collect enough α'_i and β'_i data points at different V'_m to obtain the formulas which express α_i and β_i in terms of V_m. As we will see later in the Hodgkin-Huxley and the Beeter-Reuler models, the formulas are different for different types of gates.

The derivative of α_i and β_i using the above experimental method relies on the assumption that V'_m stays fixed when a gating variable is changed from its original value to the value related to V'_m. As in the time course of an action potential, the membrane potential is always changing, violating this assumption in which case the expressions of α_i and β_i for the dynamic process may not be exactly consistent with the experimental results.

Equation Set of Ionic Membrane Model

Putting together all the information introduced above, the ionic membrane model is summarized as the following. The membrane potential is described as a capacitor charged by the ionic currents and an external current (a rewritten version of equation (2.2)):

$$\frac{dV_m}{dt} = -\frac{1}{C_m}\sum_{i=1}^{N} I_i + \frac{I_{ext}}{C_m}, \tag{2.13}$$

and each of I_i is formulated by (refer to equation (2.1) and (2.4))):

$$I_i = \overline{g_i}\prod_{j=1}^{M_i} y_{ij}(V_m - E_i) \quad (i = 1 \sim N), \tag{2.14}$$

$$E_i = \frac{RT}{zF}\ln\left(\frac{[C_i]_e}{[C_i]_i}\right). \tag{2.15}$$

The above equations assume there are N types of ionic currents, $I_1 \sim I_N$, and there are M_i number of gates, $y_{i1} \sim y_{iM_i}$ controlling the ion channel of ion type i. When the variation of ionic concentration is considered, additional equations are required to describe the extracellular and intracellular concentration of ion i, $[C_i]_e$ and $[C_i]_i$ [18][44][45]. The usage of the Nernst equation for the cases in which the concentrations are changing is an approximation. The Nernst equation is satisfied only for ions at electrochemical equilibrium, i.e., no net movement of the ion occurs [26](pp. 22).

The opening portion of individual gates can by expressed by (refer to equation (2.6)):

$$\frac{dy_{ij}}{dt} = \alpha_{ij}(1 - y_{ij}) - \beta_{ij}\cdot y_{ij} \quad (j = 1 \sim M_i), \tag{2.16}$$

$$\alpha_{ij} = F_{ij}(V_m), \tag{2.17}$$

$$\beta_{ij} = G_{ij}(V_m), \tag{2.18}$$

where F_{ij} and G_{ij} are functions of V_m, obtained from experiment as introduced

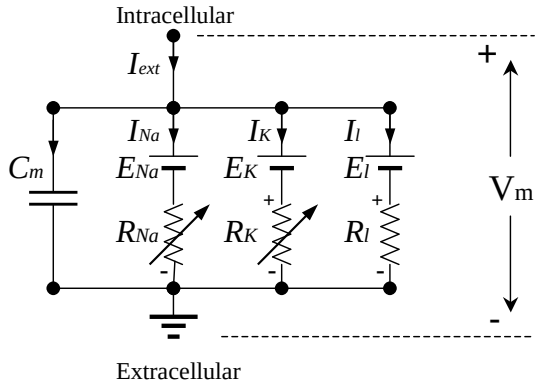

Figure 2.7: Equivalent circuits for the squid axon model of Hodgkin & Huxley. $R_{Na} = 1/(\overline{g_{Na}}m^3h)$; $R_K = 1/(\overline{g_K}n^4)$; and $R_l = 1/\overline{g_l}$.

previously.

The above set of equations describe the basic electrophysiological behavior of a single cell.

Hodgkin-Huxley Model

The Hodgkin-Huxley model describes the dynamic electrophysiology of a giant squid axon membrane from measurements of its electrical behavior using voltage clamp [7]. The membrane is modeled as a circuit consisting of a capacitor, resistors, and voltage sources, as illustrated in Figure 2.7. The membrane potential is still defined with a first-order differential equation (refer to equation (2.13)):

$$\frac{dV_m}{dt} = -\frac{1}{C_m}I_{ion} + \frac{I_{ext}}{C_m}, \tag{2.19}$$

with all the notations following the same meanings of those in equation (2.2). The model splits the ionic current into three terms:

$$I_{ion} = I_{Na} + I_K + I_l, \tag{2.20}$$

where I_{Na} is the voltage- and time-dependent sodium current, I_K is the voltage- and time-dependent potassium current, and I_l is a voltage-dependent leakage current made up by chloride and other ions. The currents are determined by the conductances g_{Na}, g_K, and g_l, respectively, as well as the difference between the membrane potential and their equilibrium potentials:

$$I_{Na} = g_{Na}(V_m - E_{Na}) = \overline{g_{Na}} m^3 h (V_m - E_{Na}), \tag{2.21}$$

$$I_K = g_K(V_m - E_K) = \overline{g_K} n^4 (V_m - E_K), \tag{2.22}$$

$$I_l = g_l(V_m - E_l) = \overline{g_l}(V_m - E_l), \tag{2.23}$$

where $\overline{g_{Na}}$, $\overline{g_K}$, and $\overline{g_l}$ are conductance constants, m, h, and n are gating variables, and E_{Na}, E_K, and E_l are the Nernst potentials.

$\overline{g_{Na}}$ and $\overline{g_K}$ represent the maximal conductances for sodium and potassium ions. The conductance for the leakage current I_l is assumed to be a constant $\overline{g_l}$. The values of these conductances are given by:

$$\overline{g_{Na}} = 120 mS/cm^2,\ \overline{g_K} = 36 mS/cm^2,\ \overline{g_l} = 0.3 mS/cm^2. \tag{2.24}$$

The ionic concentrations are supposed to be invariant in the model, and this leads to non-varying equilibrium potentials:

$$E_{Na} = 55mV,\ E_K = -72mV,\ E_l = -49.387mV. \tag{2.25}$$

The gating variables m, h, and n are controlled by their opening and closing rate coefficients, and described by the following equations:

$$\frac{dm}{dt} = \alpha_m(1-m) - \beta_m \cdot m, \tag{2.26}$$

$$\frac{dh}{dt} = \alpha_h(1-h) - \beta_h \cdot h, \tag{2.27}$$

$$\frac{dn}{dt} = \alpha_n(1-n) - \beta_n \cdot n, \tag{2.28}$$

Table 2.2: Units used in the Hodgkin-Huxley equations

Description	Unit	Description	Unit
Currents	$\mu A/cm^2$	Potentials	mV
Conductance	mS/cm^2	Time t	ms

where the voltage-dependent rate coefficients, extracted by curve fitting the experimental data [7], are given by:

$$\alpha_m = \frac{0.1(V_m+35)}{(1-e^{-\frac{V_m+35}{10}})}, \tag{2.29}$$

$$\beta_m = 4e^{-\frac{V_m+60}{18}}, \tag{2.30}$$

$$\alpha_h = 0.07e^{-\frac{V_m+60}{20}}, \tag{2.31}$$

$$\beta_h = \frac{1}{e^{-\frac{V_m+30}{10}}+1}, \tag{2.32}$$

$$\alpha_n = \frac{0.01(V_m+50)}{(1-e^{-\frac{V_m+50}{10}})}, \tag{2.33}$$

$$\beta_n = 0.125e^{-\frac{Vm+60}{80}}. \tag{2.34}$$

The units used in the Hodgkin-Huxley equations are listed in Table 2.2.

The Hodgkin-Huxley formulation assumes that the conductances of ion channels are continuous and deterministic. The assumption arises from the limitation of the experimental method, voltage clamp, which is at the cellular level and only capable of measuring the macroscopic ionic currents resulting from a population of channels. The model can not be used to describe the discrete ion channels and their random opening and closing behaviors, which are later formulated by Markov processes after the patch clamp technique was invented and studies of single channels became possible[46].

The Hodgkin and Huxley model was the first to describe the way in which individual ionic currents vary with membrane potential and time. Its structure

forms a basis for almost all models of excitable membrane behavior.

2.3.3 Beeler-Reuter Model

Next, we focus on presenting the mathematical model used in our VLSI design work, namely the Beeler-Reuter model. The employment of Beeler-Reuter's model in this work for simulating the action potential relies on its less complex formulation, while still keeping the description of the basics of membrane ionic flows between the intra- and extracellular media.

The Beeler-Reuter model was constructed to describe the electrophysiology of a mammalian ventricular myocardium in 1977 [15], and incorporated the majority of the experimental evidence achieved at that time by using the voltage-clamp techniques. The model represented a numerical simulation of the ventricular action potential, and described a system containing four types of ionic current and six gating variables. The ion flux of the model includes: a time-independent outward potassium current, I_{K1}; a time-activated potassium outward current I_{x1}; a fast voltage- and time-dependent inward current carried primarily by sodium, I_{Na}; and a slow voltage- and time-dependent inward current, I_s, carried mainly by calcium ions. The formulation of the time and voltage dependence of the gating variables in the Beeler-Reuter model follows the Hodgkin-Huxley equations.

The Beeler-Reuter model reproduces a typical ventricular myocardial action potential as shown in Figure 2.8. The threshold of excitation is -60 mV (refer to Figure 2.3(b)) [15]. During the rapid depolarization phase, the upstroke velocity is 115 V/sec. The peak of the upstroke is about 30 mV. In the plateau phase the potential reaches maximum 17 mV, and the positive potential lasts for 153 $msec$. The maximum rate of repolarization is about 11 V/sec. The duration of

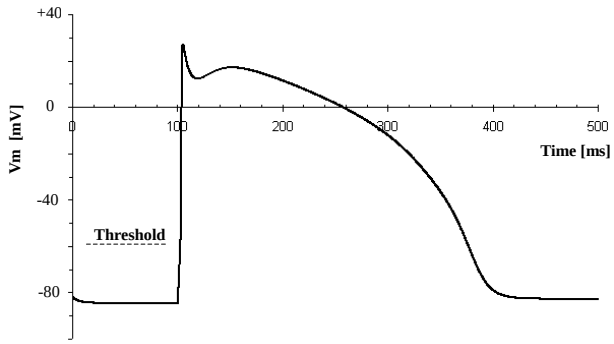

Figure 2.8: Simulated ventricular action potential using the Beeler-Reuter model.

the action potential, measured at the point where re-polarization is 90% complete, is 285 $msec$. The resting potential is -84 mV.

Ionic currents in Beeler-Reuter Model

The formulation of the potassium current I_{K1} and I_{x1} is based on the available experimental results in ventricular myocardium and follows the approach presented by McAllister et al. in [14], which mathematically described the electrophysiology of a Purkinje fiber. The experimental evidence indicates the presence of two outward currents: a background current and a single time-activated current. The background current, modeled as I_{K1}, is determined only by the membrane potential, and thus can be simply described by a function in terms of V_m. The time-activated outward current, modeled as I_{x1}, is observed to show a non-linear, rectifying, current-voltage relationship when fully activated. In order to characterize this current, the Beeter-Reuler model adopted the formulation proposed by McAllister et al., which is analogous to the linear case, as shown in the following:

$$I_{x1} = \overline{I_{x1}} \cdot x1, \tag{2.35}$$

where $\overline{I_{x1}}$ is the maximum current I_{x1} can reach, and $x1$ is a gating variable, formulated by a first-order ODE like equation (2.6). Both I_{K1} and I_{x1} are outward due to the dominating outward chemical force caused by the much larger intracellular potassium concentration compared to the extracelllar media.

The inward sodium current I_{Na} can be divided into two components [5](pp. 174), as described as follows:

$$I_{Na} = I_{NaC} + I_{NaV}. \tag{2.36}$$

I_{NaC} represents the time independent component in the sodium current, and is to reproduce the measured steady sodium leakage current. It is expressed as the following equation, which is very similar to equation (2.4), except that the membrane conductance is not controlled by any gating variables in this case:

$$I_{NaC} = \overline{g_{NaC}}(V_m - E_{Na}). \tag{2.37}$$

The second component I_{NaV} is time- and voltage-dependent, and is responsible for the fast upstroke of the action voltage. This sodium current is governed by three types of gates, described as follows:

$$I_{NaV} = \overline{g_{NaV}} m^3 hj(V_m - E_{Na}), \tag{2.38}$$

where $\overline{g_{NaV}}$ are the maximal conductance for the time-varying sodium current, and m, h, and j are the three gating variables. This formula adopts the sodium gating variable m determined for squid axon by Hodgkin & Huxley, to simulate the rapid depolarization phase (refer to equation (2.21)). The re-polarization process, in which the sodium current diminishes due to closing of the inactivation gates, cannot be simulated with a single simple parameter for the ventricular action potential. Therefore, two parameters, h and j, are introduced to describe the

process. All these three gating variables are formulated using equation (2.8), with different α_i and β_i. The Beeler-Reuter model assumes that the ionic concentration of sodium keeps unchanged during the action potential, and hence the sodium equilibrium potential E_{Na} is a constant.

The slow inward calcium current in the Beeler-Reuter model is expressed by:

$$I_s = \overline{g_s} df (V_m - E_s). \tag{2.39}$$

When all the gates are fully open, I_s is determined by the linear current-voltage relation: $\overline{g_s}(V_m - E_s)$ [47][48], in which, $\overline{g_s}$ defines the maximal conductance of calcium, and E_s is the equilibrium potential for calcium. In reality, only a fraction of the ionic channels are open, and this is described by using the gating variables d and f. Their time derivatives are functions of the membrane potential. Here we adopt the original notations from [15], and d and f correspond to y_1 and y_2 in equation (2.5). Particular attention was given by Beeler-Reuter to model the calcium equilibrium voltage, E_s, by considering the change of calcium concentration inside a cell. The formulation of the calcium concentration is a first approximation to the experimental results obtained by Bassingthwaighte & Reuter in [49], in which the interrelationship of clamped membrane potential, observed calcium current, and the equilibrium potential were studied. The influx of calcium is modeled by treating the calcium current as though it flows into a small distribution volume within the cell, from which the calcium concentration is reduced exponentially by an uptake mechanism. The equilibrium potential E_s is then calculated from the calcium concentration with the Nernst equation.

Equations and Values that Define Beeler-Reuter Model

The time derivative of the membrane potential is defined as before:

$$\frac{dV_m}{dt} = -\frac{1}{C_m} I_{ion} + \frac{I_{ext}}{C_m}, \tag{2.40}$$

but now,

$$I_{ion} = I_{K1} + I_{x1} + I_{Na} + I_s, \tag{2.41}$$

where I_{K1}, I_{x1}, I_{Na}, and I_s sum up to be the total ionic current I_{ion}, and I_{ext} is an external current that can be used as a stimulus to trigger the action potential. The membrane capacity C_m is set at 1 $\mu F/cm^2$ in the model, which is a generally accepted value for the capacity of biological membranes [15]. The unit of the membrane potential, as well as other potentials used in the model, is set to mV. The time t has a unit of ms.

Some of the equations of the ionic currents have been given previously. Here we put these current equations together and provide the values of the constants and the function expressions of some variables (the gating variables and E_s are given in equations (2.46)$\sim$(2.60)).

$$I_{K1} = 0.35\left[\frac{4(e^{0.04(V_m+85)}-1)}{e^{0.08(V_m+53)}+e^{0.04(V_m+53)}} + \frac{0.2(V_m+23)}{1-e^{-0.04(V_m+23)}}\right], \tag{2.42}$$

$$I_{x1} = \overline{I_{x1}} x_1 = \frac{0.8(e^{0.04(V_m+77)}-1)}{e^{0.04(V_m+35)}} x_1, \tag{2.43}$$

$$\begin{aligned} I_{Na} &= \overline{g_{NaC}}(V_m - E_{Na}) + \overline{g_{NaV}} m^3 hj (V_m - E_{Na}) \\ &= (0.003 + 4m^3 hj)(V_m - 50), \end{aligned} \tag{2.44}$$

$$I_s = \overline{g_s} df (V_m - E_s) = 0.09 df (V_m - E_s). \tag{2.45}$$

Since the experimental results were measured on a space-clamped patch of membrane of about one square centimeter, all ionic current in the above equations are actually current densities, and have a unit $\mu A/cm^2$.

The six gating variables $x1$, m, h, j, d, and f are defined by a set of equations similar to equation (2.6):

$$\frac{dz}{dt} = \alpha_z(1-z) - \beta_z \cdot z, \tag{2.46}$$

where z is $x1$, m, h, j, d, or f, and their opening and closing rate coefficients are described by the following equations:

$$\alpha_{x1} = \frac{0.0005e^{0.083(V_m+50)}}{e^{0.057(V_m+50)}+1}, \tag{2.47}$$

$$\beta_{x1} = \frac{0.0013e^{-0.06(V_m+20)}}{e^{-0.04(V_m+20)}+1}, \tag{2.48}$$

$$\alpha_m = \frac{-(V_m+47)}{e^{-0.1(V_m+47)}-1}, \tag{2.49}$$

$$\beta_m = 40e^{-0.056(V_m+72)}, \tag{2.50}$$

$$\alpha_h = 0.126e^{-0.25(V_m+77)}, \tag{2.51}$$

$$\beta_h = \frac{1.7}{e^{-0.082(V_m+22.5)}+1}, \tag{2.52}$$

$$\alpha_j = \frac{0.055e^{-0.25(V_m+78)}}{e^{-0.2(V_m+78)}+1}, \tag{2.53}$$

$$\beta_j = \frac{0.3}{e^{-0.1(V_m+32)}+1}, \tag{2.54}$$

$$\alpha_d = \frac{0.095e^{-0.01(V_m-5)}}{e^{-0.072(V_m-5)}+1}, \tag{2.55}$$

$$\beta_d = \frac{0.07e^{-0.017(V_m+44)}}{e^{0.05(V_m+44)}+1}, \tag{2.56}$$

$$\alpha_f = \frac{0.012e^{-0.008(V_m+28)}}{e^{0.15(V_m+28)}+1}, \tag{2.57}$$

$$\beta_f = \frac{0.0065e^{-0.02(V_m+30)}}{e^{-0.2(V_m+30)}+1}. \tag{2.58}$$

The equations for calcium intercellular concentration $[Ca]_i$ and the equilibrium potential E_s are given here:

$$E_s = -82.3 - 13.0287\ln[Ca]_i, \tag{2.59}$$

$$\frac{d[Ca]_i}{dt} = -10^{-7}I_s + 0.07(10^{-7} - [Ca]_i). \tag{2.60}$$

Table 2.3: Initial conditions for the Beeler-Reuter Model

V_m (mV)	$x1$	m	h	j	d	f	$[Ca]_i$ (mol/l)
-84	0.0088	0.01979	0.9464	0.937	0.003763	1	10^{-7}

The unit of the calcium concentration is mol/l.

When a cardiac cell is resting, the differential system is at an equilibrium state, and all the variables remain constant until the system is disturbed by a stimulus. The values of the derivative variables at a resting membrane are taken as the initial conditions for the differential equations. The initial values are obtained by setting all the time derivative terms to be equal to zero, that is the variables are not changing along the time. The initial conditions are listed in Table 2.3.

All the above equations are incorporated into the Beeler-Reuter model, which numerically allows simulation of the action potential of mammalian ventricles. The variable dependence in the equation set is illustrated in Figure 2.2. The model formulates four ionic currents, I_{K1}, I_{x1}, I_{Na}, and I_s, and describes a degree-eight system of first order differential equations, which are for the membrane potential, V_m, six gating variables, $x1$, m, h, j, d, and f, and a varying calcium concentration, $[Ca]_i$.

Chapter 3

VLSI Design of the Beeler-Reuter Model

3.1 Overview

To achieve solutions to hard mathematical problems, numerical analysis is usually carried out, in which continuous problems are discretized and functions are represented by a finite amount of data. For a given problem, the numerical analysis includes finding an iterative method that leads successive approximations to converge to solutions, discretization of continuous domains with a finite number of points, and the study of errors and numerical stability [50]. Software programming is usually involved in implementing the algorithms of numerical computation. In this chapter, we will present a very different technique for obtaining numerical solutions of mathematical problems, that is using analog VLSI circuits.

The primitives of the analog VLSI implemented computation arise from the physics of the devices, and their functioning greatly depends on the $I - V$ characteristics of the devices used, especially the transistors. Computing with VLSI

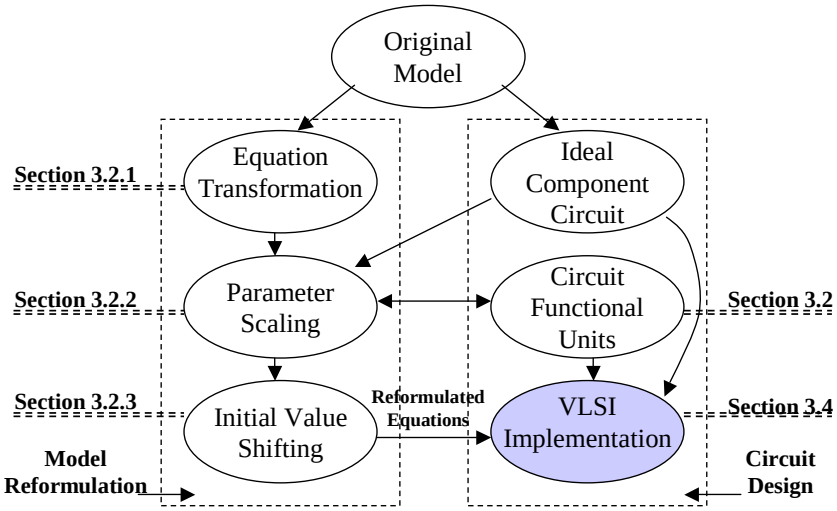

Figure 3.1: Design flow of VLSI Realization.

takes advantage of the integration properties of capacitors, and thus the calculation of complex differential equations can be greatly sped up. The methodology of the VLSI design process is illustrated in Figure 3.1. The design entry starts from the original mathematical model, i.e. the Beeler-Reuter model in our case, and splits the design flow into two paths. One is, shown on the left side of the figure, the steps of reformulating the mathematical descriptions, and the other, shown on the right side, is more directly related to the circuit designs, in which the shaded oval is our final goal. Equation transformation (the left top oval) is the process that changes equations to the formulas that are feasible for the realization using circuits. The transformed equations next go through parameter scaling, a step that scales the values of variables and parameters into proper ranges for the circuit implementation. The scaling process needs the overall consideration of all equations, and usually requires the guidance of the numerical information, which can be achieved from the simulation of ideal component circuits (the right top oval), and demands the acknowledgment of the restrictions of working ranges of

the functional circuits (the right middle oval), which is reversely decided by the scaling step for the requirement of the function types to be realized. The scaled equations then undergo initial value shifting (the left bottom oval), in which initial conditions of the differential equations are altered to all zeros for alleviating their complexity in the circuits. The reformulated equations are put into the final implementing step, which takes the functional circuit units as building blocks and the ideal component circuit as a rough blueprint.

In the rest of the chapter, we will first introduce the equation reformulation techniques, namely, equation transformation, parameter scaling, and initial value shifting, and then provide the resultant equations of the Beeler-Reuter model after applying the reformulation process. The functional circuits that realize a set of mathematical expressions are described next. The ideal component circuits and the VLSI design of the Beeler-Reuter model are presented finally.

3.2 Model Reformulation

3.2.1 Transformation of Mathematical Description

It is not surprising that circuits are capable of doing mathematical calculations. One simple example is we can perform an addition $a + b$ using a circuit in which, two current sources with values a and b are wired together with a third wire. The result of $a+b$ is then the current in the third wire. Benefited from Kirchhoff's law, linear operations, such as addition, subtraction, magnifying or diminishing with a constant factor, can be easily realized by using currents as signal representatives. Non-linear operations like multiplication and division are also possible using circuits. CMOS current multipliers have been published in [51]−[54], and multipliers

taking voltage as signals are also reported in [55]−[57], as well as current/voltage dividers [58][59]. Other operations such as exponentiation are also realizable with circuits [60][61]. However, the abundance of mathematical function types is far beyond the availability of the implementation circuits, and thus most mathematical operations do not have corresponding circuit realization. In addition, all sorts of operations can be combined and nested, which make the circuit implementation very difficult or even impossible. The complexities of employing circuits in function computation prompts the need for transforming the equations to other forms that are feasible to be mapped into circuits.

Fortunately, for most equations in the Beeler-Reuter model, methods have been found for circuit realization by straightforward means, which results in relatively simple circuit topologies. There are only two equations which really need to be transformed in the model, equations (2.42) and (2.49), as repeated in the following:

$$I_{K1} = 0.35\left[\frac{4(e^{0.04(V_m+85)}-1)}{e^{0.08(V_m+53)}+e^{0.04(V_m+53)}}+\frac{0.2(V_m+23)}{1-e^{-0.04(V_m+23)}}\right], \tag{3.1}$$

$$\alpha_m = \frac{-(V_m+47)}{e^{-0.1(V_m+47)}-1}. \tag{3.2}$$

Since the numerical range of V_m is about -90 mV to 40 mV [27], the above equations present zeros in the denominators in the working range of V_m; one is at $V_m = -23\ mV$, and the other is at $V_m = -47\ mV$, and let us call them the zero-denominator points. Note that the zeros in the denominators do not cause poles because the corresponding numerators also have zeros at the same V_m. By expanding the denominators using Tylor series around $V_m = -23\ mV$ for I_{K1} and $V_m = -47\ mV$ for α_m, the terms containing V_m can be canceled in the denominators and the numerators, and this makes the functions of I_{K1} and α_m continuous

at the zero-denominator points, i.e. we have:

$$\lim_{V_m \Rightarrow -23} I_{K1} = 2.82, \tag{3.3}$$

$$\lim_{V_m \Rightarrow -47} \alpha_m = 10. \tag{3.4}$$

However, the VLSL design of the equations of I_{K1} and α_m are very challenging, because the circuits have to handle the zero-divided-by-zero case, and there is no circuit that can directly represent the equations as a whole. Hence, we intentionally remove the zero-denominator points with the equation transformation process, in which an equation is represented by a different equation that gives values very close to those calculated from the original equations in a required working range, and this will be explained the following.

The transformation is performed using the Matlab Curve Fitting Toolbox. Due to the exponential tendency in the original data, we decide to let the fit equations still contain exponential terms, and specify the type of fit to customize the equations that favor the implementation of using emitter-coupled pairs (refer to section 3.3.2). The fit curves are also shown in Figure 3.2 and 3.3, which indicate the fits are quite successful because we nearly can not distinguish the fitted curves from the original data. The resulting transformed equations are:

$$I_{K1} = 2.742 + \frac{3.632}{e^{-0.05966(V_m - 32.77)} + 1} - \frac{5.879}{e^{0.1177(V_m + 88.23)} + 1} \tag{3.5}$$

for equation (3.1), and

$$\alpha_m = 109.7 + V_m - \frac{62.92}{e^{-0.05687(V_m + 76.2089)} + 1} \tag{3.6}$$

for equation (3.2).

The goodness of fit is evaluated with Sum of Squares Due to Error (SSE), R-square, adjusted R-square, and Root Mean Squared Error (RMSE) [62], and Table

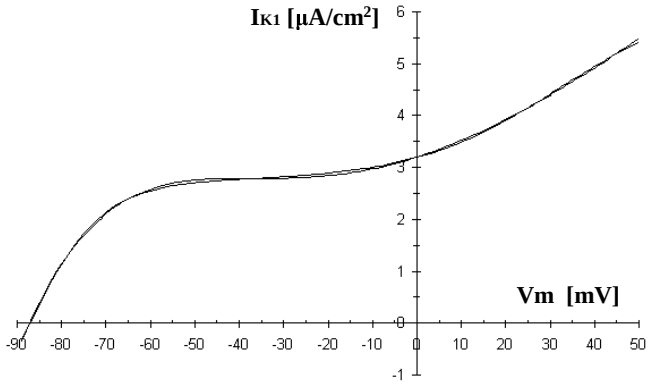

Figure 3.2: Plot of transformed I_{k1} equation and its original equation.

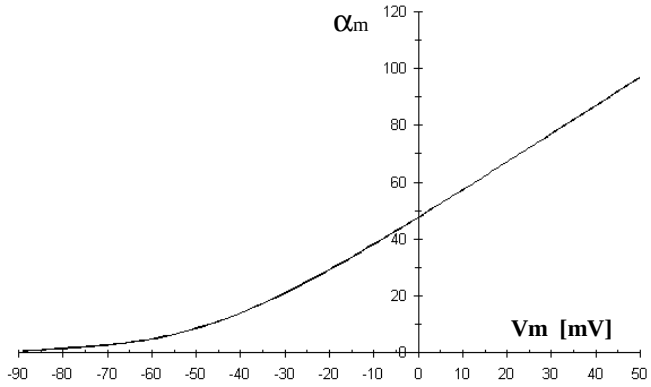

Figure 3.3: Plot of transformed α_m equation and its original equation.

Table 3.1: Statistics of goodness of fit for equations (3.5) and (3.6)

	Sum of Squares Due to Error	R-square	Adjusted R-square	Root Mean Squared Error
I_{K1}	0.09225	0.9995	0.9995	0.02634
α_m	5.621	1	1	0.2033

3.1 lists the fit statistics for equation (3.5) and (3.6). SSE is defined as the sum of squared residuals, which are the differences between the response values (the original data) and the predicted values (fitted curves). A SSE closer to 0 indicates the fit is more useful for prediction. R-square is the square of the correlation between the response values and the predicted values, and adjusted R-square is based on R-square and adjusted with the residual degree of freedom, which is defined as the number of response values minus the number of fitted coefficients estimated from the response values. Both R-square and adjusted R-square take values between 0 and 1, and a value closer to 1 means a better fit for adjusted R-square, but not always for R-square. RMSE, also known as the fit standard error, is an estimate of the standard deviation of the random component in the data. Like SSE, a RMSE closer to 0 indicates a fit that is more useful for prediction. As shown in Table 3.1, the goodness of the fit for I_{k1} and α_m is quite satisfactory, with adjusted R-square being 0.9995 for I_{k1}, and 1 for α_m.

3.2.2 Parameter Scaling for VLSI Design

Parameter scaling is needed to linearly convert the values of variables and some constants to be in the ranges that are feasible to be represented with electrical signals in circuits. As introduced in chapter 2, the units utilized in the Beeler-Reuter model are "small", for instance, the unit for the membrane potential is mV, and the unit for currents is $\mu A/cm^2$. Consequently, the values of variables in the equations are normally big, for example, the values of membrane potential can be up to about a hundred (here we care only the value, i.e. "a hundred", not its unit mV, because VLSI implementation models mathematical equations and ignores their physics meanings, and this decides that VLSI can be also used to simulate

non-electrical systems). Therefore, in order to describe such big numbers in the VLSI circuits, parameter scaling is necessary to shrink the values. In addition, we care only about the equations and the values of variables for circuit realization, and ignore their physical meanings in the model, and thus the circuit design of the cardiac cell model does not have to preserve the original electrical meanings of the variables. For example, the calcium equilibrium potential E_s does not have to be voltage in the circuit, and can be represented with a VLSI current and scaled into the normal magnitude of a current. Moreover, there are some variables, such as ionic concentrations and gating variables, that are not electrical signals. Hence, in order to represent these variables, parameter scaling is usually required to convert their values.

As introduced in chapter 2, the cardiac cell model consists of a set of equations that are inter-dependent, and no variables can be decided by a single formula. Hence, the influence of parameter scaling can be divided into two parts, one is the effect on the equation which defines the scaled variable, the other is the effect to the equation(s) that takes the variable as an input. For the first case, variables can appear as totally independent terms in equations, like equation (2.42)−(2.45) that define ionic currents, equation (2.47)−(2.59) that describe gate opening/closing rates, and equation (2.60) that expresses calcium equilibrium potential; or, the variables can be defined in time derivative equations, like equation (2.40) which defines V_m, equation (2.46) that formulates gating variables, and equation (2.60) that describes the calcium concentration.

Let us abstract an equation that formulates a variable x to be:

$$x = F(z_1, z_2, ..z_N), \tag{3.7}$$

where z_i $(i = 1, 2...N)$ are the variables that are determining x through the function

F. Suppose the equation that uses x (assuming there is only one equation that takes x as an input) can be abstracted to be:

$$y = G(x, z_1, z_2, ..z_N), \tag{3.8}$$

where y is another variable, and G is a function that relies on variable x and z_i. After performing scaling $x' = kx$, where k is a constant, equation (3.7) becomes:

$$x' = k \cdot F(z_1, z_2, ..z_N) = F'(z_1, z_2, ..z_N), \tag{3.9}$$

and the expression for y is changed to the following as a result of scaling x:

$$y = G(\frac{x'}{k}, z_1, z_2, ..z_N) = G'(x', z_1, z_2, ..z_N). \tag{3.10}$$

After scaling, reorganization, such as combining coefficients, is usually needed to construct the equations to be friendly for circuit implementing.

The above scaling technique may sound quite simple, however, the parameter scaling process for circuit design requires comprehensive consideration of all variables, constant terms, and coefficients in the equations, and demands the acknowledgment of the existence and limitations of available mathematical functions in the form of circuits and apply the acknowledgment into scaling to fit the working ranges of the circuits. To scale an equation set, like the Beeler-Reuter model, in which more than twenty variables and equations are involved, a simulation of its non-scaling ideal components with PSpice (or with Matlab SimuLink alternatively) is usually necessary to carry out in order to achieve useful numerical ranges before the actual scaling can be done.

The representatives of variables in circuits (either voltages or currents) are also decided during the scaling process, because VLSI currents are normally small numerically, for example in the magnitude of several 10^{-6} with unit A, and the values

of voltages are big, for instance in the magnitude of a few decimals with unit V. The electrical representatives of some variables may be pre-determined by their appearances in equations, relying on the convenience of their VLSI implementation. For example, we select calcium concentration $[Ca]_i$ to be a current, because it appears in a logarithms in equation (2.59) and logarithms can be realized using a bipolar transistor whose base-emitter voltage is decided by the logarithm of its collector current. Another example, the equations of the opening/closing gate ratios (equations (2.47)−(2.58)) have many exponential terms whose powers contain V_m, and this leads to the desirability to let V_m to be a voltage in circuits due to the circuit realization of an exponential being, again, via bipolar transistors.

The above discussion of parameter scaling does not include the scaling for time. Time scaling can be treated absolutely independent of the scaling of other parameters, since it only affects the width of a signal on the time axis, and can be easily adjusted by multiplying the capacitance values of all the capacitors that realize time derivatives by a constant.

3.2.3 Initial Value Shifting

As introduced in chapter 2, the variable values associated with the resting state of a membrane are taken as the initial conditions of the differential system, and their values are listed in Table 2.3. This means that a reset mechanism is required to set the initial states of the devices which implement the time derivative. In the case that capacitors are used to realize the time derivative in differential equations, the initial voltages across the capacitors need to be set. This requirement brings complexity for circuits. It is necessary for the reset circuits to work as batteries to provide desired voltages and currents for charging the capacitors at a reset stage,

and also to be able to be switched off (or not influence) the capacitors when the circuits are operating as an activated cell. Here we propose an initial value shifting method to avoid the reset circuits. We shift the resting state of the differential system to the origin and make the initial conditions all zeros while keeping the same waveform of V_m created by the model.

In the Beeler-Reuter model, there are eight variables that are time dependent, these being the membrane potential V_m (equation (2.40)), six gating variables, $x1$, m, h, j, d, and f (equation (2.46)), and a varying calcium concentration, $[Ca]_i$ (equation (2.60)). Their equations are special cases of:

$$\begin{cases} b_0 \frac{dx}{dt} = b_1 + b_2 x, \\ x(t=0) = x_0, \end{cases} \tag{3.11}$$

where b_0 is a constant, b_1 and b_2 can be constants or variables that do not explicitly depend on time. In the case of V_m, the second term on the right side $b_2 x$ does not exist, i.e. $b_2 = 0$. The initial value shifting takes place by replacing x with $\widehat{x} + x_0$, that is, setting $x = \widehat{x} + x_0$, equation (3.11) then becomes:

$$\begin{cases} b_0 \frac{d\widehat{x}}{dt} = b_1 + b_2(\widehat{x} + x_0), \\ \widehat{x}(t=0) = 0. \end{cases} \tag{3.12}$$

Equation (3.11) and (3.12) can be both mapped into the circuit depicted in Figure 3.4, by setting different parameters. For simplicity of discussion, here we ignore the scaling issue, and assume the parameters in the equation are suitable for VLSI realization. In Figure 3.4 the capacitor C, with a capacitance of b_0, is charged by a current source b_1 and a controlled output current from $G1$, whose transconductance is equal to $b2$. The output current from $G1$ is $b_2(x + V_a)$, where x is the voltage across C and V_a is a bias voltage. The linear voltage to voltage converter E, serving as the output stage of the whole circuit, takes the input x and

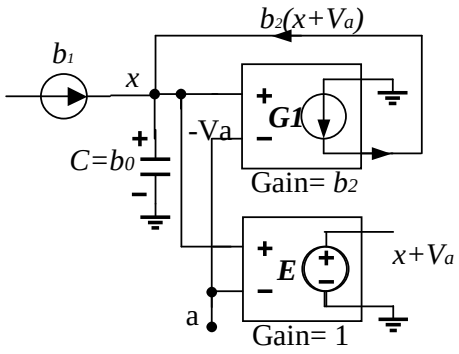

Figure 3.4: Initial value shifting for differential equations.

$-V_a$ and subtracts them to create the output. When V_a is connected to ground, i.e. $V_a = 0$, the diagram represents equation (3.11) and the initial voltage of C is required to be set to x_0. The output of E is then $x - 0 = x$. Following equation (3.12), the initial condition shifting process is performed by setting V_a to x_0 in the circuit. The initial voltage of C then can be left to 0, with the output of E being unchanged: $\widehat{x} + V_a = (x - x_0) + x_0 = x$.

The initial value shifting method takes the advantage of the circuit realization of the linear transconductance and linear voltage converter, which have a pair of input voltages whose difference linearly determines the output. It is worth mentioning that the presented method is not limited to shifting the initial value for the mathematical description with the form of equation (3.11). It can be extended to more general situations as formulated with:

$$b_0 \frac{dx}{dt} = F(x) \quad (x(t = 0) = x_0). \tag{3.13}$$

The equation after the initial value shifting is then written as:

$$b_0 \frac{d\widehat{x}}{dt} = F(\widehat{x} + x_0) \quad (\widehat{x}(t = 0) = 0). \tag{3.14}$$

3.2.4 Reformulated Beeler-Reuter Equations for VLSI Design

After applying equation transformation, parameter scaling, and capacitance initial value shifting on the Beeler-Reuter model, the resulting equations can be mapped directly into circuits. The new set of equations have one-to-one correspondence to equations (2.40)−(2.60), with (2.42) and (2.49) being replaced by (3.5) and (3.6). To avoid redundancy, we list in Table 3.2 only the equations that relate the new variables, denoted with a single quotation mark, with the original variables. These equations result from the parameter scaling and initial value shifting, and can be taken into the original model equations (except replacing (2.42) and (2.49) with (3.5) and (3.6)) to create a new set of equations, which are the ones we use for VLSI design. The new equations represent a differential system that has all-zero initial conditions. In Table 3.2, the second column shows the variable conversions, and the third column lists the electrical representative of the variables in our VLSI circuits.

3.3 Circuit Blocks of Function Units

In this section we will present the sub-circuits that implement the mathematical functions needed by the Beeler-Reuter cardiac cell model. The determination of the necessary functions is dependent on the mathematical description of the original model formulations and also the parameter scaling process, in which the electrical representatives of the signals are decided. The circuits of the function units are summarized in Table 3.3, and most of them are based on existing circuit architectures, with some being modified in order to obtain required functions or

Table 3.2: Relations of original variables and the scaled and shifted variables, and their electrical representative in circuits.

Variable	Conversion Equation	Circuit Representative
V_m	$= 100V'_m$	Voltage
I_{ion} (includes I_{K1}, I_{x1}, I_{Na}, and I_{Ca})	$= 10^6 I'_{ion}$	Current
z (includes $x1$, m, h, j, d, and f)	$= 2 \times 10^5 z'$	Current
α_{x1}	$= 10^3 \alpha'_{x1}$	Current
β_{x1}	$= 10^3 \beta'_{x1}$	Current
α_m	$= 10^7 \alpha'_m$	Current
β_m	$= 10^7 \beta'_m$	Current
α_h	$= 2 \times 10^5 \alpha'_h$	Current
β_h	$= 2 \times 10^5 \beta'_h$	Current
α_j	$= 2 \times 10^4 \alpha'_j$	Current
β_j	$= 2 \times 10^4 \beta'_j$	Current
α_d	$= 10^4 \alpha'_d$	Current
β_d	$= 10^4 \beta'_d$	Current
α_f	$= 10^3 \alpha'_f$	Current
β_f	$= 10^3 \beta'_f$	Current
E_s	$= 10^8 E'_s$	Current
$[Ca]_i$	$=[Ca]'_i$	Current

Table 3.3: Summary of function circuits. C_i $(i = 1, 2...N)$ are constant.

Function	Description	Circuit
$I_{out} = C_1 V_{in}$	Linear voltage to current converter	Figure 3.5(a)
$V_{out} = V_{in1} \pm V_{in2}$	Voltage adder/subtractor	Figure 3.6
$V_{out} = V_{in}$	Voltage buffer	Figure 3.7
$I_{out} = \frac{C_1}{e^{C_2(V_{in}+C_3)}+1}$	Sigmoid function	Figure 3.12
$I_{out} = C_1 e^{(C_2 V_{in}+C_3)}$	Exponential function	Figure 3.13
$I_{out} = \frac{C_1 e^{C_2 x}}{e^{C_3(V_{in}+C_4)}+1}$	Exponentialized sigmoid function	Figure 3.12, 3.13
$V_{out} = C_1 \ln(C_2 I_{in})$	Logarithm function	Figure 3.14
$I_{out} = \frac{I_{in1} I_{in2}}{C_1}$	Two inputs current multiplier	Figure 3.15
$I_{out} = \frac{I_{in1} I_{in2} I_{in3} ... I_{in,N+1}}{C_1 C_2 ... C_N}$	Multiple inputs current multiplier	Figure 3.17

achieve higher accuracy in the circuit realization of the mathematical expressions. The working ranges of the circuits are discussed in terms of the accuracy the circuit implementation of the functions can reach. A scheme for implementing big capacitors with small capacitors using a NPN-based circuit is introduced at the end of this section. For the readers that are familiar with VLSI circuits, this section can be skipped to continue the reading from section 3.4, in which the circuits for realizing the cardiac cell model are presented.

The circuits presented here are not limited by a particular fabrication process and can be implemented by any BiCMOS technologies. For the technologies with smaller feature sizes, VLSI circuits can be more densely integrated and are more power efficient. For our heart model application, we give the first priority to the accuracy of the circuit realization of mathematical functions, and hence we prefer to using technologies with larger feature sizes, which have less high order

effects introduced by short-channel MOS devices and thus are more feasible to implement equations with their I-V characteristics. As an example, we select AMI Semiconductor 1.5 μm ABN technology to realize the cardiac cell model. AMI 1.5 μm ABN process is a n-well CMOS process with two metal layers and two poly layers. It provides an NPN option and also can be used to make capacitors with PiP (poly2 over insulator over poly).

The presented VLSI circuit of the cardiac cell model is essentially MOSFET. Many circuit blocks in our VLSI design use the voltage-controlled-current properties of MOS devices, and take advantage of the thin insulating layers under the gates and the resulting good isolation MOS devices provide to the preceding and the succeeding circuits. We select current to represent signals in most situations as shown in Table 3.2, because current allows performing addition and subtraction simply, and can represent positive and negative numbers with large ranges easily. This is opposite to voltages, whose magnitudes are limited by the dynamic range of circuits, which is highly dependent on the supply voltages. Therefore, most arithmetic circuit blocks presented take currents as input and output. Currents also can be consumed by capacitors for integration. NPN devices are used in our application to realize exponential functions. It is worth mentioning that the proposed circuits with NPN transistors do not depend on the reverse saturation currents of the devices, and hence the circuits can be transmitted to other fabrication technologies with minimal modification of the bipolar devices.

In the rest of this section, we will introduce the basic arithmetic function blocks used in the VLSI design of the Beeler-Reuter model. The function circuits can be organized into three categories: linear function circuits, exponential circuits, and multipliers. Table 3.3 summaries the functions of the presented circuits.

The following presentation will frequently use the equations that describe the $I-V$ characteristics of MOS and NPN transistors. To avoid verbosity, some commonly used symbols and notational conventions are listed alphabetically below:

- C_{ox} is the gate oxide capacitance per unit area.
- I_{ci} (or I_c) is the collector current of NPN transistor Qi (i=1,2...).
- I_{Mi} is the drain-to-source current of transistor Mi (i=1,2...).
- I_{s0} is the reverse saturation current of a NPN transistor.
- K_{ni} (or K_n, K_{pi}, K_p, K) is the fabrication-dependent parameter of NMOS device Mi (i=1,2...): $K_{ni} = \frac{\mu_n C_{ox}}{2}\frac{W_i}{L_i}$.
- μ_n (or μ_p) is the mobility of electrons (holes).
- L_i (or L) is the gate length of transistor Mi (i=1,2...).
- λ_{ni} (or λ_n, λ_{pi}, λ_p, λ) is the channel-length modulation parameter of NMOS (or PMOS) transistor Mi (i=1,2...).
- V_{gsi} is the gate-source voltage of transistor Mi (i=1,2...).
- V_{bei} is the base-emitter voltage of NPN transistor Qi (i=1,2...).
- V_{tni} (or V_{tpi}, V_{tn}, V_{tp}, V_t)is the threshold voltage of NMOS (or PMOS) transistor Mi (i=1,2...).
- V_T is the thermal voltage.
- W_i (or W) is the gate width of transistor Mi (i=1,2...).

3.3.1 Linear Function Circuits

With currents being signal representatives, the linear operations, such as addition, subtraction, and multiplication with a constant, can be easily realized using current mirrors and wire connections, governed by the Kirchhoff's law. In the following, we will introduce the circuits that perform linear operations based on voltage inputs or (and) outputs.

Linear Voltage to Current Converter (VCC)

One of the techniques to realize a linear voltage to current converter (VCC) is using differential pairs as shown in Figure 3.5(a) [63]. $M1$ and $M2$ are the NMOS input stage, whose tail current I_0 is provided by the current sink transistor $M9$. The current distribution in the two input transistors $M1$ and $M2$ is controlled by their gate voltages, and these two currents are transmitted to the output stage by current mirrors that are composed of $M3 - M8$. The output I_{out} current is the difference between the two currents passing through transistors $M6$ and $M8$. By varying the sink current I_0, and the amplification factors of the current mirrors, the transconductance of the differential pair can be adjusted.

Assume that $M1$ and $M2$ are identical and both working in the saturation region, neglecting the channel length modulation, the source currents of $M1$ and $M2$ are expressed by:

$$I_{M1} = K(V_{gs1} - V_t)^2 = K(\Delta V + V_{gs2} - V_t)^2, \tag{3.15}$$

$$I_{M2} = K(V_{gs2} - V_t)^2, \tag{3.16}$$

where ΔV is the difference between the two voltage inputs:

$$\Delta V = V_+ - V_- = V_{gs1} - V_{gs2}. \tag{3.17}$$

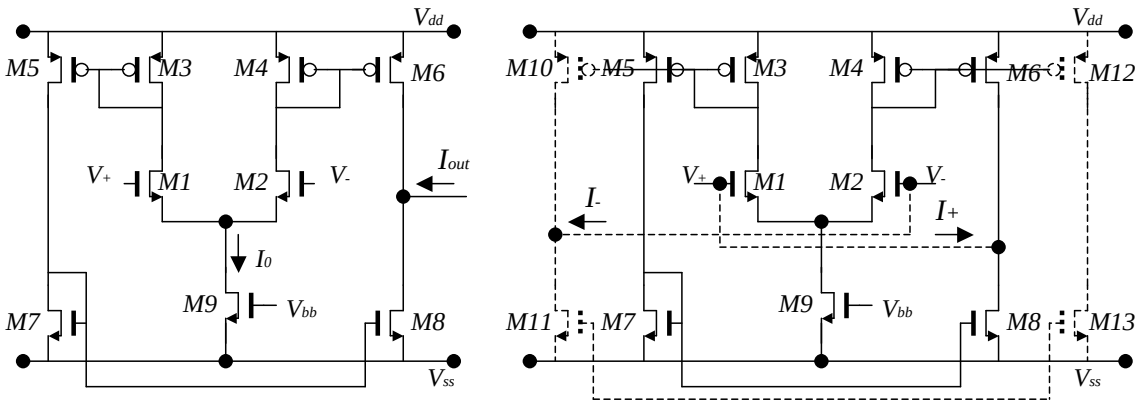

Figure 3.5: CMOS differential pair works as a linear voltage to current converter. (a)Differential pair circuit. (b)Altered differential pair that works as a linear resistor.

From equations (3.15) and (3.16), we can derive the following equations by using $I_0 = I_{M1} + I_{M2}$:

$$I_{M1} = \frac{1}{2}\left(I_0 + K\Delta V\sqrt{\frac{2I_0}{K} - \Delta V^2}\right), \tag{3.18}$$

$$I_{M2} = \frac{1}{2}\left(I_0 - K\Delta V\sqrt{\frac{2I_0}{K} - \Delta V^2}\right). \tag{3.19}$$

Therefore, the transconductance of the circuit is expressed by:

$$g_m = \frac{I_{M8} - I_{M6}}{\Delta V} = A\frac{I_{M1} - I_{M2}}{\Delta V} = AK\sqrt{\frac{2I_0}{K} - \Delta V^2}, \tag{3.20}$$

where A is the amplification factor of the current mirrors composed of $M3 - M8$, and $M4$ and $M6$. From equation (3.20), we can derive the range of ΔV for a given linearity requirement on the transconductance by a Tylor series expansion of the square root:

$$\Delta V^2 < \eta\frac{4I_0}{K}, \tag{3.21}$$

where η is the maximum allowable transconductance difference in percentage, i.e. $\eta = max((g_{m0} - g_m)/g_{m0}) * 100\%$ where g_{m0} is the transconductance at $\Delta V = 0$,and g_m is an arbitrary transconductance.

Ignoring the slight changes in I_0 caused by the variation of V_{ds9}, the non-linearity of the transconductance relies on the term ΔV^2 in equation (3.20). Hence, according to the equation, in order to achieve a good linearity of the transconductance, the magnitude of the differential input ΔV needs to be kept much smaller than $\frac{2I_0}{K}$, or at the same ΔV, I_0 can be enlarged, under the restriction that all transistors are still in the saturation region.

The circuit of the differential pair can be used to implement linear resistors, as illustrated in Figure 3.5(b). The transistors and wires drawn with dotted lines are newly added upon the circuit shown in Figure 3.5(a). The added transistors make the circuit topology of the left side and the right side perfectly symmetrical, and thus $I_+ = -I_-$. When $V_+ > V_-$, the current flowing into the V_+ port is provided by $M6$ and $M8$, and the current flowing out of the V_- port is sourced from $M10$ and $M11$. The working condition of the circuit in Figure 3.5(b) is that the inputs V_+ and V_- are within the range which makes the output transistors $M6$, $M8$, $M10$ and $M11$ working in the saturation region.

Linear Current to Voltage Converter (CVC)

The circuit of a linear current to voltage converter, shown in Figure 3.6, is proposed in [64]. It is composed of two NMOS and two PMOS transistors. $M1$ and $M2$ are identical in size. $M3$ and $M4$ are also identical in size, and are connected like a current mirror. V_a is a bias voltage, which determines the current in $M1$. When the input current I_{in} is zero, the currents in all the transistors are the same, and

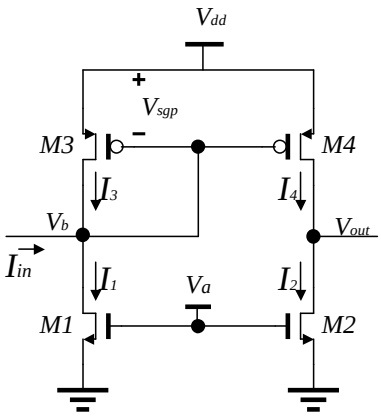

Figure 3.6: Linear current to voltage converter.

thus $V_{out} = V_b$ when there is no load drawing current from the output. Let us use V_{out0} to denote the output voltage associated with $I_{in} = 0$, and I_Q to represent the drain current flowing in $M1$ when $I_{in} = 0$.

If there is a small negative input current, V_b can be taken as nearly unchanged due to the small current I_{in}. Since the current I_4 is mirrored from I_3, and I_2 is mirrored from I_1, when the output does not take any current, the output voltage V_{out} needs to increase significantly to cancel out the difference between I_2 and I_4 using the channel length modulation effect. As we will see in the following, the change in the output voltage is almost linearly decided by the input current.

For the transistors $M1$ and $M3$, the following equations describe their currents:

$$I_3 + I_{in} = I_1, \tag{3.22}$$

$$I_1 = K_n \times (V_a - V_{tn})^2(1 + \lambda_n V_b), \tag{3.23}$$

$$I_3 = K_p \times (V_{dd} - V_b - V_{tp})^2(1 + \lambda_p(V_{dd} - V_b)). \tag{3.24}$$

Similarly the currents in $M2$ and $M4$ are expressed by the following equations:

$$I_2 = I_4, \tag{3.25}$$

$$I_2 = K_n \times (V_a - V_{tn})^2(1 + \lambda_n V_{out}), \tag{3.26}$$

$$I_4 = K_p \times (V_{dd} - V_b - V_{tp})^2(1 + \lambda_p(V_{dd} - V_{out})). \tag{3.27}$$

From equation (3.22)−(3.27), we can derive the relation of V_{out} vs. I_{in} as follows:

$$I_{in} = (V_b - V_{out})\frac{K_n(V_a - V_{tn})^2(\lambda_n + \lambda_p + \lambda_n\lambda_p V_{dd})}{1 + \lambda_p(V_{dd} - V_{out})}. \tag{3.28}$$

If we neglect the change of V_b caused by the small input I_{in}, that is, take $V_b = V_{out0}$, and treat $\lambda_p(V_{dd} - V_{out})$ as much less than 1 and, thus, ignore it in the denominator of equation (3.28), the change of the transimpedance, i.e. the relation of the change of the output and the input, then becomes purely linear, which is expressed by:

$$\frac{\Delta V_{out}}{I_{in}} = -\frac{1}{K_n(V_a - V_{tn})^2(\lambda_n + \lambda_p + \lambda_n\lambda_p V_{dd})} \tag{3.29}$$

$$\simeq -\frac{1}{I_Q(\lambda_n + \lambda_p)}, \tag{3.30}$$

where ΔV_{out} is the change in V_{out}, caused by I_{in} and defined as: $\Delta V_{out} = V_{out} - V_{out0}$.

The nonlinearity of the ΔV_{out} to I_{in} ratio comes from the terms $\lambda_p(V_{dd} - V_{out})$ and V_b in equation (3.28). $\lambda_p(V_{dd} - V_{out})$ can cause a variance of the ΔV_{out}-to-I_{in} ratio on the order of 1% assuming $\lambda_p \simeq 0.01$. V_b can be derived from equation (3.22)−(3.24) and is determined by the following equation:

$$K_p \times (V_{dd} - V_b - V_{tp})^2(1 + \lambda_p(V_{dd} - V_b)) + I_{in} = K_n \times (V_a - V_{tn})^2(1 + \lambda_n V_b). \tag{3.31}$$

Take $\lambda_n = \lambda_p \approx 0$ in equation (3.31), V_b is expressed by:

$$V_b = (V_{dd} - V_{tp}) - \frac{1}{\sqrt{K_p}}\sqrt{K_n(V_a - V_{tn})^2 - I_{in}}. \tag{3.32}$$

According to equation (3.32), I_{in} needs to be small compared to $K_n(V_a - V_{tn})^2$ in order to diminish the dependence of V_b on I_{in}. $K_n(V_a - V_{tn})^2$ can be approximated as the current in $M1$ when $I_{in} = 0$, and hence the condition for a good linearity of

the ΔV_{out}-to-I_{in} ratio is that I_{in} needs to be kept small compared to I_Q, i.e. the current of $M1$ when $I_{in} = 0$.

V_{out0} usually varies with the selection of different sizes of the transistors for a current to voltage converter (CVC), and the transistor sizes also decide the values of the ΔV_{out}-to -I_{in} ratio. It is not easy to adjust the circuit to achieve both the specified ΔV_{out}-to-I_{in} ratio and V_{out0} with a restricted value. Therefore, in the heart VLSI circuits, CVCs are employed in pairs, and this will be discussed in section 3.3.2.

A working condition of the CVC circuit is that the output does not take any current, due to the great sensitivity of the output voltage to the current changes in $M2$ and $M4$. In order to provide a current to a succeeding circuit that utilizes the linearly changed output voltage from a CVC, it is necessary to add a voltage buffer to copy the output voltage and also to deliver a certain among of current. The voltage buffer is introduced in the following.

Voltage Buffer

An ordinary CMOS voltage buffer [65], shown in Figure 3.7(a), is composed of complementary source followers. On the input side, the current of $M1$ and $M3$ is decided by the bias current I_{n0} and I_{p0}, and $I_{n0} = I_{p0}$. Because $M2$ is set identical to $M1$, and $M4$ is to $M3$, the currents I_{n0} and I_{p0} are fully mirrored on the output side if no output current is drawn, and hence $V_{out} = V_{in}$. The circuit has very low voltage offset, with the voltage offset mainly due to transistor mismatch [66].

In the VLSI design of the heart model, the voltage buffer services as a stage that isolates the next circuit block, which takes voltage as an input but also consumes some amount of current depending on the input voltage, from the previous stage.

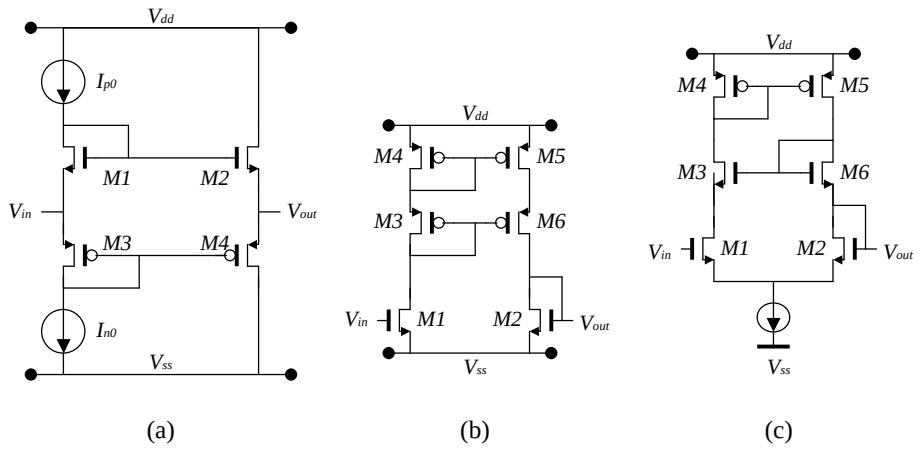

Figure 3.7: Voltage buffer. (a)Traditional voltage buffer. (b)Proposed voltage buffer for the heart implementation. (c)Another version of proposed voltage buffer, modified for reducing drain-source voltage difference of $M1$ and $M2$.

For a circuit like the CVC presented in the previous section, its output voltage can be easily distorted by its output current. Therefore, the buffer is required to take no current from the previous stage, or equivalently the two bias currents I_{n0} and I_{p0} need to be matched very well in order to prohibit current flowing through the input terminal. Since it is unavoidable for the non-ideal bias currents to vary a little bit with the changing input voltage, the requirement of no input current is obtained by letting the changes of I_{n0} and I_{p0} be in the same direction and also by the same amount which brings much complexity to the transistor circuits. This makes the ordinary voltage buffer presented in [65] not applicable to our implementation. In order to achieve high enough input resistance, the gate of a NMOS device, which does not draw any current, is selected as the input stage of the proposed buffer. The topology of the circuit is depicted in figure 3.7(b). Transistors $M3 - M6$, working in the saturation region, compose a cascode current mirror, which keeps the currents going through $M1$ and $M2$ the same. The output transistor $M2$

is identical to $M1$. When the effect of the drain-source voltage on the current is ignored, the gate-source voltages are the same for $M1$ and $M2$ due to their identical currents, and this results in $V_{out} = V_{in}$. Suppose the current required by the next stage is much less than the current provided by $M6$, the influence of the output current to the output voltage is then very small and can be neglected. This assumption can be satisfied by selecting the parameters of $M1$ to let the current in $M6$ much bigger than the required current output.

The $I - V$ characteristics of $M1$ and $M2$ can be described as follows, with the effect of their drain-source voltages taken into account:

$$\begin{aligned} I_{M1} &= K(V_{in} - V_{ss} - V_t)^2(1 + \lambda V_{ds1}) \qquad (3.33) \\ &= K(V_{in} - V_{ss} - V_t)^2(1 + \lambda V_{ds2} + \lambda \Delta V_{ds}), \\ I_{M2} &= K(V_{out} - V_{ss} - V_t)^2(1 + \lambda V_{ds2}) \qquad (3.34) \\ &= K(V_{in} + \Delta V_{out} - V_{ss} - V_t)^2(1 + \lambda V_{ds2}), \end{aligned}$$

where ΔV_{out} is the output error caused by the channel modulation effect, $\Delta V_{out} = V_{out} - V_{in}$, and ΔV_{ds} is the difference of the drain-source voltages of $M1$ and $M2$ is $\Delta V_{ds} = V_{ds1} - V_{ds2}$. Ignoring the current difference of I_{M1} and I_{M2} introduced by the non-idealism of the current mirror, after combining equations (3.33) and (3.34), and replacing V_{ds2} (i.e. V_{gs2}) with $V_{in} - V_{ss}$, we express ΔV_{out} in terms of ΔV_{ds}:

$$\Delta V_{out} = (V_{in} - V_{ss} - V_t)(\sqrt{1 + \frac{\lambda \Delta V_{ds}}{1 + \lambda(V_{in} - V_{ss})}} - 1), \qquad (3.35)$$

which can be expanded with Taylor approximation into:

$$\begin{aligned} \Delta V_{out} &\simeq \frac{1}{2}(V_{in} - V_{ss} - V_t) \times \frac{\lambda \Delta V_{ds}}{1 + \lambda(V_{in} - V_{ss})} \qquad (3.36) \\ &\simeq \frac{1}{2}(V_{in} - V_{ss} - V_t) \times \lambda \Delta V_{ds}. \end{aligned}$$

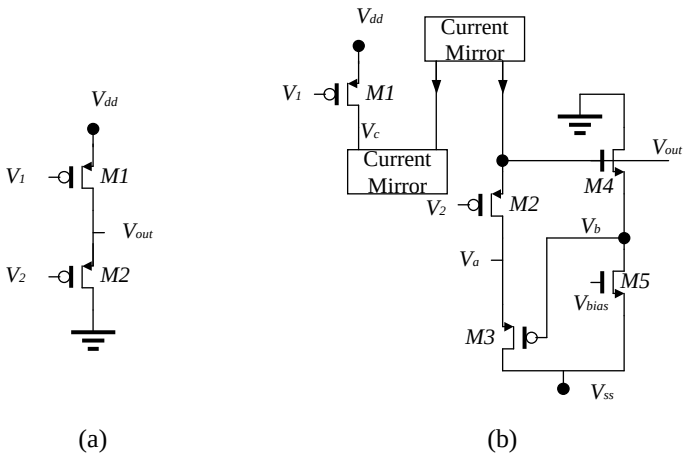

Figure 3.8: Voltage subtractor. (a)Maundy voltage subtractor. (b)Improved voltage subtractor.

Equation (3.36) expresses the voltage offset in the output in terms of the difference in the drain-source voltages of $M1$ and $M2$. The reduction of the average of ΔV_{ds} can efficiently minimize the voltage offset. Figure 3.7(c) shows another version of the proposed voltage buffer, which efficiently reduces the magnitude of ΔV_{ds}. The currents in the NMOS transistors $M3$ and $M6$ are the same as the currents in $M4$ and $M5$, and, thus, the gate-source voltages of $M3$ and $M6$ are equal. Therefore, the drain-source voltages of $M1$ and $M2$ are equal. I_{bias} is used to constrain the currents in $M1$ and $M2$.

Voltage Subtractor and Adder

Figure 3.8(a) illustrates the idea of a voltage subtractor presented by Maundy in [55], where the circuit is introduced to make low-voltage multipliers. The sizes $M1$ and $M2$ are equalized, and both transistors work in the saturation region. When the channel length modulation effect is not considered, the following equations are

satisfied:

$$\begin{cases} I_{M1} = K_p(V_{gs1} - V_{tp})^2 = K(V_{dd} - V_1 - V_{tp})^2 \\ I_{M2} = K_p(V_{gs2} - V_{tp})^2 = K(V_{out} - V_2 - V_{tp})^2 \\ I_{M1} = I_{M2} = I \end{cases} \tag{3.37}$$

$$\Rightarrow V_{out} = V_{dd} - V_1 + V_2. \tag{3.38}$$

Hence this circuit operates like a subtractor. Multiples of this circuit can be cascaded to construct mathematical functions with mixed additions and subtractions [55].

The performance of Maundy's voltage subtractor is degraded due to the channel length modulation effect. If the channel length modulation effect is taken into account, the equations for $M1$ and $M2$ become the following:

$$\begin{cases} I_{M1} = K_p(V_{dd} - V_1 - V_{tp})^2(1 + \lambda_p(V_{dd} - V_{out})), \\ I_{M2} = K_p(V_{out} - V_2 - V_{tp})^2(1 + \lambda_p V_{out}). \end{cases} \tag{3.39}$$

Assume there is a drop of amount ΔV_1 on input V_1, and input V_2 stays unchanged. With $I_{M1} = I_{M2}$, according to equation (3.39), V_{out} does not increase the same amount as V_1 reduces, and the difference between the increase and that of the ideal case is on the same order as λ_p or bigger, decided by the values of V_1, V_2, and V_{dd}. We propose two methods to improve Maundy's subtraction circuit, based on considering the two transistors $M1$ and $M2$ separately. $M1$ is the key transistor that decides the current of the circuit. In the non-ideal case, the output voltage can influence the current. If $M1$ can be replaced by a perfect current source, and the value of the current is independent of the output, the inaccuracy introduced by the drain-source voltage of $M1$ can be eliminated. For $M2$, if a feedback circuit can be added to control the drain voltage of $M2$ to make it follow V_{out}, the channel length modulation effect caused by the changing V_{ds2} can be diminished.

Figure 3.8(b) depicts the circuit of the improved voltage subtractor. In the circuit, $M1$ and $M2$ serve the same functions as in Figure 3.8(a). Two current mirrors are added to isolate the input $V1$ from the output. The lower current mirror is required to employ large size transistors to minimize the change of V_c caused by the change of V_1. Cascode current mirrors are also recommended to reduce the channel modulation effect on the current. The transistors $M3 - M5$ consist of a feedback loop that makes V_a follow V_{out}. $M4$ and $M5$, the same in size, incorporate a subtraction circuit just like the one shown in Figure 3.8(a), except NMOS transistors are used this time. Hence the following equation is approximately satisfied following equation (3.38):

$$V_{out} - V_b \approx V_{bias} - V_{ss} = \text{constant}. \tag{3.40}$$

According to the equation, when V_{out} changes, V_b changes in the same direction with about an identical amount. If $M3$ is big in size, and the changed current caused by V_1 results in little change on V_{gs3}, then V_a can be taken as following V_b. As a result, V_a follows V_{out}, and the drain-source voltage effect of $M2$ is mitigated by the feedback circuit comprised of $M3 - M5$.

Another implementation of a voltage subtractor (or adder) is from [67], called the pool circuit, which, as depicted in Figure 3.9, consists of two differential pairs. The currents of $M1$ and $M2$, derived with the same method for equation (3.23), are described be the following equations:

$$I_{M1} = \frac{1}{2}\left(I_{B1} + K_n \Delta V \sqrt{\frac{2I_{B1}}{K_n} - \Delta V^2}\right), \tag{3.41}$$

$$I_{M2} = \frac{1}{2}\left(I_{B1} - K_n \Delta V \sqrt{\frac{2I_{B1}}{K_n} - \Delta V^2}\right), \tag{3.42}$$

where ΔV is the difference of the gate voltages of $M1$ and $M2$:

$$\Delta V = V_1 - V_{out}. \tag{3.43}$$

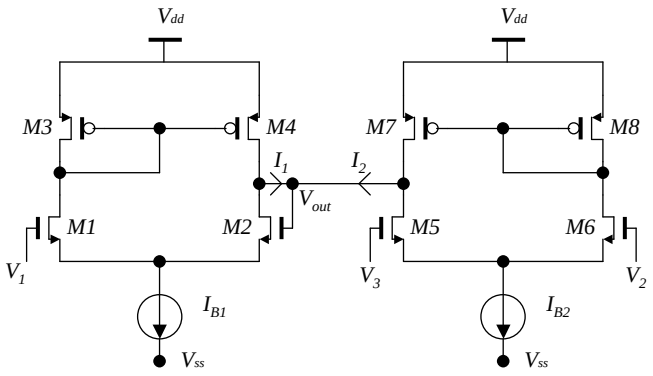

Figure 3.9: Pool circuit works as voltage adder/subtractor.

Since $M3$ and $M4$ is connected as a current mirror, the current in $M4$ is forced to equal that in $M1$. Therefore, the output current from the left differential pair is the difference of the currents in $M1$ and $M2$:

$$\begin{aligned} I_1 &= I_{M4} - I_{M2} = I_{M1} - I_{M2} \\ &= K_n(V_1 - V_{out})\sqrt{\frac{2I_{B1}}{K_n} - (V_1 - V_{out})^2}. \end{aligned} \tag{3.44}$$

Similarly, I_2 can be derived from the differential pair on the right side:

$$\begin{aligned} I_2 &= I_{M7} - I_{M5} = I_{M6} - I_{M5} \\ &= K_n(V_2 - V_3)\sqrt{\frac{2I_{B2}}{K_n} - (V_2 - V_3)^2}. \end{aligned} \tag{3.45}$$

If $I_{B1} = I_{B2}$, with the use of the relation $I_1 = -I_2$, combining equations (3.44) and (3.45) yields the expression for the output voltage in terms of V_1, V_2 and V_3:

$$V_{out} = V_1 + V_2 - V_3. \tag{3.46}$$

Therefore, the pool circuit can be used as a subtractor with V_1 or V_2 being fixed, or a adder with V_3 being fixed. Compared to Maundy's voltage subtractor/adder, the pool circuit is more flexible to the inputs and can work alone as an operational

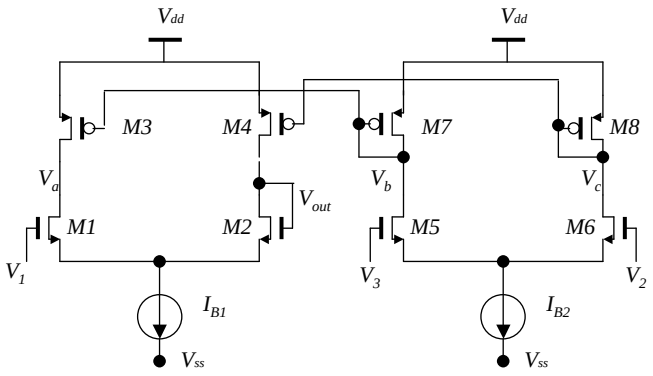

Figure 3.10: Improved pool circuit.

unit, whereas Maundy's circuit needs to be cascaded to cancel V_{dd} in equation (3.38), and is limited by the saturation region of $M1$ and $M2$ in Figure 3.8 and thus requires $V_1 > V_2 + 2V_{tp}$, derived from:

$$\begin{cases} V_1 > V_{out} + V_{tp}, \\ V_{out} - V_2 > V_{tp}. \end{cases} \tag{3.47}$$

The linearity of the pool circuit is limited by the channel length modulation effect, and the effect influences both the left side and the right side of the circuit. We propose a new version of the pool circuit, shown in Figure 3.10, to alleviate the channel length modulation effect. The wire connections among $M3$, $M4$, $M7$, and $M8$ are changed to make the currents of $M3$ and $M4$ mirrored from the currents of $M7$ and $M8$ separately. Hence, $I_{M1} - I_{M2} = I_{M5} - I_{M6}$ is satisfied, and this leads to the same expression of the output voltage as equation (3.46). The advantage of the new circuit is that the right part of the circuit is totally independent of the output. $M3$, $M4$, $M7$, and $M8$ can be applied with large size transistors to minimize their source-gate voltage changes caused by the inputs, and make V_b and V_c roughly equal.

3.3.2 Exponential Functions

We select NPN transistors to implement the exponential functions needed in the heart model. The exponential property of a NPN transistor comes from its $I-V$ characteristics in the forward-active region that can be described by:

$$I_c = I_{s0} e^{\frac{V_{be}}{V_T}}, \tag{3.48}$$

where I_{s0} is the reverse saturation current, and V_T is the thermal voltage. In order to obtain an exponential function, a voltage is taken as the input and connected to the base of a NPN transistor. The current of the collector is then exponentially decided by the base voltage. NPN transistors can also be used to calculate logarithms, if the base-emitter voltage is taken as output when the collector current is treated as the input.

Different from the gates of MOS transistors, NPN devices demand currents on the bases. When the base serves as an input terminal, we can no long consider the NPN well isolated from the preceding circuit and neglect its influence. In addition, the base voltage needs to be controlled to be less than about 0.7 V to avoid large current and high power consumption. These constraints add new design requirements absent from MOS circuit designs. In the following, we will discuss circuits based on NPN transistors. It is worth to mention that in our circuits, the equations of the input-output relations of the function circuits are independent of I_{s0}. We use a single size for all NPN transistors and add compensation circuits to cancel the I_{s0} terms in the equations. The advantage is that the function circuits can be more easily exported to different technologies which may have variant device parameters, and still keep the same input-output relationship.

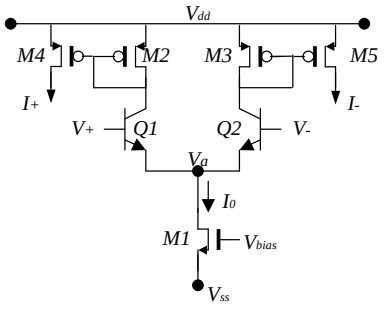

Figure 3.11: Emitter-coupled circuit.

Exponential Circuit Using Differential Pairs

The most frequently used exponential function in the Beeler-Reuter model has the form:

$$F(x) = \frac{C_1}{e^{C_2(x+C_3)} + 1}, \tag{3.49}$$

where C_1, C_2, C_3 are constants. This equation is very similar to the current expressions for the emitter-coupled pair circuit, shown in Figure 3.11. $M1$ provides a current I_0 whose value is decided by a bias voltage V_{bias}, and $M2$ and $M3$ serve as active loads of $Q1$ and $Q2$. $M4$ and $M5$ copy the currents in $Q1$ and $Q2$ and send them to the outputs. The transistors are matched on the left side and the right side. The currents of Q1 and Q2 are described by the following equations:

$$I_{c1} = I_{s0} e^{\frac{V_+ - V_a}{V_T}}, \tag{3.50}$$

$$I_{c2} = I_{s0} e^{\frac{V_- - V_a}{V_T}}, \tag{3.51}$$

$$I_0 \times \alpha_F = I_{c1} + I_{c2}, \tag{3.52}$$

where α_F is defined by the transistor forward current gain β_F and is approximately equal to 1: $\alpha_F = \frac{\beta_F}{\beta_F + 1} \simeq 1$. Equation (3.50)$-$(3.52) leads to the following

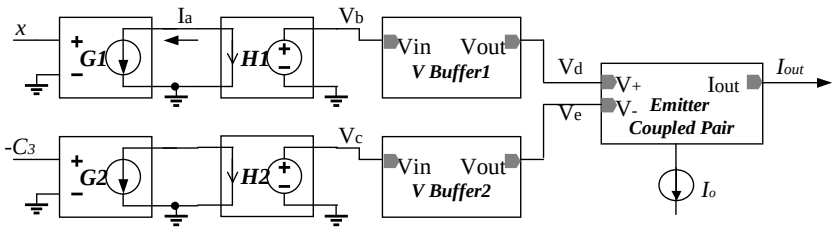

Figure 3.12: Circuit that implements equation (3.49).

expressions:

$$I_{c1} = \frac{I_0}{e^{(-\frac{\Delta V}{V_T})}+1}, \tag{3.53}$$

$$I_{c2} = \frac{I_0}{e^{(\frac{\Delta V}{V_T})}+1}, \tag{3.54}$$

where we take $\alpha_F = 1$, and ΔV is the difference of the two inputs $\Delta V = V_+ - V_-$.

The great similarity between equations (3.53) (3.54) and equation (3.49) indicates that the emitter-coupled pair circuit can be used to provide the function described in equation (3.49). The main task to adopt it arises from the differences of the exponential powers in the equations, which require linear transformations between x and ΔV. To solve the problem, linear modules introduced in section 3.3.1 are applied to perform the conversion, as illustrated in Figure 3.12. $G1$ and $G2$ are identical voltage to current converters (VCC), whose transconductance is $g1$. They can be implemented with the differential circuit introduced previously in Figure 3.5. $H1$ and $H2$ are identical current to voltage converters (CVC), whose transimpedance is $h1$. They can be realized with the circuit presented in section 3.3.1, Figure 3.6. The voltage V_b is expressed by the following equation:

$$\begin{aligned} V_b &= I_a h_1 + b_{H1} = h_1(x \cdot g_1 + b_{G1}) + b_{H1} \\ &= x \cdot g_1 h_1 + b_{G1} h_1 + b_{H1}, \end{aligned} \tag{3.55}$$

where b_{G1} and b_{H1} are the output offsets of $G1$ and $H1$ when their inputs are zero. Similarly, V_c can be expressed by:

$$V_c = -C_3 g_1 h_1 + b_{G1} h_1 + b_{H1}. \tag{3.56}$$

Two voltage buffers replicate V_b and V_c to be V_d and V_e and provide currents to the bases of the NPN transistors in the emitter-coupled circuit. Following equations (3.53) and (3.54), I_{out} can be expressed by:

$$I_{out} = \frac{I_0}{e^{-\frac{g_1 h_1 (x+C_3)}{V_T}} + 1}, \tag{3.57}$$

or

$$I_{out} = \frac{I_0}{e^{\frac{g_1 h_1 (x+C_3)}{V_T}} + 1}, \tag{3.58}$$

depending on which side of the emitter-coupled pair the current comes from. Let I_0 equal to C_1, and $\frac{g_1 h_1}{V_T}$ equal to C_2, the equation of I_{out} then becomes the same as equation (3.49).

The advantages of using double VCCs and CVCs are the offsets in their outputs can be canceled. From the other point of view, if only a single VCC and CVC are used, the offset terms $b_{G1} h_1 + b_{H1}$ in equation (3.55) will be required to implement C_3. This makes the design very challenging, because C_2 and C_3 in equation (3.49) are, though independent of each other, now implemented to be determined by the parameters of $H1$, and h_1 and b_{H1} can not be adjusted independently in the introduced CVC circuit.

Single Exponential Term

In this section, we introduce how we realize the circuit to calculate a single exponential term, which can be described with the equation:

$$F(x) = C_1 e^{(C_2 x + C_3)}, \tag{3.59}$$

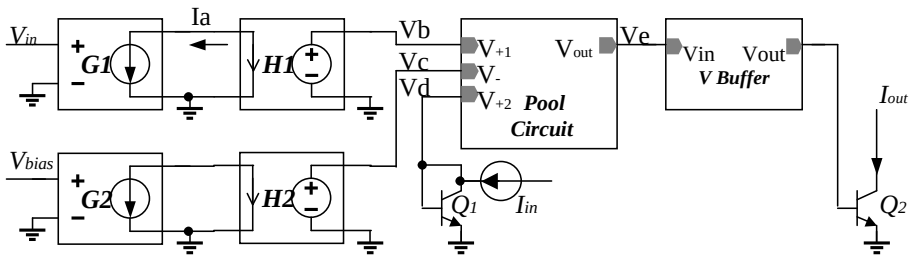

Figure 3.13: Circuit implementation of equation (3.60).

where $C_1,\ C_2,\ C_3$ are constants. The above equation is equivalent to:

$$F(x) = C_4 e^{\frac{C_5(x+C_6)}{V_T}}, \tag{3.60}$$

where $C_4,\ C_5,\ C_6$ are constants and restricted by:

$$\begin{cases} \frac{C_5}{V_T} = C_2, \\ C_4 e^{\frac{C_5 C_6}{V_T}} = C_1 e^{C_3}. \end{cases} \tag{3.61}$$

The similarity between equation (3.60) and equation (3.48) allows the circuit implementation of equation (3.60) using the exponential properties of NPN transistors.

Looking at the circuit shown in Figure 3.13, $G1$ is a linear transconductance, and $H1$ is a linear transimpedance. $G1$ and $H1$ convert the input V_{in} to V_b, which can be expressed by:

$$\begin{aligned} V_b &= I_a h_1 + b_{H1} = h_1(V_{in} g_1 + b_{G1}) + b_{H1} \\ &= V_{in} g_1 h_1 + b_{G1} h_1 + b_{H1}, \end{aligned} \tag{3.62}$$

where g_1 and h_1 are the transconductance and transimpedance of $G1$ and $H1$, and b_{G1} and b_{H1} are their offsets when the inputs of $G1$ and $H1$ are zero. Suppose $G2$ and $H2$ are exactly the same as $G1$ and $H1$, taking $V_{in} = V_{bias}$ into equation (3.62) we then obtain the equation for V_c using the equation for V_b:

$$V_c = V_{bias} g_1 h_1 + b_{G1} h_1 + b_{H1}. \tag{3.63}$$

The second pair of transconductor and transresistor $G2$ and $H2$ are used to cancel the offset $b_{G1}h_1 + b_{H1}$ as we will see soon.

$Q1$ and I_{in} compose a logarithm function, and the voltage V_d is decided by the current I_{in}. Assuming the forward current gain β_F of $Q1$ is large, so that the current flowing into the base can be ignored and $I_{in} \approx I_{c,Q1}$, V_d is then described by the following formula, derived from equation (3.48):

$$V_d = V_T \ln \frac{I_{in}}{I_{s0}}. \tag{3.64}$$

A pool circuit, introduced in section 3.3.1, puts V_b, V_c, and V_d together following equation (3.46), and yields an output voltage expressed by:

$$V_e = V_b - V_c + V_d. \tag{3.65}$$

Replacing V_b, V_c, and V_d with equation (3.62), (3.63), and (3.64) generates:

$$V_e = (V_{in} - V_{bias})g_1h_1 + V_T \ln \frac{I_{in}}{I_{s0}}. \tag{3.66}$$

Note that the offset in $G1$ and $H1$ are canceled by that of $G2$ and $H2$.

V_e is sent to the output transistor $Q2$ through a voltage buffer to control the output current I_{out}. The voltage buffer, presented in section 3.3.1, reproduces the voltage V_e in its output and provides current to the base of $Q2$. Hence the collector current of $Q2$ can be described in terms of V_e using the $I-V$ characteristics of an NPN transistors:

$$\begin{aligned} I_{out} &= I_{s0}e^{\frac{V_e}{V_T}} \\ &= I_{s0}e^{\frac{(V_{in}-V_{bias})g_1h_1+V_T \ln \frac{I_{in}}{I_{s0}}}{V_T}} \\ &= I_{in}e^{\frac{g_1h_1(V_{in}-V_{bias})}{V_T}}. \end{aligned} \tag{3.67}$$

Substitute I_{in} with C_4, and substitute g_1h_1 with C_5, V_{bias} with $-C_6$, and V_{in} with x in equation (3.67), we obtain the same expression as equation (3.60). Hence,

the circuit in Figure 3.13 is a realization of equation (3.60). The circuit does not require C_5 to be positive, because V_{in} and $-C_6$ can be connected to the negative input terminal of $G1$, and thus in equation (3.67) there is an additional "-" sign in front of $g_1 h_1$ for this case. Parameter scaling is involved when C_4 can not be directly represented by I_{in} in a circuit.

The circuit is restricted by the base voltage of $Q2$, or equivalently V_e, with taking account of the power on $Q2$. Since the collector currents increase dramatically with increasing base-emitter voltage, the current can be amazingly high when V_e reaches above a certain value. To avoid this situation, V_e is normally constrained to be under 0.7 V. The restriction can be expressed mathematically by the following equation, using equation (3.66):

$$(V_{in} + C_6) g_1 h_1 + V_{be1} < 0.7, \tag{3.68}$$

$$\Rightarrow (V_{in} + C_6) g_1 h_1 < 0.7 - V_{be1}. \tag{3.69}$$

The restriction can be satisfied by selecting proper C_4 and C_6 under the constraint described by equation (3.61). Note the input voltage of the "V buffer" V_e is not required to be higher than 0. When $V_e < 0$, the collector current of $Q2$ is nearly (if not absolutely) 0.

The circuit of Figure 3.13 can be used to replace the I_0 in Figure 3.12 to realize functions of the form:

$$F(x) = \frac{D_1 e^{D_2 x}}{e^{D_3 (x + D_4)} + 1}, \tag{3.70}$$

where $D_1 - D_4$ are constants.

Logarithm Function

The circuit that is used here to realize logarithm functions is depicted in Figure 3.14. The NPN transistors $Q1$ and $Q2$, connected like diodes, take I_x and I_c as

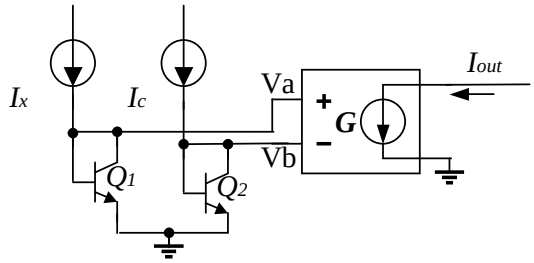

Figure 3.14: Circuit implementation of logarithm function.

their collector currents, with I_c, a constant, working as a bias, and I_x being taken as a variable. V_a and V_b are determined by the base voltages and described by:

$$V_a = V_T \ln \frac{I_x}{I_{s0}}, \tag{3.71}$$

$$V_b = V_T \ln \frac{I_c}{I_{s0}}. \tag{3.72}$$

The output current of the circuit I_{out} is controlled by V_a and V_b through a linear voltage to current converter $G1$ (refer to section 3.3.1), and is expressed with:

$$I_{out} = g_1(V_a - V_b) = g_1 V_T \ln I_x - g_1 V_T \ln I_c = g_1 V_T \ln \frac{I_x}{I_c}, \tag{3.73}$$

where g_1 is the transimpedance of $G1$. Therefore the circuit in Figure 3.14 is the implementation of functions of the form:

$$F(x) = C_1 \ln C_2 x, \tag{3.74}$$

where C_1 and C_2 are constants, if we let $g_1 = C_1/V_T$ and let $I_c = 1/C_2$. Current mirrors and parameter scaling can be used to handle the difference between C_1 and $g_1 V_T$.

3.3.3 Multipliers

Analogue multipliers are important building blocks in analog signal processing. The literature [56] gives a review on the multiplier circuits that are based on the

Gilbert cell. Those circuits take voltages as inputs, and output currents. In the VLSI design of the heart model, because in most cases signals are represented by currents (refer to Table 3.2) due to the easy manipulation of current signals compared to voltage signals, we focus on current multipliers here. Various CMOS current multiplier circuits have been published, with transistors operating in either the subthreshold region or the strong inversion region [51]−[54]. Many of them, like the circuits introduced in literature [51] and [52], are composed of both NMOS and PMOS transistors and require their parameters to be equal, i.e. $K_n = K_p$ or (and) $V_{tn} = V_{tp}$. This restriction is usually not easy to satisfied because of the limitation of fabrication technologies. In this section, we present a current multiplier proposed by Tanno. After that, we will introduce a multiplier based on bipolar transistors for implementing cascaded multiplications. A scheme of making big capacitors based on the bipolar multiplier will be presented last.

Tanno Multiplier

The Tanno multiplier is developed based on the quarter square technique, which is defined by:

$$I_o = (I_x + I_y)^2 - (I_x - I_y)^2 = 4I_xI_y. \tag{3.75}$$

The technique uses addition and subtraction operations, as well as squaring operations. The requirement decides that current-squaring circuits are needed in the multiplier circuits.

The squaring circuit used by the Tanno multiplier is depicted in Figure 3.15(a) [54]. The transistors work in the strong inversion region. $M1$ and $M2$ are identical, and they incorporate the bias circuit, in which V_b is decided by the bias current I_B. $M3$ and $M4$ are also identical in size. The sources and gates of $M1 - M4$ are

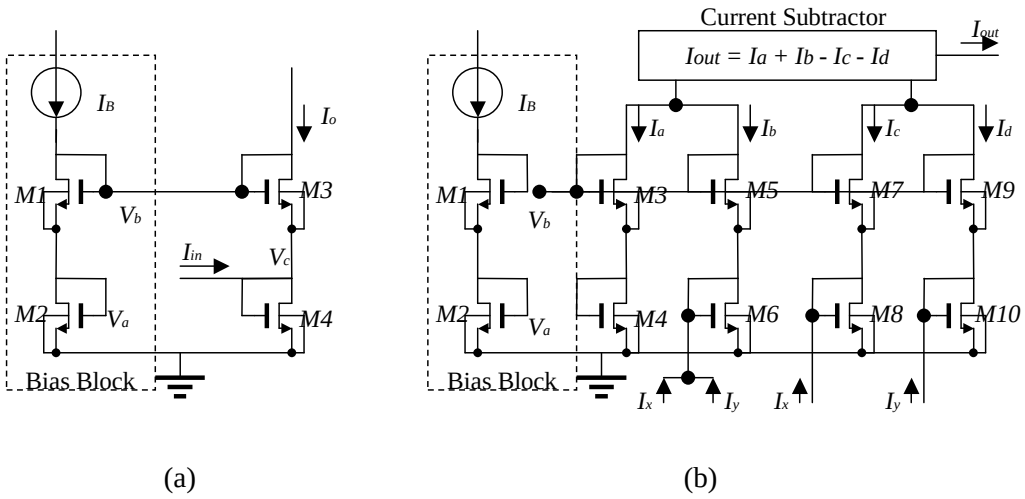

(a) (b)

Figure 3.15: Tanno current multiplier. (a)Basic block of Tanno multiplier. (b)Tanno multiplier.

connected into a loop, and hence their gate-source voltages follow:

$$V_{gs1} + V_{gs2} = V_{gs3} + V_{gs4}. \tag{3.76}$$

Their gate-source voltages can be expressed in terms of their currents:

$$V_{gs1} = V_{gs2} = \sqrt{\frac{I_B}{K_{M1}}} + V_t, \tag{3.77}$$

$$V_{gsi} = \sqrt{\frac{I_i}{K_{M3}}} + V_t \quad (i = 3, 4), \tag{3.78}$$

where we assume the body-source voltages of the transistors are the same, so that the threshold voltages are all equal to V_t. When $K_{M1} = K_{M3}$, we have:

$$2\sqrt{I_B} = \sqrt{I_{M3}} + \sqrt{I_{M4}}. \tag{3.79}$$

From Figure 3.15(a), the current in $M3$ is:

$$I_{M3} = I_o = I_{M4} - I_{in}. \tag{3.80}$$

Combining equation (3.79) and (3.80) yields:

$$I_{M3} + I_{M4} = 2I_B + \frac{I_{in}^2}{8I_B}, \tag{3.81}$$

and thus:

$$I_o = \frac{(I_{in} - 4I_B)^2}{16I_B}. \tag{3.82}$$

The sizes of $M1$ and $M2$ are not necessary to be the same as for $M3$ and $M4$. Assume $K_{M1} = mK_{M3}$, then I_o of Figure 3.15(a) is described as:

$$I_o = \frac{(mI_{in} - 4I_B)^2}{16mI_B}. \tag{3.83}$$

The Tanno multiplier is composed of one bias block, four output blocks, and a current adder/subtractor, as depicted in Figure 3.15(b). The current I_a, I_b, I_c, and I_d can be expressed by equation (3.83) with the replacement of I_{in} with 0, $I_x + I_y$, I_x and I_y respectively. The output of the multiplier circuit is then described by the following:

$$I_{out} \;=\; I_a + I_b - I_c - I_d = \frac{m}{8} \times \frac{I_x I_y}{I_B}. \tag{3.84}$$

The current subtractor in Figure 3.15(b) can be realized with the circuit shown in Figure 3.16, in which I_{in1} and I_{in2} are copied with current mirrors and changed directions so that I_{out} is $I_{in1} - I_{in2}$.

A limitation of the Tanno multiplier relies on the assumption that the threshold voltages of $M1 - M4$ are identical in Figure 3.15(a) so that the threshold voltage V_t can be canceled out to obtain equation (3.79). This assumption may not be true if the transistor bodies are not connected like in Figure 3.15(a), because V_c changes along I_{in}, and this makes the source voltage of $M3$ vary and, thus, the threshold voltage of $M3$ can be different from that of $M1$ due to the body effect. For the AMI 1.5 μm ABN process we select for the VLSI design, the differentiation of V_t

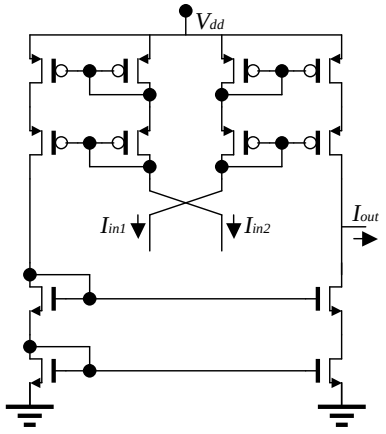

Figure 3.16: Current subtractor.

results from the connection of the bodies of all NMOS transistors to V_{ss}, and hence the threshold voltages of $M1$, $M2$, $M3$ and $M4$ are no long equalized. Therefore, we use PMOS devices to build the Tanno multiplier in our circuit to tie the bodies and the sources of PMOS transistor to n-wells for diminishing the body effect.

Compared to other current multipliers, the Tanno multiplier has relatively simple circuit topology. The Tanno multiplier has another advantage that its two inputs are completely equivalent, i.e. its output current is identical to the result obtained after switching I_x and I_y, ignoring the errors caused by transistor mismatch. This is opposite to some multipliers, for example the Wiegerink Multiplier [53], in which the product results differ after switching the input multiplicands due to the non-symmetrical inputs caused by unavoidable high order effects of the transistors.

The working ranges of the Tanno multiplier are restricted by the prerequisite of the circuit that all transistors work in the saturation region. Taking the circuit branch of $M7$ and $M8$ as an example, when $I_x \geq 0$, we have:

$$I_{M7} + I_x = I_{M8} > I_x > 0. \tag{3.85}$$

The upper bound of the magnitude of the input current I_x is limited by the gate voltage of $M8$, which needs to be lower than V_b to make $M7$ and $M8$ work in the saturation region. V_b is given by $V_b = 2V_a = 2(\sqrt{\frac{I_B}{mK_{M8}}} + V_t)$. Therefore I_{M8} can be bounded by:

$$\begin{aligned} I_{M8} &= K_{M8}(V_{gs,M8} - V_t)^2 \\ &< K_{M8}(V_b - V_t)^2 \qquad (3.86) \\ &= K_{M8}[2(\sqrt{\frac{I_B}{mK_{M8}}} + V_t) - V_t]^2 \\ &< K_{M8}(2\sqrt{\frac{I_B}{mK_{M8}}})^2 \\ &= 4\frac{I_B}{m}. \qquad (3.87) \end{aligned}$$

Combining equation (3.87) with (3.85), we have:

$$\begin{aligned} 4\frac{I_B}{m} > I_{M8} > I_x > 0 \\ \Rightarrow I_x < \frac{4}{m}I_B \quad (I_x \geq 0). \qquad (3.88) \end{aligned}$$

Similarly, when $I_x < 0$, we can derive that:

$$-I_x < \frac{4}{m}I_B \quad (I_x < 0). \qquad (3.89)$$

Putting the equations for $I_x \geq 0$ and $I_x < 0$ together, and applying them to the circuit branches of inputs $I_x + I_y$ and I_y, we derive the working range of the inputs of the Tanno multiplier as described below:

$$\begin{cases} |I_x + I_y| < \frac{4}{m}I_B, \\ |I_x| < \frac{4}{m}I_B, \\ |I_y| < \frac{4}{m}I_B. \end{cases} \qquad (3.90)$$

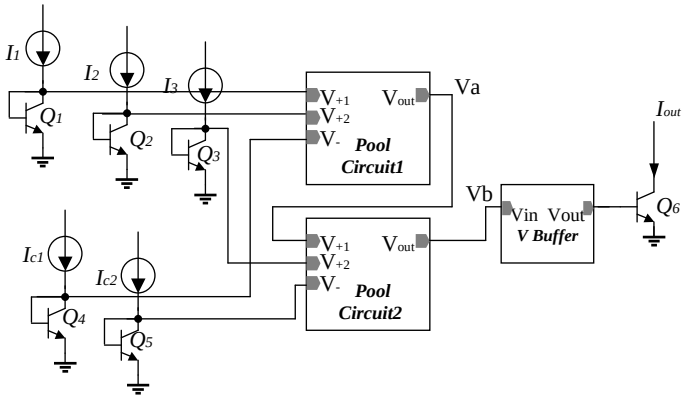

Figure 3.17: Multiplier based on NPN transistors.

Multipliers Based on Bipolar Devices

The Tanno multiplier perform the multiplication of two inputs. In the case that the product of several variables is to be calculated, the multiplier can be cascaded. However a cascaded multiplier has a problem of accumulating errors, and due to the peripheral circuits necessary to duplicate currents in the inputs and sometimes to inverse the current directions in the input or output, the extra circuits may introduce further inaccuracies. An operation like the one presented in the Beeler-Reuter model, m^3hj (refer to the equations (2.44)), requires the multiplication to be carried out four times, which results in a big complicated Tanno type of multiplier circuit, and this motivates us to find a circuit for easy cascaded multiplication. We observe that the input variables of m^3hj are all positive from their physical meanings, and this inspires us to take advantage of the exponential property of NPN transistors for realizing the cascaded multiplication, and the implemented multiplier is the first quadrant multiplier.

In the example presented below there are three multiplicands: I_1, I_2 and I_3, which are all positive. The circuit implementation is illustrated in Figure 3.17.

$Q1 - Q5$ are connected as diodes and their base voltages are decided by $I_1 - I_3$, I_{c1} and I_{c2} in the logarithm relation described by:

$$V_{be,z} = V_T \ln \frac{I_z}{I_{s0}} \quad (z \; is \; 1, \; 2, \; 3, \; c1 \; or \; c2, \; I_z > 0). \tag{3.91}$$

I_{c1} and I_{c2} are constant bias currents. The pool circuits (refer to section 3.3.1 Figure 3.9) add I_1, I_2 and I_3 together, and subtract I_{c1} and I_{c2} from the sum, i.e. V_b is:

$$V_b = V_a + V_{be3} - V_{be,c2} = (V_{be1} + V_{be2} - V_{be,c1}) + V_{be3} - V_{be,c2}. \tag{3.92}$$

Note that the inputs of the pool circuits are the gates of MOS transistors, and, thus, the effect of the pool circuit on $Q1 - Q5$ can be treated as none. Therefore, when $I_{c1} = I_{c2}$, $Q4$ or $Q5$ can be saved with one NPN transistor driving two inputs of the pool circuit due to the ignorable loading effect from the pool circuit.

The voltage buffer (refer to section 3.3.1) copies V_b to the output, and provides current to the base of the output transistor $Q6$. The current of $Q6$ collector is exponentially decided by the base-emitter voltage, and can be expressed in terms of the input currents from equation (3.92):

$$I_{out} \quad = \quad I_{s0} e^{\frac{V_b}{V_T}} = \frac{I_1 I_2 I_3}{I_{c1} I_{c2}}. \tag{3.93}$$

The coefficient difference between I_{out} and the real product of $I_1 \cdot I_2 \cdot I_3$ can be easily fixed with parameter scaling and current mirrors.

For a general situation in which $N+1$ multiplicands are involved, the circuit in Figure 3.17, specifying the case $N = 2$, can be extended by adding NPN transistors and the pool circuits. For an operation with $N+1$ multiplicands, $N+1$ NPN devices are needed to port the input currents $I_1 - I_{N+1}$, N NPN transistors are used to host the constant currents $I_{c1} - I_{cN}$ for canceling the I_{s0} terms in the equation of

the product result, and N pool circuits are needed to perform the addition and subtraction. If there are identical currents among $I_{c1} - I_{cN}$, some bias NPN devices can saved. For example, in Figure 3.17, if $I_{c1} = I_{c2}$, Q_5 can be saved by connecting the base of $Q4$ to the second pool circuit. The circuit represents a mathematical equation expressed as follows:

$$I_{out} = \frac{I_1 I_2 I_3 ... I_{N+1}}{I_{c1} I_{c2} ... I_{cN}}. \tag{3.94}$$

Like other cascaded circuits, this type of multiplier circuit also has the issue of accumulated errors. The magnitude of the error largely depends on the accuracy of the linear addition/subtraction operation of the pool circuits. Fortunately, for designing circuits of the Beeler-Reuter model, the errors can be kept well under control. In the pool circuit shown in Figure 3.10, the error mainly comes from the channel length modulation effect of $M3$ and $M4$. For the case that the swing of the inputs is small, it is possible to reduce the difference of V_{ds3} and V_{ds4} to a very small range. Due to the restriction of the physical meanings in the heart cell model, the input currents of the multiplier can never reach the value of absolute zero and usually have a relative range (i.e. the maximal value divided by their minimal value) within 10^5. Hence, the input voltages of the pool circuits are normally between $0.4V$ and $0.7V$, corresponding to a range of current changing between $\times 1$ and $\times 10^5$. Therefore, the fluctuation of the inputs are within $0.3V$, which can be treated small for reducing the channel length modulation effect.

Shrinking Current with Bipolar-Based Circuit

Current mirrors are probably the most popular current amplifying/shrinking circuits. They work based on the linear dependence of the drain-source currents of MOS transistors on the W:L ratio, or the linear dependence of the collector cur-

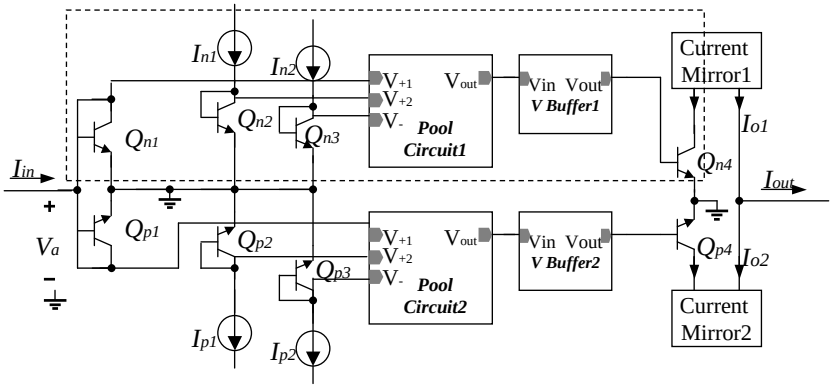

Figure 3.18: Current amplifier/shrinker based on bipolar transistors.

rents of NPN transistors on the size of their emitters. However, current mirrors may take big layout areas. In the case that a current needs to be shrunk by 10^4 times, it is impractical to build a current mirror circuit composed of transistors with one having a W:L ratio of 10^4 times of another. Then, cascaded current mirrors are needed for this case. In the following, we propose a new approach to implement current amplifiers/shrinkers, and it is based on bipolar transistors.

The circuit is depicted in Figure 3.18, in which, the dotted area is a multiplier circuit like the one shown in Figure 3.17, except in this circuit only two multiplicands I_{in} and I_{n1} are illustrated, and I_{n1} is fixed. The lower half of the circuit, based on PNP transistors, works just the same way as the upper half except working compensatively for the case $I_{in} < 0$. When $I_{in} > 0$, I_{in} goes through Q_{n1}, which decides the voltage V_a, and Q_{p1} does not take any current. Hence the voltages on the bases of the output transistors Q_{n4} and Q_{p4} are:

$$\begin{cases} V_{be,n4} = V_a + V_{be,n2} - V_{be,n3}, \\ V_{be,p4} = V_a + V_{be,p2} - V_{be,p3}. \end{cases} \tag{3.95}$$

If the selection of the currents I_{n1}, I_{n2}, I_{p1} and I_{p1} makes $|V_{be,n2} - V_{be,n3}| < |V_a|$ and $|V_{be,p2} - V_{be,p3}| < |V_a|$, the voltages on the bases of the output transistors Q_{n4}

and Q_{p4} are then both positive in equation (3.95). Therefore Q_{n4} creates a non-zero collector current, while Q_{p4} is in the cut-off region and conducts no current. Similarly, when $I_{in} < 0$, I_{in} goes through Q_{p1} alternatively, and the output current I_{out} is delivered by Q_{p4} while Q_{n4} is cut off. Therefore the collector currents in Q_{n4} and Q_{p4} are expressed by:

$$I_{c,n4} = \begin{cases} \frac{I_{in}I_{n1}}{I_{n2}} & (I_{in} \geq 0), \\ 0 & (I_{in} < 0). \end{cases} \tag{3.96}$$

$$I_{c,p4} = \begin{cases} 0 & (I_{in} \geq 0), \\ \frac{I_{in}I_{p1}}{I_{p2}} & (I_{in} < 0). \end{cases} \tag{3.97}$$

The current mirrors on the right reverse the direction of $I_{c,n4}$ and $I_{c,p4}$, and send the currents to the output:

$$I_{out} = kI_{in}, \tag{3.98}$$

where the amplification factor k is decided by $k = \frac{I_{n1}}{I_{n2}} = \frac{I_{p1}}{I_{p2}}$.

The proposed current amplifier/shrinker circuit can be used to magnify capacitances in our VLSI heart circuits. Capacitors serve as integration devices in our VLSI design, and their voltages are the outputs that drive the inputs of the succeeding circuits. Since the inputs of the succeeding circuits are gates of MOS transistors and take no currents, we can build the integration circuits with smaller capacitors using the current shrinker circuits and still keep the waveforms of the voltages across the capacitors. This will be introduced in section 3.4.7.

3.4 VLSI Design of Beeler-Reuter Model

In this section, we are going to present the VLSI circuit for implementing the Beeler-Reuter model. The mathematical description of the model for VLSI realiza-

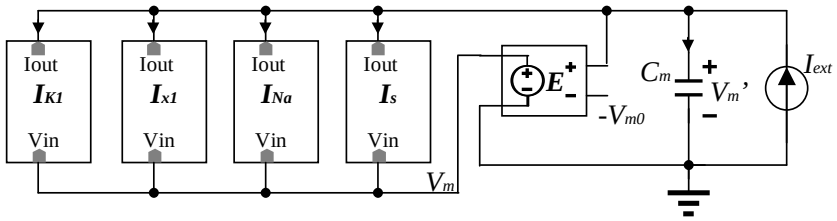

Figure 3.19: Top-level circuit diagram of the Beeler-Reuter model.

tion was summarized in section 3.2.4. The circuit building blocks of mathematical functions need for the cardiac cell model have all been introduced in section 3.3.

A top level block diagram for realizing the cardiac cell model is shown in Figure 3.19, and it is mapped from the equations that describe the membrane potential V_m with the initial condition shifting process (refer to section 3.2.3), i.e. equations (2.40) and (2.41), which are combined and rewritten as follows:

$$C_m \frac{dV_m}{dt} = -(I_{K1} + I_{x1} + I_{Na} + I_s) + I_{ext}. \tag{3.99}$$

In the diagram in Figure 3.19, the membrane capacitor C_m is charged by five current sources, an external current I_{ext} which serves as the stimulus to activate the cardiac cell model, and four ionic channel currents, I_{K1}, I_{x1}, I_{Na}, and I_s. E is used to shift the resting initial voltage of the capacitor to zero, and V_{m0} is the original initial condition of V_m. Note that the positive input terminal of E, connected with one side of the capacitor, does not take any current and, hence, E does not contribute any current to charge the capacitor. The ionic current modules are nonlinearly controlled by the membrane potential V_m and do not draw any currents at their inputs.

Figure 3.20 provides more details for the four ionic currents. I_{K1}, having the simplest formulation among the four, is determined only by V_m, and thus can be described by a voltage-controlled current source, as shown in Figure 3.20(a). I_{x1}

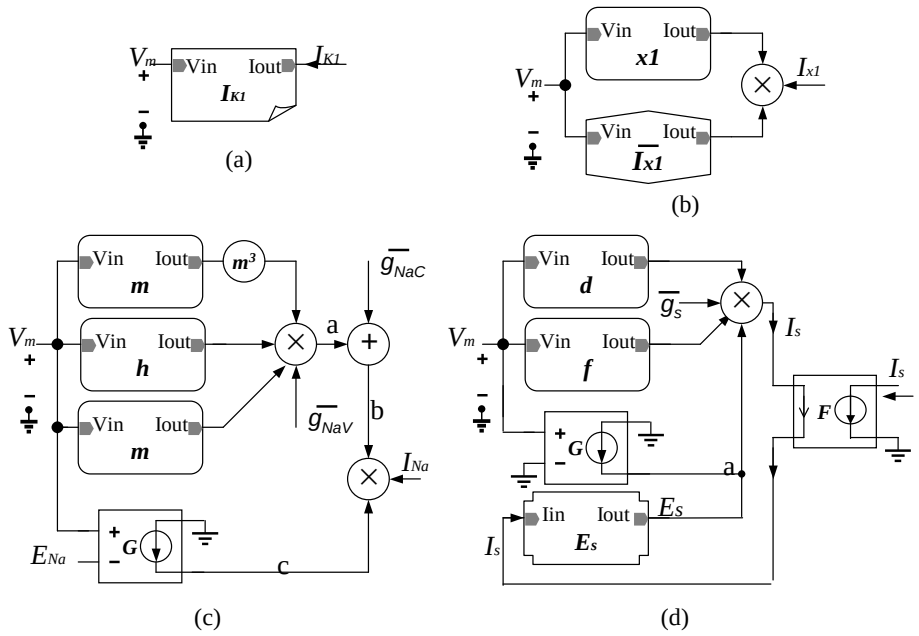

Figure 3.20: Diagrams of ionic current modules: (a)I_{K1}, (b)I_{x1}, (c)I_{Na}, (d)I_s.

can be separated into two parts as stated in equation (2.43): the V_m dependent $\overline{I_{x1}}$, and a potential- and time-dependent gating variable $x1$. Hence, I_{x1} can be modeled as the product of $\overline{I_{x1}}$ and $x1$, as illustrated in Figure 3.20(b). The diagram for I_{Na} is shown in Figure 3.20(c), in which gating variable m is cubed and multiplied by the gating variables h and j, and the product, amplified by a factor of $\overline{g_{NaV}}$ and then added with the constant sodium conductance $\overline{g_{NaC}}$, is multiplied with the output of the linear transconductance G whose output current is linearly decided by $V_m - E_{Na}$; this implements equation (2.44). The diagram for I_s is shown in Figure 3.20(d). As described in equation (2.45), I_s is the product of a constant transmembrane conductance $\overline{g_s}$, two gating variables d and f, and the difference of V_m and the calcium equilibrium potential E_s. The resulting I_s is duplicated into two copies in Figure 3.20(d), with one being the output to charge the membrane capacitor C_m, and the other feeding back to control the generation of E_s.

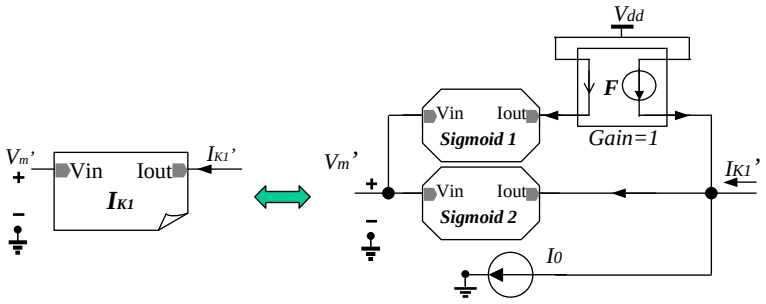

Figure 3.21: I_{K1} module is composed of a constant current source and two sigmoid-function circuits. Refer to Appendix A, schematics page *Sch*-2 to *Sch*-4 for transistor circuits.

Next we will introduce how the ionic currents are implemented with transistor circuits using the function blocks presented in section 3.3, and explain the structure of each ionic current module based on Figure 3.20. In the rest of the presentation, we use the notations with a single quotation mark to represent the variables associated with reformulated equations. The simulation results of the VLSI circuits are also provided in the following sections.

3.4.1 Time-Independent Potassium Current I_{K1}

The description of I_{K1} is given in equation (3.5), and is rewritten as follows after the variables are scaled:

$$I'_{K1} = 2.742 \times 10^{-6} + \frac{3.632 \times 10^{-6}}{e^{-5.966(V'_m - 0.3277)} + 1} - \frac{5.879 \times 10^{-6}}{e^{11.77(V'_m + 0.8823)} + 1}. \qquad (3.100)$$

Following equation (3.100), the overall diagram for modeling I_{K1} can be depicted in Figure 3.21, where the constant current source I_0 represents the first term on the right side of the equation, and the two sigmoid sub-circuits implement the two terms containing exponentials in the equation. The sigmoid functions are realized

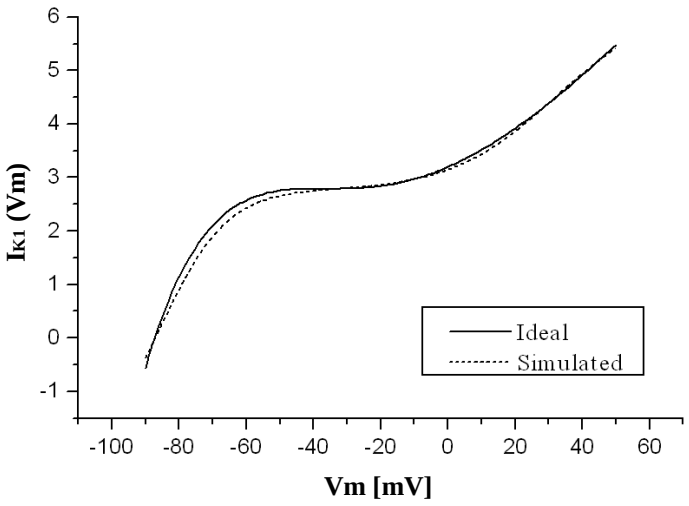

Figure 3.22: Ideal and simulated curves: I_{K1} vs. V_m.

using the coupled-emitter circuit shown in Figure 3.12. The current to current converter F is a current mirror and is used to switch the direction of the output current of the top sigmoid block in Figure 3.21. The complete transistor circuits for ionic current I_{K1} are provided in Appendix A, schematics page Sch-2 to Sch-4.

The simulation result of implementing equation (3.100) using transistor circuits is shown in Figure 3.22. The x-axis is the membrane potential V_m, whose value ranges from -90 mV to 50 mV during an action potential. The solid line depicts the ideal I_{K1} vs. V_m curve, i.e. calculated directly from equation (2.42), and the dashed line is the simulated I_{K1} which is scaled back to the original magnitude (the scaling equation is provided in Table 3.2, $I_{K1} = 10^6 I'_{K1}$) in order to be compared with the ideal values. We adopt the average signal-to-error ratio (SER) and R-square as the metrics to evaluate how close the circuit realization is to the original equations. The definition of the signal-to-error ratio follows the signal-to-noise ratio, which describes the power ratio of a given transmitted signal to the background noise,

and it is formulated as the following:

$$SER = \frac{1}{N}\sum_{i=1}^{N} 10\log\frac{E_i^2}{(E_i - O_i)^2} \quad \text{(Unit: dB)}, \tag{3.101}$$

where E_i are the expected values, i.e. the values calculated from the mathematical model, and O_i are the observed value, i.e. the circuit simulation results. R-square is a statistic that measures how similar the waveforms of data sets are to each other [68], and is also called the square of the multiple correlation coefficient. R-square is defined as:

$$\text{R-square} = 1 - \frac{\sum_{i=1}^{N}(E_i - O_i)^2}{\sum_{i=1}^{N}(E_i - \bar{O})^2}, \tag{3.102}$$

where E_i and O_i have the same meaning of those in equation (3.101), and $\bar{O}$ is the mean over the N observed values. R-square takes any value between 0 and 1, and a value closer to 1 indicates higher similarity between two data sets. The average SER for realizing the function of I_{K1} with VLSI circuits is 36.0 dB. The R-square between the ideal data and the simulated data for I_{K1} is 0.9966.

3.4.2 Gating Variables

Gating variables are described by first-order differential equations, which are given in equation (2.46) and are rewritten in the following:

$$\frac{dz}{dt} = \alpha_z - (\alpha_z + \beta_z)z, \tag{3.103}$$

where z is one of the gating variables, $x1$, m, h, j, d, or f. The six gating variables of the Beeler-Reuter model can be implemented with a circuit of the same structure, as illustrated in Figure 3.23, with different parameters. In the diagram shown in Figure 3.23, α *Function* and β *Function* are two black boxes that model the opening and closing rates of the gating variable, and their VLSI

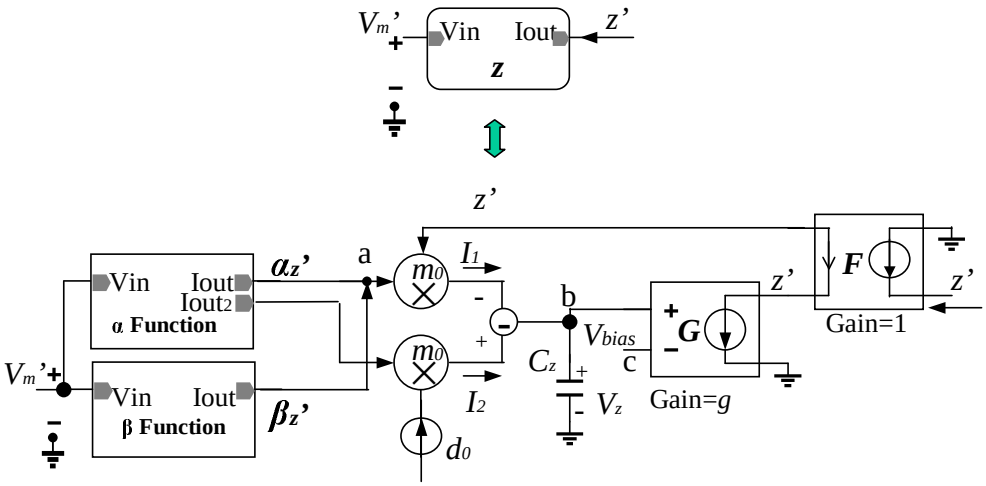

Figure 3.23: Detailed structure of gating variable circuits $x1$, m, h, j, d, and f.

circuits are all different as they depend on the equations of the opening and closing rates (provided in equations (2.47)-(2.58)). The α *Function* and the β *Function* are controlled by voltage V'_m, i.e. the scaled membrane potential V_m, and create output currents α'_z and β'_z. The α *Function* has two identical outputs, with one, joined with β'_z at point a, going to the upper multiplier, and the other alone feeding into the lower multiplier. The products of the multipliers, in the form of currents, are subtracted and charge the capacitor C_z. The voltage of the capacitor V_z is connected to a linear transconductor G, whose negative terminal is connected to a constant voltage V_{bias}, which is used to shift the initial voltage of the capacitor C_z as introduced in 3.2.3. The output current of G is replicated into two copies, and one copy is the output which is sent to the succeeding circuits in the cardiac cell system, and the other copy serves as another multiplicand of the upper multiplier. Here we use z', α'_z and β'_z to indicate the variables after being scaled, to distinguish them from the original ones denoted with z, α_z and β_z.

In Figure 3.23 the voltage across the capacitors is described by:

$$C_z \frac{dV_z}{dt} = I_2 - I_1. \tag{3.104}$$

Using the relation of V_z and z' and the description of the input/output of the multipliers (refer to section 3.3.3 equation (3.84)) provided as follows:

$$z' = (V_z - V_{bias}) \cdot g, \tag{3.105}$$

$$I_1 = (\alpha'_z + \beta'_z) z' m_0, \tag{3.106}$$

$$I_2 = \alpha'_z d_0 m_0, \tag{3.107}$$

where g is the transconductance of G, d_0 is a constant current, and m_0 is a constant factor of the multipliers. We therefore obtain the following equations:

$$\begin{aligned} & \frac{C_z}{g}\frac{dz'}{dt} = \alpha'_z d_0 m_0 - (\alpha'_z + \beta'_z) z' m_0, \\ \Rightarrow \quad & \frac{dz'}{dt} = \alpha'_z \frac{d_0 m_0 g}{C_z} - (\alpha'_z + \beta'_z)\frac{z' m_0 g}{C_z}. \end{aligned} \tag{3.108}$$

Suppose the scaling factor for α_z and β_z is $A_{\alpha z}$, and the scaling factor for z is A_z, we have:

$$\begin{cases} z = A_z z', \\ \alpha_z = A_{\alpha z} \alpha'_z, \\ \beta_z = A_{\alpha z} \beta'_z. \end{cases} \tag{3.109}$$

Taking the above scaling equations into equation (3.103), we derive the following:

$$\begin{aligned} & A_z \frac{dz'}{dt} = A_{\alpha z}\alpha'_z - A_{\alpha z}(\alpha'_z + \beta'_z) A_z z', \\ \Rightarrow \quad & \frac{dz'}{dt} = \frac{A_{\alpha z}}{A_z}\alpha'_z - A_{\alpha z}(\alpha'_z + \beta'_z) z'. \end{aligned} \tag{3.110}$$

Table 3.4: V_{bias} for initial conditions of gating variable capacitors (unit: V).

Gating variable	$x1$	m	h	j	d	f
V_{bias}	-0.0044	-0.00989	-0.4732	-0.468	-0.00188	-0.5

Comparing equation (3.108) with (3.110) yields the expression for the relation between the scaling factors and the constant parameters of the circuit:

$$A_z = \frac{1}{d_0}, \tag{3.111}$$

$$A_{\alpha z} = \frac{m_0 g}{C_z}. \tag{3.112}$$

The selection of the scaling factors and the circuit parameters are restricted by the realization circuit of G (refer to section 3.3.1). The range of variation of V_z is required to be small enough in order to achieve high linearity in the transconductor G. In our VLSI design, the variation of the differential input of G is constrained to be within 0.5 V in the circuit. The constant current source d_0 is selected to be 5 μA, and, hence, z is scaled down by a factor of 2×10^5 (refer to Table 3.2 for the scaling of z). m_0 and g are set to 10^5 and 10^{-5} respectively. The scaling factor of α_z and β_z is determined by their original maximum values, which, after being scaled, are restricted to be within the working ranges of the multipliers. The maximum magnitude of α_z and β_z are different for for different gating variables, ranging from 10^{-3} to 10^2 , and this decides different values of the capacitance C_z in the circuit. The scaling factors of α_z (and β_z) are given in Table 3.2 for the six gating variables in the Beeler-Reuter model, and the corresponding C_z will be provided in section 3.4.7, discussed together with the time scale.

In Figure 3.23, the negative input terminal of G is connected to a non-zero voltage V_{bias} to shift the initial voltage of C_z to be zero, as introduced in section 3.2.3. The magnitude of V_{bias} is decided by the original initial condition of the

gating variable, provided in Table 2.3, and the ratio of the capacitor voltage V_z to the original gating variable z. Table 3.4 lists the values of V_{bias} for the gating variables in the cardiac cell model, which make $V_z(t=0)=0$.

The transistor circuits of realizing the gating variables of the Beeler-Reuter model are provided in Appendix A, and will be mentioned in the following sections when presenting corresponding ionic currents.

3.4.3 Time-Dependent Potassium Current I_{x1}

Opening/Closing Rate of $x1$

The circuit for realizing gating variable $x1$ has been introduced in the previous section and given in Figure 3.23. Here we only present the black boxes α *Function* and β *Function* in the $x1$ circuit. The mathematical descriptions of α_{x1} and β_{x1} are provided in equations (2.47) and (2.48). They are rewritten as follows:

$$\alpha'_{x1} = \frac{2.012\times10^{-3}e^{8.3(V'_m-0.5)}}{e^{5.7(V'_m+0.5)}+1}, \tag{3.113}$$

$$\beta'_{x1} = \frac{8.67\times10^{-5}e^{-6(V'_m+0.9)}}{e^{-4(V'_m+0.2)}+1}, \tag{3.114}$$

where V'_m, α'_{x1} and β'_{x1} are the membrane potential V_m, the opening rate α_{x1} and the closing rate β_{x1} after being scaled. Here we reorganize the constant coefficients in the equations for easier circuit design. For instance, in the original equation of α'_{x1} (2.47), the coefficient 0.0005 and the exponential with a constant power $e^{0.083\times50}$ is re-organized as follows:

$$0.0005\times e^{0.083\times50} = 0.0005\times e^{(+0.083\times100)}e^{(0.083\times50-0.083\times100)} = 2.012\times e^{(-0.083\times50)}. \tag{3.115}$$

It is the term $2.012\times10^{-3}e^{(-8.3\times0.5)}$ in equation (3.113) after being scaled. Equations (3.113) and (3.114), very similar to exponential-sigmoid equation (3.70), can

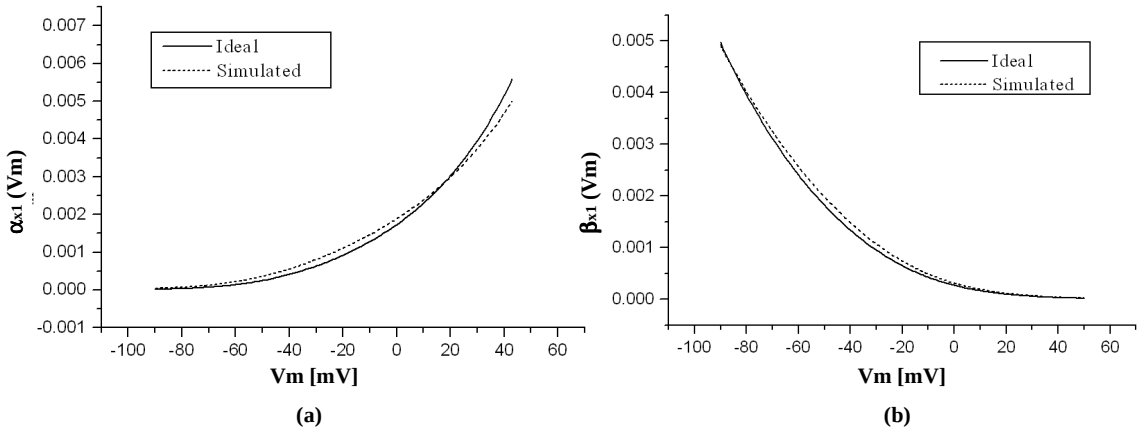

Figure 3.24: Ideal and simulated opening and closing rate of $x1$. (a)α_{x1}, (b)β_{x1}.

be implemented with the emitter-coupled pairs combined with a single exponential circuit block introduced in section 3.3.2. The block diagram of the exponential-sigmoid circuit is shown in Figure 3.12, with I_0 being replaced with the output current created by the circuit depicted in Figure 3.13. The transistor circuits for α'_{x1} and β'_{x1} are given in Appendix A, schematics page *Sch*-6 and *Sch*-7. The simulation results of the transistor circuits are shown in Figure 3.24(a), for α_{x1}, and 3.24(b), for β_{x1}. In both figures, the solid curves depict the ideal relations of the opening/closing rates vs. V_m, calculated from equations (2.47) and (2.48), and the dashed curves are the simulated results of the implementing circuits (schematics page *Sch*-6 and *Sch*-7 in Appendix A) after being scaled back to the original magnitude for comparison (refer to Table 3.2 for the scaling of α_{x1} and β_{x1}). The average SER (signal-to-error ratio) for the circuit realization of α_{x1} is 15 dB, and is 20.5 dB for β_{x1}, and the corresponding R-square is 0.9907 for α_{x1} and 0.9978 for β_{x1}.

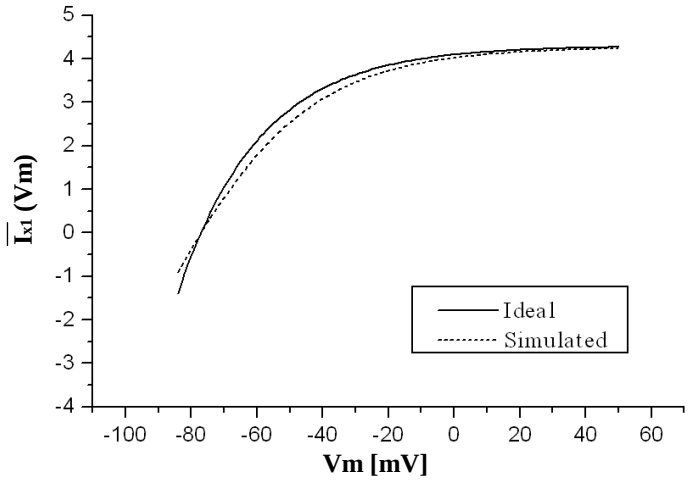

Figure 3.25: Ideal and simulated curves: $\overline{I_{x1}}$ vs. V_m.

Maximum Current of Time-dependent Potassium Channel: $\overline{I_{x1}}$

As depicted in Figure 3.20(b), I_{x1} is the product of $x1$ and $\overline{I_{x1}}$. The expression for $\overline{I_{x1}}$, given in equation (2.43), is transformed with the Matlab Curve Fitting Toolbox for easier circuit realization, and is rewritten as follows after scaling the variables:

$$\overline{I_{x1}}' = 4.264 \times 10^{-6} - \frac{50 \times 10^{-6}}{e^{4.345(V_m'+1.31)} + 1}, \tag{3.116}$$

where we select the scale factor of $\overline{I_{x1}}$ to be 10^6, i.e. $\overline{I_{x1}} = 10^6 \cdot \overline{I_{x1}}'$. Following equation (3.116), $\overline{I_{x1}}'$ is realized in a VLSI circuit with a constant current source and the sigmoid-function circuit illustrated in Figure 3.12. The transistor circuit for $\overline{I_{x1}}'$ is in Appendix A, schematics page *Sch*-8. The PSpice simulated $\overline{I_{x1}}'$ vs. V_m', after being scaled back, is shown in Figure 3.25 with the dashed line, compared with the ideal $\overline{I_{x1}}$ vs. V_m curve of equation (2.43) depicted with the solid line in the same Figure. The average SER (signal-to-error ratio) for the circuit implementation of $\overline{I_{x1}}$ is 27.7 dB, and the R-square between the ideal and the simulated data is 0.9886.

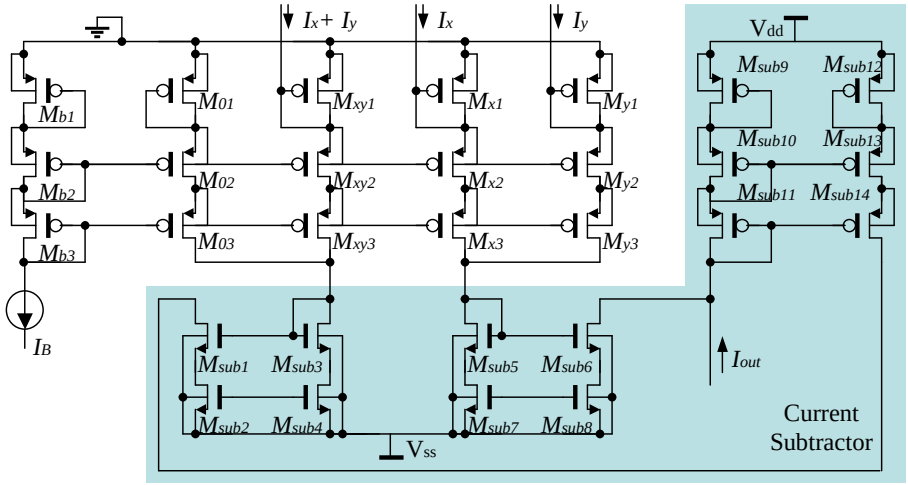

Figure 3.26: PMOS current multiplier based on Tanno multiplier.

Multiplier for $\overline{I_{x1}} \cdot x1$

$\overline{I_{x1}}$ is multiplied with the gating variable $x1$ to generate the final potassium current I_{x1}, as illustrated in the diagram in Figure 3.20(b), and described by equation (2.43). After the scaling and initial value shifting processes (provided in Table 3.2), equation (2.43) is changed to the following:

$$I'_{x1} = 2 \times 10^5 \overline{I_{x1}}' x1'. \tag{3.117}$$

The multiplier is based on the Tanno circuit, as introduced in section 3.3.3, with some modification to adapt it to our application. The transistor circuit of the multiplier is depicted in Figure 3.26, which is composed of a quarter squarer, shown as the unshaded area in Figure 3.26, and a current subtractor, shown in the shaded area in the figure. Different upper-rail voltages are applied for these two parts of the circuit because of the constraints from the usage of the inputs and the output of the multiplier module. These constraints follow from the fact that the input currents, coming from current mirrors of the previous stage, restrict the

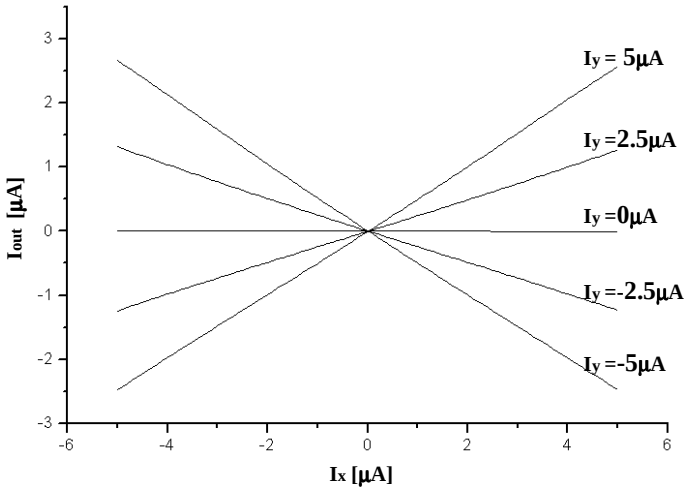

Figure 3.27: Simulation results of modified Tanno multiplier.

voltages on the inputs to make the output transistors of the current mirrors work in the saturation region. Since the voltages at the inputs are decided by the input transistors M_{xy1}, M_{x1}, and M_{y1}, the sourcing PMOS transistors of the current mirrors have very small working ranges in the saturation region if the previous stage and the quarter squarer are powered by the same upper-rail supply voltages. Hence, ground is employed instead of V_{dd} to serve as the upper rail voltage for the quarter squarer circuit. For the output of the multiplier, the output voltage, determined by the succeeding circuit, is limited to around 0 for our application, and thus the current subtractor remains powered by V_{dd}. Different from the original Tanno multiplier, PMOS transistors are used alternatively, and cascode structures are employed in the bias block M_{b2} and M_{b3}, and in the current subtractor to mitigate the channel modulation effect. The complete circuit of this multiplier with transistor parameters is provided in Appendix A, schematics page *Sch*-9. The PSpice simulation result of the modified Tanno current multiplier is shown in Figure 3.27.

Table 3.5: Equations of the opening and closing rate variables for I_{Na}.

Variable	Reformulated Equation	Sig-to-Err Ratio (dB)	R-Square
α'_m	$1.097 \times 10^{-5} + V'_m \times 10^{-5} - \frac{6.292\times10^{-6}}{e^{-5.687(V'_m+0.762089)}+1}$	25.9	0.9989
β'_m	$1.096 \times 10^{-5} e^{-0.05690(V'_m+0.9)}$	17.0	0.9943
α'_h	$1.625 \times 10^{-5} e^{-25(V'_m+0.9)}$	-54.5	0.8776
β'_h	$\frac{8.5\times10^{-6}}{e^{-0.082(V'_m+0.225)}+1}$	39.8	0.9999
α'_j	$\frac{5.53\times10^{-5} e^{-25(V'_m+0.78)}}{e^{-2(V'_m+0.78)}+1}$	-52.0	0.9972
β'_j	$\frac{1.5\times10^{-5}}{e^{-10(V'_m+0.32)}+1}$	28.2	0.9995

3.4.4 Time-Dependent Inward Sodium Current I_{Na}

Opening/Closing Rates of Sodium Gating Variables

There are three gating variables for the fast sodium current, m, h, and j. Their realization circuits, illustrated in Figure 3.23, have been presented in section 3.4.2. Hence, we will only introduce the circuit implementing the black boxes for the opening and closing rate variables next.

The original equations for the opening and closing rates are provided in equations (2.49)−(2.54), which are rewritten in Table 3.5 to take into account the reformulation processes as described in section 3.2. The third and the fourth columns of Table 3.5 list the SER (signal-to-error ratio) and R-square of the PSpice simulated results for the transistor circuit realization of the opening and closing rate variables vs. the values given from the equations, and this will be discussed after the simulation results are presented.

α'_m is realized following its expression shown in Table 3.5 by a constant current source for the first term in the expression, a linear voltage to current converter for

the second term, and a sigmoid-function circuit for the third term. The differential circuit introduced in section 3.3.1, Figure 3.5, is adopted to realize the linear voltage to current converter. The sigmoid-function circuit is shown in Figure 3.12 and presented in section 3.3.2. The detailed transistor circuit for implementing α_m is provided in Appendix A, schematics page *Sch*-11. The PSpice simulation results of the circuit for α_m compared with the ideal values calculated from the equation are shown in Figure 3.28(a). β'_m is implemented with the single exponential circuit depicted in Figure 3.13 according to the expression of β'_m given in Table 3.5, and its transistor circuit is presented in Appendix A, schematics page *Sch*-12. The circuit simulation results for β_m are shown in Figure 3.28(b).

The expression for α'_h in Table 3.5 contains a single exponential term, and thus can be modeled with the exponential circuit illustrated in Figure 3.13. The circuit for realizing the sigmoid function for β'_h is depicted in Figure 3.12. The transistor circuits for implementing α_h and β_h are provided in Appendix A, schematics page *Sch*-13 and *Sch*-14, and their PSpice simulation results are shown in Figure 3.28(c) and (d) respectively with the dashed curves, compared with the ideal values depicted with the solid curves.

The circuit for realizing α'_j uses the sigmoid circuit in Figure 3.12, but with replacement of I_0 with the output current of the single exponential circuit shown in Figure 3.13, whose value is exponentially decided by the input voltage. The equation of β'_j is realized, again, with the sigmoid-function circuit illustrated in Figure 3.12. The transistor circuits for implementing α_j and β_j are provided in Appendix A, schematics page *Sch*-15 and *Sch*-16. The curves of the circuit simulated and ideal values of α_j and β_j vs. Vm are shown in Figure 3.28(e) and (f).

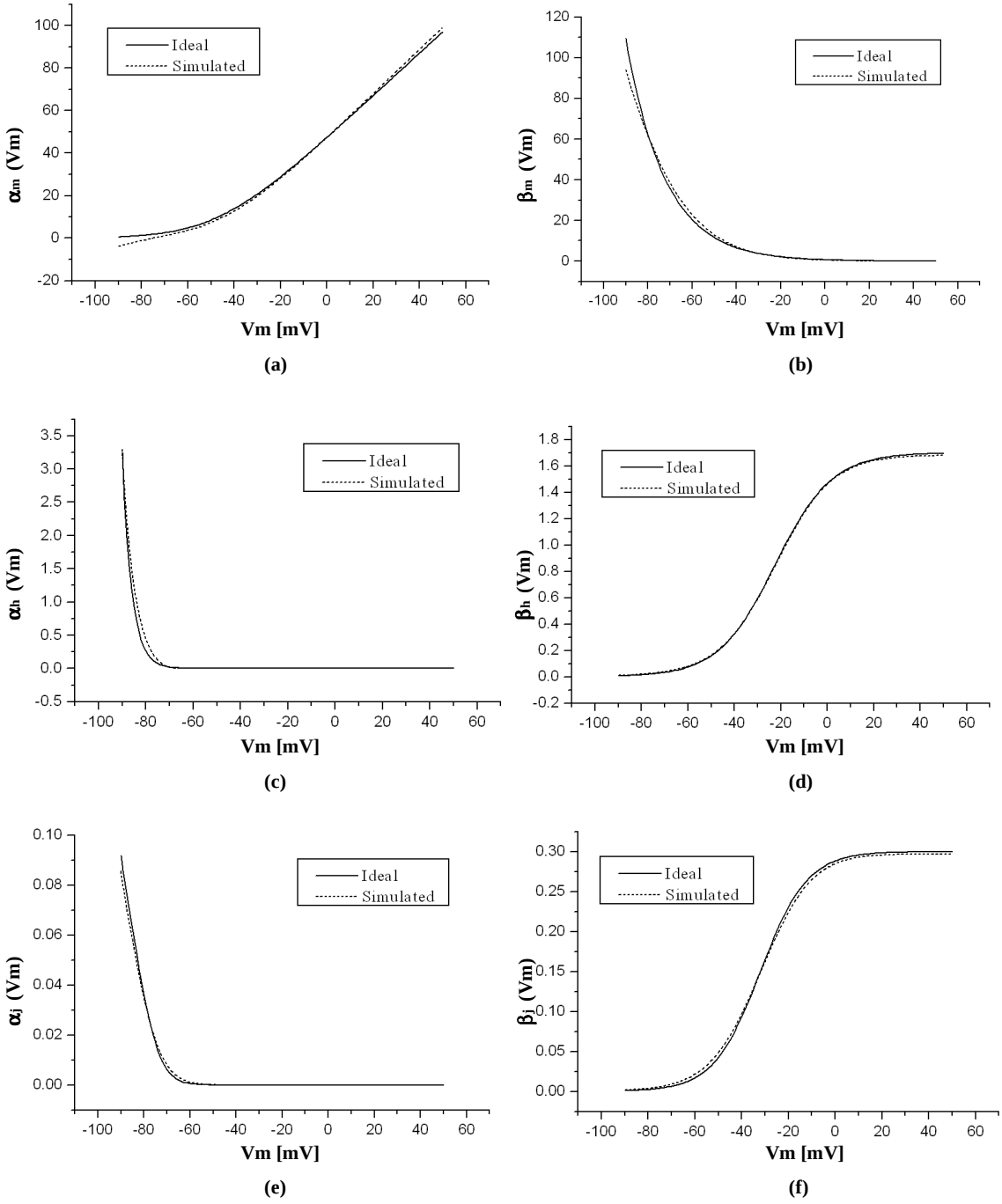

Figure 3.28: Ideal and simulated opening and closing rates of gating variables for I_{Na}. (a)α_m. (b)β_m. (c)α_h. (d)β_h. (e)α_j. (f)β_j.

All circuits for the sodium opening and closing rates show high R-square values as listed in Table 3.5, which indicate good correlation between the ideal and the simulated results. Most circuits show good average SER, except α_h and α_j. The low SER of α_h and α_j is because that, in a large range of the working region of V_m, α_h and α_j are nearly zero, and this can be seen in Figure 3.28(c) and 3.28(e). According to the definition of SER, i.e. equation (3.101), when the expected value E_i tends to be zero and the observed value O_i is not as close to zero as E_i, the SER then becomes negative and indicates a big difference between the expected results and the observed value. The ideal value of α_h drops fast from around 3 at $V_m = -90\ mV$ to about 10^{-5} at $V_m = -50\ mV$ and reaches the order of 10^{-15} with increasing V_m. Similarly α_j drops from around 0.09 at $V_m = -90\ mV$ to the order of 10^{-16} with increasing V_m. We observe that in the equation of gating variable h (or j), that is equation (3.103), when α_h (or α_j) is close to zero, β_h (or β_j) has high enough value to keep the term $\beta_z \cdot z$ dominating the right side of the equation (if z is not zero). Therefore we assume the close-to-zero values of α_h and α_j are not as important as their larger values. Thus we ignore the big SERs of α_h and α_j for the close-to-zero values. Recalculating the average SERs for α_h in the range $V_m = [-90, -60]\ mV$ and for α_j in the range $V_m = [-90, -50]\ mV$, where their values are not so close to zero, the circuit implementation for α_h and α_j presents a SER of 10.7 dB and 14.3 dB for each.

Sodium Current I_{Na}

The equation for implementing sodium current I_{Na} is from equation (2.44) and is given as follows:

$$I'_{Na} = 1.28 \times 10^{23} m'^3 h' j' (V'_m - 0.5) + 3 \times 10^{-7} (V'_m - 0.5), \tag{3.118}$$

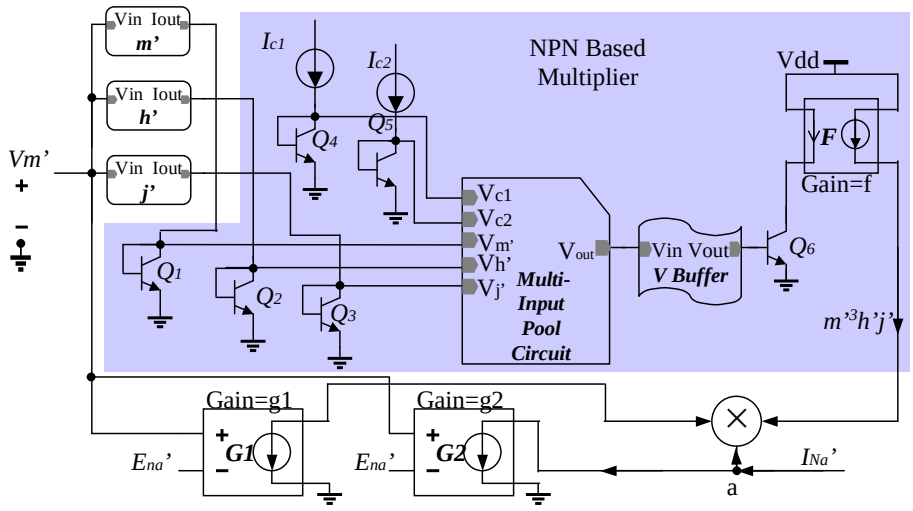

Figure 3.29: Circuit diagram of I_{Na}. Refer to Appendix A, schematics page *Sch*-10 for transistor circuits.

where I'_{Na} is the scaled sodium current, V'_m is the scaled membrane potential, and m', h', and j' are the scaled gating variables. The scaling factors are listed in Table 3.2. Following this equation, Figure 3.29 provides more details of the implementation circuit for I_{Na}. The three modules on the left top corner model the gating variables m', h', and j' and can be realized with the circuit structure introduced in Figure 3.23. $G1$ and $G2$ are linear transconductors, with gains of $g1 = 5\mu$ and $g2 = 0.3\mu$, respectively, and realize $V'_m - E'_{Na}$ with different amplification factors, where E'_{Na} is, according to equation (3.118), 0.5 V. The shaded area is a NPN-based multi-input multiplier that implements $m'^3h'j'$. The output of the NPN-based multiplier is then multiplied with the output current created by $G1$, and the product is added to the output of $G2$ to achieve the final I'_{Na}.

In the NPN-based multiplier depicted in Figure 3.29, Q_1, Q_2, Q_3 take the output currents from the gating variable modules and convert them into voltages.

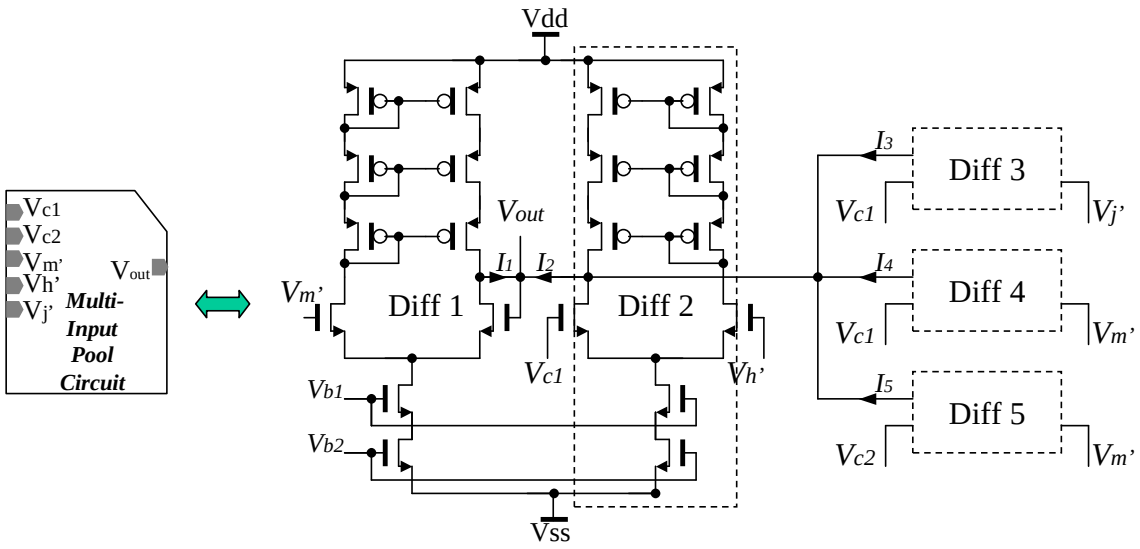

Figure 3.30: Circuit of a multi-input adder/subtractor for I_{Na} module. Refer to Appendix A, schematics page *Sch*-17 for transistor circuits.

Q_4 and Q_5 provide biasing voltages. *V-Buffer* and Q_6 transfer voltage back to current. F serves to change the direction of the output current from the multiplier and has a gain $f = 1$. Different from Figure 3.17, which uses cascaded pool circuits as the adder/subtractor (refer to section 3.3.1), this NPN-based multiplier for I_{Na} is based on the pool circuit shown in Figure 3.9 which is expanded for multiple inputs as illustrated in Figure 3.30. *Diff 1* corresponds to the differential circuit on the left side of the pool circuit in Figure 3.9. *Diff 2* to *Diff 5*, with each being equivalent to the differential circuit on the right side of the pool circuit in Figure 3.9, are identical and are all connected to the output point V_{out}. V_{out} is connected to the input of *V-Buffer* as shown in Figure 3.29, which does not draw any current (refer to Figure 3.7(b) for *V-Buffer*). Hence, we have $I_1 = -(I_2 + I_3 + I_4 + I_5)$. The expression of I_1 follows equation (3.44), and I_i $(i = 2, 3, 4, 5)$ follow equation (3.45). If the non-linear terms $(V_1 - V_{out})^2$ and $(V_2 - V_3)^2$ in equations (3.44) and

(3.45) are ignored, the currents can be linearly added to yield the output expression for Figure 3.30:

$$\begin{cases} I_1 = K_n(V_1 - V_{out})\sqrt{\frac{2I_{B1}}{K_n}}, \\ I_{2,D2} + I_{2,D3} + I_{2,D4} + I_{2,D5} = K_n(V_{2,D2} - V_{3,D2} + V_{2,D3} \\ \qquad -V_{3,D3} + V_{2,D4} - V_{2,D4} + V_{2,D5} - V_{3,D5})\sqrt{\frac{2I_{B2}}{K_n}}, \\ I_1 = -(I_{2,D2} + I_{2,D3} + I_{2,D4} + I_{2,D5}), \end{cases} \tag{3.119}$$

$$\begin{aligned} \Rightarrow \quad & V_{out} = V_1 + (V_{2,D2} - V_{3,D2} + V_{2,D3} - V_{3,D3} + V_{2,D4} \\ - \quad & V_{2,D4} + V_{2,D5} - V_{3,D5}), \end{aligned} \tag{3.120}$$

where, in order to make the symbols agree with those in equation (3.45), we use $I_{2,Di}$ $(i = 2, 3, 4, 5)$ to represent current I_i from *Diff i*, and use $V_{2,Di}$ and $V_{3,Di}$ $(i = 2, 3, 4, 5)$ to represent the voltages of the positive and negative terminals of *Diff i*. Following equation (3.120), the output V_{out} in Figure 3.30 is described by:

$$V_{out} = 3V'_m + V'_h + V'_j - (3V_{c1} + V_{c2}), \tag{3.121}$$

where $V_{m'}$, $V_{h'}$, $V_{j'}$, V_{c1}, and V_{c2} are the emitter-base voltages of $Q1 - Q5$ in Figure 3.29. The output of the NPN-based multiplier is then expressed by:

$$I_{Q6} = \frac{m'^3 h' j'}{(I_{c1})^3 \cdot I_{c2}}. \tag{3.122}$$

The detailed transistor circuits of the I_{Na} diagram in Figure 3.29 is provided in Appendix A, schematics page *Sch*-10.

3.4.5 Time-Dependent Slow Inward Calcium Current I_s

Opening/Closing Rates of Calcium Gating Variables

There are two gating variables for the calcium current I_s: d and f. They are realized by the gating variable circuit provided in Figure 3.23. The equations for

the opening and closing rates of gating variable d are rewritten from equations (2.54) and (2.55) as follows:

$$\alpha'_d = \frac{2.456 \times 10^{-5} e^{-(V'_m+0.9)}}{e^{-7.2(V'_m-0.05)}+1}, \tag{3.123}$$

$$\beta'_d = \frac{1.48 \times 10^{-5} e^{-1.7(V'_m+0.9)}}{e^{5(V'_m+0.44)}+1}, \tag{3.124}$$

where, again, we use single quotations to distinguish the scaled variables from the original ones where the scaling factors are provided in Table 3.2. Here we re-organize the constant coefficients of the equations for easier circuit design. For example, $0.095e^{[-0.01\times(-5)]}$ in the original equation (2.54) is converted as follows:

$$0.095e^{[-0.01\times(-5)]} = 0.095 \cdot e^{+(0.01\times 95)} \cdot e^{(0.01\times 5 - 0.01\times 95)} = 2.456 \times 10^{-5} e^{(-0.01\times 90)}, \tag{3.125}$$

and it is rewritten as $2.456\times10^{-5}e^{(-0.9)}$ in equation (3.123). Similarly, the equations of α_f and β_f are rewritten by re-organizing the constant coefficients as follows from equation (2.56) and (2.57):

$$\alpha'_f = \frac{1.97 \times 10^{-5} e^{-0.8(V'_m+0.9)}}{e^{15(V'_m+0.28)}+1}, \tag{3.126}$$

$$\beta'_f = \frac{2.16 \times 10^{-5} e^{-2(V'_m+0.9)}}{e^{-20(V'_m+0.3)}+1}. \tag{3.127}$$

Equations (3.123) to (3.127) are all (3.70)-type of equations, and, thus, can be implemented with the sigmoid-function circuit shown in Figure 3.12, with I_0 being substituted by the exponential circuit provided in Figure 3.13. The transistor circuits for realizing equations (3.123)-(3.127)are provided in Appendix A, schematics page *Sch*-20 to *Sch*-23. Figure 3.31(a)(b) shows the simulation results of the implementation circuits for α_d and β_d and also the curves of the ideal cases, calculated directly from equations (2.54) and (2.55). The SER (signal-to-error ratio) of the circuit realization for α_d is 37 dB, and 26.8 dB for β_d, and the R-square

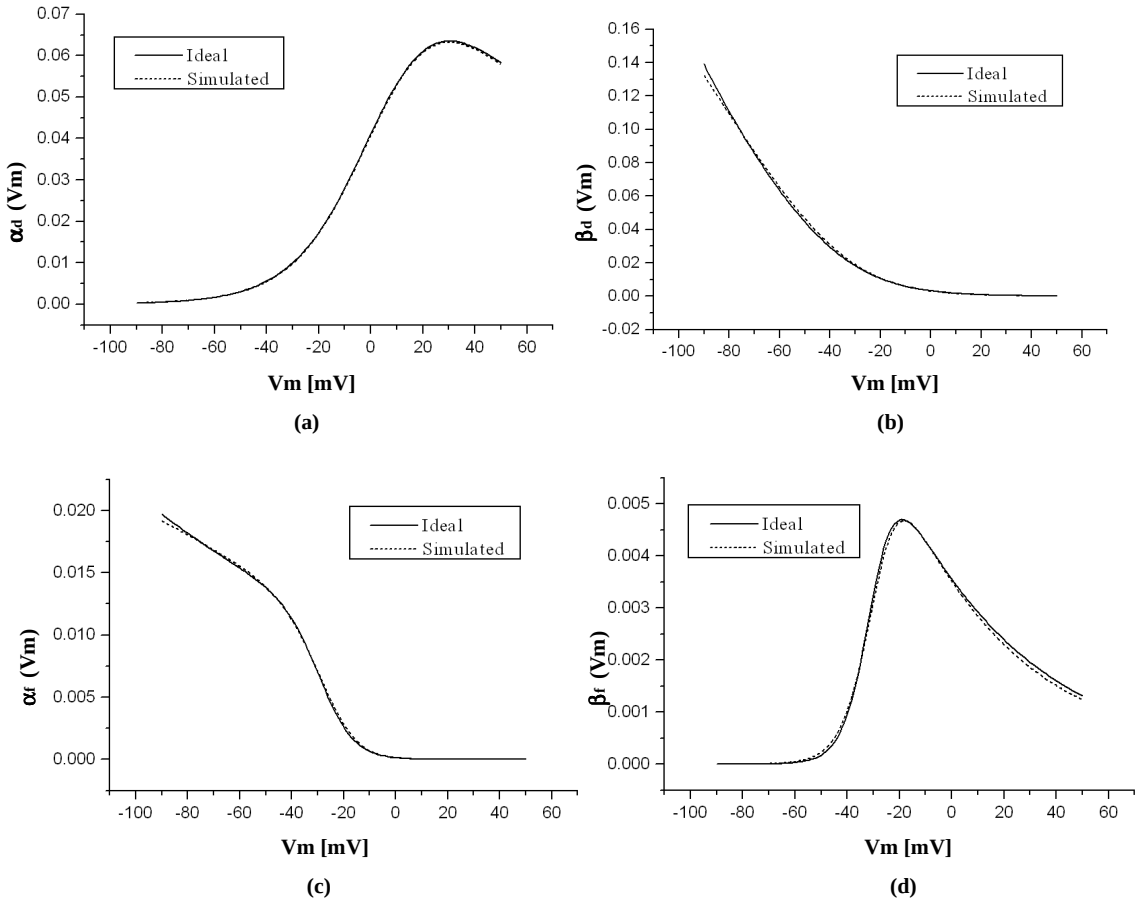

Figure 3.31: Ideal and simulated opening and closing rate variables for I_s. (a)α_d. (b)β_d. (c)α_f. (d)β_f.

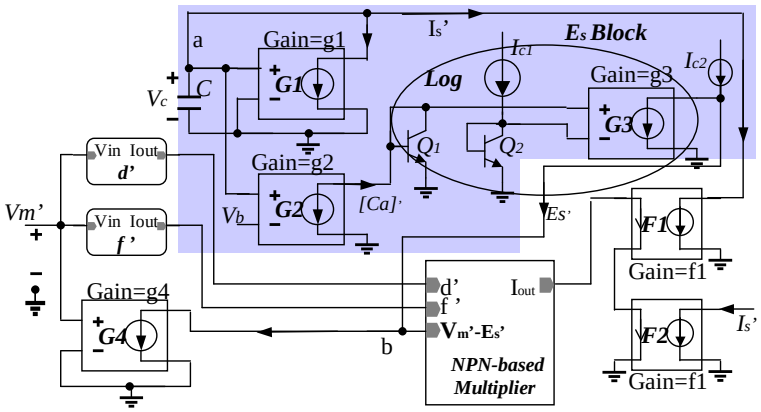

Figure 3.32: Circuit diagram of I_s. Refer to Appendix A, schematics page *Sch*-19 for transistor circuits.

for α_d and β_d are 1.0000 and 0.9933, respectively. The simulated results and the ideal values for α_f and β_f are shown in Figure 3.31(c)(d). The SER of α_f is 28.7 dB, and the SER of β_f is 22.4 dB. The R-square for α_f and β_f are 0.9998 and 0.9990, respectively.

Calcium Current I_s

Equations (3.128) to (3.130) provide the reformulated equations for the calcium current I_s after the scaling and initial condition shifting processes (refer to section 3.2.2 and 3.2.3, and Table 3.2) are performed on the original equations of the Beeler-Reuter model (2.45), (2.59), and (2.60):

$$I'_s = 3.6 \times 10^5 d' f' (V'_m - E'_s \times 10^4), \tag{3.128}$$

$$E'_s = -8.23 \times 10^{-7} - 1.30287 \times 10^{-7} \ln [Ca]'_i, \tag{3.129}$$

$$\frac{d[Ca]'_i}{dt} = -0.1 I'_s + 0.07(10^{-7} - [Ca]'_i). \tag{3.130}$$

The diagram for implementing I_s is illustrated in Figure 3.32. The d' and f' modules on the left consist of the gating variable circuit depicted in Figure 3.23.

The voltage V'_m is linearly converted by the same scale factor as E'_s by $G4$, subtracts E'_s at node b, and then feeds the current into an NPN-based multiplier. The NPN-based multiplier follows the same design strategy presented in section 3.3.3, and a similar multiplier has been introduced as when we discussed the multiplier circuit for I_{Na}. Therefore, we do not repeat the details for the NPN-based multiplier for I_s here; its transistor circuit can be found in Appendix A, schematics page *Sch*-26. The calcium equilibrium potential E'_s is created at node b by the circuit illustrated in the shaded area of Figure 3.32, i.e. the *Es Block*. I'_s is generated by a NPN-based multiplier, which takes the scaled d', f' and $V'_m - E'_s$ as the inputs, and delivers its output current, i.e. I'_s, to $F1$ and $F2$. $F1$ and $F2$ duplicate I'_s and sends one copy via $F2$ to charge the membrane capacitor in the succeeding circuit and the other via $F1$ as a feedback to the *Es block*.

In the *Es Block* in Figure 3.32, a capacitor C and a linear transconductor $G1$ with a transconductance g_1 construct the derivative function for equation (3.130). The voltage across the capacitor V_c, is described by the following equation:

$$C\frac{dV_c}{dt} = -I'_s - V_c \times g_1, \tag{3.131}$$

where V_c has the relation with $[Ca']$ that can be expressed by the following equation using g_2, the gain of $G2$:

$$V_c = \frac{[Ca]'_i}{g_2} + V_b, \tag{3.132}$$

where V_b is the bias voltage on the negative terminal of $G2$. Taking equation (3.132) into (3.131) creates:

$$\frac{C}{g_2}\frac{d[Ca]'_i}{dt} = -I'_s + g_1 \times (-V_b - \frac{[Ca]'_i}{g_2}). \tag{3.133}$$

Equation (3.133) can be equivalent with equation (3.130) by selecting proper values of the circuit parameters. In our VLSI design, g_1 is set to 7μ, g_2 is set to 10μ, V_b is

-0.01 V, and C is 0.1 μF. The transistor circuit for implementing equation (3.130) is shown in Appendix A, schematics page Sch-24. $[Ca]_i'$, generated by $G2$, is sent to a logarithm circuit, shown in the oval in Figure 3.32, which implements equation (3.129). The same as the logarithm circuit introduced in Figure 3.14, the logarithm circuit for Es is composed of two NPN transistors Q_1 and Q_2, a constant current sources I_{c1}, and a linear transconductor $G3$ with a gain $g_3 = 5\mu$. The logarithm circuit together with I_{c2} realize equation (3.129). The two bias currents I_{c1} and I_{c2} are set to $10\mu A$ and $0.674\mu A$, respectively. The detailed transistor circuit for creating E_s is also provided in page Sch-24 in Appendix A.

3.4.6 Action Potential V_m

Putting the circuits of the ionic currents presented in the previous sections together, the VLSI circuit that imitates the behavior of a membrane potential is established as shown in the block diagram in Figure 3.19 and in the schematics page Sch-1 in appendix A. More than three thousand transistors are used to build the full circuit for modeling the electrical activity of a single cardiac cell. When the external stimulating source sends a current impulse of 20 μA for a duration of about 0.003 second, the circuit creates an action potential across the capacitor C_m and the waveform is shown with the dashed line in Figure 3.33. The simulation results, after being scaled back to the original magnitude, indicate that the circuit-generated V_m has a resting potential of about -84.7 mV, a peak of the upstroke of 47.7 mV, and a re-polarization duration (measured at 90% of re-polarization completion) of 300 ms. The results are compared with the ideal V_m which is calculated from the original Beeler-Reuter equations and depicted with the solid line in Figure 3.33. At the same amount of stimulus (compared with the de-scaled

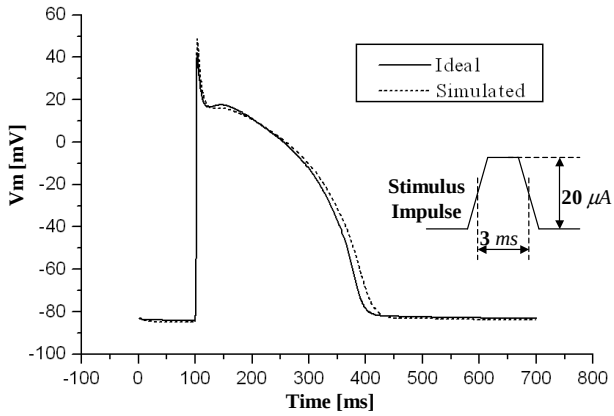

Figure 3.33: Ideal and simulated action potential.

stimulus), the ideal action potential has a resting potential of -83.0 mV, the peak of the upstroke of 41.7 mV, and a re-polarization duration of 287 ms.

The waveforms of the ionic currents I_{K1}, I_{x1}, I_{Na}, and I_s during an action potential are provided in Figure 3.34, with solid curves representing the ideal ionic currents and the dashed curves depicting the simulated values of the VLSI circuits. I_{K1} and I_{x1} are outward currents and responsible for discharging the membrane capacitance. Their maximum values are about 5.0 $\mu A/cm^2$ and 1.5 $\mu A/cm^2$ respectively. I_{Na} and I_s are inward currents (being negative), which charge the membrane capacitance. The magnitude of I_s is on the same order as I_{K1} and I_{x1}, which is about 4.3 $\mu A/cm^2$. I_{Na}, responsible for creating the steep upstroke at the start of an action potential, has a very big magnitude compared to the other ionic currents, which is around 140 $\mu A/cm^2$. I_{Na} is almost zero most of the time, except in the spike in the upstroke phase of an action potential. This is because most of the time, either the activation gating variable m or the inactivation gating variables h and j are closed, and only in the upstroke phase when m transits to open and h and j start to close, there is a narrow time period that all the

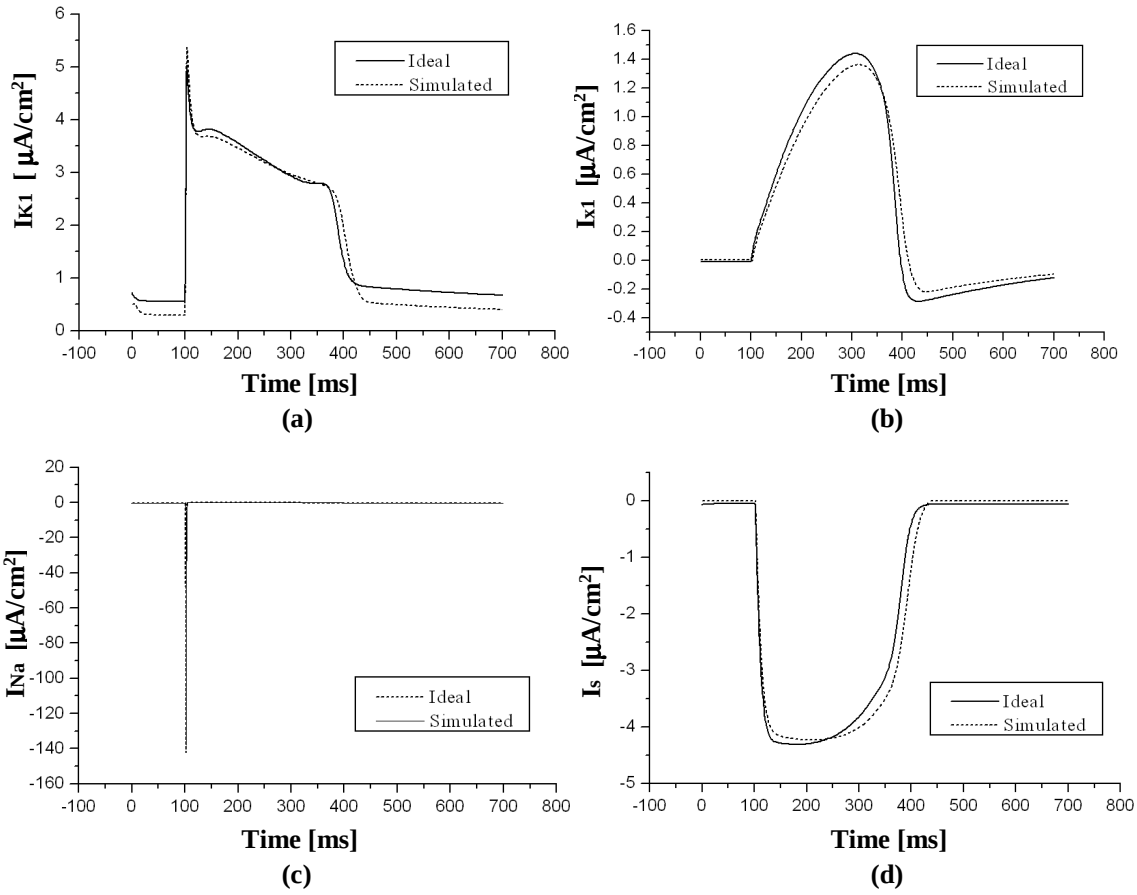

Figure 3.34: Ideal and simulated membrane ionic currents. (a)I_{K1}. (b)I_{x1}. (c)I_{Na}. (d)I_s.

gating variables are open to allow the passage of the sodium ions. This property of sodium channel decides the un-excitability of a cardiac cell for another action potential when it is still in the first action potential and the gating variables m, h and j have not flipped back to the state of a resting cell. This will be discussed again in chapter 4, when reentry and refractory period are introduced.

3.4.7 Discussions

Experimental Data of Beeler-Reuter Model

We have evaluated how close the VLSI realization is to the original equations in the Beeler-Reuter model using the average signal-to-error ratio (SER) and R-square for V_m-dependent equations. In this section, we will discuss the correlation between the experimental data from which the cardiac cell model is extracted and the equations of the model, and compare the correlation to that between the equation and the PSpice simulated results, as illustrated in Figure 3.35. The comparison of the data and the equations is difficult and sometimes not possible due to missing details in literature. The mathematical equations of the model are mostly based on multiple results of experiments carried out by different researchers, and can be adjusted from the original data with re-scaling or shifting along axis by Beeler and Reuter to simulate the ventricle, whereas the information of how the different data is combined to obtain the formulas and how the equations are re-scaled and shifted are not mentioned in [15]. In addition, most experimental data is provided by graphs rather than numbers, and this brings more difficulties to make numerical comparison of the data and the models. Hence, we do not provide full comparison of the data and the Beeler-Reuter model, and only present two examples to roughly show how close the resulted equations in the model are to the original experimental

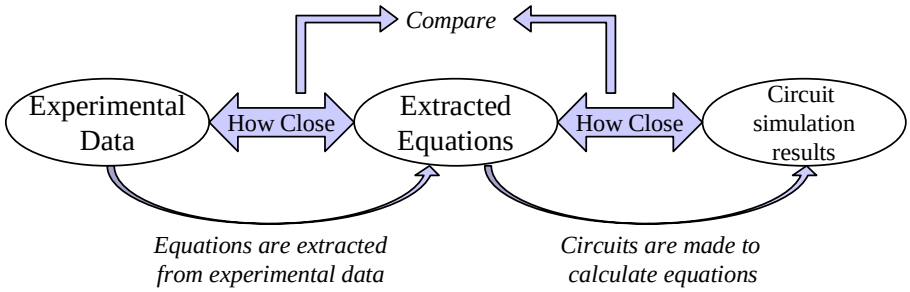

Figure 3.35: Comparison among experimental data, extracted equations, and circuit simulation results.

data, and also how close the equations are to simulation of the presented VLSI design.

In the first example, we discuss the formulation of I_{K1}. The formula of I_{K1} in the Beeler-Reuter model is converted from the equation used by McAllister etc. in [14], whose parameters were selected to give a current vs. voltage diagram similar to the experimental data published in [69]. The data points, totally 15, are shown graphically in [69], and we measured them with a ruler for their values and re-draw the data in Figure 3.36. The final equation of I_{K1} in the Beeler-Reuter model has been re-scaled and shifted from McAllister's equation and this information is not published, and, thus, we scale and shift the equation of I_{K1} (2.42) by the following formula to let the resulted equation give a best fit to the experimental data:

$$\widetilde{I_{K1}} = a_1 F_{K1}(a_3 V_m + a_4) + a_2, \tag{3.134}$$

where $\widetilde{I_{K1}}$ is the potassium current after being re-scaled and shifted for matching the data points, function $F_{K1}(V_m)$ is the right side of equation (2.42) for I_{K1}, and a_1, a_2, a_3, and a_4 are constants for scaling and shifting the X and Y axis. a_1, a_2, a_3, and a_4 are decided to let equation (3.134) best fit the experimental data, and the resulting $\widetilde{I_{K1}}$ curve is illustrated in Figure 3.36. Compared to Figure 3.22,

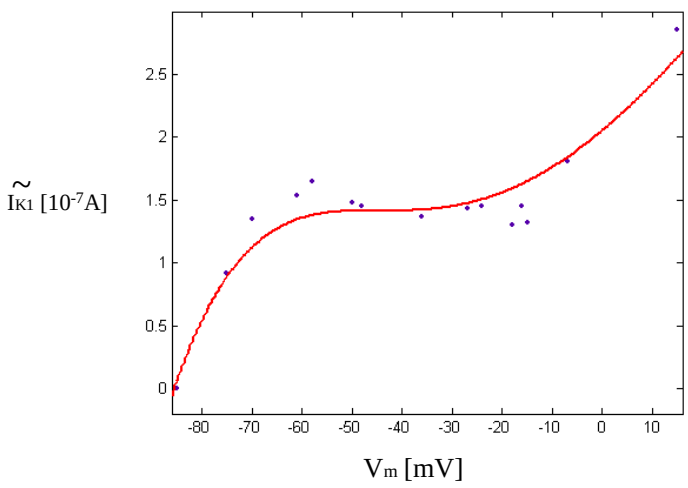

Figure 3.36: Experimental data [14] (dots) and its fitting curve of steady-state current-voltage relation of outward current in purkinje fibers.

which shows the I_{K1} curve calculated from the equation and the PSpice simulated I_{K1} curve, the data points in Figure 3.36 are more scattered around the equation curve than the simulated results. The average signal-to-error ratio (SER) of the experimental data and the curve of equation (3.134) in Figure 3.36 is 23.1 dB, and the R-square is 0.9490, showing worse correlation compared to the SER and the R-square of the Beeler-Reuter equation calculated curve and the PSpice simulated curve of Figure 3.22, 36.0 dB and 0.9966.

In the second example, we discuss the experimental data for obtaining the equations of the gate opening/closing rates (α_d and β_d) of the gating variable d (equations (2.55) and (2.56)). The equations of α_d and β_d are decided by the measurement results of the time constant τ_d and the steady value d_∞ at different command voltage steps (refer to chapter 2 section 2.3.2). The relation between α_d

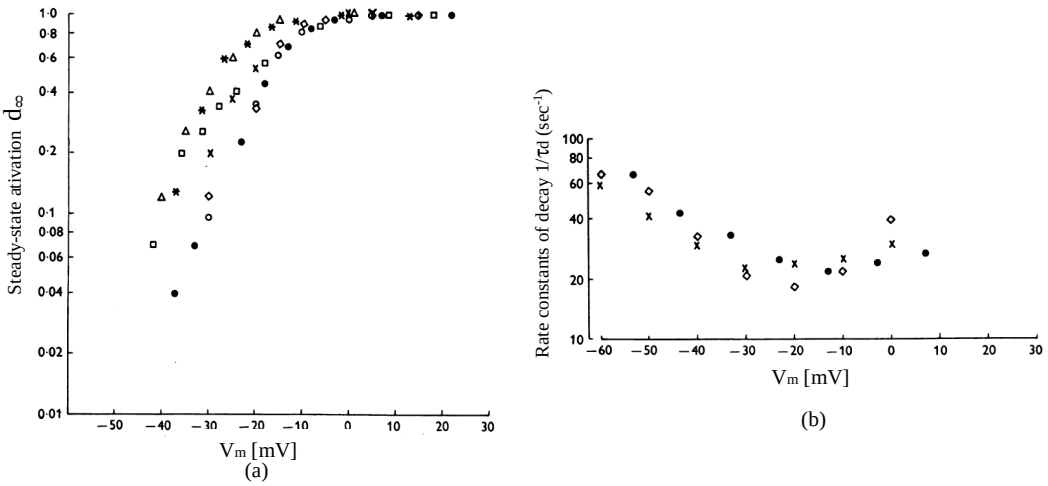

Figure 3.37: [48] (a) Steady-state activation d_∞ of calcium current I_s; data obtained from five cow ventricular trabeculae superfused with solution containing 0.2(∘), 0.45(×) or 1.8 mM $CaCl_2$ ($\bullet \star \square \triangle$). (b) Rate constant for decay $1/\tau_d$, measured with solution containing 0.2($\diamond$), 0.45(×) or 1.8 mM $CaCl_2$ (•).

and β_d, and τ_d and d_∞ is formulated as, rewritten from equations (2.9) and (2.10):

$$\tau_d = 1/(\alpha_d + \beta_d), \tag{3.135}$$

$$d_\infty = \alpha_d/(\alpha_d + \beta_d). \tag{3.136}$$

The τ_d and d_∞ curves used for defining the equations of α_d and β_d in the Beeler-Reuter model represent a collection of experimental results published in [47], [48], and [70]-[73]. Here, in Figure 3.37 [48], we show one set of the data measured by Reuter and Scholz. Figure 3.37 depicts τ_d^{-1} in (a) and normalized d_∞ in (b) in a semi-logarithm scale. Different symbols represent different samples in three solutions with different calcium concentration. We get the equation data of τ_d and d_∞ from equations (3.135) and (3.136) from the mathematical description of α_d and β_d in the Beeler-Reuter model, and then compare the calculated values to the experimental data. Again, the values of the experimental data is obtained

by measuring the data points in the graphs with a ruler. The SER of the experimental data and calculated values is 13.5 dB for d_∞ and 13.2 dB for τ_d, and the corresponding R-square is 0.8800 and 0.7115. The equation calculated τ_d and d_∞ are also compared to those obtained from the PSpice simulation. Again equations (3.135) and (3.136) are used to achieve simulated data of τ_d and d_∞ from the simulated α_d and β_d values (simulation curves are shown in Figure 3.31(a)(b)). The SER of the simulated data and the calculated values is 40.4 dB for d_∞ and 38.2 dB for τ_d, and the corresponding R-square is 0.9999 and 0.9986.

In the above two examples, we showed the experimental data for I_{K1}, τ_d and d_∞, and numerically estimated how close the data is to the extracted mathematical model by computing the average signal-to-error ratio and the R-square coefficient. The correlation metrics were compared with those derived from evaluating the similarity between the model and the PSpice simulated results. The comparison shows that the transistor circuits' simulated data has higher correlation to the model than the experimental data. Hence, we conclude the accuracy of the VLSI design of the Beeler-Reuter model is satisfactory.

Time Scale and Capacitors

There are eight capacitors in the VLSI cardiac cell model: one is for the membrane capacitance, one is for the differential equation of the calcium concentration, and the rest are for the gating variables $x1$, m, h, j, d, and f. The magnitude of the capacitance is decided by the original equations in the Beeler-Reuter model and also variable scaling factors (when ignoring time scaling). Take the membrane capacitance C_m as an example, it is defined in equation (2.40) and related to V_m and the ionic currents. Since V_m is numerically shrunk by a factor of 100 (ignoring

Table 3.6: Capacitances in the VLSI realization of Beeler-Reuter model (unit: F).

Schematics	V_m	I_{x1}	I_{Na}			I_s		
Cap Name	C_m	C_{x1}	C_m	C_h	C_j	C_d	C_f	$C_{[Ca]i}$
Cap in F	10^{-7}	10^{-6}	10^{-10}	5×10^{-9}	5×10^{-8}	10^{-6}	10^{-7}	10^{-7}

the unit) in the VLSI realization and I_{ion} is reduced by a factor of 10^6 (refer to Table 3.2), according to equation (2.40), C_m needs to be 10^4 times smaller than the original needed value 1 F in order to balance the right and the left sides of the equation, and, thus, in the circuit, the capacitance of C_m is 0.1 mF. Note that the units of variables employed by the cardiac cell model do not influence the variable scaling and are ignored, and only the values of the variables matter.

Time can be scaled easily by increasing or decreasing the capacitors with a same factor. When the capacitors are enlarged, it takes longer time to charge the capacitors, and, thus, the waveforms of the variables on the time axis are expanded. Vise versa, reduced capacitances spend less time to be charged and make the waveforms narrower. The Beeler-Reuter model uses ms as its time unit, and an action potential lasts for about 300 time units (300 ms). Therefore, when the model is mapped into the circuit, which is based on the second as the time unit, the duration of an action potential becomes 300 s. In order to make the circuit' generated waveforms consistent with those generated from the Beeler-Reuter model, the capacitance of the eight capacitors for implementing the Beeler-Reuter model in VLSI are shrunk by 1000 times. All the simulation results shown previously are with the scaled capacitors. The values of the capacitors are summarized in Table 3.6.

The VLSI circuits of the Beeler-Reuter model presented previously are able to

be realized on-chip, except for the capacitors. As shown in Table 3.6, the sizes of the capacitors range from 100 pF to 1 μF. A capacitance as big as 1 μF is hard to be realized on a chip. In the following we will discuss the methods for implementing big capacitors with smaller capacitors to solve this issue. Capacitor multipliers have been proposed for increasing the capacitances of compensation capacitors in [74]-[76]. However their schemes are not applicable to our circuit design of the heart model as next discussed. The compensation capacitors are used to introduce poles and are small, and, thus, the capacitor multiplication factors which are less than hundreds are sufficient to make on-chip compensation capacitors. In the VLSI design of the heart model, as provided in Table 3.6, the capacitance can be as high as 1 μF, and this requires a multiplication factor of at least 10^4. Different from the compensation capacitors, the capacitors in the heart model are used as integration devices, and, hence, demand higher accuracy and also bi-direction. The additional requirement of accuracy and bi-direction brings more difficulties in using the published capacitor multiplication techniques. Capacitor multiplication schemes can be divided into two categories: voltage-mode and current-mode. Voltage-mode, working the same way as amplifying Miller capacitance, can not be used in our case, because it amplifies the voltage signal with the same factor as the capacitor, which makes a voltage signal too high to be supplied by the power sources. The current-mode method amplifies capacitance by decreasing the capacitor currents. For example, if a capacitor is 1 μF and its maximum input current is 1 μA, the capacitor can be substituted with a capacitor 10^6 smaller by shrinking the current by a factor of 10^6, i.e. the maximum input current becomes 1 pA, with the time scale unchanged. A difficulty of implementing this method is the current shrinker. Implemented with current mirrors, a current reduction factor of 10^6 means not only

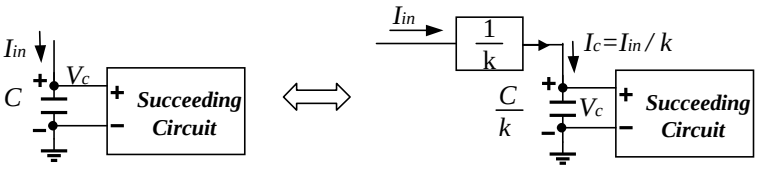

Figure 3.38: Current amplifier/shrinker circuit used for amplifying capacitance.

transistors of very big sizes in a cascaded circuit topology, but also tremendous challenge in designing circuits with accuracies to pA because high-order effects of transistors can easily overwhelm the tiny currents.

Here we propose a capacitor amplification circuit that can be used in the VLSI heart model. The circuit is based on current-mode, and has been mentioned in section 3.3.3 when we introduce the bipolar-based shrinking-current circuit provided in Figure 3.18. A diagram is given in Figure 3.38 to show how a current shrinker can be used to magnify the capacitance in our application. On the left side of the figure, the capacitor C serves as an integration device and its voltage, simulating a derivative variable in the heart model, drives a succeeding circuit which does not draw any current from the capacitor (connecting to the gates of MOS transistors). This circuit can be implemented with a capacitor k times smaller by using a current shrinker of factor $\frac{1}{k}$ (refer to Figure 3.18 for the current shrinker circuit), illustrated on the right side of Figure 3.38, while the capacitor voltage V_c remains the same for driving the succeeding circuit.

In the following example, we show the simulation results of the presented circuit for magnifying the capacitance for 10^4 times. Since the present educational VLSI MOSIS runs, using AMI 1.5 μm ABN technology, do not support PNP transistors, the PNP devices in the current shrinker shown in Figure 3.18 are replaced with NPNs. The circuit is modified accordingly and redrawn in Figure 3.39, in which Q_{pi}

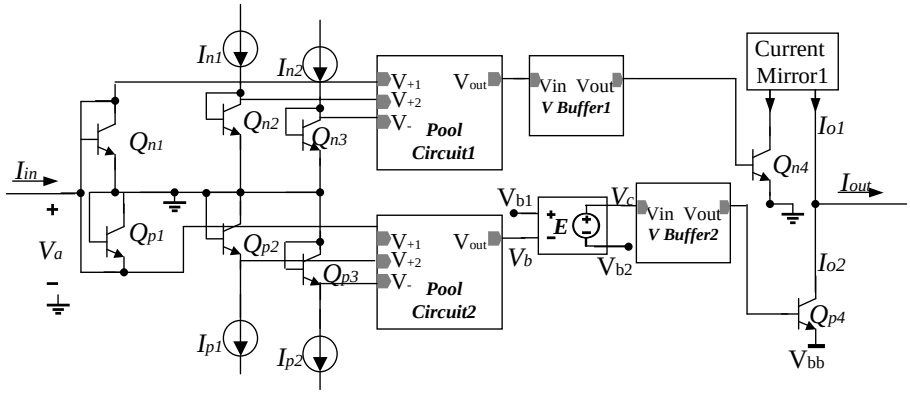

Figure 3.39: Current amplifier/shrinker circuit using NPN transistors.

($i = 1, 2, 3, 4$) are the NPN transistors and they keep the names of PNP transistors used in Figure 3.18. A voltage-to-voltage converter E is added to convert the output voltage of *Pool Circuit2* V_b to V_c, and $V_c = V_{b1} + V_{b2} - V_b$, where V_{b1} and V_{b2} are constant voltages. Note that in order to use NPN transistors, E needs to be added, which introduces more errors. Hence, if PNP is available, the original circuit shown in Figure 3.18 is preferred. The circuit in Figure 3.39 works the same way as the circuit in Figure 3.18. When $I_{in} > 0$, Q_{n1} and Q_{n4} are activated, Q_{p1} and Q_{p4} are cut off, and the output current I_{out} is supplied by Q_{n4}. When $I_{in} < 0$, Q_{p1} and Q_{p4} are activated, Q_{n1} and Q_{n4} are cut off, and the output current I_{out} is supplied by Q_{p4}.

We set the circuit parameters to let $I_{out} = 10^{-4} I_{in}$, and build the circuits like the ones shown in Figure 3.38 without "Succeeding circuit". The original capacitance is $C = 1\mu F$, and with the current shrinker, the integration function can be implemented with a capacitor 10^4 smaller, i.e. $C/k = 100pF$. The waveforms of the capacitor voltage are shown in Figure 3.40(a), with the solid line being the voltage across capacitor C, and the dashed line being the voltage across capacitor

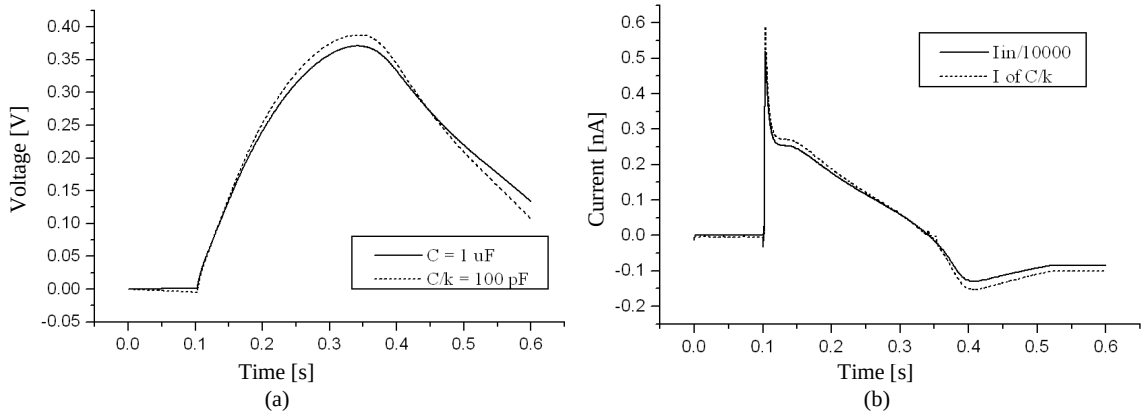

Figure 3.40: Simulation results of using current shrinker circuit to amplify capacitance. (a)Voltages of original capacitor and amplified capacitor. (b)Currents of original capacitor and amplified capacitor.

C/k. The currents going into the capacitors are shown in Figure 3.40(b), where the solid curve is the current of capacitor C (i.e. I_{in}) minimized by a factor of 10^4 in order to be compared with the current in C/k, and the dashed curve is the current of capacitor C/k. Here we adopt the current running through the capacitor of the gating variable $x1$ during an action potential as the input current I_{in}. The difference between the ideal I_{out} (i.e. $I_{in}/10^4$) and simulated I_{out} is caused by error sources such as the Early effect of the NPN transistors, and the non-idealism of the voltage adders, i.e. the pool circuits, voltage buffers, and the voltage-to-voltage converter E. More accurate voltage adders can be used to reduce the error and improve the linearity between I_{in} and I_{out}. Figure 3.41 shows a scheme to mitigate the Early effect by using the cascode structure. The figure depicts only the upper half of the circuit in Figure 3.39 for improvement, and the lower half can be modified the same way. The shaded areas are newly added. Q_{n5} and Q_{n6}, together with Q_{n1} and Q_{n4} incorporate the cascode structure, which reduces the

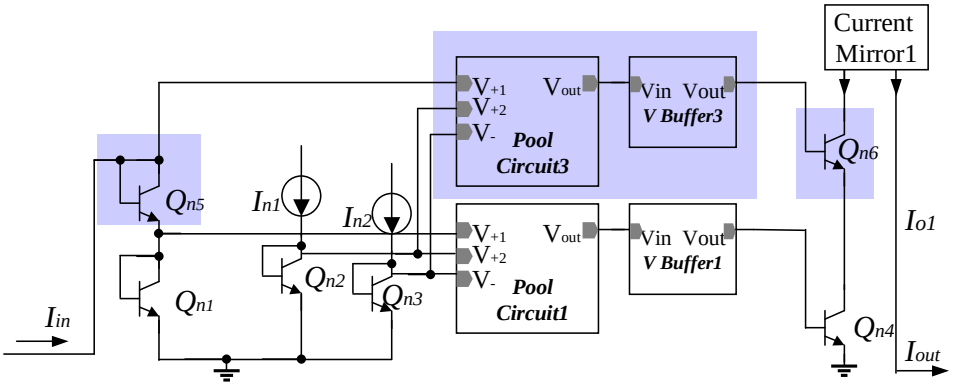

Figure 3.41: Cascode structure can be used to minimize the Early effect on Q_{n4} and improve the accuracy of I_{out}.

impact of the Early effect on the output current.

The presented capacitor amplification circuit is limited by the leakage current of the bipolar transistors. When a current is shrunk to be too small, the leakage current dominates the overall output current of the current shrinker and breaks the linear relationship between I_{in} and I_{out}. Hence, bipolar devices with low leakage currents are desirable for implementing the proposed capacitor amplification method.

Note it is possible to implement the circuit in Figure 3.18 with all NPN and PNP transistors being replaced by NMOS and PMOS transistors that work in the subthreshold region. The current in a subthreshold MOS transistor is given by [77]:

$$I_{DS} = I_0 e^{(kV_{GB}/V_T)}(e^{(-V_{SB}/V_T)} - e^{(-V_{DB}/V_T)}) \quad (3.137)$$

$$= I_0 e^{(kV_{GB}/V_T)}[e^{(-V_{SB}/V_T)}(1 - e^{(-V_{DS}/V_T)})], \quad (3.138)$$

where I_0 is the subthreshold current-scaling parameter, k is the subthreshold exponential coefficient, and V_T is the thermal voltage. When $V_{DS} > 5V_T$, the term

$e^{(-V_{DS}/V_T)}$ can be ignored, and the above equation can be rewritten to:

$$I_{DS} = I_0 e^{(-V_{SB}/V_T)} e^{(kV_{GB}/V_T)} \quad (3.139)$$

$$= I_0 e^{(kV_{SB}-V_{SB})/V_T} e^{(kV_{GS}/V_T)}. \quad (3.140)$$

When V_{SB} is a constant, the current I_{DS} is only exponentially dependent on the gate-source voltage V_{GS}, which makes the I-V properties of subthreshold MOS devices very similar to bipolar transistors. Therefore, the capacitor amplification circuit in Figure 3.18 can work the same way when its bipolar devices are replaced by MOS transistors by connecting the gate, source and drain of MOS devices where the base, emitter and collector of the NPN devices originally are connected respectively, and connecting the body to V_{ss}. With MOS transistors, the currents of the input and output terminals, and the bias currents I_{n1}, I_{n2}, I_{p1}, and I_{p2} in the circuit in Figure 3.18 have to be restricted within proper ranges to necessitate the subthreshold conditions of the replacing MOS transistors.

In the VLSI design of the cardiac cell model, the integration capacitors can be further minimized by shrinking the time scale. The current VLSI circuit is able to function properly as a cardiac cell with a time scale shrunk by up to 1000 times of the current time scale, that is, the generated action potential has a duration of about 300 μs after the time is scaled, and the capacitances are 1000 times smaller of the values listed in Table 3.6. For further shrinking the time scale, analysis of the high frequency operation of the VLSI circuit needs to be done, and this is one of the future works.

Impact of Parameter Variations on Design

In this section, we analyze the threshold voltage variation sensitivity of the following circuits: linear voltage to current converters, linear current to voltage convert-

ers, voltage buffers, and the pool circuits. These circuits are the building blocks of sigmoid functions and exponential functions, which, due to their exponential properties, are considered to be very sensitive to the fluctuation of circuit parameters.

Due to the imperfect control of fabrication processes, chips often display variations in transistor characteristics, such as the threshold voltage and drain currents [78][79]. Variabilities are roughly classified into two types [80]. One is chip-to-chip variability, which results from factors such as processing temperature and equipment properties. The other is within-chip fluctuations, which is caused by random factors, such as the spatial distribution of dopant and channel length variation. In the following discussion, we focus on the impact of within-chip threshold voltage variation on our VLSI design for the heart model. We consider that the threshold voltage is one of the most critical parameters that influences the accuracies of circuit realization of mathematical equations, because many output vs. input equations introduced in section 3.3 are dependent on the threshold voltage, and, current mirrors, one of the most often used circuit structures, require the proper match of the threshold voltages of the transistors at the input and output stages.

The Monte Carlo statistical tool provided by PSpice is used to investigate the threshold voltage variation sensitivity of the heart model circuits. The Monte Carlo analysis varies device parameters randomly and independently within a specified tolerance and performs multiple runs of analysis (DC, AC, or transient). In our simulation, the tolerance of the threshold voltage is determined from 62 sets of test data (MOSIS run numbers $T18K$ to $T1CL$) [81] from different fabrication runs for the AMI Semiconductor 1.5 μm ABN technology. Figure 3.42 shows the histogram of the NMOS threshold voltage and the Gaussian fitting curve for this experimentally determined data. The mean of the Gaussian curve is 0.53788 V,

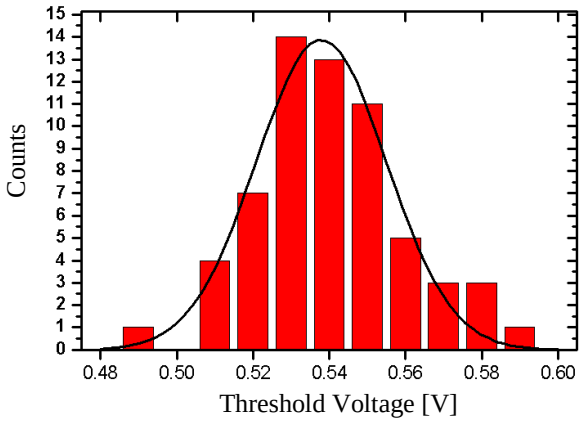

Figure 3.42: Histogram and Gaussian fit for the NMOS threshold voltages measured from 62 sets of data (AMI 1.5 μm technology).

and the standard deviation σ is 0.017 V. Therefore, the variation for our purpose is taken to be $0.017/0.53788 \simeq 3.2\%$. Note that this is a chip-to-chip variation, so we need to modify it to get the within-chip variation. The within-chip variation is estimated from the chip-to-chip variation in a way presented in the following.

It was reported in [80] that in a 0.35 μm process, the variation of the saturation current within a wafer is 3%, and its variation within 58 lots is 15%. Since a wafer holds many chips, we assume that the within-chip variation does not exceed the variation over a single wafer, and the lot-to-lot variation is equivalent to the chip-to-chip variation. Then the ratio of the chip-to-chip variation to the within-chip variation for the saturation current is higher by a factor of $\%15:\%3 = 5$. Since the saturation current is dependent on the threshold voltage through a square law, thus, the saturation current variation is worse than the threshold voltage. Also, by considering that the within-chip component of the variability becomes larger when the process scales down [80], we estimate that the within-chip variation of the threshold voltage for AMI 1.5 μm technology is lower than one fifth of the

Table 3.7: Monte Carlo analysis of threshold voltage variation on circuits

Circuit Function	Figure Number	σ	Variation
Voltage-Current Converter	Figure 3.5(a)	0.12 μA	2.1 %
Current-Voltage Converter #1	Figure 3.6	0.265 V	140%
Current-Voltage Converter #2	Figure 3.44(a)	1.3 mV	0.1 %
Voltage Buffer	Figure 3.7	1.5 mV	0.2%
Pool Circuit	Figure 3.9	3.9 mV	1.0%

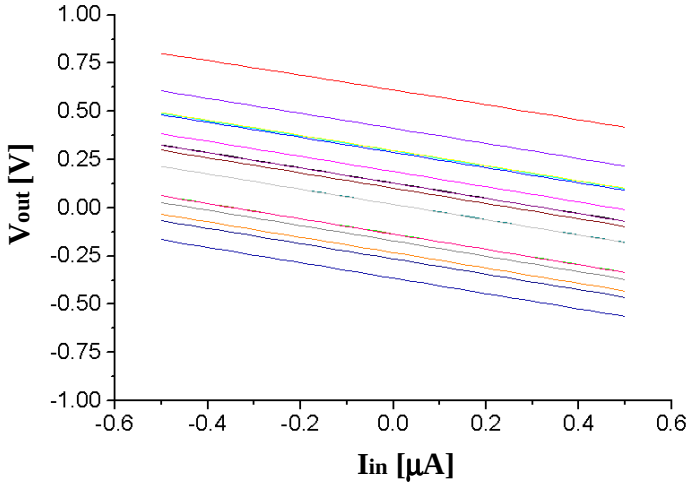

Figure 3.43: Monte Carlo analysis of *Current-Voltage Converter #1* (Figure 3.6).

chip-to-chip variation, that is $3.2\%/5 \simeq 0.6\%$. Therefore, 0.6% is taken as the tolerance of the threshold voltage in our simulation, and we use the Gaussian as the distribution type.

The results of the Monte Carlo analysis of the threshold voltage variation on the heart model circuits are provided in Table 3.7. The first column lists the circuit functions. All the circuits have been introduced in section 3.3, except the *Current-Voltage Converter* #2, which will be introduced shortly. The second column shows the figure numbers of the circuits. The third and the fourth columns are average standard deviations and average variations in percentage of circuit outputs caused by the fluctuation of the threshold voltage. The results given in Table 3.7 correspond to the Monte Carlo analysis of 20 PSpice runs.

As we can see from Table 3.7, most circuits we analyzed presented small variations, except *Current-Voltage Converter* #1 introduced in section 3.3.1. As shown in Figure 3.6, the linear V_{out} vs. I_{in} relationship relies on the channel modulation effect. That is, when there is a small input current, the current difference caused in $M2$ and $M4$ are canceled by the shifting of the output voltage. Due to the high sensitivity of V_{out} to current changes at the output stage, the implemented transimpedance is high, and the proper functioning of the linear current to voltage converter demands that $M1$ and $M2$, and $M3$ and $M4$ match very well. The mismatch introduced by the threshold voltage fluctuation severely shifts the output voltage as shown in Figure 3.43, hence, this presented circuit can not tolerate the variance of the threshold voltage we specify.

Figure 3.44(a) shows a proposed alternative linear current to voltage converter. It is the same as the input stage circuit of a bi-directional current mirror. By using equations of the saturation currents on both transistors as the following (under the

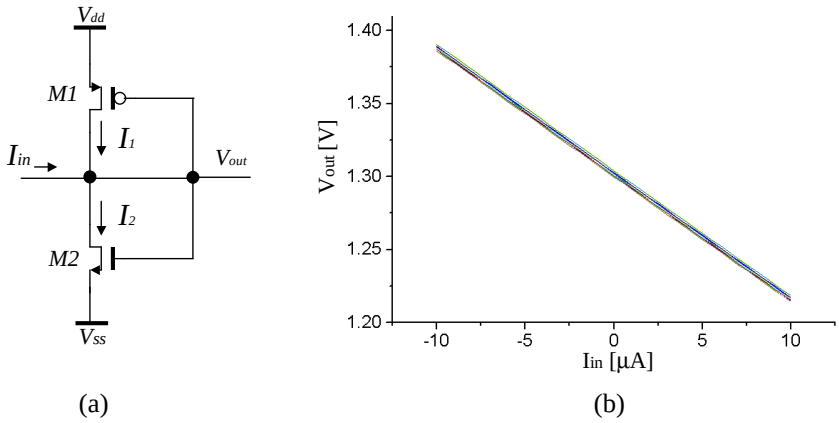

(a) (b)

Figure 3.44: Proposed linear current to voltage converter. (a) Circuit of linear current to voltage converter. (b) Monte Carlo analysis: 20 runs.

no load DC conditions, for which it is used):

$$\begin{cases} I_1 = K_p \times (V_{dd} - V_{out} - |V_{tp}|)^2, \\ I_2 = K_n \times (V_{out} - V_{ss} - V_{tn})^2, \\ I_1 + I_{in} = I_2, \end{cases} \tag{3.141}$$

we derive a second order polynomial equation that contains the output voltage and the input current:

$$A \cdot V_{out}^2 + B \cdot V_{out} + C - I_{in} = 0, \tag{3.142}$$

where

$$\begin{cases} A = K_n - K_p, \\ B = -2 \cdot (K_p(V_{dd} - |V_{tp})| + K_n(V_{ss} + V_{tn})), \\ C = K_p(V_{dd} - |V_{tp}|)^2 + K_n(V_{ss} + V_{tn})^2. \end{cases} \tag{3.143}$$

When K_n is close to K_p, V_{out} can be approximated by the linear term of a Taylor series expansion to give a linear function of I_{in}. Then the change of V_{out} to I_{in} ratio is expressed by:

$$\frac{\Delta V_{out}}{I_{in}} = -\frac{1}{2 \cdot (K_p(V_{dd} - |V_{tp}|) + K_n(V_{ss} + V_{tn}))}, \tag{3.144}$$

which is constant in terms of I_{in}. The offset can be obtained from equation (3.142) by setting $I_{in} = 0$:

$$V_{out}|_{I_{in}=0} = \frac{K_p(V_{dd} - |V_{tp}|)^2 + K_n(V_{ss} + V_{tn})^2}{2 \cdot (K_p(V_{dd} - |V_{tp}|) + K_n(V_{ss} + V_{tn}))}. \tag{3.145}$$

Figure 3.44(b) shows the simulation results of V_{out} vs. I_{in} for the proposed linear current to voltage converter with the transistor parameters being set to W_{M1}:L_{M1}= 16μ:8μ and W_{M2}:L_{M2}=6.4μ:32μ. Its numerical results of the Monte Carlo analysis are provided in Table 3.7 in the row for *Current-Voltage Converter* #2.

By using the Monte Carlo analysis results shown in Table 3.7, we are able to estimate the deviation of the outputs of sigmoid function circuits and NPN exponential function circuits. The circuit structure of sigmoid functions is illustrated in Figure 3.12. Similar to how we obtained the equations (3.55) and (3.56) for V_b and V_c (i.e. V_d and V_e when the threshold voltage variation is not considered), we re-derive the equations of V_d and V_e by taking into account the variation of the threshold voltage as follows:

$$\begin{aligned} V_d &= V_b + \Delta V_{buf1} = (I_a h_1 + b_{H1} + \Delta V_{H1}) + \Delta V_{buf1} \\ &= (x \cdot g_1 + b_{G1} + \Delta I_{G1}) h_1 + b_{H1} + \Delta V_{H1} + \Delta V_{buf1} \\ &= V_{d0} + h_1 \Delta I_{G1} + \Delta V_{H1} + \Delta V_{buf1}, \end{aligned} \tag{3.146}$$

where g_1, h_1, b_{G1}, and b_{H1}, have the same meanings as for equation (3.55), and, thus, are the transconductance and transimpedance of $G1$ and $H1$, and the output offsets of $G1$ and $H1$, V_{d0} is the original V_d (equal to V_b) expressed by equation (3.55), and ΔI_{G1}, ΔV_{H1}, and ΔV_{buf1} are the random differences of the outputs of $G1$, $H1$, and *V Buffer1* caused by the threshold voltage fluctuation. The equation for V_e is re-derived in the same way:

$$V_e = V_{e0} + h_1 \Delta I_{G2} + \Delta V_{H2} + \Delta V_{buf2}. \tag{3.147}$$

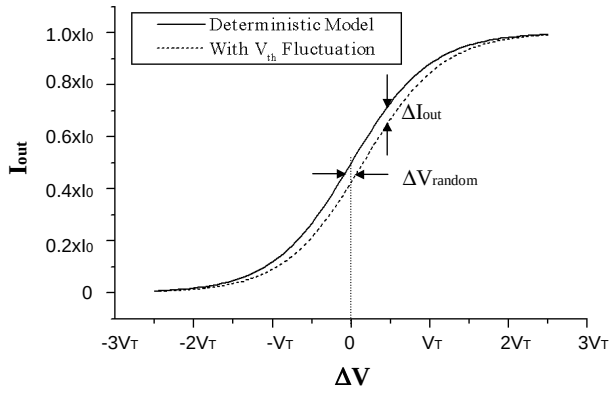

Figure 3.45: Difference of I_{out} in sigmoid function circuit caused by variation of the threshold voltage. $\Delta V_{random}/V_T = 0.3$.

where V_{e0} is the original V_e (equal to V_c) expressed by equation (3.56), and ΔI_{G2}, ΔV_{H2}, and ΔV_{buf2} are the random differences of the outputs of $G2$, $H2$, and *V Buffer2*.

Due to the random variation at the inputs of the *Emitter Coupled Pair* in Figure 3.12, V_d and V_e, the output vs. the input curve has a horizontal shift ΔV_{random}, which causes a non-deterministic difference of the output value ΔI_{out}, as illustrated in Figure 3.45. From equations (3.146) and (3.147), ΔV_{random} is expressed by:

$$\Delta V_{random} = (h_1 \Delta I_{G1} + \Delta V_{H1} + \Delta V_{buf1}) - (h_1 \Delta I_{G2} + \Delta V_{H2} + \Delta V_{buf2}). \quad (3.148)$$

By taking ΔV_{random} into the equation of the emitter coupled pair, which is rewritten here from equations (3.53) and (3.54)

$$I_{out} = \frac{I_0}{e^{(\frac{\pm \Delta V}{V_T})} + 1}, \quad (3.149)$$

where ΔV is $V_d - V_e$ in this case, we can estimate the upper bound of the percentage difference $|\Delta I_{out}/I_{out}|$ in terms of $\Delta V_{random}/V_T$. The maximum $|\Delta I_{out}/I_{out}|$ occurs, as seen from Figure 3.45, when the deterministic parts of the emitter coupled pair

inputs are equal, i.e. $V_{d0} = V_{e0}$. Therefore, we have:

$$\begin{aligned} max(|\frac{\Delta I_{out}}{I_{out}}|) &= |(\frac{I_0}{e^0+1} - \frac{I_0}{e^{(0+\frac{\pm\Delta V_{random}}{V_T})}+1}) \div \frac{I_0}{e^0+1}| \\ &= |1 - \frac{2}{e^{(\frac{\pm\Delta V_{random}}{V_T})}+1}| \simeq |\frac{\Delta V_{random}}{2V_T}|, \end{aligned} \tag{3.150}$$

where we replace $e^{\pm(\Delta V_{random}/V_T)}$ by its linear Taylor approximation $1 \pm \Delta V_{random}/V_T$, assuming $|\Delta V_{random}/V_T| < 1$. By using the data of the standard deviation in Table 3.7 (here we use *Current-Voltage converter*#2) and the slope of the line in Figure 3.44(b) for $h1$, we can estimate the magnitude of ΔV_{random} from equation (3.148): $|\Delta V_{random}| \leq 2 \times (8500 \times 0.12\mu + 1.3m + 1.5m) \simeq 7.64mV$. Hence, the upper bound of the percentage difference $max(|\frac{\Delta I_{out}}{I_{out}}|)$ is about $7.64mV/2V_T = 14.7\%$. Figure 3.45 shows a normalized sigmoid curve in the case when $\Delta V_{random}/V_T = -0.3$. The corresponding output difference is 15%. We still use R-square and signal-to-noise ratio (SER) to evaluate how close the shifted curve is to the original curve. The R-square and SER for the curves in Figure 3.45 are 0.9903 and 22.8 dB respectively.

Using the same analysis methods as presented above, we can derive the equation for the percentage difference of the output of our NPN exponential circuit shown in Figure 3.13. The equation for the base-emitter voltage of $Q2$ is, by taking account of the threshold voltage variation, expressed as follows:

$$\begin{aligned} V_{be,Q2} &= V_b - V_c + V_d + \Delta V_{buf} + \Delta V_{pool} \\ &= (V_{b0} + h_1\Delta I_{G1} + \Delta V_{H1}) - (V_{c0} + h_1\Delta I_{G2} + \Delta V_{H2}) + V_d + \Delta V_{buf} + \Delta V_{pool} \\ &= V_{be,Q2,0} + (h_1\Delta I_{G1} + \Delta V_{H1}) - (h_1\Delta I_{G2} + \Delta V_{H2}) + \Delta V_{buf} + \Delta V_{pool} \\ &= V_{be,Q2,0} + \Delta V_{random}, \end{aligned} \tag{3.151}$$

where ΔI_{G1}, ΔI_{G2}, ΔV_{H1}, ΔV_{H2}, ΔV_{buf}, and ΔV_{pool} are the random variation of the outputs of $G1$, $G2$, $H1$, $H2$, *V Buffer*, and *Pool Circuit* caused by the

fluctuation of the threshold voltage, and $V_{be,Q2,0}$ is the base-emitter voltage of $Q2$ when the threshold voltage fluctuation is 0. By using the data in Table 3.7 and Figure 3.44(b), we estimate the magnitude of ΔV_{random} to be: $|\Delta V_{random}| \leq 2 \times (8500 \times 0.12\mu + 1.3m) + 3.9m + 1.5m = 10.0mV$.

The output percentage difference caused by ΔV_{random} is derived as follows:

$$\begin{aligned} |\frac{\Delta I_{out}}{I_{out}}| &= |(I_{s0}e^{\frac{V_{be,Q2,0}}{V_T}} - I_{s0}e^{\frac{V_{be,Q2}}{V_T}}) \div I_{s0}e^{\frac{V_{be,Q2,0}}{V_T}}| \\ &= |1 - \frac{I_{s0}e^{\frac{V_{be,Q2}}{V_T}}}{I_{s0}e^{\frac{V_{be,Q2,0}}{V_T}}}| \\ &= |1 - e^{\Delta V_{random}}| \simeq |\frac{\Delta V_{random}}{V_T}|, \end{aligned} \tag{3.152}$$

where we also use Taylor expansion to approximate the exponential term $e^{\Delta V_{random}} \simeq 1+\Delta V_{random}$. By using the ΔV_{random} value estimated previously, the percentage difference can be obtained from equation (3.152), which is about $\frac{\Delta V_{random}}{V_T} = 38.5\%$. The corresponding R-square of the original exponential curve and the random shifted curve is 0.8689, and SER is 9.1 dB.

As analyzed above, the output percentage differences caused by the threshold voltage randomness of the MOS transistors in sigmoid function circuits and NPN exponential circuits are highly dependent on the thermal voltage V_T. By increasing V_T, the percentage difference can be reduced. Despite of the fact that V_T can not be adjusted manually, we can increase the numerators of equations (3.150) and (3.152) by factors of integers by changing the circuit structures of the emitter coupled pair, and the NPN transistor circuitries in the exponential function circuit. Figure 3.46(a) shows the new emitter coupled pair, modified for enhancing circuit immunity to device parameter changes. This circuit, compared with the one in Figure 3.11, uses two levels of cascode NPN devices. The equations of the output

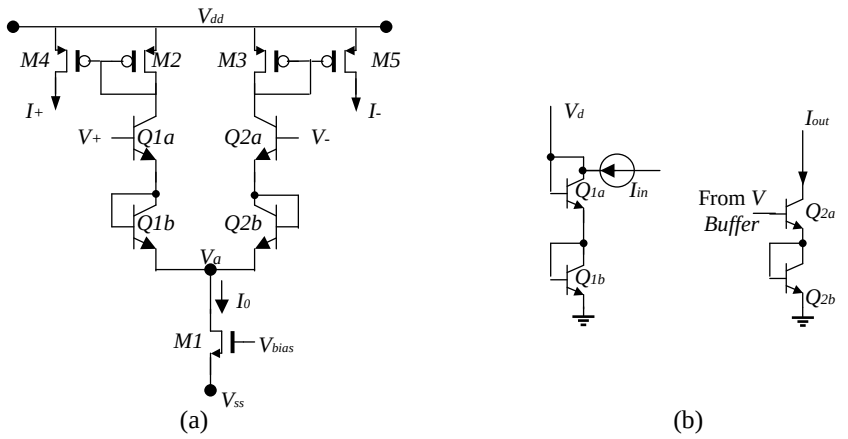

Figure 3.46: (a)Modified emitter coupled pair using cascode NPN devices; (b)Cascode NPN structure used in exponential function circuit.

currents are changed from equations (3.53) and (3.54) to:

$$I_{c1} = \frac{I_0}{e^{(-\frac{\Delta V}{2V_T})}+1}, \tag{3.153}$$

$$I_{c2} = \frac{I_0}{e^{(\frac{\Delta V}{2V_T})}+1}, \tag{3.154}$$

which are equivalent to the expressions for the case when V_T is magnified by two times for the original emitter coupled circuit. The modification for the NPN exponential function circuit is shown in Figure 3.46(b). Cascode-connected $Q1a$ and $Q1b$ replace the $Q1$ in Figure 3.13, and $Q2a$ and $Q2b$ replace the $Q2$. The expression of I_{out} in Figure 3.13 then becomes:

$$I_{out} = I_{in} e^{\frac{g_1 h_1 (V_{in}-V_{bias})}{2V_T}}.$$

With the same methods, we can connect more than two NPN transistors in cascode, with the limitation being that of power supply voltages. As a result, the output percentage difference caused by circuit parameter variation, expressed by equations (3.150) and (3.152), can be reduced by the number of the cascode-connected NPN transistors.

Chapter 4

Propagation of Electrical Activity in Cardiac Tissue

4.1 Introduction

The specialized excitatory and conductive cardiac muscles are capable of conducting electrical signals, i.e. action potentials, throughout the heart, and incorporate an excitatory and transmission system which is tightly coupled with the mechanical activity and responsible for the contraction and relaxation of the heart muscle.

Cardiac cells are typically cylindrical, 30-100 μm long and with radius 8-20 μm [36][38]. They connect end to end to form elongated fibers, which are arranged in parallel to construct fibrous bundles. The two ends of a cardiac cell are separated from their neighbors by *intercalated disks*, the membranes that separate adjacent cells in cardiac tissues. The conduction of electrical signals from one cell to the next cell depends on *gap junctions* (nexi), very permeable pathways present in the intercalated disks, allowing relatively free diffusion of ions and thus the passage of the electrical signals. Gap junctions exist in the borders between cells connected

longitudinally, and they are sparse or absent in the borders between cardiac fibers that lie side by side. Therefore, current flows more easily in the direction along the longer axis than the transverse directions [82].

Two different approaches of modeling the spread of the electrical activity have been developed by treating cardiac tissues as either a discrete system of coupled cells, or a continuous medium, called cellular automata and core-conductor models respectively [5][83]. The cellular automata is a highly abstract model, in which a discrete network representing the spatial structure of cardiac tissue is constructed, with each node (a cardiac cell) taking one of a finite set of states at each moment. The state of each node evolves according to deterministic rules and is decided by the last states of this node and its neighbors. Because of the simplicities of the cellular automata model, it is capable of efficiently simulating the excitation propagation throughout the whole heart. However, the model is not related to cellular electrophysiology and, thus, can not describe biophysical details of cellular excitability [83]. The weakness of the automata model is overcome by the core-conductor model, also known as excitable dynamics equations, which, by combining the models of cardiac ionic membranes, describes the cardiac propagation behaviors using coupled PDE-ODE (partial differential equation - ordinary differential equation) equations. The core-conductor models incorporate the greatest amount of present knowledge about the ionic basis for the action potential, and thus become dominant computational approaches to study wave phenomena in cardiac tissue for today.

In this chapter, we will present how to obtain the numerical results of the partial differential equation of the cardiac propagation model using VLSI circuits. The propagation model belongs to a special category of partial differential equation,

namely reaction-diffusion equations. The circuit mapping of the generalized form of reaction-diffusion equation is introduced, and we then show the circuit setup for simulating the electrical propagation over a small piece of ventricular muscle using simplified spatial configuration of the cardiac muscle. The modeling of the cardiac cell structure details, such as the orientation of cardiac fibers, cellular geometry, and the anatomic structure of the heart, are beyond our efforts. Hence, here we do not intend to construct a circuit to simulate the electrical propagation over the whole heart, but propose a methodology of calculating reaction-diffusion equations with analog circuits, especially for the cardiac system.

In the rest of the chapter, we will first introduce the model of 1-dimensional cable theory and its extended multi-dimensional equations which describe the propagation of cardiac electrical activity using partial differential equations. Next we will present the circuit mapping of reaction-diffusion systems, a methodology of computing reaction-diffusion equations with circuits. It is worth to mention that the proposed methodology is also applicable to the reaction-diffusion systems that are irrelevant to electrical phenomenons, such as population model of genetics [84][85], model of morphogenesis [86], and model of the Belousov-Zhabotinsky reaction [87][88]. The simulation of a VLSI circuit and an ideal component circuit that implement cardiac propagation is provided finally.

4.2 Electrical Propagation Model of the Heart

The core-conductor class of models are evolved from the cable theory [89][90], which was developed more than a century ago by Kelvin in [91] to describe the transmission of an electrical telegraph. The cable equations were first modified to apply in the biological sciences in 1879 by Hermann [89][92] for analysis of

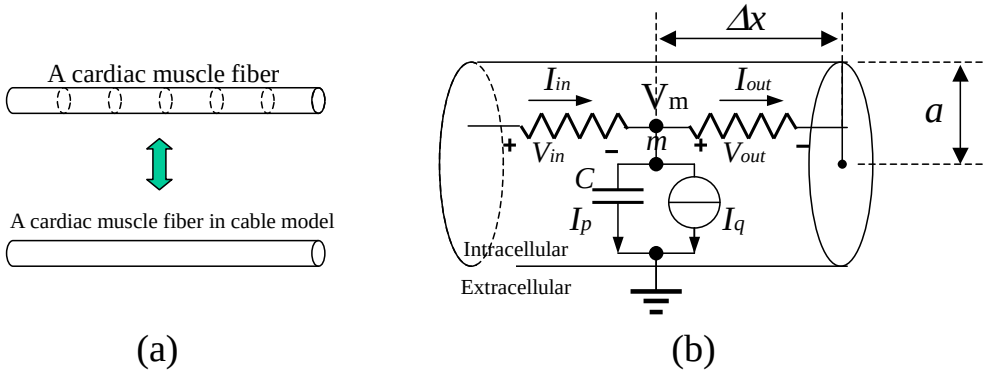

Figure 4.1: 1-Dimensional cable model for cardiac tissue. (a)A 6-cell cardiac muscle fiber (top) and its representative (bottom) in cable model - a continuous media that does not consider the boundaries of cells. (b)Circuit diagram of cable model.

nerves. Since then such models have been proven successful in studies of electrical propagation in nerves [7]-[9] and cardiac muscle [12][82][83] up to today.

4.2.1 1-Dimension Cable Model in Cardiac tissue

The 1-dimensional cable model prototypes a single fiber and characterizes the electrical propagation over a bundle of parallel muscle fibers [31]. The cable model is a continuous model that does not consider the boundaries of cells, as illustrated in Figure 4.1(a). In the top of Figure 4.1(a) shows a portion of a cardiac fiber that contain 6 cells, and in the bottom of the figure is the representative of the fiber in the cable model, a continuous and uniform cylindric medium.

Consider a segment of cardiac fiber in the cable model (let us call it a cardiac cable to distinguish it from a real cardiac fiber which has cell-to-cell connections), as shown in Figure 4.1(b). There are three elements of currents in the cardiac cable: 1) the ionic current, denoted with I_q in the figure, that flows between the intrcellular space (the cable) and the extracellular space (the ground); 2) I_p, the

current of the membrane capacitor C; 3) I_{in} and I_{out}, the current flowing through the resistance caused by gap junctions and cytoplasm [1]. I_p and I_q can be expressed by the membrane current per unit (cable surface) area I_m and the ionic current per unit area I_{ion} multiplied with the cable surface area of the membrane segment:

$$I_p = C\frac{\partial V_m}{\partial t} = 2\pi a\Delta x \cdot C_m\frac{\partial V_m}{\partial t}, \tag{4.1}$$

$$I_q = 2\pi a\Delta x \cdot I_{ion}, \tag{4.2}$$

where a is the radius of the cable, Δx is the length of the small segment of cardiac cable, and $2\pi a\Delta x$ is the lateral area of the cable. I_{in} and I_{out} can be formulated using Ohm's law:

$$I_{in} = \Delta V_{in}/R = \Delta V_{in}/(\frac{\rho\Delta x}{\pi a^2}), \tag{4.3}$$

$$I_{out} = \Delta V_{out}/R = \Delta V_{out}/(\frac{\rho\Delta x}{\pi a^2}), \tag{4.4}$$

where R is the resistance of the cable segment which is determined by the resistivity ρ times the length Δx and divided by the area of the cross section πa^2. Putting equations (4.1)− (4.4) together by Kirchhoff's current law, which is formulated as:

$$\sum I = I_{in} - I_{out} - I_p - I_q = 0 \quad \Rightarrow \quad I_{in} - I_{out} = I_p + I_q, \tag{4.5}$$

we derive:

$$\frac{\pi a^2}{\rho}\frac{\Delta V_{in}}{\Delta x} - \frac{\pi a^2}{\rho}\frac{\Delta V_{out}}{\Delta x} = 2\pi a\Delta x C_m\frac{\partial V_m}{\partial t} + 2\pi a\Delta x I_{ion}. \tag{4.6}$$

By letting $\Delta x \to 0$, equation (4.6) becomes a continuous differential equation:

$$\frac{a}{2\rho}\frac{\partial^2 V_m}{\partial x^2} = C_m\frac{\partial V_m}{\partial t} + I_{ion}. \tag{4.7}$$

[1]Cytoplasm is the fluid enclosed by a cell membrane and filled with dispersed particles and organelles [2](pp. 10-12).

Replacing resistivity ρ by the conductivity $d = 1/\rho$, and representing $a/2$ by the inverse of the surface-to-volume ratio $\beta = (2\pi a\Delta x/\pi a^2\Delta x) = 2/a$, we obtain the cable model of 1-dimensional cardiac fiber, written as:

$$\frac{d}{\beta}\frac{\partial^2 V_m}{\partial x^2} = C_m\frac{\partial V_m}{\partial t} + I_{ion}, \tag{4.8}$$

which is:

$$\frac{1}{\beta}\nabla\cdot(d\nabla V_m) = C_m\frac{\partial V_m}{\partial t} + I_{ion}. \tag{4.9}$$

Assumption of Cable Model

The basis of the cable model is that it treats a cardiac fiber as 1-dimensional and reduces the problem to a single spatial dimension [93]. 1-dimension is only in the sense that the current and voltage potentials are uniformly distributed across any cross section perpendicular to the longitudinal direction of the cable [94].

The resistance shown in Figure 4.1(b) corresponds to the average resistance of the intracellular space, which in reality is composed of cytoplasmic and gap junctional resistances [95][96]. This model, called the continuous model, therefore considers the cardiac tissue as a medium with continuous diffusive properties and is only capable of preserving macroscopic details [90]. The gap junctions, which are relatively discrete due to their short length but sizable resistance compared to cytoplasmic [31], introduce jumps in the voltage patterns among cardiac cells, and this can be modeled by a variation of the original cable model, in which, the gap junctions are represented by a change in resistance [97]-[99].

The presented model assumes that the resistivity of the extracellular media is negligible and can be treated as isopotential, and only considers the propagation of electrical signals within the cells by taking the extracellular space as grounded as shown in Figure 4.1. This assumption relies on the experimental observation

that the extracellular medium has a much higher conductivity compared to the intracellular medium (a typical factor of 8 is reported in the longitudinal direction in [100]).

4.2.2 Multi-Dimensional Cardiac Propagation Model

The multi-dimensional cardiac propagation model is extended from equation (4.9) and takes into account the anisotropic electrical properties of cardiac media. This type of equation is also called an excitable dynamics equation and is formulated with a reaction-diffusion equation as given below [5]:

$$\nabla \cdot (D_i \nabla V_m) \quad = \quad \beta(C_m \frac{\partial V_m}{\partial t} + I_{ion}), \tag{4.10}$$

where V_m, β, C_m and I_{ion}, the same as in equation (4.8), are the membrane potential, the surface-to-volume ratio, the membrane capacitance, and the transmembrane current per unit area. D_i is the intracellular conductivity tensor, which incorporates the conduction properties of the intracellular space. D_i is a single variable d in equation (4.8) for the 1-dimensional case, and for 2-dimensional and 3-dimensional cases, it is expressed by:

$$\begin{bmatrix} d_{\gamma\gamma} & d_{\gamma\delta} \\ d_{\delta\gamma} & d_{\delta\delta} \end{bmatrix}, \tag{4.11}$$

and

$$\begin{bmatrix} d_{\gamma\gamma} & d_{\gamma\delta} & d_{\gamma\epsilon} \\ d_{\delta\gamma} & d_{\delta\delta} & d_{\delta\epsilon} \\ d_{\epsilon\gamma} & d_{\epsilon\delta} & d_{\epsilon\epsilon} \end{bmatrix}, \tag{4.12}$$

respectively, where γ, δ, and ϵ are three axes in the selected Cartesian coordinate system. When the cardiac fibers are considered as parallel and straight, it is

mathematically convenient to adopt the Cartesian coordinate system and align it with the principal axes of D_i to make D_i a diagonal matrix. When modeled cardiac tissues are curved or rotated, D_i generally cannot be diagonalized by selecting the axes [36].

The most commonly applied boundary condition for equation (4.10) is a no-flux, or Neumann condition, expressed as:

$$(D_i \nabla V_m) \cdot \vec{n} = 0, \tag{4.13}$$

where $\vec{n}$ is the normal vector to the boundary. The no-flux condition, also known as sealed boundary condition, defines no current flows into or out of the edge of a piece of cardiac muscle (including intracellular and extracellular space), and can represent naturally the outer surface of the heart.

4.2.3 Summary of Cardiac Propagation Model

The present quantitative description of electrical signal propagation in cardiac tissue is based on two classical models. They are the Hodgkin-Huxley model, which describes the active membrane properties using the kinetics of the ionic currents, and the cable equation of Kelvin, which relates the current and voltage along a continuous one-dimensional structure [90]. For the propagation model we select for VLSI implementation, the Beeler-Reuter model, which has been designed with VLSI circuits as introduced in chapter 3, is chosen to describe the membrane excitable properties and the non-linear ionic currents, and the continuous core-conductor model expressed by equation (4.10) is employed to formulate the electrical activities transmitted in the intracellular space.

Put all the equations together for our propagation model, equation (4.10), replacing equation (2.40), becomes the top level of formulation, with its boundary

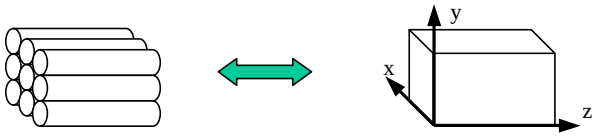

Simplified cardiac muscle

Cardiac muscle as continuous medium in cable-theory-based model

Figure 4.2: Simplified structure of cardiac tissue and its continuous representative in cable-model.

condition being represented by equation (4.13). All the other equations in the Beeler-Reuter model, from (2.41) to (2.60) are still valid. Note that in equation (4.10), the propagation term $\nabla \cdot (D_i \nabla V_m)$ substitutes I_{ext} in the equation (2.40). As explained in chapter 2, I_{ext} represents the external influence applied on a cell and can be used as a stimulus to trigger the action potential. Therefore, in the propagation model, it is the current transmitted along the myocardium fiber that activate a cardiac cell to create an action potential.

For the circuit implementation, we simplify the structure of cardiac fibers to be as in the left side of Figure 4.2, where we assume all the muscle fibers are parallel and straight by ignoring the curved shapes of the heart muscles and the different orientations between different cardiac fibers. Therefore, the intracellular conductivity tensor D_i can be made a diagonal matrix by properly selecting the coordinates. On the right side of Figure 4.2 is the representative of the cardiac muscle in the cable-theory-based model, which is a continuous medium that does not differentiate the boundaries of individual cells. As illustrated in Figure 4.2, we select the Cartesian coordinate system and assume that x and y, orthogonal to each other, are both transversal to the fiber axis; and z is parallel to the fiber longitudinal direction. Expanding the nabla operator on the diagonalized D_i,

equation (4.10) becomes equation (4.14):

$$d_x \frac{\partial^2 V_m}{\partial x^2} + d_y \frac{\partial^2 V_m}{\partial y^2} + d_z \frac{\partial^2 V_m}{\partial z^2} = \beta(C_m \frac{\partial V_m}{\partial t} + I_{ion}), \tag{4.14}$$

where d_x, d_y and d_z are the conductivity in the direction x, y and z respectively, all assumed to be constant.

In section 4.3, we will show the circuit simulation of the electrical propagation over the cardiac tissues based on equation (4.14). We will only present the simulation for 1-dimensional and 2-dimensional propagation, due to the lack of the transillumination imaging techniques [101] needed for the visualization of 3-dimensional propagation. The propagation over 3-dimensional cardiac tissues can be realized by circuits using the same methodology, which will be described in section 4.3.1.

4.3 Modeling Propagation of Cardiac Active Potential with VLSI

Core-conductor models involve the fewest simplifying assumptions and incorporate the greatest amount of present knowledge about the ionic basis for the action potential, and, thus, are widely used for the study of cardiology. Since the 1950s, core-conductor models have been descretized to divide a continuous fiber model into segments to allow the studies of propagation with circuits and later with high-speed computers [20]-[22][37][102]. However, the ionic-membrane-based cardiac cell model described by the reaction-diffusion equation (4.10) (and equation (4.14)), can substantially increase the complexity to obtain a numerical solution with computers [96]. Equation (4.10) formulates a special coupled PDE-ODE (partial differential equation - ordinary differential equation) system, with the PDE

formulating the propagation and the ODE presenting the membrane ionic mechanism. In the heart model, the ODE system and the PDE system, though coupled through the voltage and current, are independent of each other. At any point in the space, the activation of V_m, or the generation of the action potential, relies on the spatial conduction of electrical signals described by the PDE to transmit the stimulating current, whereas, the shape of the action potential at that point is totally decided by the ODE equations. The ODE system determines the sole dependance of the gating variables and ionic concentrations on V_m at each spatial point, and, thus, their boundary conditions are not available. Because of the complexity of the problem, computation with digital computers is very expensive and challenging. The rapid upstroke in an action potential of a ventricular cell can require the time discretization on the order of 0.01 ms [103], and the steep wave front in space may require the space discretization on the order of 0.1 mm. This means to simulate 1 s of the heart beat on a uniformly grided 3-dimentional tissue of size 1 cm^3, there are 10^{11} unknown V_m. If the Beeler-Reuter model (a degree-eight ODE system) is used to formulate the membrane ionic mechanism, there are 8×10^{11} unknown values coupled together through time and space. The tremendous complexity in computation with digital computers promotes the use of analog circuits to perform the calculation.

Simulating propagation with circuits can be traced back to Schmitt's circuit of the electronic neural network implementation [104], and the active pulse transmission line constructed by Nagumo etc. [9][105]. Nagumo etc. used a capacitor, a tunnel diode, and an inductor to simulate the ionic behavior of a segment of an animal nerve axon; the segments are coupled with resistors to construct an active transmission line. The purpose of segmenting the continuous propagation model

for circuit implementation is just the same as meshing numerical regions for finding solutions with computers, which is to use a finite number of data to present a continuous space.

Despite the great similarity of the circuit implementation and the presented cable model (both are nonlinear RC networks), the proposed methodology of circuit computation is valid for calculating not only the electrical propagation models for cardiac tissue, but also applicable to other reaction-diffusion systems in biology, physics, chemistry, etc [84]-[88].

4.3.1 Computation of Discretized Reaction-Diffusion Equation with Circuits in Cartesian Coordinates

The partial differential equation for a general reaction-diffusion system is formulated as [87][106][107]:

$$\nabla \cdot (A_j \nabla u_j) \;=\; b_j \frac{\partial u_j}{\partial t} + f_j(u_1, ..., u_M), \qquad (j = 1, 2, ...M), \tag{4.15}$$

where u_j are characteristics of the diffusion medium, b_j are constants, f_j, representing the reaction in the reaction-diffusion system, are functions of u_j, and A_j are diffusion tensors. The presented set of partial differential equations (4.15) describe a system that has M diffusion variables, which, with each being time- and space-dependent, are coupled together to make the system cooperative by the reaction functions f_j. We use Cartesian coordinates and consider only the case when the diffusion tensors are fixed, i.e., they do not change with the space axis, and all A_j are isotropic. Hence, the Cartesian coordinates can be selected to make

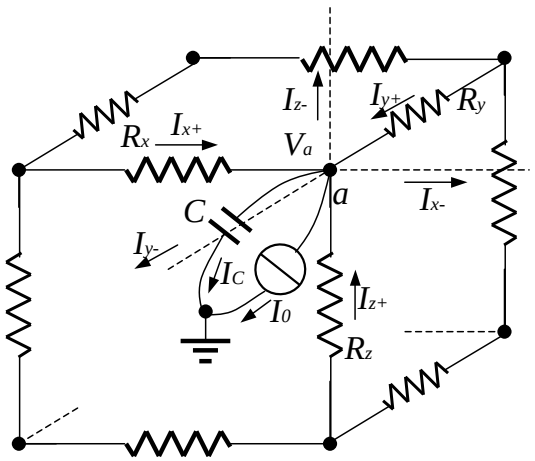

Figure 4.3: Using an RC network to implement reaction-diffusion systems.

A_j diagonal matrices which are expressed as:

$$\begin{bmatrix} a_{jx} & 0 & 0 \\ 0 & a_{jy} & 0 \\ 0 & 0 & a_{jz} \end{bmatrix}, \tag{4.16}$$

where a_{jx}, a_{jy}, and a_{jz}, are the diffusion coefficients for the directions x, y and z. In the following discussion, we will show how the RC network shown in Figure 4.3 can be used to implement the reaction-diffusion system formulated by equations (4.15) (and (4.16)) after (4.15) is discretized. Note that the circuit shown in Figure 4.3 is to realize one of the equation set formulated by (4.15). To represent the whole system, M of the same RC circuit with different parameters are needed, and all circuits are coupled together through the current sources I_0 in Figure 4.3. The following discussion is for the jth equation in the reaction-diffusion system.

Equation (4.15) can be rewritten by expanding the nabla operation as follows:

$$a_{jx}\frac{\partial^2 u_j}{\partial x^2} + a_{jy}\frac{\partial^2 u_j}{\partial y^2} + a_{jz}\frac{\partial^2 u_j}{\partial z^2} = b_j\frac{\partial u_j}{\partial t} + f_j. \tag{4.17}$$

The partial differential equation (4.17) can be discretized spatially by letting ∂i (i

is x, y, or z) transition to segments Δi with non-zero lengths, and the equation then is changed to:

$$\begin{aligned}(a_{jx}\frac{\Delta u_{jx+}}{\Delta x^2} - a_{jx}\frac{\Delta u_{jx-}}{\Delta x^2}) &+ (a_{jy}\frac{\Delta u_{jy+}}{\Delta y^2} - a_{jy}\frac{\Delta u_{jy-}}{\Delta y^2}) \\ +(a_{jz}\frac{\Delta u_{jz+}}{\Delta z^2} - a_{jz}\frac{\Delta u_{jz-}}{\Delta z^2}) &= b_j\frac{\partial u_j}{\partial t} + f_j, \end{aligned} \tag{4.18}$$

where Δu_{ji+} and Δu_{ji-} (i is x, y, or z) are the changes of u_j in the positive and negative i direction. Equation (4.18) becomes equation (4.17) when the Δi (i is x, y, or z) tend to be 0.

Let us now consider the 3-dimensional RC network shown in Figure 4.3, in which each node is joined to ground through a capacitor C and a current source I_0, and distributed nodes are bridged with resistors. At node a, from Kirchhoff's current law, the sum of the currents that flow into the point is 0, and, hence, the following equation is fulfilled:

$$(I_{x+} - I_{x-}) + (I_{y+} - I_{y-}) + (I_{z+} - I_{z-}) = I_c + I_0, \tag{4.19}$$

where I_c is the capacitor current, and I_i (i is $x+$, $x-$, $y+$, $y-$, $z+$, or $z-$.) are the currents in the six directions as illustrated in Figure 4.3. By using Ohm's law and the I-V property of the capacitor, equation (4.19) becomes:

$$\begin{aligned}(\frac{\Delta V_{x+}}{R_x} - \frac{\Delta V_{x-}}{R_x}) &+ (\frac{\Delta V_{y+}}{R_y} - \frac{\Delta V_{y-}}{R_y}) \\ +(\frac{\Delta V_{z+}}{R_z} - \frac{\Delta V_{z-}}{R_z}) &= C\frac{\partial V_a}{\partial t} + I_0, \end{aligned} \tag{4.20}$$

where ΔV_{i+} and ΔV_{i-} (i is x, y, or z) are the voltage differences in the positive and negative direction i, and R_i (i is x, y, or z) are the resistance in direction i.

There is a great similarity between equations (4.18) and (4.20), and thus, (4.20) can be made the same as (4.18) by letting the circuit parameters satisfy:

$$R_x = \frac{\Delta x^2}{a_{jx}}, \tag{4.21}$$

$$R_y = \frac{\Delta y^2}{a_{jy}}, \tag{4.22}$$

$$R_z = \frac{\Delta z^2}{a_{jz}}, \tag{4.23}$$

$$C = b_j, \tag{4.24}$$

$$I_0 = f_j. \tag{4.25}$$

Note that I_0 is normally variable due to the dependence of f_j on $u_1, u_2, ..., u_M$. Since equation (4.18) comes from (4.15), the RC circuit shown in Figure 4.3 with parameters selected following equation (4.21)-(4.25) describes the same reaction-diffusion system as equation (4.15) when $\Delta i \to 0$ $(i = x, y, or\ z)$.

Equations (4.21)-(4.25) is not a unique solution for mapping a reaction-diffusion system into the RC circuit in Figure 4.3. Multiplying by a constant on both sides of equation (4.15) creates another equation that describes exactly the same system. Hence the circuit mapping equations provided by (4.21)-(4.25) can be expanded to be the following:

$$\begin{cases} R_i C = (\Delta i)^2 \times \frac{b_j}{a_{ji}}, \\ R_i I_0 = (\Delta i)^2 \times \frac{f_j}{a_{ji}}, \end{cases} \quad (i = x,\ y, or\ z). \tag{4.26}$$

The 3-dimensional RC network shown in Figure 4.3 can be changed to implement reaction-diffusion systems of 1-dimension or 2-dimension by removing the parts of the circuit in the direction(s) that does not exist in the corresponding system as shown in Figure 4.4. Figure 4.4(a) illustrates a 1-dimensional RC circuit with 3 discretized non-ground nodes. Figure 4.4(b) depicts the RC circuit for a 2-dimensional case, and there are 4 nodes in the figure. Figure 4.4(a) and (b) describe the reaction-diffusion systems formulated with:

$$a_{jx}\frac{\partial^2 u_j}{\partial x^2} = b_j \frac{\partial u_j}{\partial t} + f_j, \tag{4.27}$$

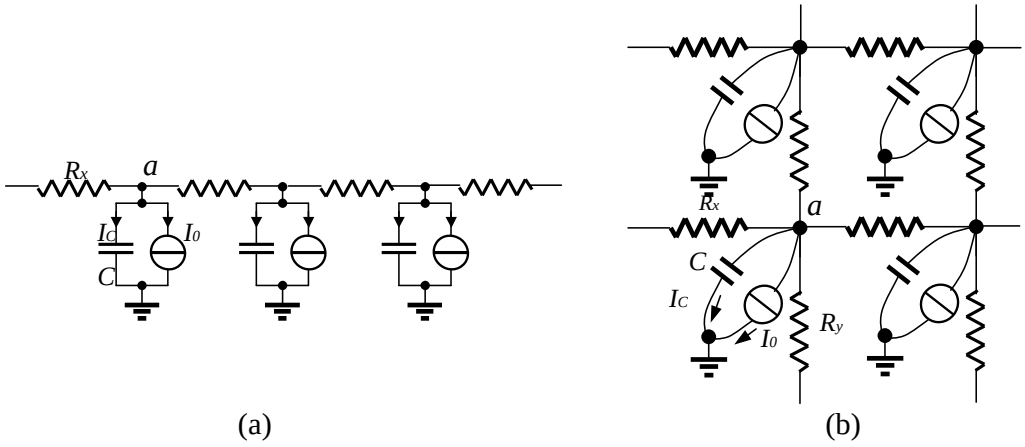

Figure 4.4: Using an RC network to implement reaction-diffusion systems in the case of (a) 1-dimensional, (b) 2-dimensional.

and

$$a_{jx}\frac{\partial^2 u_j}{\partial x^2} + a_{jy}\frac{\partial^2 u_j}{\partial y^2} = b_j\frac{\partial u_j}{\partial t} + f_j, \tag{4.28}$$

with the circuit parameters being still restricted by equation (4.26).

The feasibility of using a circuit to represent a reaction-diffusion system relies on the fact that an RC network is also a reaction-diffusion system, and all reaction-diffusion systems actually describe scenarios of the same nature, which is the movement of a certain physical substance over a particular media through a diffusion process. The boundary conditions are similar for most reaction-diffusion systems. Two common boundary conditions are a) the no-flux condition, a situation where substances can not move across the boundary, and b) the fix amount condition, which reflects the situation when the substance amount is fixed by external conditions [107].

The proposed circuit mapping methodology is limited by the requirement that the space is uniformly gridded for individual directions. The limitation arises from

the derivation of equation (4.20), where the resistances R_i (i is x, y, or z) are constants and do not change by varying positions. Due to the relation between R_i and Δi (i is x, y, or z) defined by equation (4.26), Δi needs to be fixed too. The grid sizes of different directions, however, do not need to be equal, i.e. R_x, R_y, and R_z can be different.

4.3.2 Transistor Circuit Simulation of 1-Dimensional Cardiac Propagation

The normal pattern of propagation in the heart, from the sinoatrial node, through the atrium, to the atrioventricular node, to the bundle of His to the ventricular muscle, is an essentially 1-dimensional sequence [83]. Thus the simulation of a 1-dimensional propagation system, i.e. a single cardiac fiber, gains the knowledge of normal cardiac activity and is helpful to understand the electrical system of the whole heart. A 1-dimensional cardiac model is simpler than a multi-dimensional one and is usually constructed by fewer discretized nodes and, thus, consumes less computational resources and time to simulate. Hence it is widely used by researchers to obtain prototyping results. In this section we show the simulation of the 1-dimensional cardiac propagation using an RC circuit.

Figure 4.5 illustrates the circuit setup for simulating the electrical signal propagation with a 1-dimensional model following the method presented in the previous section, and, in this case, there is only one diffusion variable, i.e. $M = 1$ in equation (4.15). Each pair of the membrane capacitor C_{mi} and the ionic current I_i ($i = 1, 2...N$) composes a single ionic membrane model that represents a segment of the cardiac fiber. N identical segments are connected with resisters ($R_1 = R_2 = ... = R_{N-1}$) in series to construct a 1-dimensional model of the heart

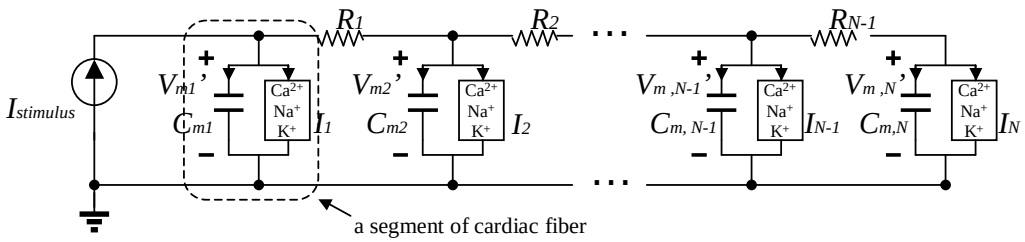

Figure 4.5: Circuit of 1-dimensional cardiac propagation.

muscle. On the left of Figure 4.5, the current source $I_{stimulus}$ is an external stimulus and is responsible to create a current to trigger the activation of the first cardiac segment consisting of C_{m1} and I_1. The excitation is then passed down through the coupling resistors to the entire chain until it reaches the last node N. The circuit, without any current flowing into node N from its right side, is naturally consistent with the no-flux boundary condition of the cardiac propagation model, formulated by equation (4.13).

The differential equation of the 1-dimensional propagation system is modified from equation (4.14) by making $d_x = 0$ and $d_y = 0$. For the other coefficients in equation (4.14), we use the values used by Bray and Wikswo in [108] in our propagation model. The surface-to-volume ratio β takes 3000 cm^{-1}, $d_z = 1.863\ mS/cm$, and $C_m = 1\mu F/cm^2$. I_{ion} is defined by the Beeler-Reuter model provided in equation (2.41)- (2.60). Equation (4.14) then is rewritten as:

$$6.21 \times 10^{-8} \frac{\partial^2 V'_m}{\partial z^2} = 10^{-7} \frac{\partial V'_m}{\partial t} + I'_{ion}, \tag{4.29}$$

where we, again, scale down the magnitude of the membrane potential by 100, the same way as we did in chapter 3, and use scaled V'_m to distinguish it from the original variable V_m, I'_{ion} is scaled I_{ion} by a factor of 10^6.

The circuit parameters of the RC implementation for equation (4.29) are se-

lected following equation (4.26). Δx is set to 600 μm, that is, two adjacent nodes in Figure 4.5 represent a section of 1-dimensional cardiac tissue with $600\mu m$ in length. Following the equations in (4.26), the circuit parameters - the resisters, the capacitors and the current sources in Figure 4.5, are set as follows:

$$\begin{cases} R_i = 5.76 \times 10^4\ \Omega, \\ C_{mi} = 0.1\ \mu F, \qquad (i = 1, 2...N), \\ I_i = I'_{ion}, \end{cases} \tag{4.30}$$

Note that the initial conditions of the reaction diffusion equation can be also shifted to zeros with the method presented in section 3.2.3, for which equation (4.29) stays unchanged after the initial value shifting process.

The circuit in Figure 4.5 is realized with VLSI by replacing each node with the implementation circuit of the Beeler-Reuter model presented in chapter 3 (the top level circuit diagram is shown in Figure 3.19) and substituting the resisters with their VLSI realization. The implementation of resistors with VLSI devices has been introduced in section 3.3.1 and shown in Figure 3.5(b). As the action potential is in the range of $[-85\ mV, 50\ mV]$, the membrane voltage on each node V'_{mi} $(i = 1, 2...N)$ is in the range of $[0\ V, 1.35\ V]$ after being scaled and shifted for the initial conditions. Hence, the transistor-implemented resisters are required to have linear V-I properties when inputs V_+ and V_- are independently changing within $[0\ V, 1.35\ V]$. The resistor circuit, being non-ideal two-terminal devices, can experience current differences in two terminals, that is the current flowing into V_+ is different from the current flowing out of V_- due to the impact from the external circuits. This happens when the currents in the output transistors in Figure 3.5(b) do not mirror properly the currents decided by the input stage. Hence, good current mirrors are important to ensure the resistor properties of the circuit,

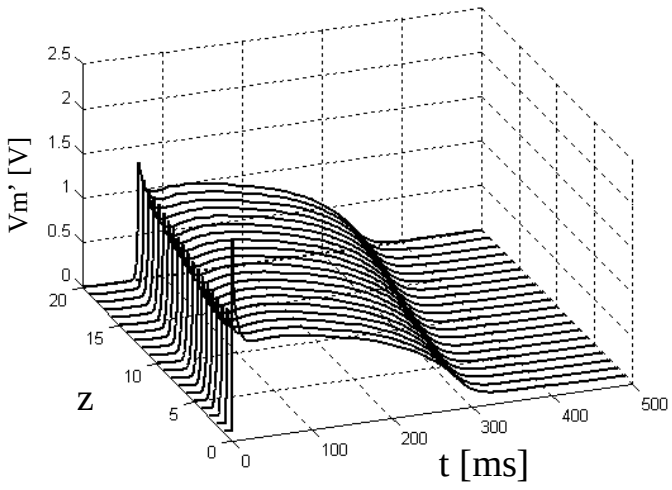

Figure 4.6: PSpice simulation results of 1-dimensional cardiac propagation constructed by transistor circuit.

and, thus, cascode current mirrors are employed for our heart implementation. In addition, making the output transistors still working in the saturation region when applied with input voltages (which are also the voltages at the outputs) is another key point to necessitate $I_+ = -I_-$. The transistor circuit of implementing the resistors $R_i = 5.76 \times 10^4\ \Omega$ $(i = 1, 2...N)$ is provided in the schematics page Sch-32 in appendix A.

In our transistor simulation circuit, totally 20 nodes are established, i.e. $N = 20$ in Figure 4.5. The stimulation $I_{stimulus}$ is set to give a square pulse (impulse) of 2.2 mA for 0.1 ms starting at 10 ms. The corresponding simulation results of the 1-dimensional model are shown in Figure 4.6. The z axis indicates the node number, from 1 to 20. The first node is excited at $t = 10$ ms, and its extremely high upstroke is because of the external stimulus. The excitation is propagated down to the other nodes, and the last (20th) node is excited at about $t = 70$ ms.

4.3.3 2-Dimensional Cardiac Propagation: Spiral Reentry

In this section, we will provide the circuit simulation for 2-dimensional cardiac propagation and present the phenomenon of reentry spiral that can be visualized only in 2-dimensional or 3-dimensional models of the heart. The spiral waves are life threatening because they can lead to abnormal rapid heart beat, that is not controlled by the pace maker of the heart, and then to ventricular fibrillation, an arrhythmia[2] leading to sudden cardiac death.

Though our heart muscles are thick enough that the electrical propagation over the heart is a 3-dimensional process, we treat the problem as 2-dimensional as do most studies of spatial patterns of electrical activity in the heart [107]. We will still adopt equation (4.14) in our simulation modified for the 2-dimensional case. The VLSI circuit realization is similar to the 1-dimensional case presented in the previous section, both using the implementation circuit of the Beeler-Reuter model discussed in chapter 3 and the same transistor circuit for resisters, and, thus, will not be repeated here. Due to the extremely expensive time cost in simulating the VLSI circuits with PSpice for the propagation model (for instance, the simulation of Figure 4.5 with $N = 20$ took 20 hours for modeling 0.6 s of the heart electrical activity), the simulation of the transistor circuits to demonstrate a 2-dimensional spiral wave is unaffordable. Since we have showed the validity of using VLSI circuits to model the cardiac propagation by applying it in the 1-dimensional case, in the following simulation, we no long adopt transistor circuits and take use of ideal component circuits to avoid the overwhelming simulation time demanded by the transistor heart model.

[2]Arrhythmia is a group of conditions in which the muscle contraction of the heart is irregular, faster, or slower than normal [26].

Reentry and Refractory Period

Under certain circumstances, a cardiac impulse may re-excite some portion of the heart through which it had passed previously. This phenomenon is called reentry [26], which is believed to be the primary mechanism underlying the tachycardia, an abnormal fast cardiac rhythm, and fibrillation, a state where cardiac muscles undergo an irregular type of contraction without proper coordination [109]-[115]. The tachycardia and fibrilation can be in the ventricle or the atria, and especially the ventricular fibrillation is most severe and is the most common cause of sudden cardiac death which is responsible for about 1 out of 6 deaths in the Western world [116]. Therefore, the dynamics of the reentry waves, the mechanisms of remedy methods and drug therapies are of interest in understanding sudden cardiac death in patients.

Reentry is tightly related to the *refractory period*. During much of the action potential, the membrane is unable to fire a second action potential, no matter how strong an external stimulus is applied to the cell. The state in which a membrane is unexcitable is called the *absolute refractory period*. The refractory state occurs because a large fraction of the sodium channels is inactivated and cannot be reopened until the membrane is repolarized [26]. This can be seen in Figure 3.34(c), which shows the sodium current I_{Na} is most of the time around zero because of the closed channels, except at the overshoot of the action potential. Figure 4.7 illustrates the membrane potential when stimulated within and out of the refractory period with a second stimulus. The thick line depicts a normal action potential, activated by a stimulus occurring at $t = 100\ ms$ with a strength $0.3\ mA/cm^2$ for $0.1\ ms$. A second stimulation, the same strength, is applied at $t = 200\ ms$, $t = 300\ ms$, $t = 350\ ms$, and $t = 380\ ms$ separately, and these do

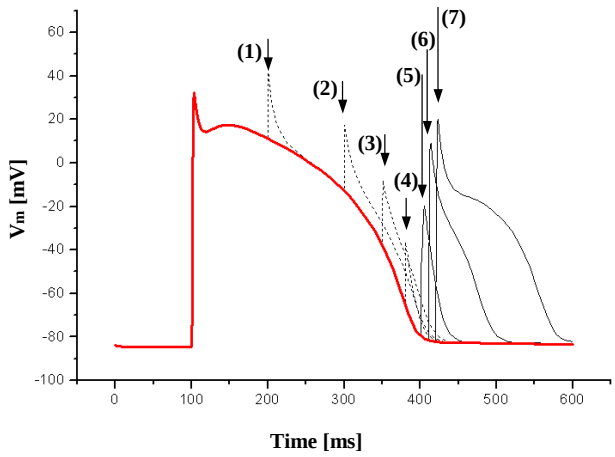

Figure 4.7: Action potential applied with a second stimulus at different moment: (1) $t = 200\ ms$, (2) $t = 300\ ms$, (3) $t = 350\ ms$, (4) $t = 380\ ms$, (5) $t = 400\ ms$, (6) $t = 410\ ms$, and (7) $t = 420\ ms$. Stimulus strength: 300 mA/cm^2 for 0.1 ms.

not cause a second action potential, as depicted by the dotted curves (1) to (4), because the stimulations happens during the refractory period. The curves (5) to (7) correspond to the stimulations, the same strength as the first one, applied at $t = 400\ ms$, $t = 410\ ms$ and $t = 420\ ms$ respectively, and the waveforms show that the activated action potentials are more and more like normal ones as the stimulation is more and more postponed.

There are two types of reentry: anatomical reentry and functional reentry. Functional reentry involves waves circulating around refractory cardiac tissue, and this will be discussed further with our 2-dimensional propagation simulation in the next section, where we show a spiral wave, the form of reentrant pattern being in 2-dimension. Here we explain reentry with an example of anatomical reentry, in which a conduction obstacle is involved. The example [26] is shown in Figure 4.8. In each of the two panels, a single bundle of cardiac fibers splits into two branches, 1 and 2, and they are connected again by bundle 3. Normally, as shown

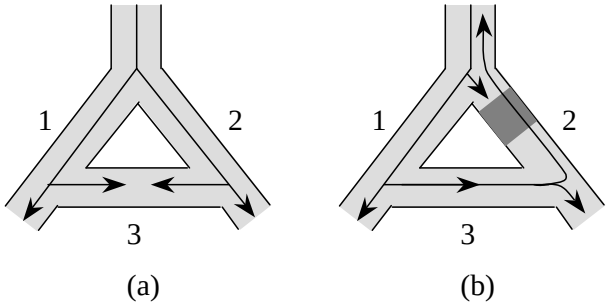

Figure 4.8: Example of reentry. (a) Action potential travels normally. (b) Reentry is caused by a unidirectional block.

in Figure 4.8(a), an action potential moving down travels in each branch 1 and 2, and then enters bundle 3 from both sides. The wave from the left side can not proceed further because the tissues on the right side are just activated by the wave from branch 2 and thus are absolutely refractory. The wave from the right side can not travel farther either for the same reason. Figure 4.8(b) shows the same bundle structure except having a unidirectional block, depicted with the dark area in branch 2. An action potential travels down branch 1 normally but is blocked in branch 2. The wave transmitted from the left side then is able to propagate to the right side and splits to travel both upwards and downwards. If when the wave penetrates the unidirectional block from the bottom, the upper portion of branch 2 has exited its refractory period and becomes excitable again; the wave can continue to travel up to where it originally comes from and also to branch 1 again, and this causes a reentry. The presented anatomical reentry example is simulated with PSpice using the 1-dimensional propagation model. A modified transistor circuit of the VLSI implementation of resistors is employed to simulate the unidirectional block. The circuit setup and the PSpice simulation results are provided in Appendix B.

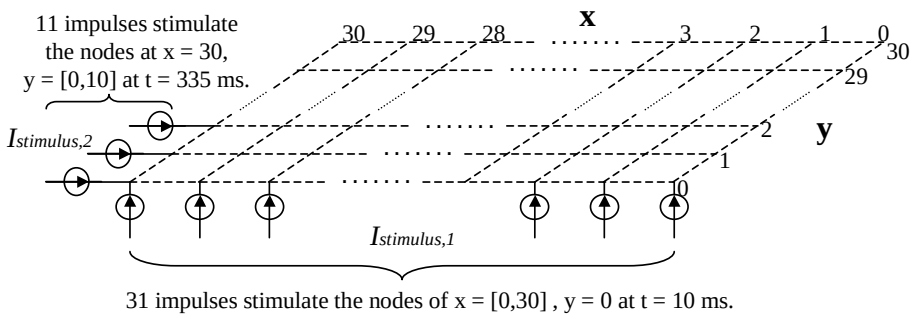

Figure 4.9: Circuit for 2-dimensional cardiac propagation.

Circuit Simulation of a Spiral Wave

The circuit setup for 2-dimensional cardiac propagation is illustrated in Figure 4.9. A 31×31 array is shown constructed with each node being composed of a membrane capacitor and a non-linear ionic current (not depicted here) as shown in Figure 4.4(b). Resistors are connected in between each two adjacent nodes, which are also not shown in Figure 4.9. The nodes are identified with their positions defined by the x axis and y axis, with integer points in the intervals $x \in [0, 30]$, $y \in [0, 30]$. Equation (4.31) is the mathematical description of the 2-dimensional propagation system we are trying to model using the circuit in Figure 4.9, and it is modified for two space dimensions and rewritten as:

$$6.21 \times 10^{-9}\left(\frac{\partial^2 V'_m}{\partial x^2} + \frac{\partial^2 V'_m}{\partial y^2}\right) = 10^{-7}\frac{\partial V'_m}{\partial t} + I'_{ion}, \tag{4.31}$$

where V'_m and I'_{ion} are scaled membrane potential and ionic current. Here we still use the values used by Bray and Wikswo in [108] for the surface-to-volume ratio $\beta = 3000\ cm^{-1}$, the conductances $d_x = d_y = 0.186\ mS/cm$, and the membrane capacitance $C_m = 1\mu F/cm^2$. Discretizing equation (4.31) by meshing the continuous spatial domain into grids, this differential equation can be mapped into the RC network shown in Figure 4.9 by setting proper values for the resistors, capacitors,

and the ionic currents in the figure; this has been introduced in section 4.3.1. We set the grids in the x and y direction to be $\Delta x = \Delta y = 160\ \mu m$. The circuit parameters are selected under the restriction of equation (4.26), and are summarized in equation (4.32):

$$\begin{cases} R_x = R_y = 4.1 \times 10^4\ \Omega, \\ C = 0.1\ \mu F, \\ I_0 = I'_{ion}, \end{cases} \tag{4.32}$$

where R_x and R_y are resistances between nodes in the x and y directions, C is node capacitance, and I_0 is the ionic current of each node (refer to Figure 4.4 for the names of circuit components). Here we still use the Beeler-Reuter model to formulate the ionic current, provided in equation (2.41)-(2.60).

In order to activate the 2-dimensional RC network and create action potentials, external stimulus is needed to be applied to the circuit. The stimulating elements are configured for generating a spiral reentry wave on the RC circuit and can be divided into two groups, as illustrated in Figure 4.9. The first group of stimulating current sources $I_{stimulus,1}$ are connected to the nodes at $y = 0$ ($x \in [0, 30]$), and they all fire a pulse at time $t = 10\ ms$, which creates a plane action potential wave that propagates in the increasing y direction. The second group of stimulating currents $I_{stimulus,2}$, connected to $x = 30$ and $y \in [0, 10]$, send an impulse at time $t = 335\ ms$. This combination triggers a spiral wave as we will see soon. $I_{stimulus,2}$, $8\ mA$ in magnitude and lasting for $0.1\ ms$, is set stronger than $I_{stimulus,1}$, $6.2\ mA$ of the same duration, in order to successfully re-activate the elements that exit the refractory period a short while ago.

The simulation results are provided in Figure 4.10. The x axis and the y axis are the same as in Figure 4.9, and the z axis is the membrane potential.

As shown in Figure 4.10(a), at $t = 10\ ms$, the first group of stimulus triggers the components at an edge of the array. After 30 ms, that is at $t = 40\ ms$, the generated action potential is transmitted to the nodes at $y = 16$, and this is depicted in Figure 4.10(b). At $t = 300\ ms$, shown in Figure 4.10(c), the action potentials have been propagated to every node in the array and the components close to the origins (at $y = 0$) are largely repolarized, i.e. back to resting potential. At $t = 335\ ms$, the second group of stimulus trigger the circuit as illustrated in Figure 4.10(d), and this situation is known to happen in the heart when a group of cells fires abnormally [37]. At this moment, many components have not been fully repolarized from the last action potential. Figure 4.10(e) shows that 10 ms later, the action potential wave triggered by the second stimulation is propagated to the neighborhood. Note that a part of the region where the second stimulus fires is still in the refractory state due to the recent passage of the plane action potential wave. Therefore, at the beginning the second wave can only propagate in the decreasing x direction to where the components become excitable. Soon more components exit the refractory period of the first action potential and recover the ability to be activated, the second wave can enter this region, propagating in the y direction first, and then going in the positive x direction. This is illustrated in Figure 4.10(f)(g)(h). The wave propagates in the negative y direction as shown in Figure 4.10(i)(j), when the components where the second wave originates exit the refractory period and fire a third action potential, giving a reentrant action potential. This process can continue, forming a rotating spiral wave pattern.

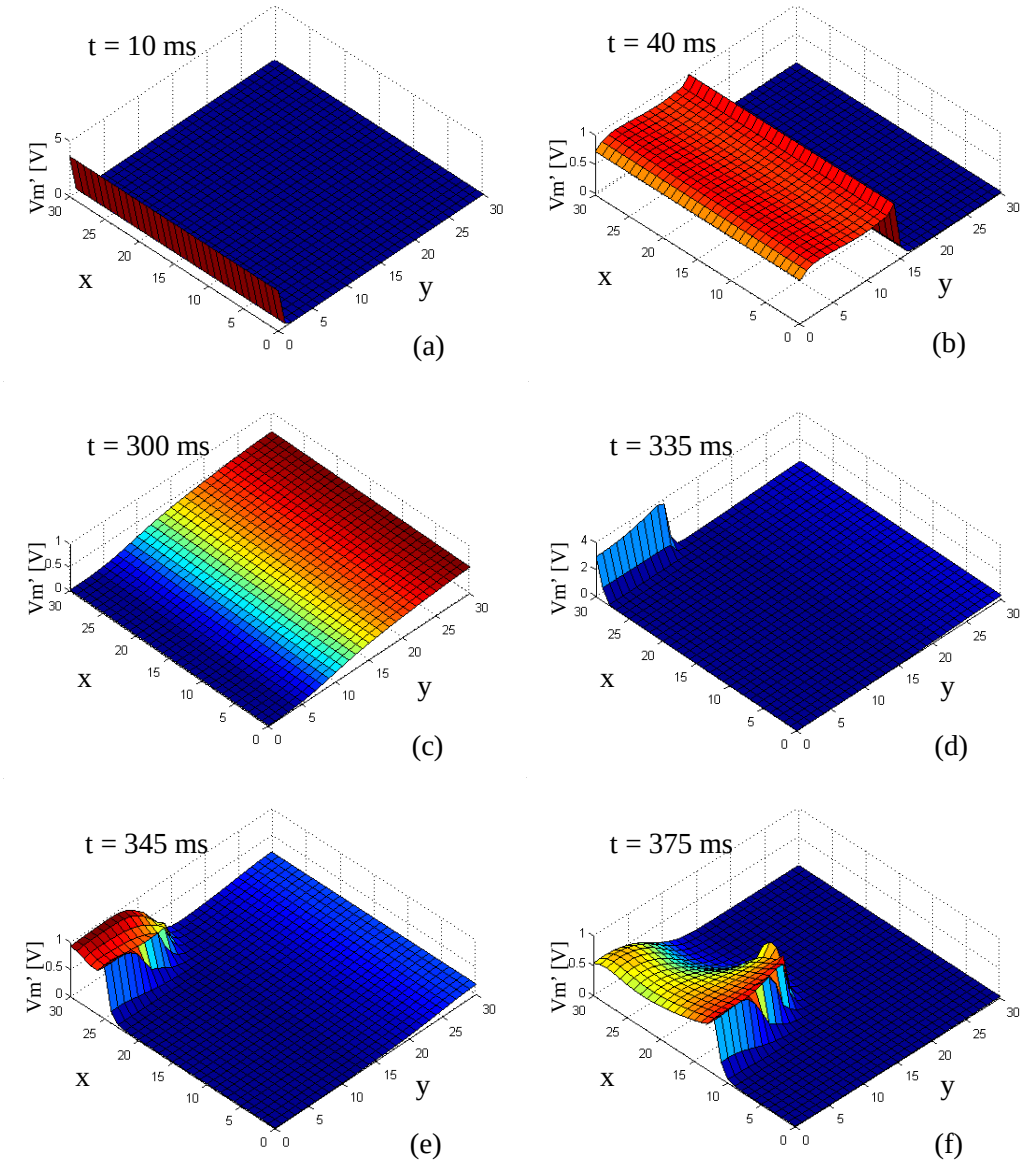
t = 10 ms
Vm' [V]
x
y
(a)
t = 40 ms
Vm' [V]
x
y
(b)
t = 300 ms
Vm' [V]
x
y
(c)
t = 335 ms
Vm' [V]
x
y
(d)
t = 345 ms
Vm' [V]
x
y
(e)
t = 375 ms
Vm' [V]
x
y
(f)

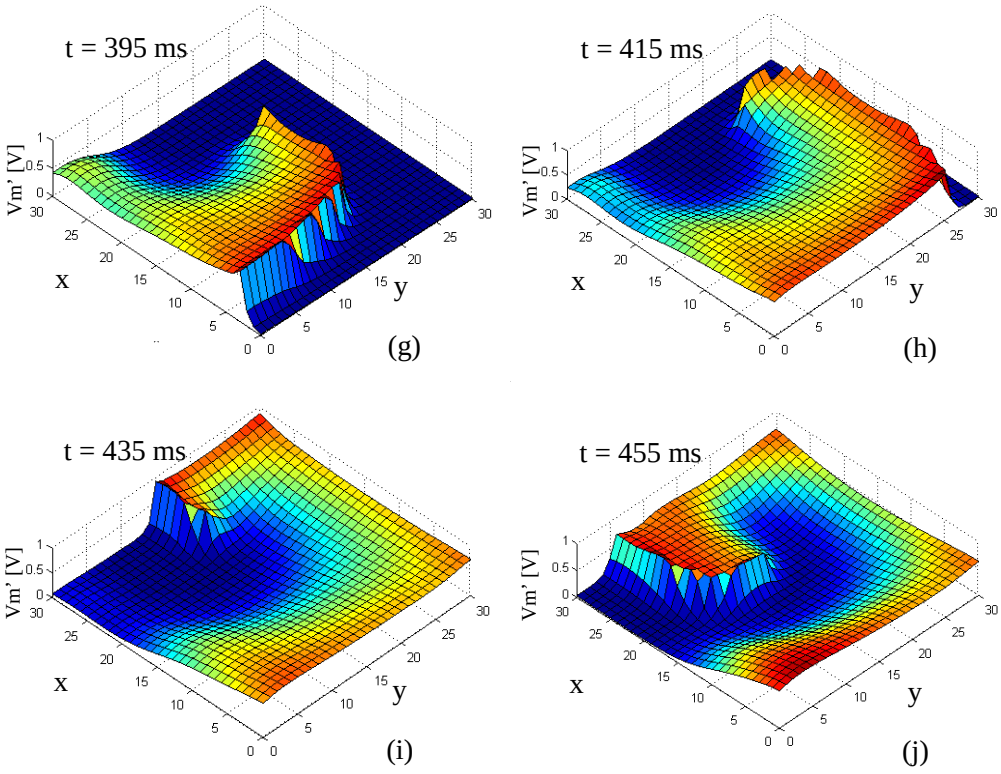

Figure 4.10: A spiral wave in 2-dimension cardiac model.

Chapter 5

Conclusions and Future Work

5.1 Conclusions

In this dissertation, we have presented analog VLSI circuits which simulate the electrical activities of the heart in chapter 3 and 4. The VLSI design of the heart model is based on the Beeler-Reuter model, describing the ionic membrane mechanism of ventricular cells, along with the continuous cardiac propagation model which evolved from cable theory. In order to implement the mathematical descriptions of the heart model in a VLSI circuit, we reformulate the Beeler-Reuter equations, and discretize the reaction-diffusion equation of the propagation model. The PSpice simulation of the transistor circuit of a cardiac cell and a segment of 1-dimensional cardiac fiber has been carried out, and the circuit simulated action potential has been discussed.

In chapter 2, we presented a review for the kinetics of the membrane ionic currents and provided the equations of the Beeler-Reuter model. The Beeler-Reuter model describes a degree-eight first order ordinary differential system, and formulates the membrane potential, four ionic currents, six gating variables, and a

varying calcium concentration. The time-based differential system is realized using the integration properties of capacitors and nonlinearities of MOS and NPN transistors, presented in chapter 3. The circuit simulated action potential of a cardiac cell showed satisfactory accuracy compared with the action potential calculated from the original equations in the Beeler-Reuter model.

In chapter 4, we discussed the cardiac propagation model, a partial differential equation that describes the variation of the membrane potential in space. The space-dependent partial differential equation is realized with a non-linear RC network. The propagation of the cardiac electrical activity has been simulated in 1-dimensional model with a transistor circuit. The important reentry phenomena and the spiral wave have been simulated successfully with a 2-dimensional model.

It is worth to emphasize that we have proposed a design flow and a set of steps for constructing analog VLSI circuits to calculate mathematical equations (in chapter 3), and this methodology can be applicable to systems other than the heart. We have introduced equation reformulation schemes to change a mathematical description for easier circuit realization; this uses the Matlab Curve Fitting Toolbox to transform equations to expressions that can be simulated by simpler circuits, a parameter scaling procedure to convert numerical ranges of variables to the feasible working region of circuit currents and voltages, and an initial value shifting scheme to change the initial conditions of differential equations to zero. We have designed a set of transistor circuit blocks of mathematical function units, implemented a time-based ordinary differential system (for a cardiac cell), and proposed the circuit structure to map reaction-diffusion systems. All the introduced methods contribute to the fundamentals for a novel technique of obtaining numerical solutions by analog VLSI circuits. Analog circuits realized on hardware have the potential

for fast computation due to their convenient and parallel calculation method for differentiation compared to the iterative method used by digital computers, and this makes it possible to produce application-specialized fast analog processing elements.

5.2 Future Work

This work can be seen as a first step towards the development of a full electrical conduction system of the entire heart using analog VLSI circuits. To construct a complete cardiac electrical system with circuits, more work is necessary. Listed below are several additional aspects that need to be studied.

- Power Characterization

Power efficiency is an important issue in terms of the satisfactory battery span in portable electronics. In the case of VLSI implementation of the heart model, the potential applications, such as portable cardiac processing devices, implantable medical electronics, etc., all demand low power dissipation. To simulate the whole heart, millions of spatial nodes may be needed, and, thus, when a full heart model is realized in silicon and membrane ionic mechanism details are implemented for each node, power consumption can become critical to necessitate the proper functioning of the whole system. Therefore, the power consumption of the VLSI heart model needs to be characterized and minimized, and low power techniques (such as decreasing the biasing currents, simplifying the circuit topologies to reduce the number of transistors, changing the working region of transistors, lowering the supply voltages, changing fabrication technology etc.) are desirable to be incorporated into the circuit design.

- Integration of Capacitors

We have shown in chapter 3 that the maximum capacitor (1 μF) used in the VLSI design of heart model can be realized by a capacitor 10^4 times smaller, that is 100 pF. Taking the selected AMI 1.5 μm IC process as an example, in which the available capacitor option PiP (poly2 over poly) is about 600 $aF/\mu m^2$, a capacitance of 100 pF needs a silicon area of about 408×408 μm^2. Thus, the required capacitor area is still very large, and further study is needed to find smaller VLSI elements that calculate integrals. One way is to improve the presented capacitance amplification schemes specified for the VLSI cardiac circuit (refer to chapter 3 section 3.4.7). As mentioned in section 3.4.7, minimizing the leakage currents of bipolar devices can reduce the limitation on the capacitor amplification factor. Shrinking the time scale is another way to avoid large capacitance, and this needs the investigation of high-frequency performance of the VLSI heart circuits of this dissertation. Also, switched-capacitor circuits [117](pp. 417) could be investigated for a possible method of magnifying capacitances, in which clock-controlled switches are used to mediate charging currents. Developing new semiconductor technology for higher capacitivity, and inventing novel integration devices to replace area-consuming capacitors could be other directions for solving the problem.

- Enhancement with Heterogeneous Membrane Properties

The presented VLSI heart model only simulates the electrical activities of the ventricular cells. The variation of the action potential generated at different portions of the heart needs to be investigated, and the development of new circuits are needed to generate these variable action potentials. The current VLSI design can be extended to include the controlabilities for adjusting the action potential for

different types of cardiac cells. Due to the great similarities of the action potentials at various kinds of cardiac cells (such as ventricle, atrial, sinus node, Purkinje fibers, etc.) and the same ionic basis of all the models, it is possible to implement the action potentials of different cells with similar circuits for changing gating opening/closing rates and channel ionic properties. A control mechanism added in the circuit implementation may be able to let the same circuit simulate various types of action potentials. In addition, the added control circuit can also serve as a handler to tune the system for simulating cardiac response in various conditions such as drug effects, emotions regulation, etc.

- Error Analysis of Implementing the Continuous Excitation Propagation Model

The same as for all the numerical method, the circuit implementation of discretized reaction-diffusion system suffers with discretization errors. The spatial discretization may introduce errors in the action potentials and influence the propagation of the action potential in space, and the wave conduction velocity is a typical and easily recognizable indicator for coarse discretization [38]. The effects of spatial segmentation in the continuous model of the cardiac excitation propagation have been discussed in previous research works [38][100]. Similar analysis of the segmentation errors introduced by finite space steps on the circuit implementation can be carried out in our heart model by taking account the continuous nature of the time domain in the VLSI heart simulation. Furthermore, as mentioned in chapter 4 section 4.2.1, the continuous cable model takes the intracellular space as a medium with continuous diffusive properties and does not consider the discrete properties of the gap junctions. Therefore, a study on how close the circuit implemented excitation propagation model is to reality is necessary to provide a helpful guidance for creating more accurate VLSI heart models.

- Real 3-dimensional - Adaption to Heart Natural Topology

Though the heart can be simplified by 1-dimensional (for the specialized excitatory and conductive system from the sinus node to the Purkinje fibers) and 2-dimensional (for the atrial and ventricular walls) models, the heart has a 3-dimensional topology, with curved and rotated muscle fibers and non-zero thickness of the atrial and ventricular walls, and, thus, 3-dimensional models are unavoidable to describe more accurately the complicated structure of the heart. However, in the VLSI implementation of the heart model, 3-dimension means huge entangled wire connections and densely occupied circuits, because the 3-dimensional network has to be projected to 2-dimension surface due to the 2-dimension nature of the current VLSI technology; this provokes the need for new semiconductor techniques for implementing heart circuits. The concepts for 3-D VLSI [118] and flexible (bendable) transistors [119] are possible directions to implement real 3-dimensional heart models with circuits. The study of the detailed anatomic structure of the heart and the orientation of the cardiac fibers is necessary to incorporate into the VLSI implementation. Irregular meshing for simulating the complex geometry of the cardiac muscle is also desirable to be investigated.

5.2.1 More - Application Perspectives

Up to now, we have been concentrating on the simulations of the cellular ionic mechanisms and the resulting electrophysiological activities in the normal heart. The eventual purpose of modeling the cardiac electrical behavior is to understand the cardiac physical phenomena and the mechanisms of heart failure, and apply this knowledge to biomedical research to contribute to the development of therapeutic strategies, drugs and medical devices. Therefore, the capability of simulating ab-

normal activities in the heart and the inclusion of other interactions with the heart electrical behaviors are imperative to make the VLSI heart model more thorough and, hence, beneficial for real life cardiology. In the following, we give an overview on what else can be included in the circuit cardiac simulation.

- Models for Diseased Cardiac Tissues

Acute ischemia in cardiac muscles can critically impair the mechanical and electrical behavior of the heart and facilitate the development of reentry waves, cardiac arrhythmias, and ventricular fibrillation [26][120]. The enhancement of the model to be able to handle ischemia cardiac tissues necessitates the simulation of the abnormal electrophysiological properties in the heart caused by ischemia. Sophisticated models that include the formulation of K^+ concentrations, ATP-sensitive K^+ channels, and effects of pH are needed to simulate this kind of diseased cardiac cells [121]. The relative previous work can be found in [120][122] for the simulation of ischemia in the heart. It is even more exciting to model the mutated cardiac cells and inherited heart disorders. Such cell models provide us insight into the genetic bases of arrhythmias and heart diseases. [123] is an example of using simulation to study the action potential changes in mutated cardiac tissue.

- Arrhythmias and Their Underlying Mechanisms

In this work we only simulated reentry waves, which is the most common mechanism of arrhythmia and plays a crucial role in the initiation of ventricular fibrillation, the most severe arrhythmia. The simulation of the progression and sustainment of ventricular fibrillation is not performed in this work but is important to gain knowledge of the dynamics of ventricular fibrillation and invent efficient

treatment. Besides, to enrich our understanding of the arrhythmia caused by reentry (i.e. abnormal impulse conduction), more precise cardiac conduction models may be favorable to extract more information from the simulation. One aspect of improving the model is to include the discrete properties of gap junctions and their dynamic resistances. Gap junctions are clusters of intercellular channels, which exhibit several conductance states [124], in which the probability of a channel being in the open state is determined by the transjunction voltage. Hence, the conductivity of gap junctions changes during the transmission process of electrical signals. [99] is a previous work that studied the influence of varying gap junction resistance on the electrical propagation in cardiac tissues.

Furthermore, there are two other basic mechanisms causing arrhythmias. Unlike reentry-caused arrhythmias, which result from abnormal impulse conduction, these two are both related to abnormal impulse generation, which arises from abnormal automaticity or triggered activity [121]. Automaticity refers to the ability of the heart to initiate its own beat, and it allows the heart to beat even when it is removed from the body [26]. Suppressed automaticity can lead to sinus node dysfunction, and enhanced automaticity can result in arrhythmias [125]. Triggered activity is the spontaneous multiple depolarization triggered by *early afterdepolarizaiton* (EAD) and *delayed afterdepolarizaiton* (DAD). Previous works that simulate abnormal automaticity and triggered activity have been reported [126]-[128].

- Medication and Treatment

It is important to include medication and other methods of treatment in the simulation model in order to study the side effects of medicines and validate new medical devices. Therefore, to include the drug effects on the ionic channels and

to model implantable electronic devices are necessary for research of investigating cures for heart diseases. The anti-arrhythmic drugs are divided into four classes according to the Vaughan-Williams classification [129], and most of the drugs work by regulating the ionic channels and adjusting the depolarization or repolarization process. There have been literatures that formulate the equations for drug effects [130]-[132] and they can be easily added to the circuit simulation by the VLSI implementation schemes presented in chapter 3. Implantable devices for heart diseases include artificial pacemakers and implantable cardioverter/defibrillators (ICD). Artificial pacemakers sense the heartbeat and send electrical charge when the heartbeat is slower than a threshold for triggering more heartbeat. ICD works in a similar way, but it "actions" when detecting heart rate being too fast and delivers an electrical shock to return the rhythm to normal. Therefore, the implantable devices can also modify the heart electrical behavior and need to be included in appropriate simulations.

- Electrocardiogram

An electrocardiogram (ECG) is a graphic produced by recording the electrical voltage on the surface of the body generated by the small cardiac currents caused by an impulse that spreads into the tissues surrounding the heart [2]. Since abnormal electrical activity of the heart alters the shapes of the waves in an ECG, an ECG is the prime clinical tool for the diagnosis of cardiovascular diseases. The capability of constructing the ECG associated with the simulated arrhythmias would enable us to link between the electrical activities inside the heart and the measurement on the surface of the body and would assist in better understanding of the mechanisms underlying the heart diseases observed clinically. Previous works such as [133] and [134] have proposed methods of modeling ECG in simulations.

- Coupling with Nervous Regulation and Mechanical Systems

So far we have been discussing the electrical activity of the heart alone. It is obvious that the heart, being embedded in the body, can be also influenced by other parts of the body. The automaticity of the heart can be regulated by extrinsic factors such as temperature, oxygen tension in the blood, nervous control, hormones, etc. There have been researches carried out to formulate mathematical models for the control of heart rate by autonomic nervous system [135]-[137]. In addition, the heart rate can be also increased by the mechanical stretch of the right atrial wall [2]. The mechanical behaviors are tightly coupled with the electrical system in the heart. On one hand, the electrical activity causes the mechanical contraction of the heart; on the other hand, the mechanics influences the electrical behavior by the mechano-electric feedback. The study of the electrical and mechanical components together allows us to expand the exploration from the cardiac electrophysiology to the full functioning of the heart, and the cardiovascular physiology and the circulatory system. The mathematical models that describe the cardiac mechanics have been studied by researchers and the simulation of the electro-mechanical coupling have been performed. The related literatures are [5][138][139].

Appendix A

Transistor Circuits of Beeler-Reuter Model Implementation

In Appendix A, we provide the complete transistor circuits for implementing the Beeler-Reuter model. The circuit schematics are divided into six categories, as listed in Table A.1: V_m, the top level circuit; I_{K1}, I_{x1}, I_{Na}, and I_s, the circuits for creating four ionic currents; and *Miscellaneous* circuits. The block diagrams of the circuits and their simulation results have been presented in chapter 3, section 3.4.

The schematics of the cardiac cell VLSI design are shown hierarchically in a top-down manner, i.e. an upper level of circuit is presented first, and its sub-circuits are provided later. The legends related to the hierarchy are illustrated in Figure A.1. Figure A.1(a) is a hierarchic module, whose module name and the schematics page number of its transistor implementation are provided below the icon. In a schematics of a module, the input and output terminals, bearing the same names

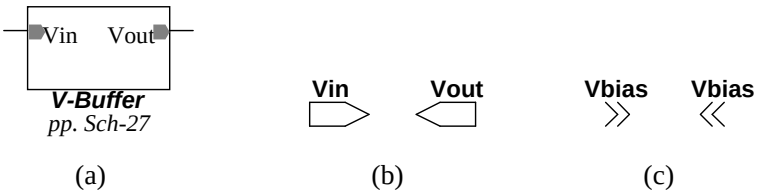

Figure A.1: Legends for hierarchical schematics.

as shown in its the module block, are represented by the symbols shown in Figure A.1(b). To help organize the schematics circuits, on-page connectors, depicted in Figure A.1(c), are used to make wire connections without drawing wires among the nodes that are distributed far away to each other in the same schematic page.

The schematics' contents are summarized in Table A.1. In each schematic, the schematic's page number is shown in the middle below the circuit, and a brief description is provided in the right bottom corner of each page.

Table A.1: List of schematics

Category	Description	Schematics Page
V_m	Top level of circuit for V_m	Sch-1
I_{K1}	Top level diagram for I_{K1}	Sch-2
	Sigmoid circuit 1 for I_{K1}	Sch-3
	Sigmoid circuit 2 for I_{K1}	Sch-4
I_{x1}	Top level diagram for I_{x1}	Sch-5
	α_{x1}, and β_{x1}	Sch-6, 7
	$\overline{I_{x1}}$	Sch-8
	Multiplier for I_{K1}	Sch-9
I_{Na}	Top level diagram for I_{Na}	Sch-10
	α_m, β_m, α_h, β_h, α_j, and β_j	Sch-11 to Sch-16
	Multi-input multiplier for I_{Na}	Sch-17
	2-input multiplier and transconductor for I_{Na}	Sch-18
I_s	Top level diagram for I_s	Sch-19
	α_d, β_d, α_f, and β_f	Sch-20 to Sch-23
	$[Ca]_i$ and E_s	Sch-24
	Transconductors for I_s	Sch-25
	3-input multiplier for I_s	Sch-26
Miscellaneous	NPN, Vbias, V-Buffer, Transconductor G1	Sch-27
	Transconductors G2, G3, G4, and G5	Sch-28
	Transconductor G6, and pool circuit 1 & 2	Sch-29
	Tanno multiplier 1	Sch-30
	Tanno multiplier 2 and current duplicator	Sch-31
	Resistor	Sch-32

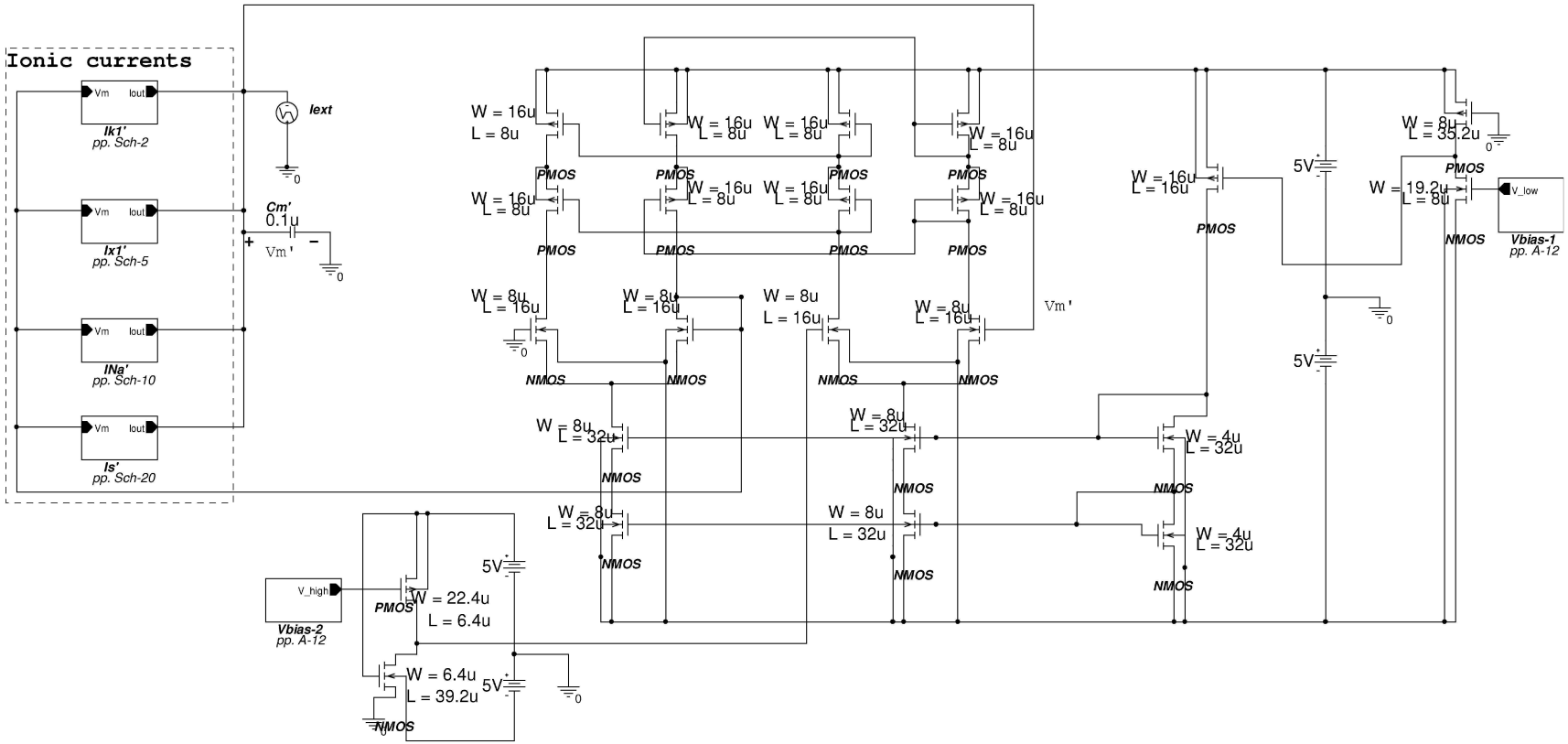

Category	Vm
Description	Top level circuit for Vm
Equation	(3.99)

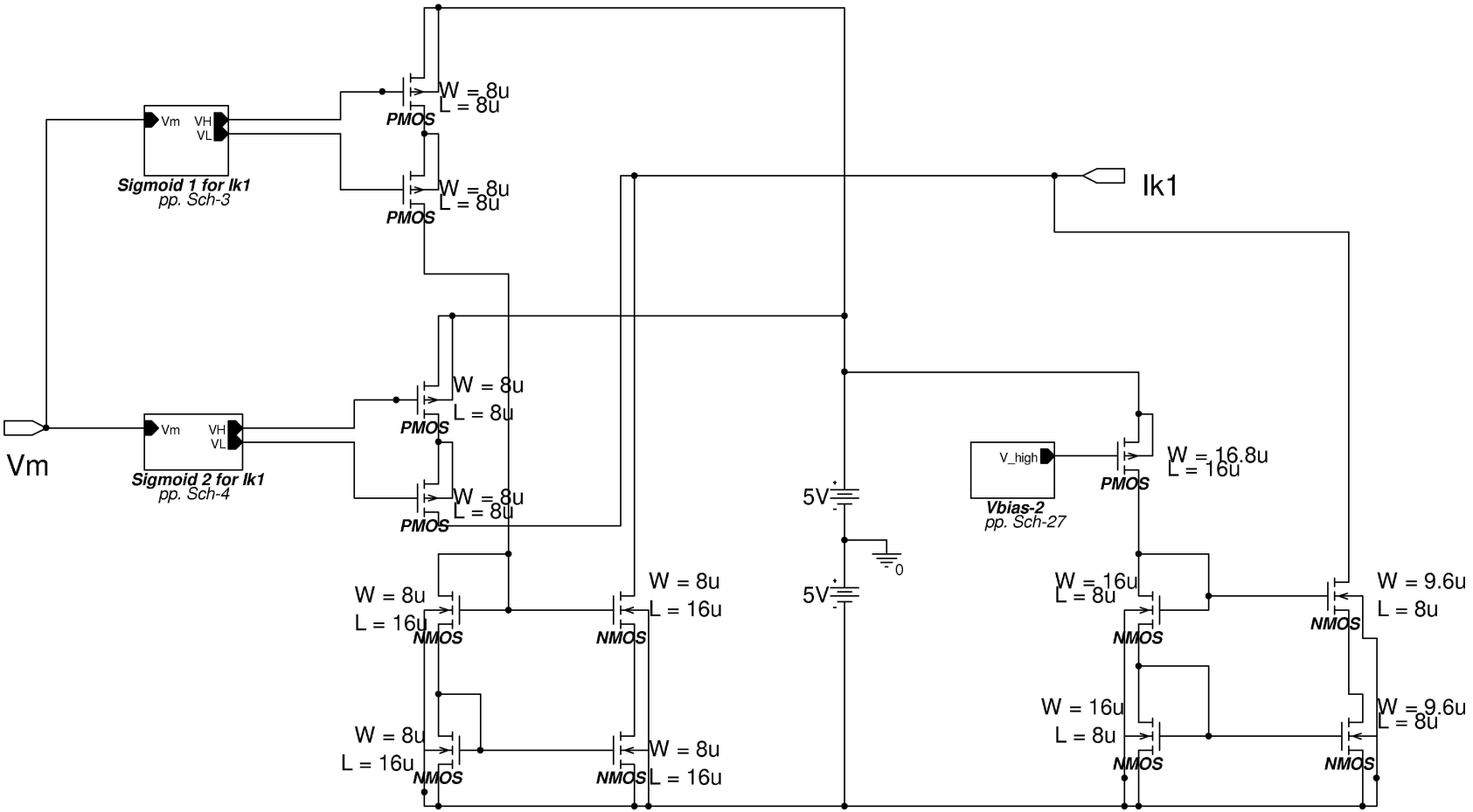

Category	I_{K1}
Description	Top level circuit for I_{K1}
Equation	(3.100)

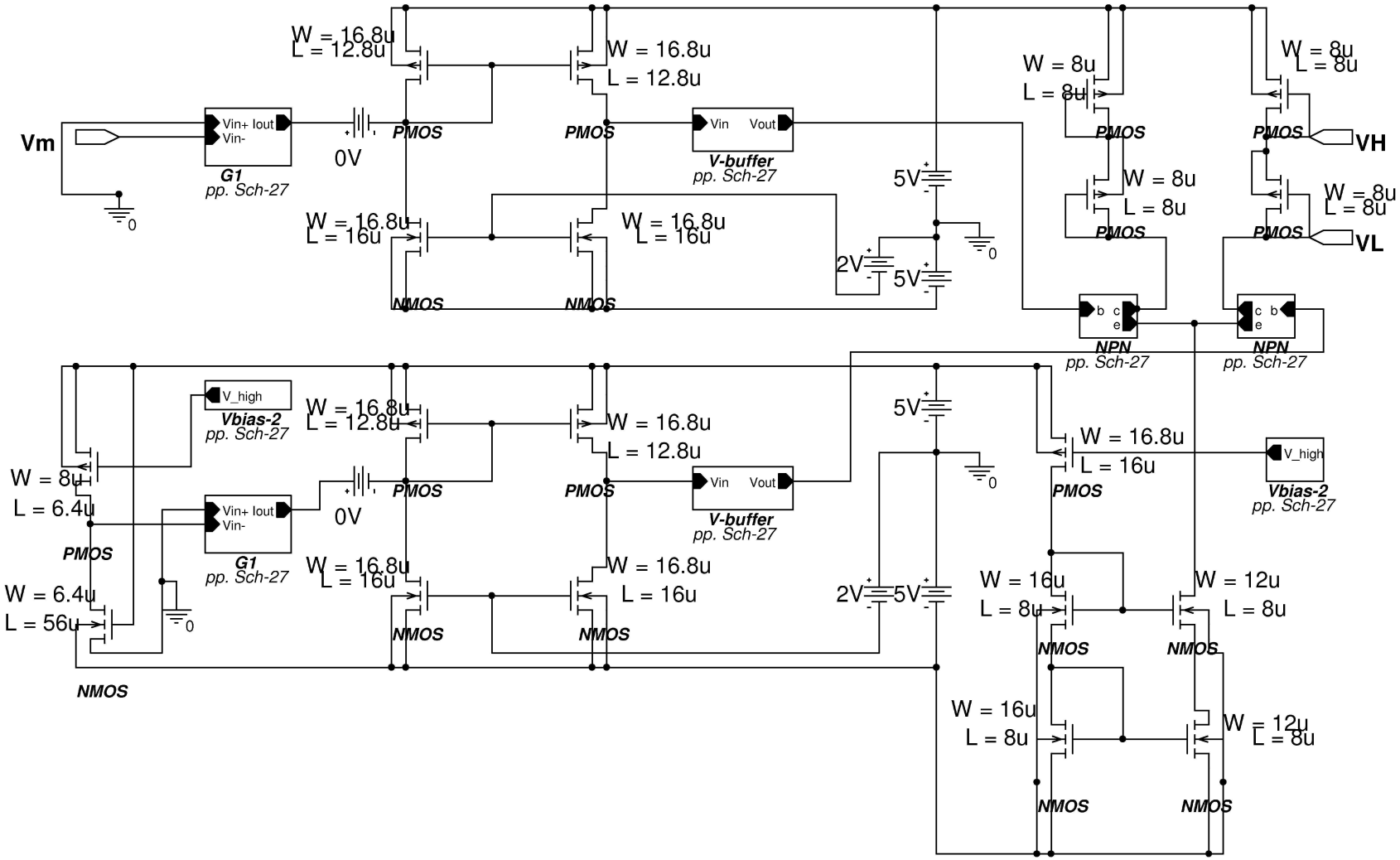

Category	I_{K1}
Description	Sigmoid circuit 1 for I_{K1}
Equation	(3.100) 2nd term

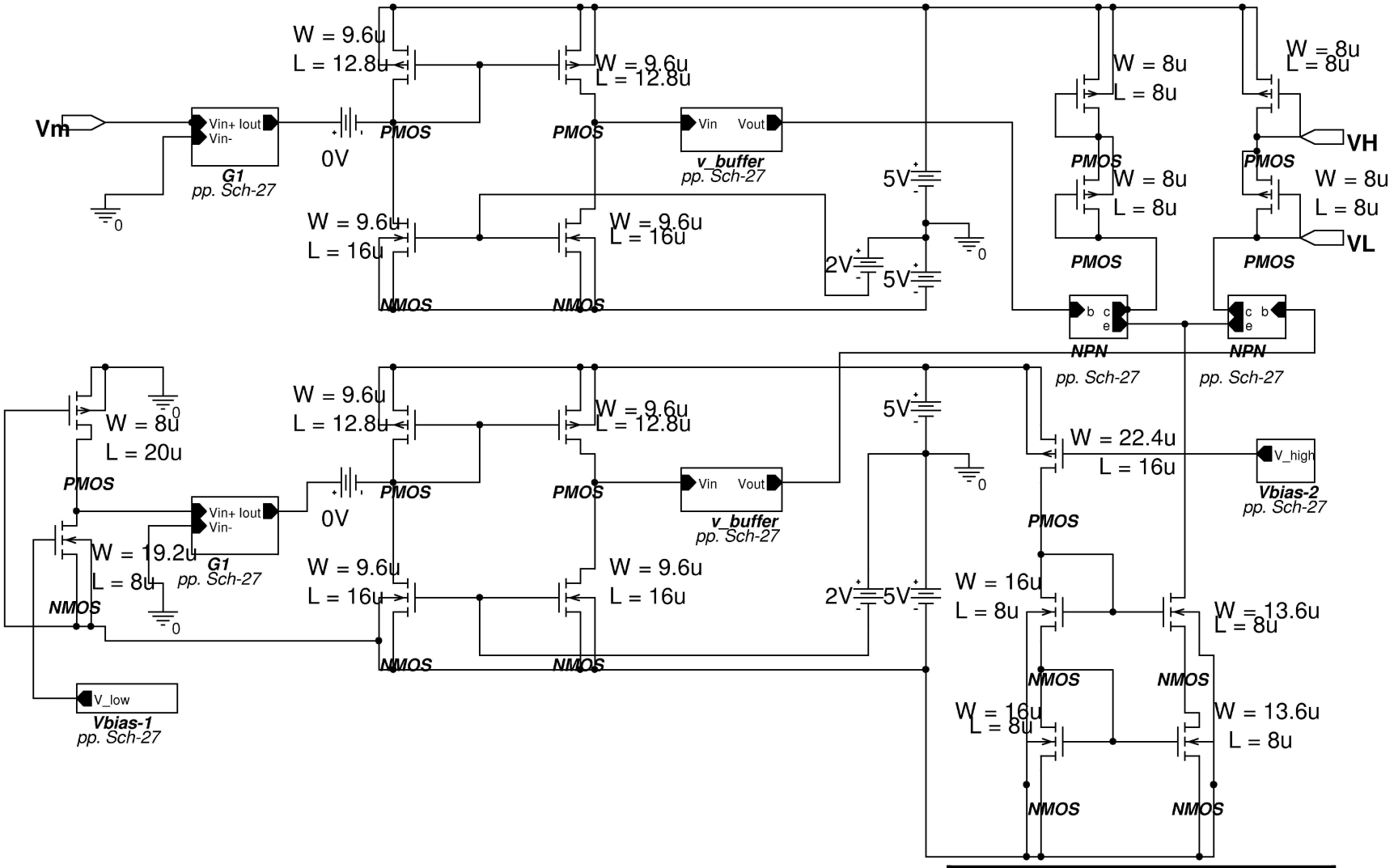

Category	I_{K1}
Description	Sigmoid circuit 2 for I_{K1}
Equation	(3.100) 3rd term

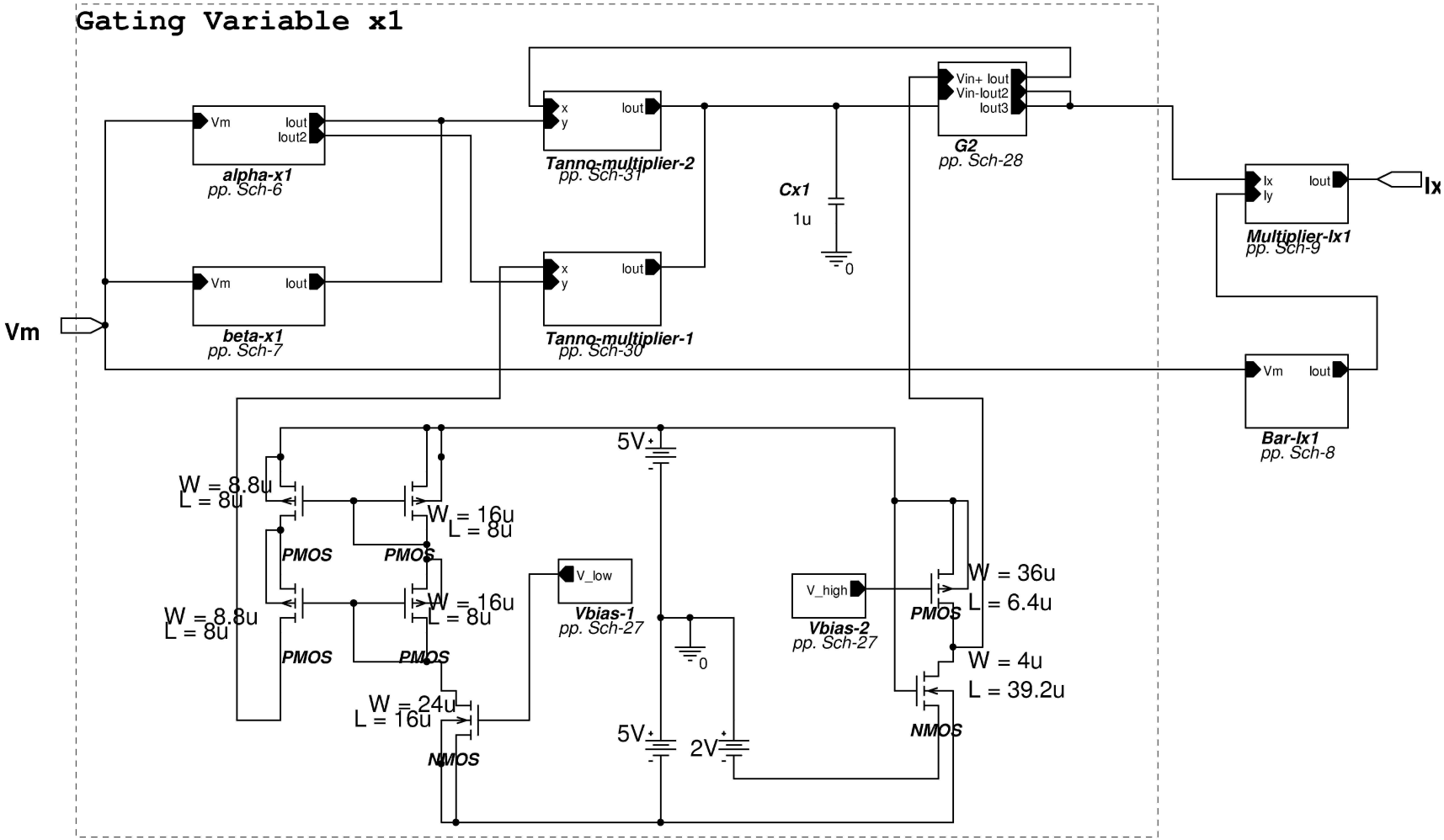

Category	I_{x1}
Description	Top level circuit for I_{x1}
Equation	(3.103), (3.117)

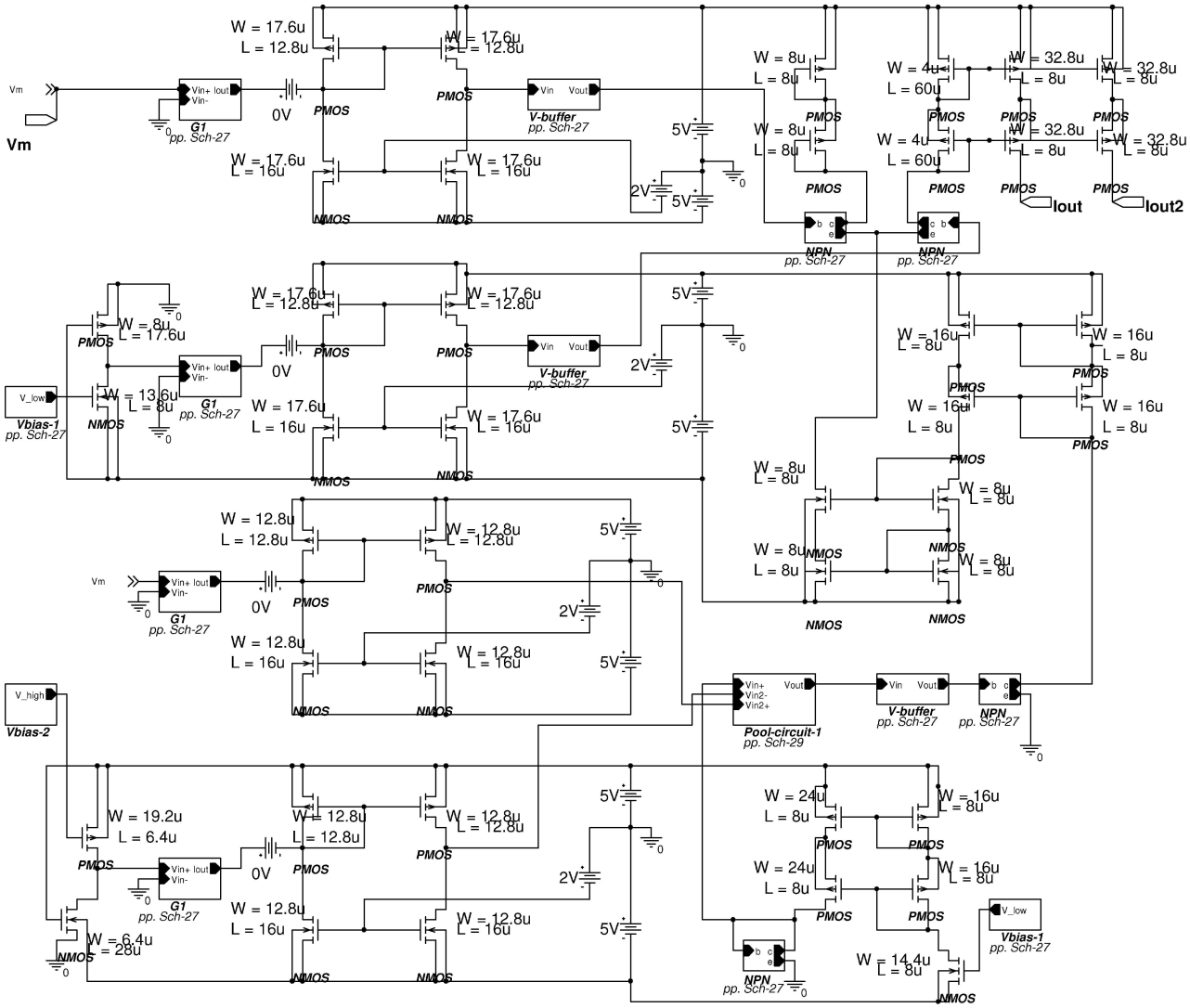

Category	I_{x1}
Description	α_{x1}
Equation	(3.113)

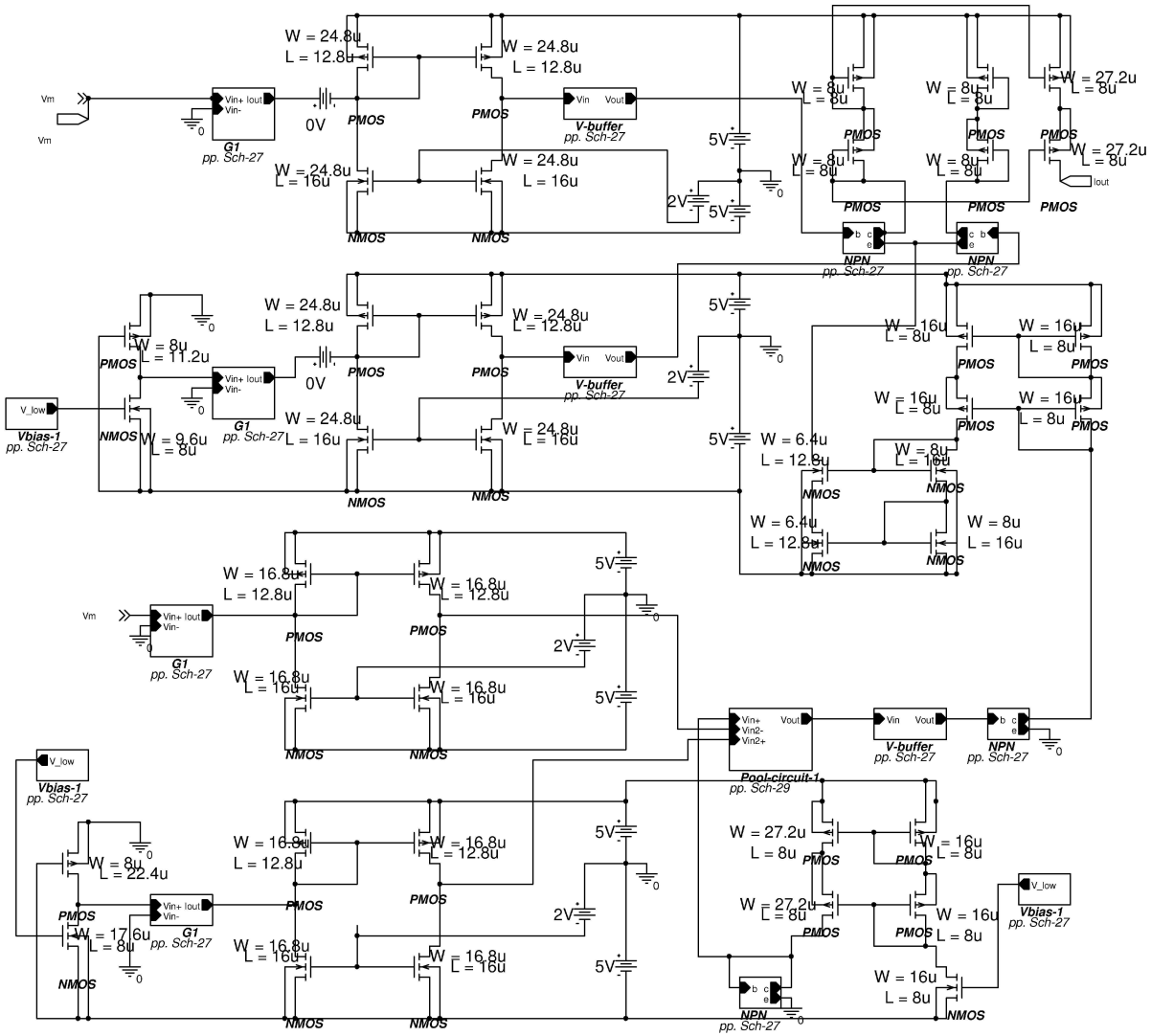

Category	I_{x1}
Description	β_{x1}
Equation	(3.114)

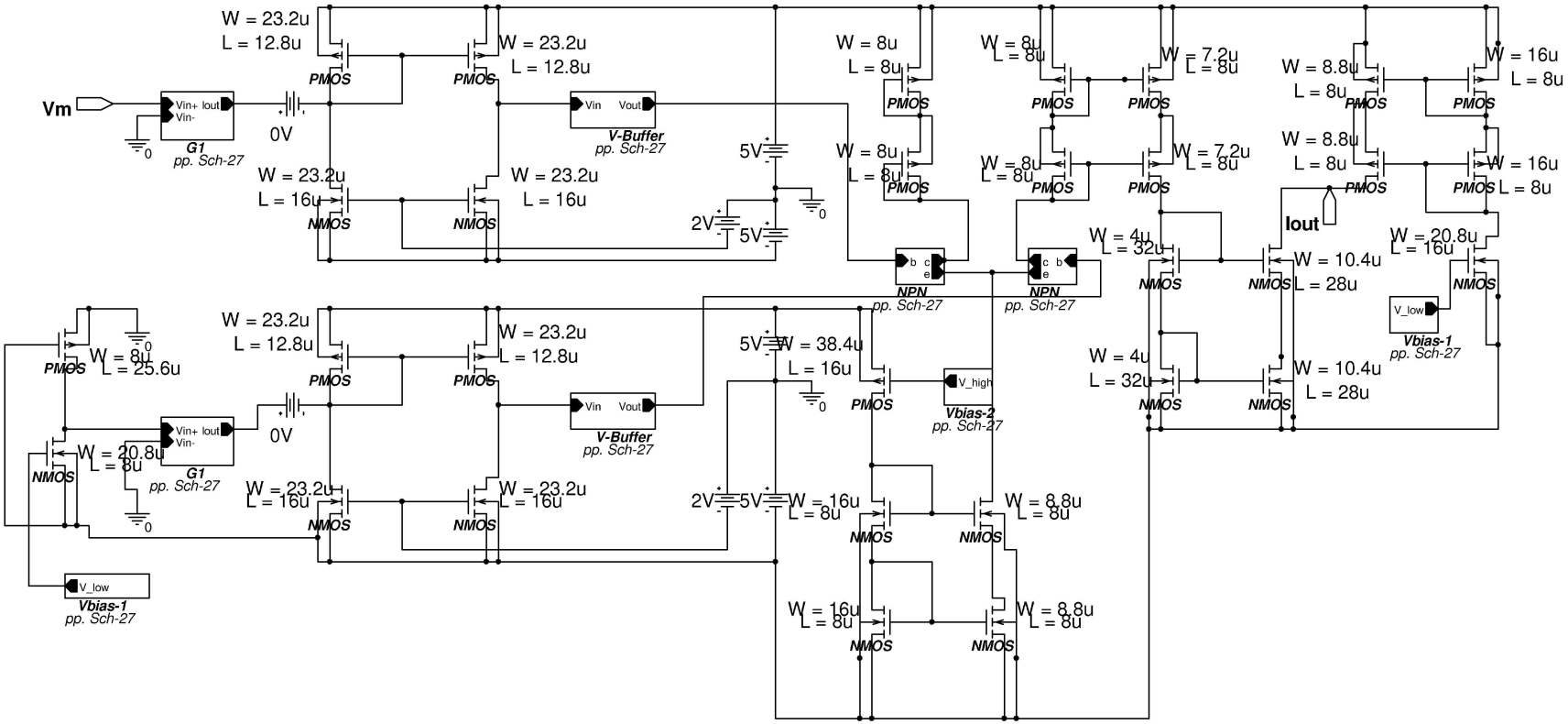

Category	I_{x1}
Description	$\overline{I_{x1}}$
Equation	(3.116)

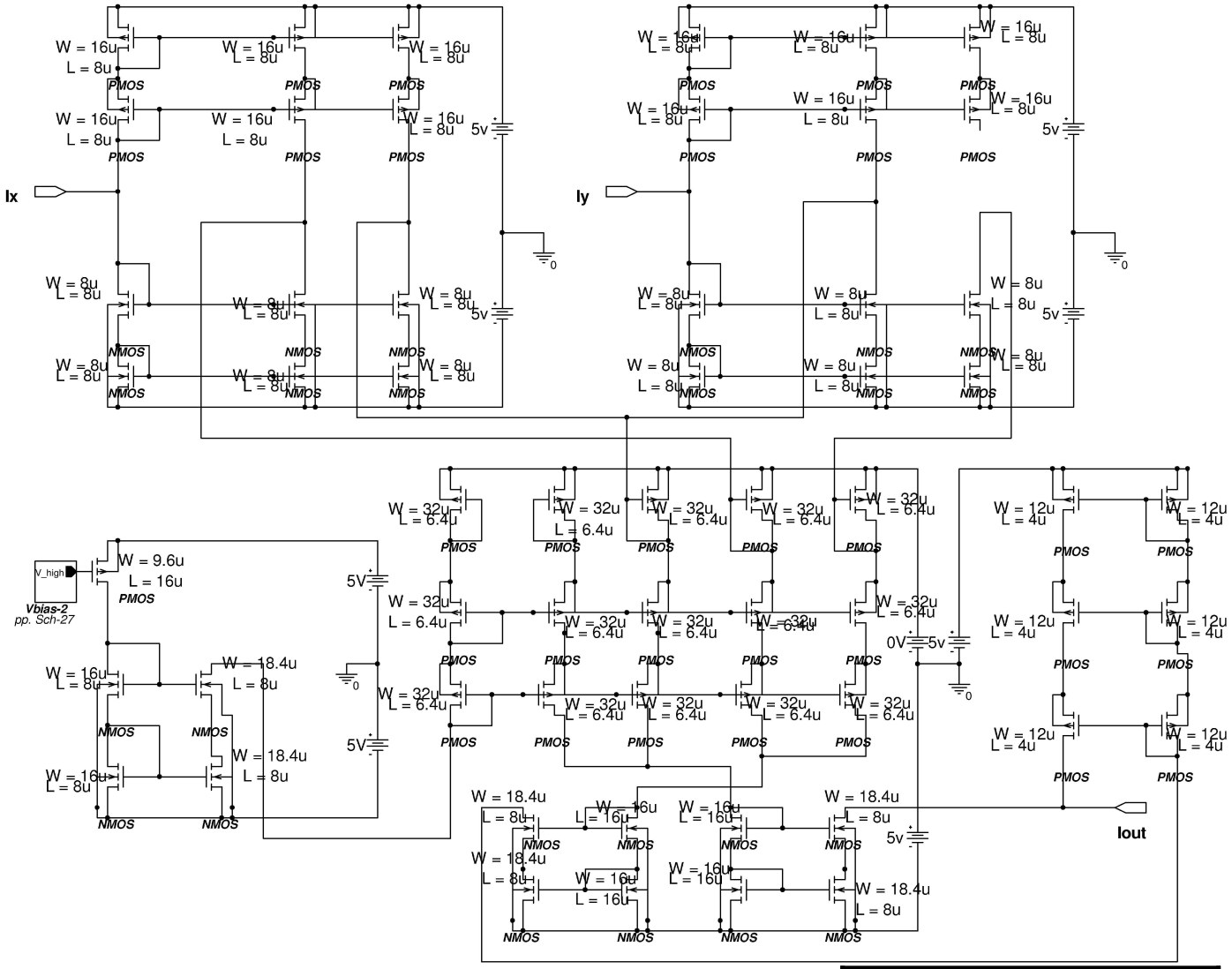

Category	I_{x1}
Description	Multiplier for x1 and $\overline{I_{x1}}$
Equation	(3.117)

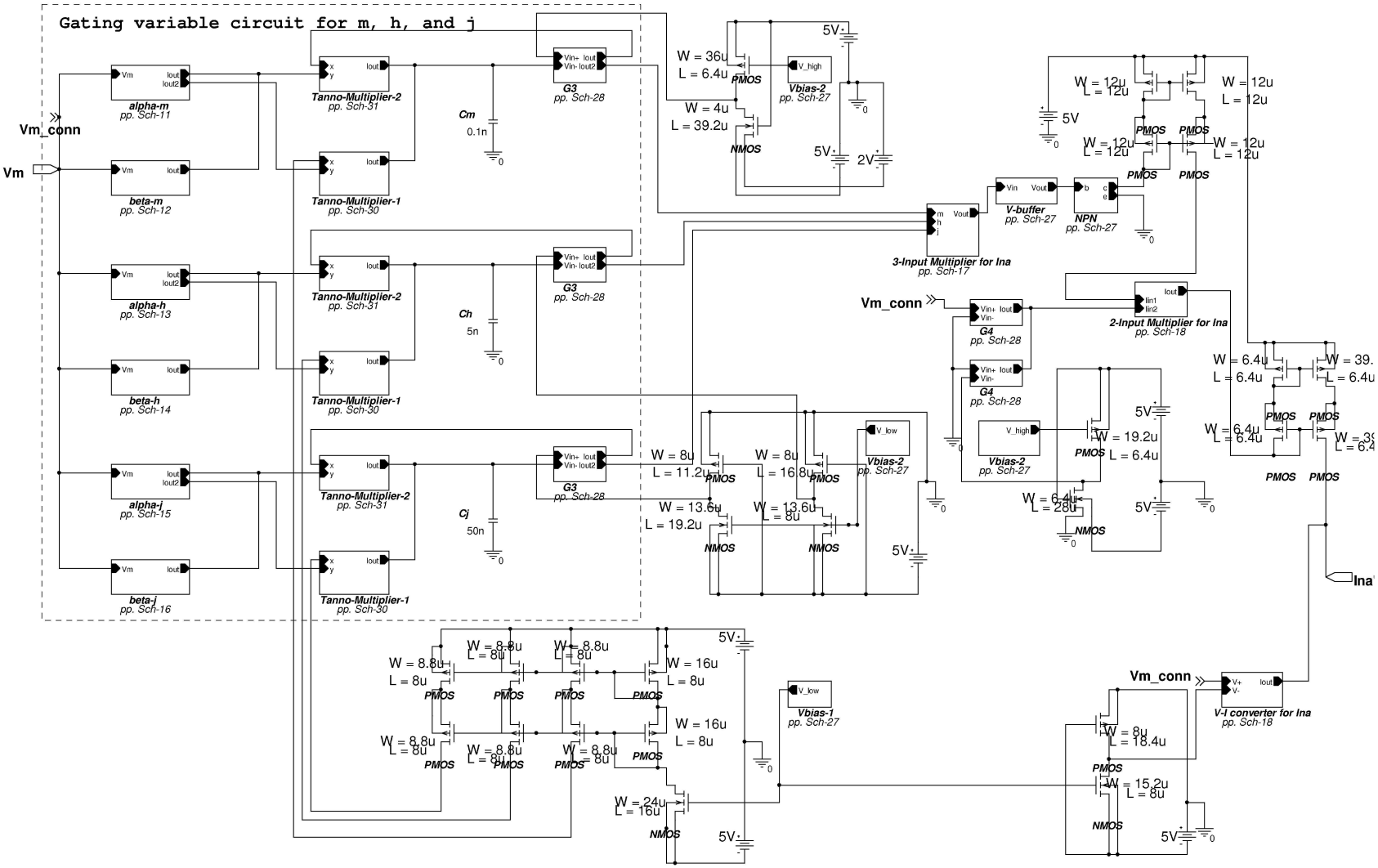

Category	I_{Na}
Description	Top level circuit for I_{Na}
Equation	(3.103), (3.118)

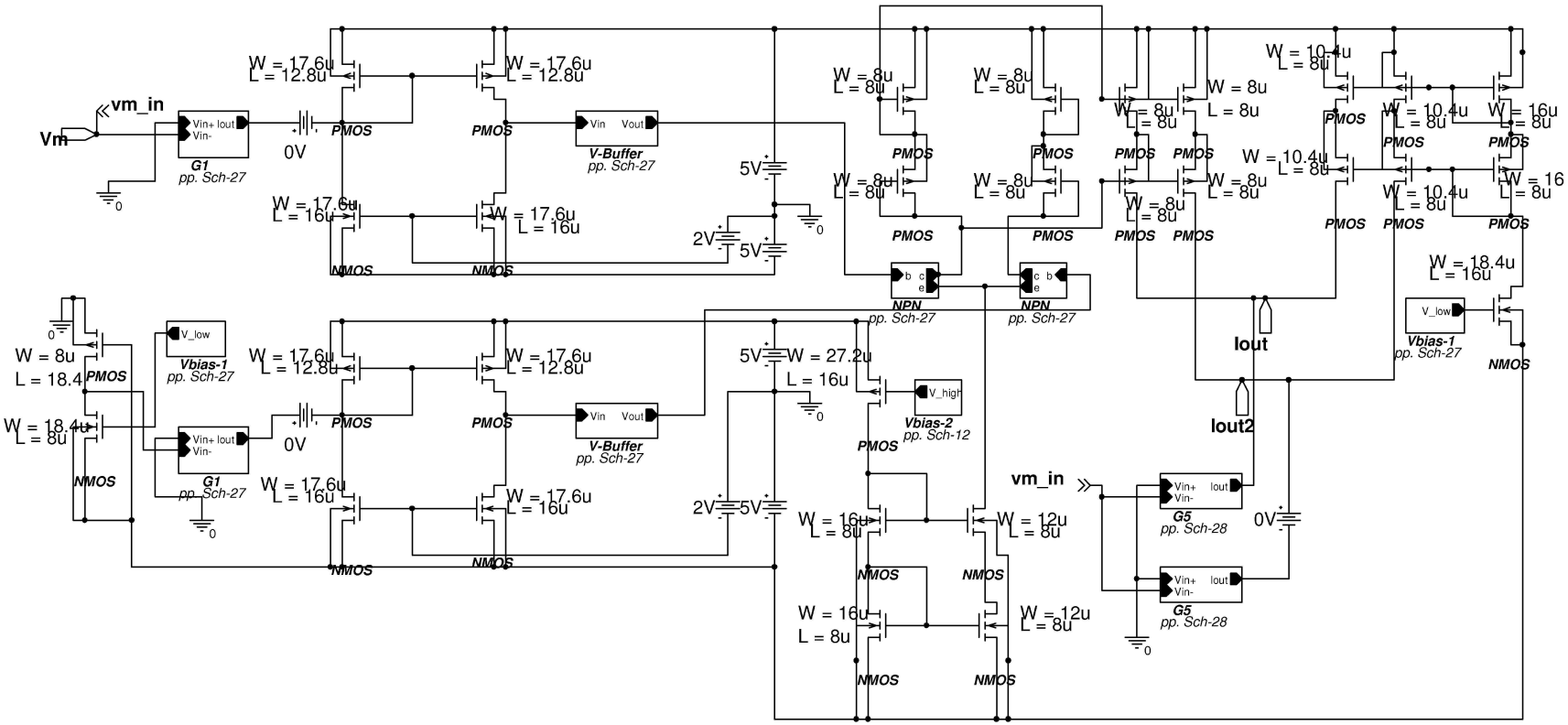

Category	I_{Na}
Description	α_m
Equation	α_m in Table 3.5

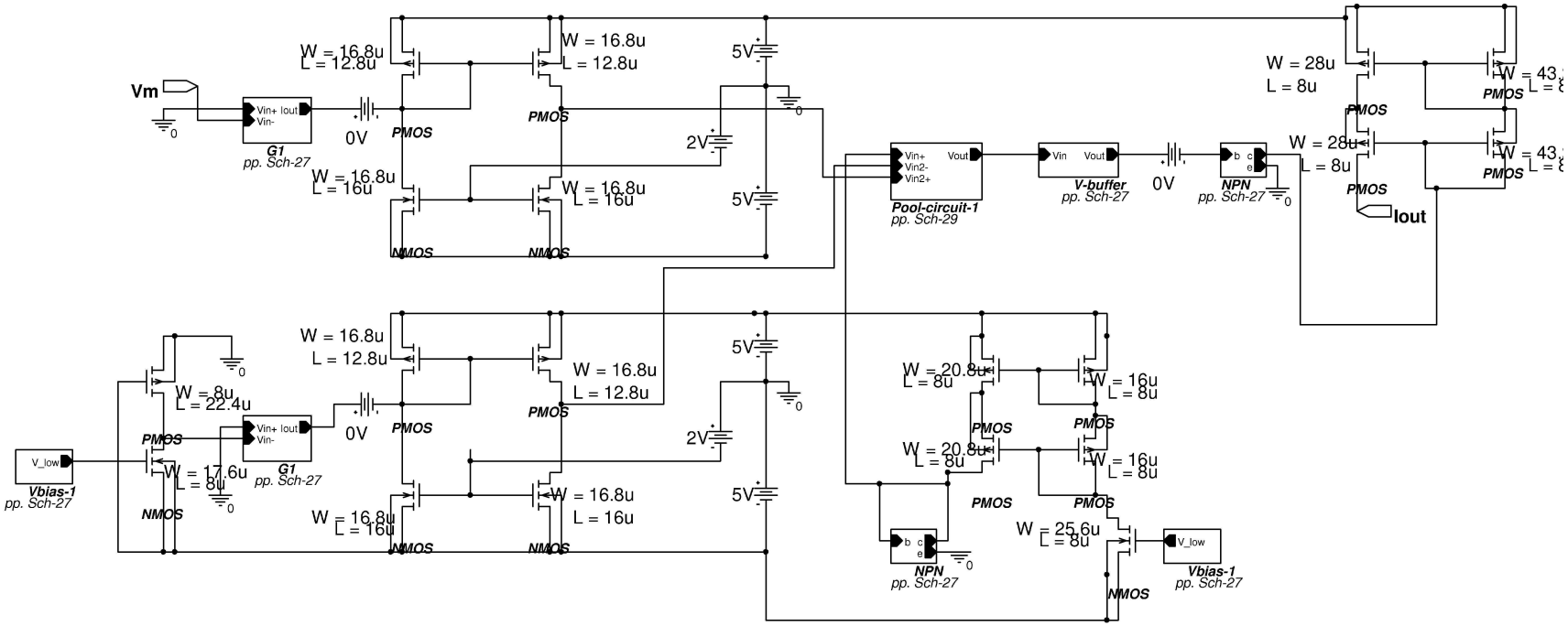

Category	I_{Na}
Description	β_m
Equation	β_m in Table 3.5

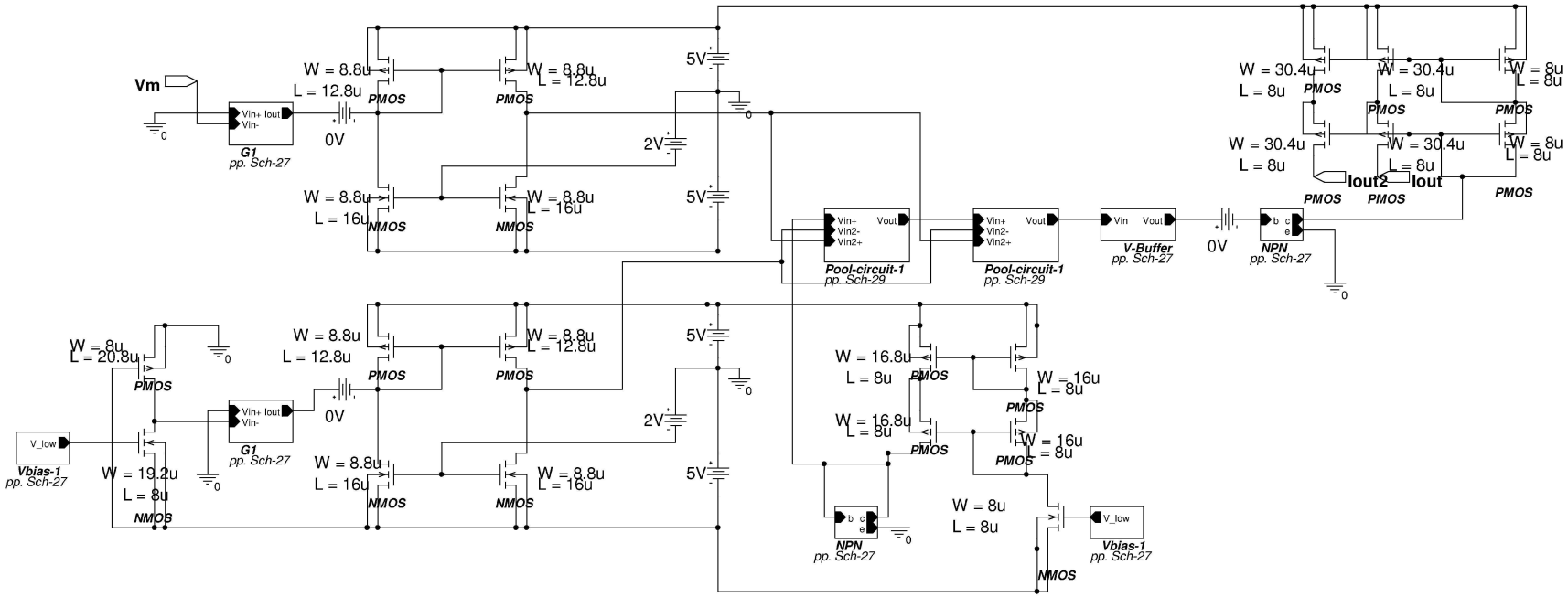

Category	I_{Na}
Description	α_h
Equation	α_h in Table 3.5

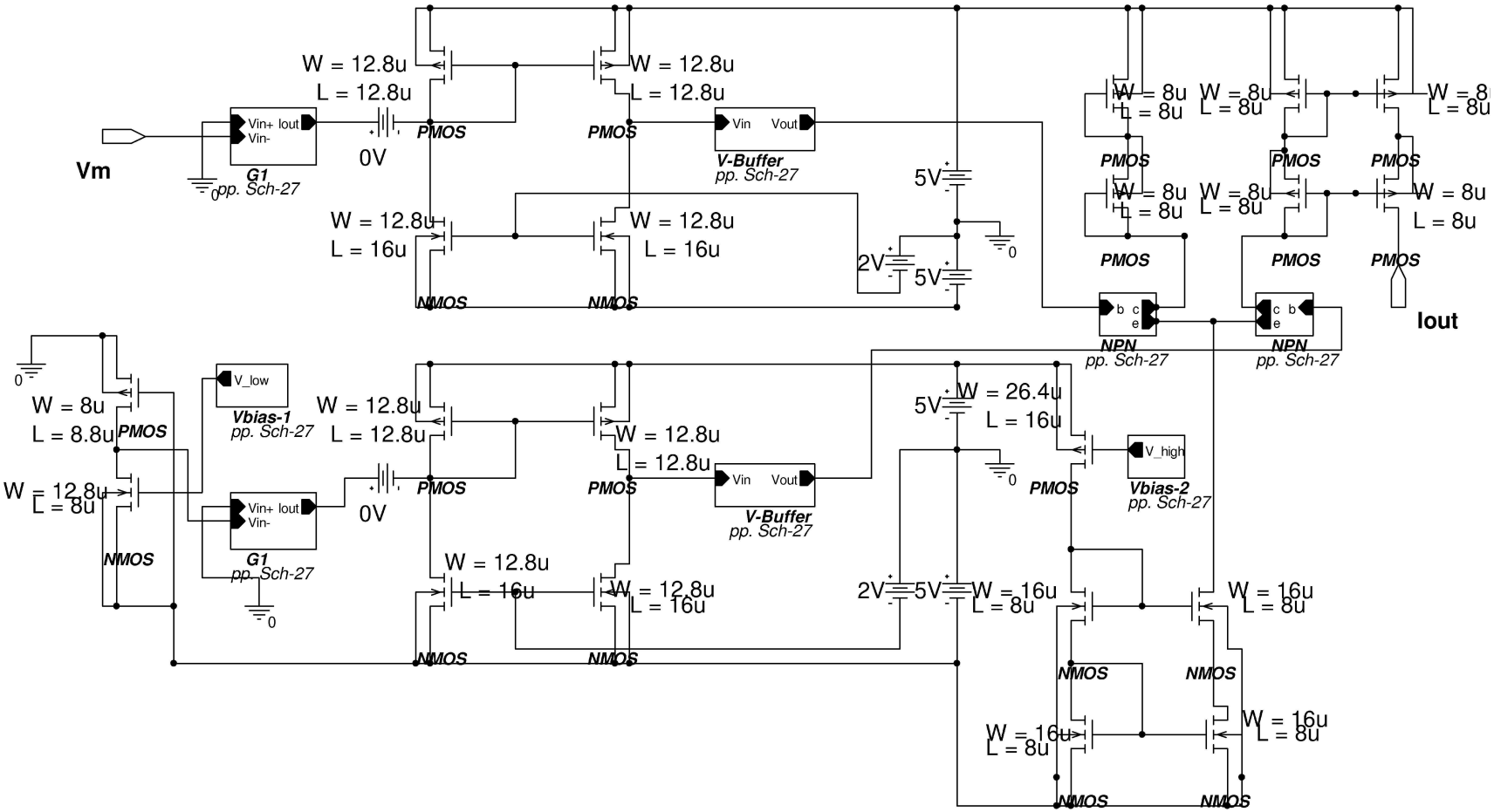

Category	I_{Na}
Description	β_h
Equation	β_h in Table 3.5

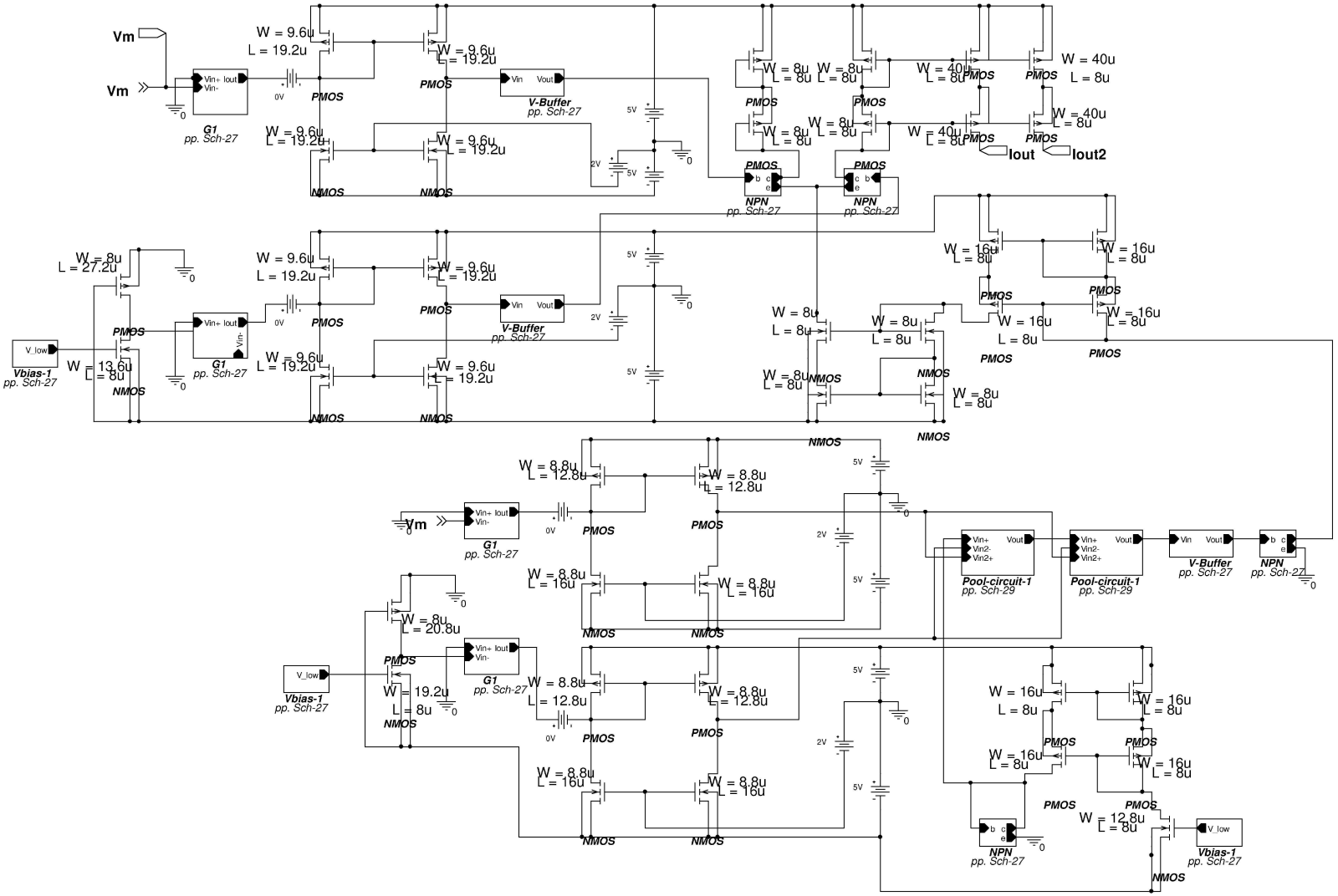

Category	I_{Na}
Description	α_j
Equation	α_j in Table 3.5

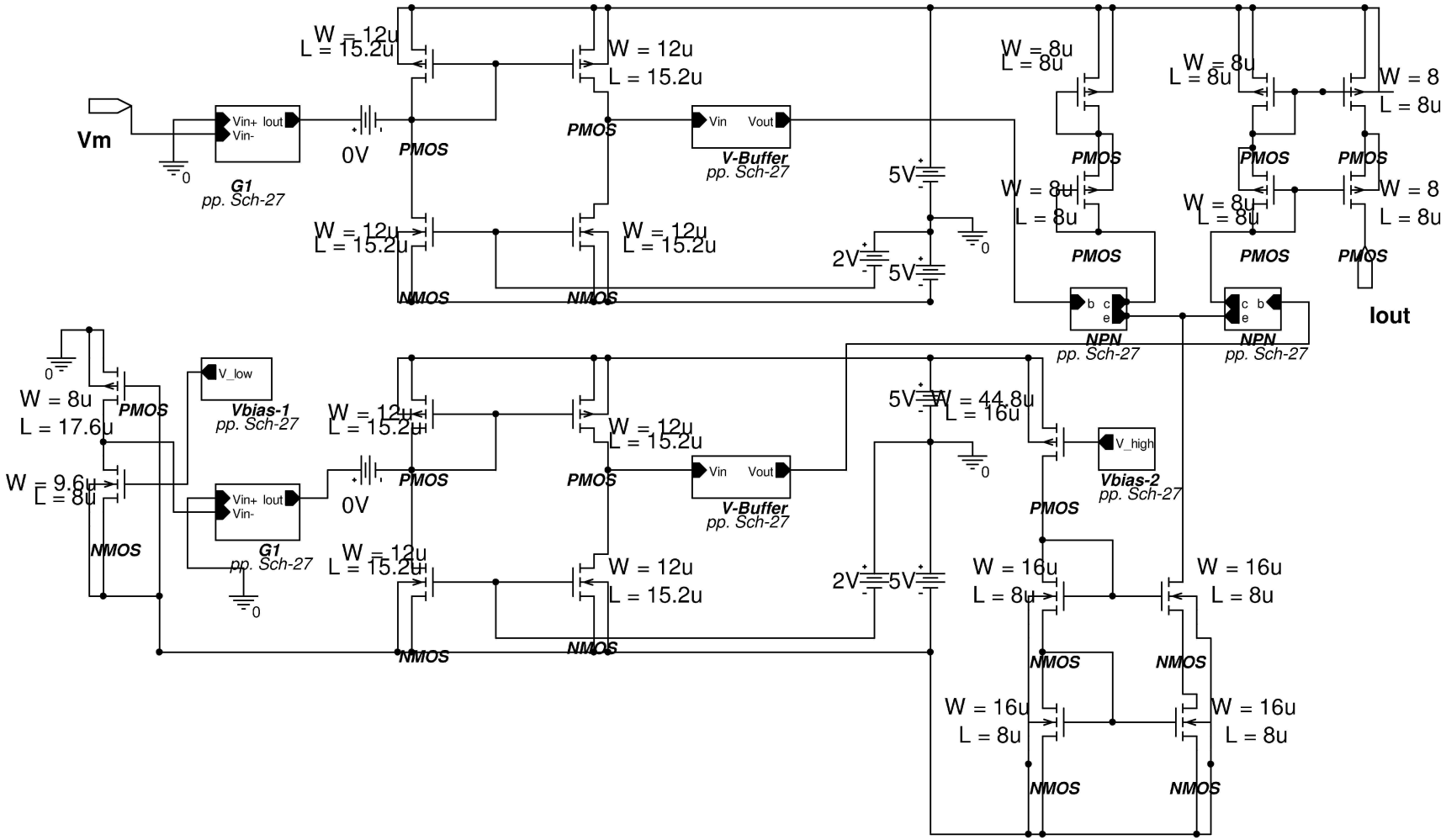

Category	I_{Na}
Description	β_j
Equation	β_j in Table 3.5

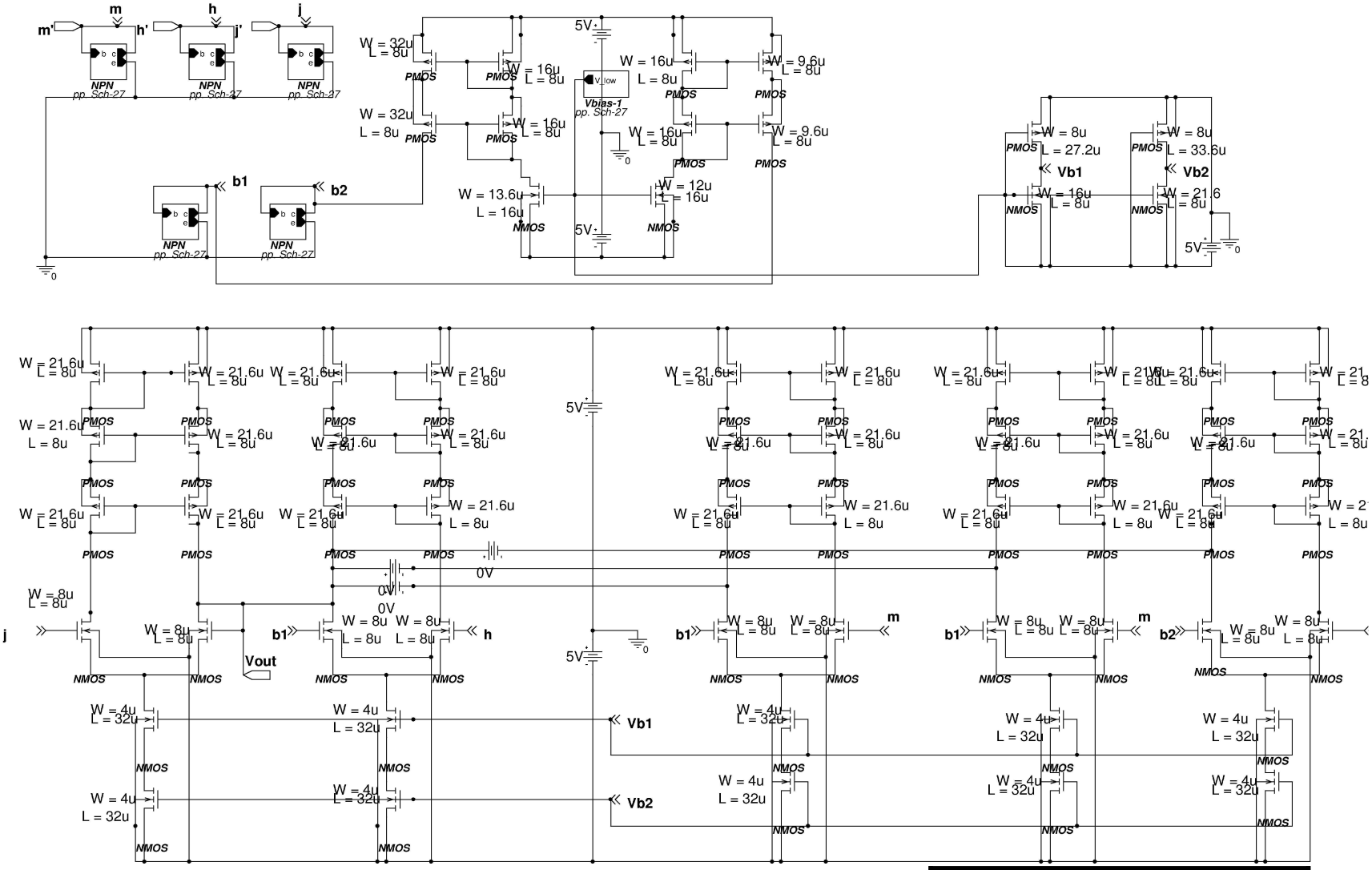

Category	I_{Na}
Description	Multiplier for I_{Na}
Equation	(3.118), Figure 3.30

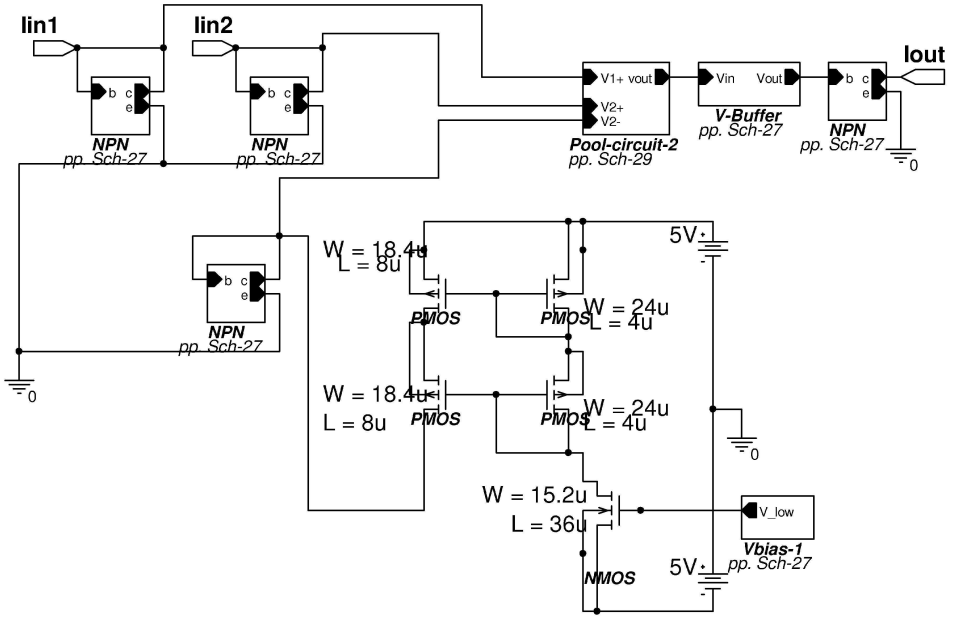

(a)

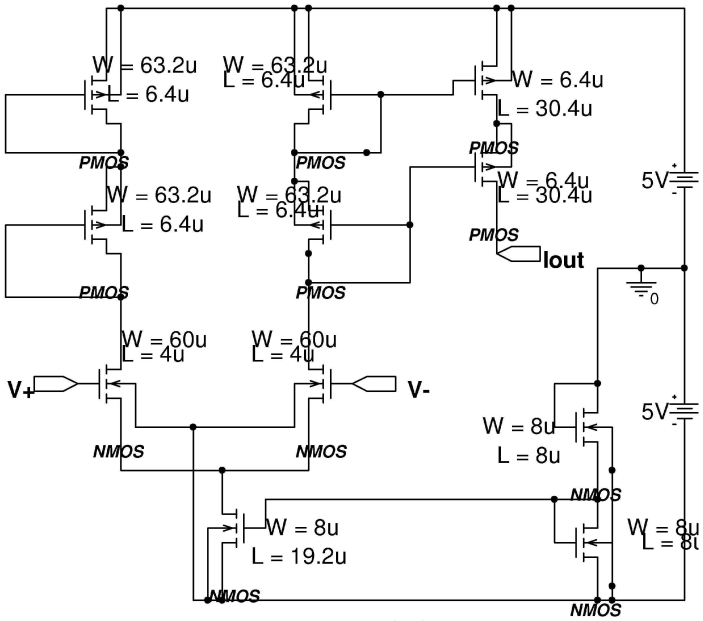

(b)

Category	I_{Na}
Description	(a) 2-Input multiplier for I_{na} (b) V-I converter for I_{Na}
Equation	(3.118)

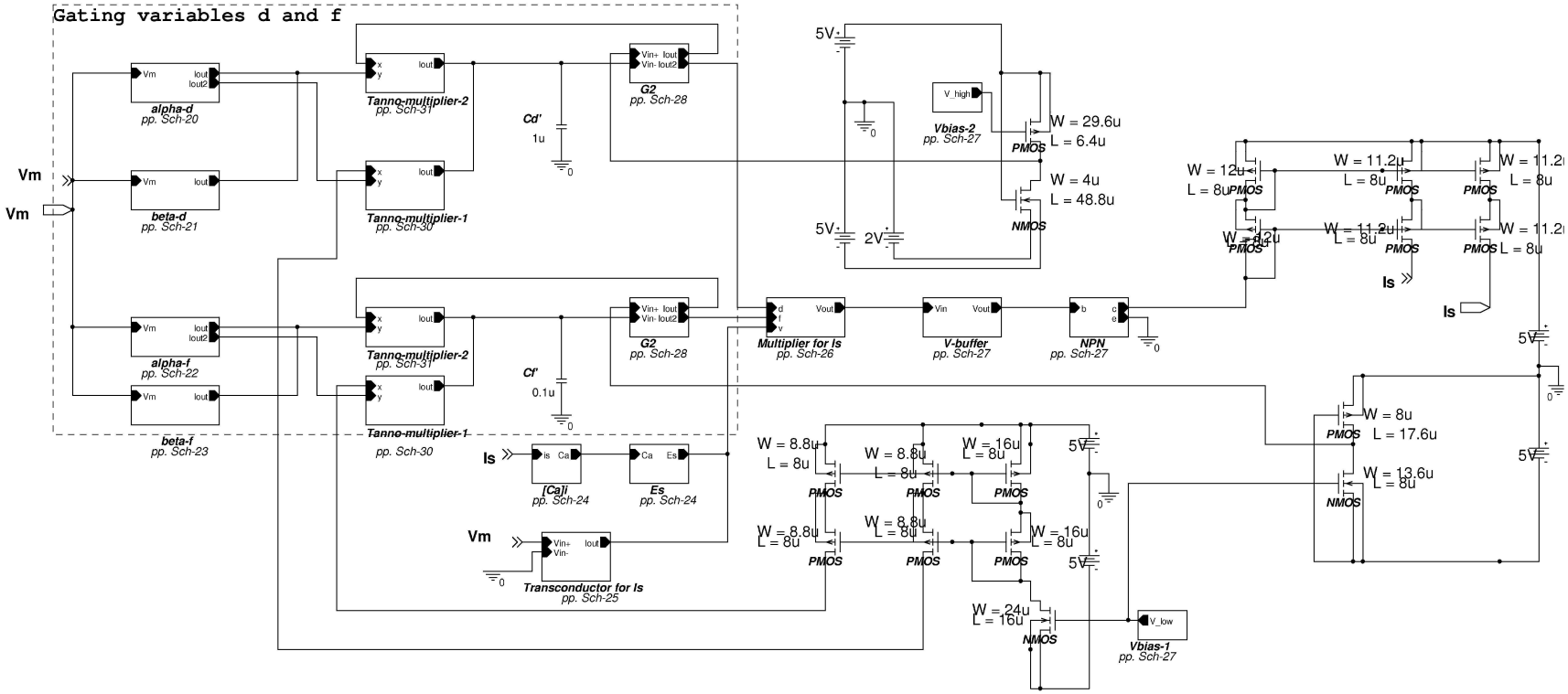

Category	I_S
Description	Top level circuit for I_S
Equation	(3.128)

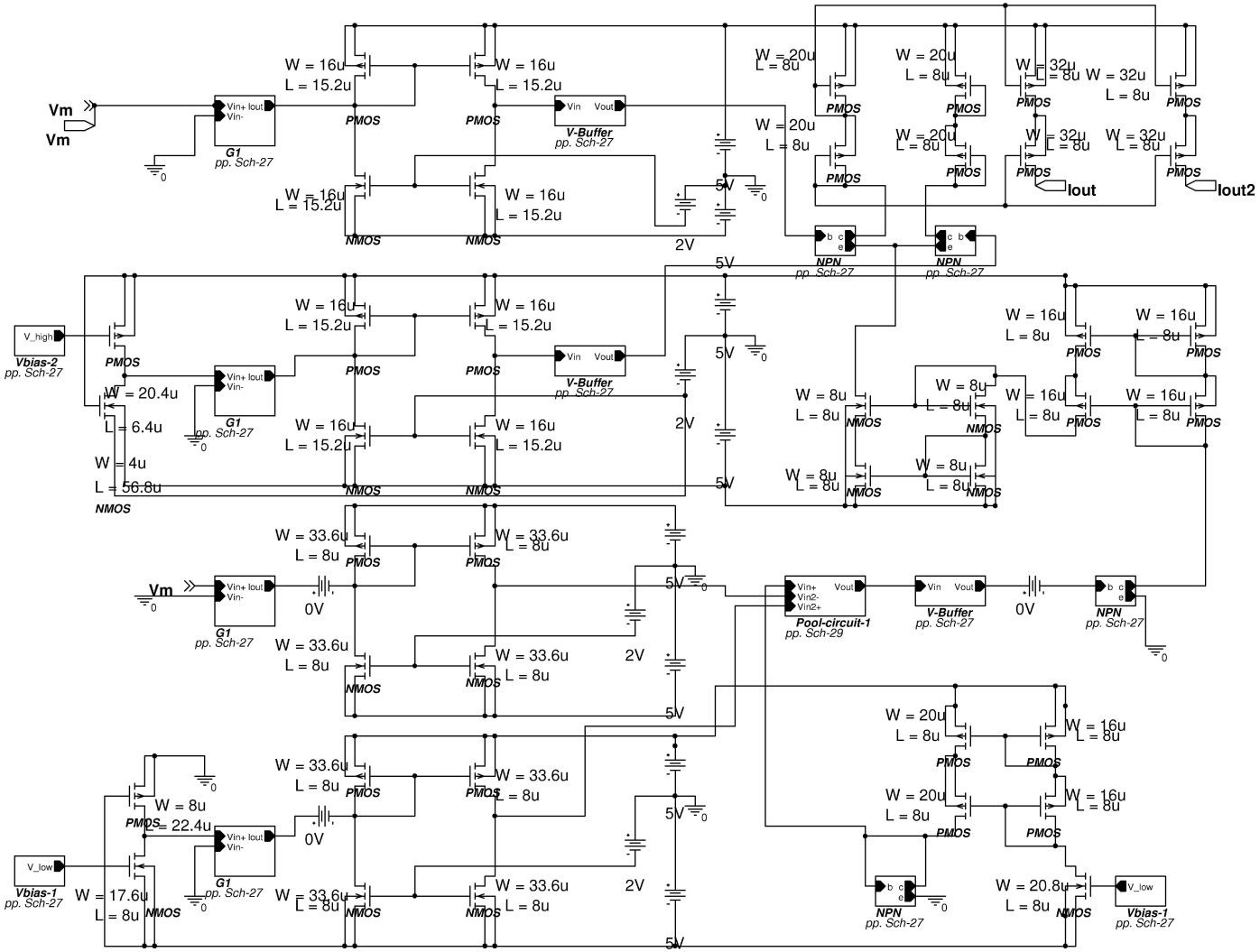

Category	I_S
Description	α_d
Equation	(3.123)

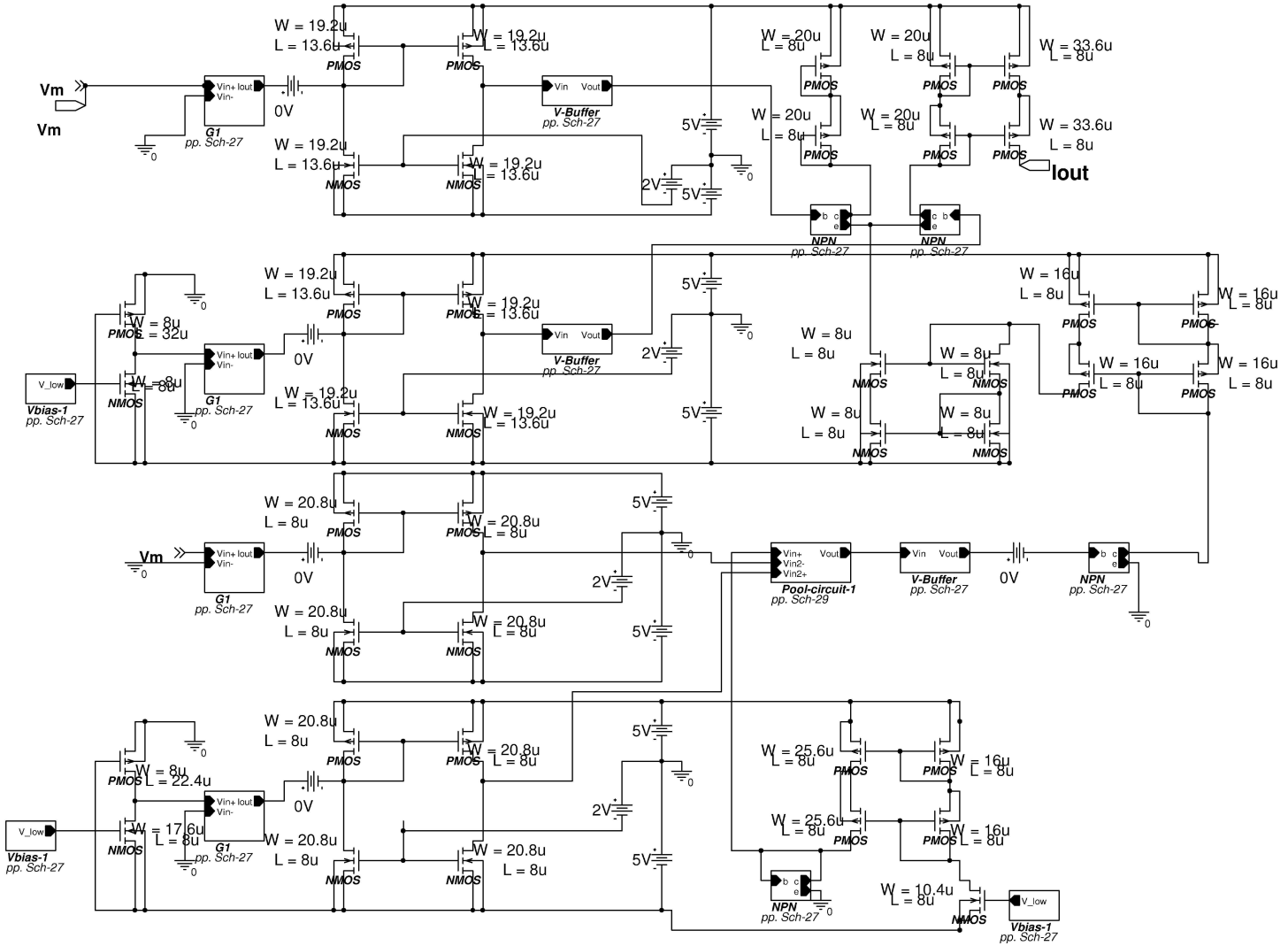

Category	I_s
Description	β_d
Equation	(3.124)

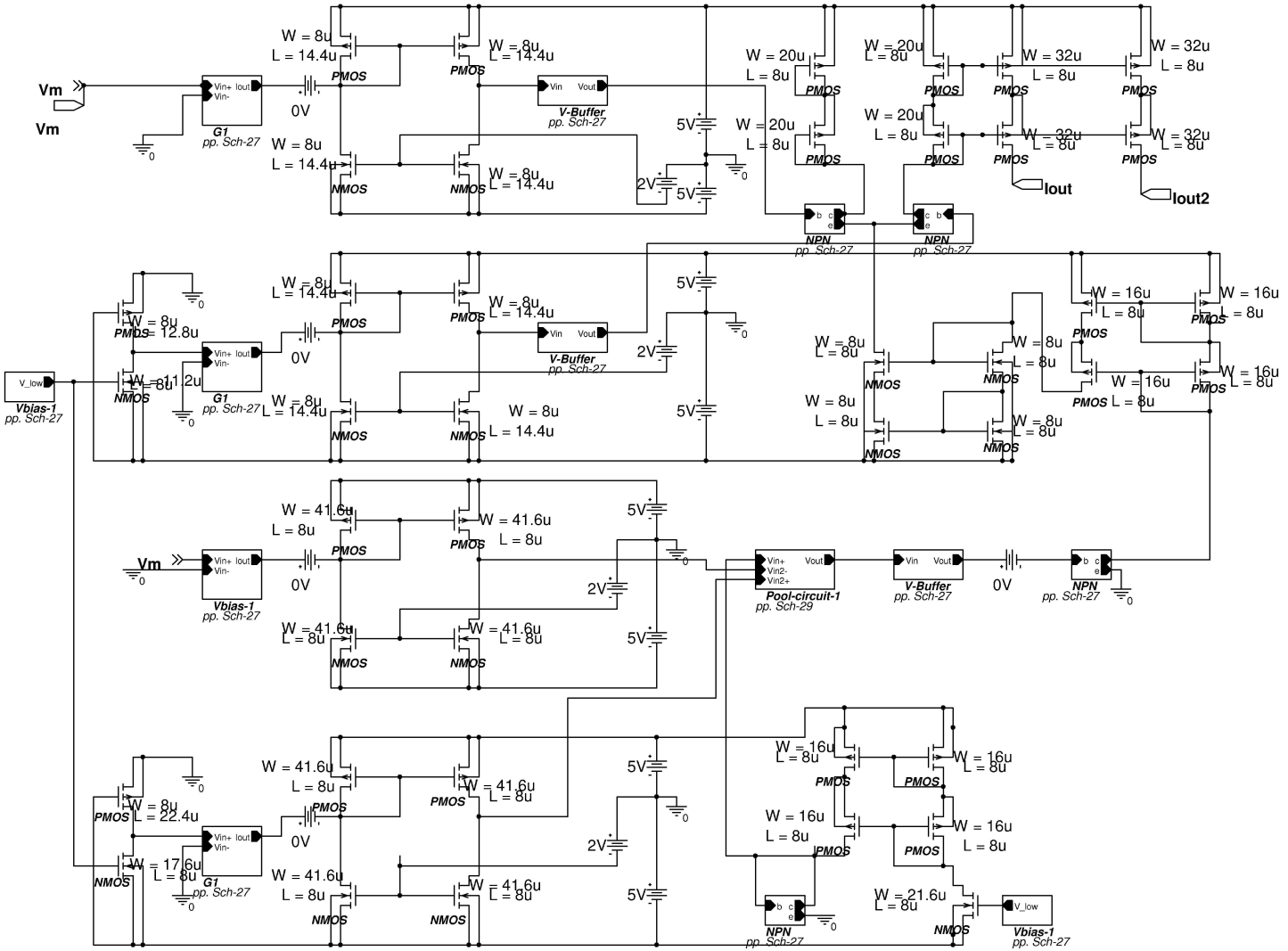

Category	I_S
Description	αf
Equation	(3.126)

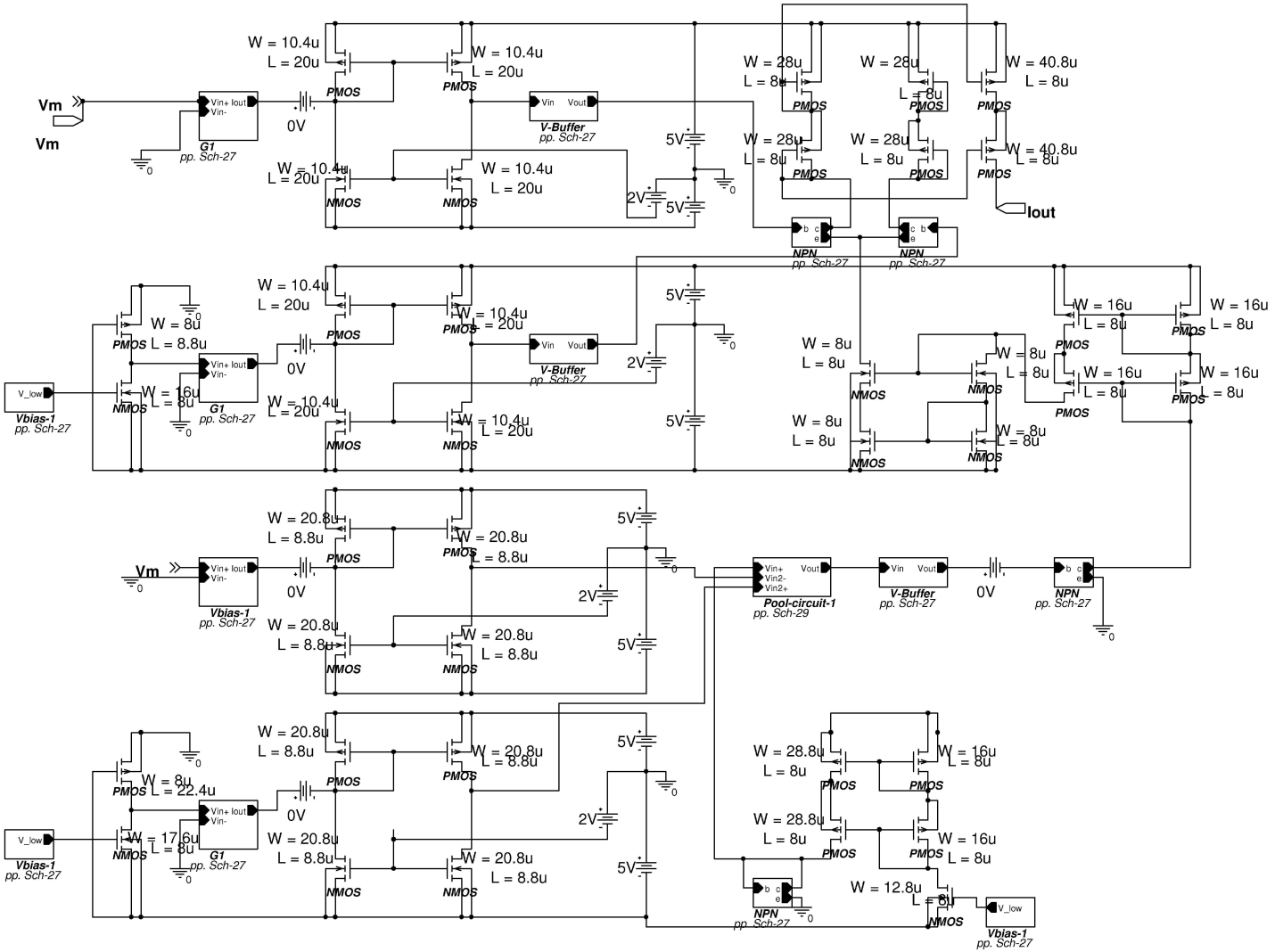

Category	I_S
Description	β_f
Equation	(3.127)

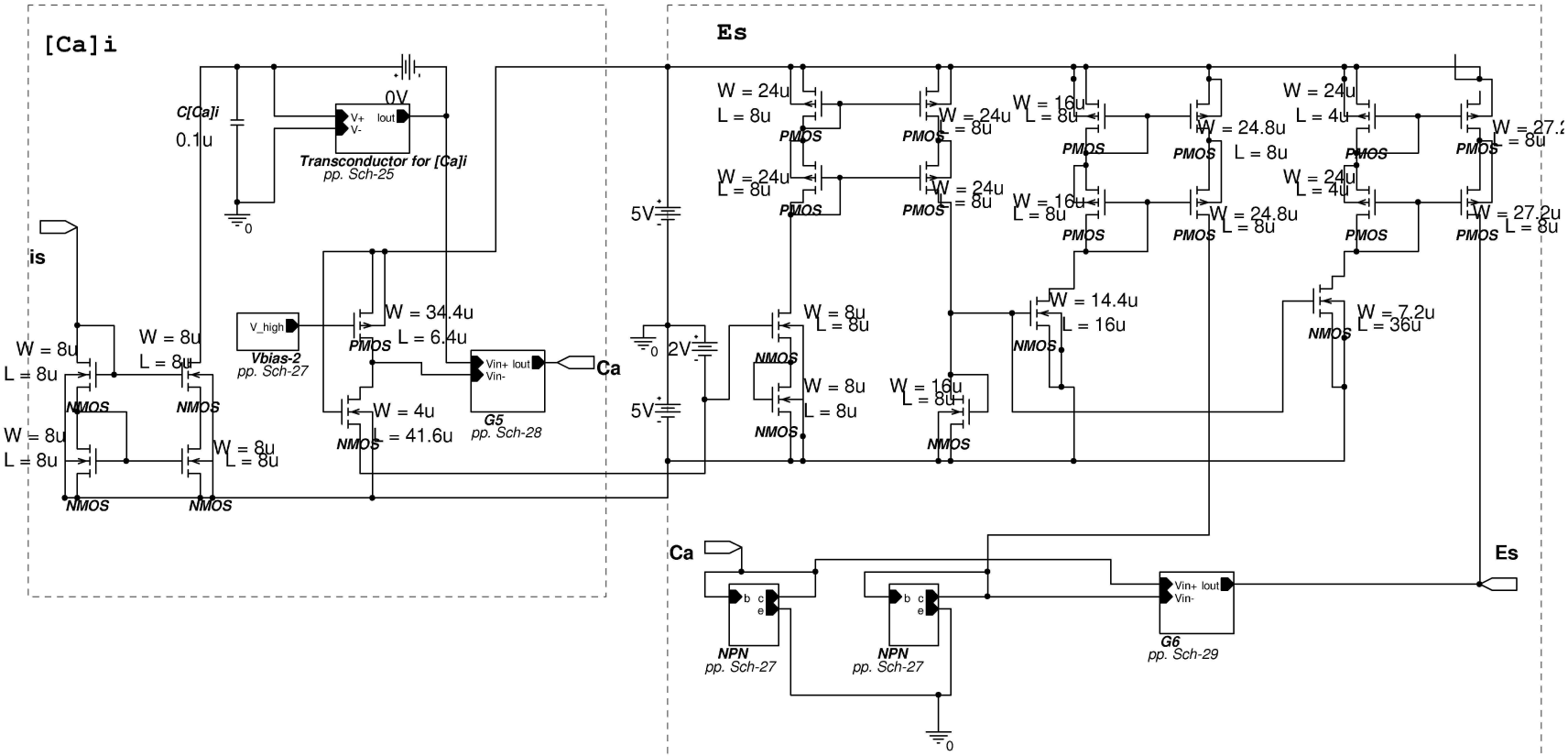

Category	I_s
Description	$[Ca]_i$ and E_s
Equation	(3.129), (3.130)

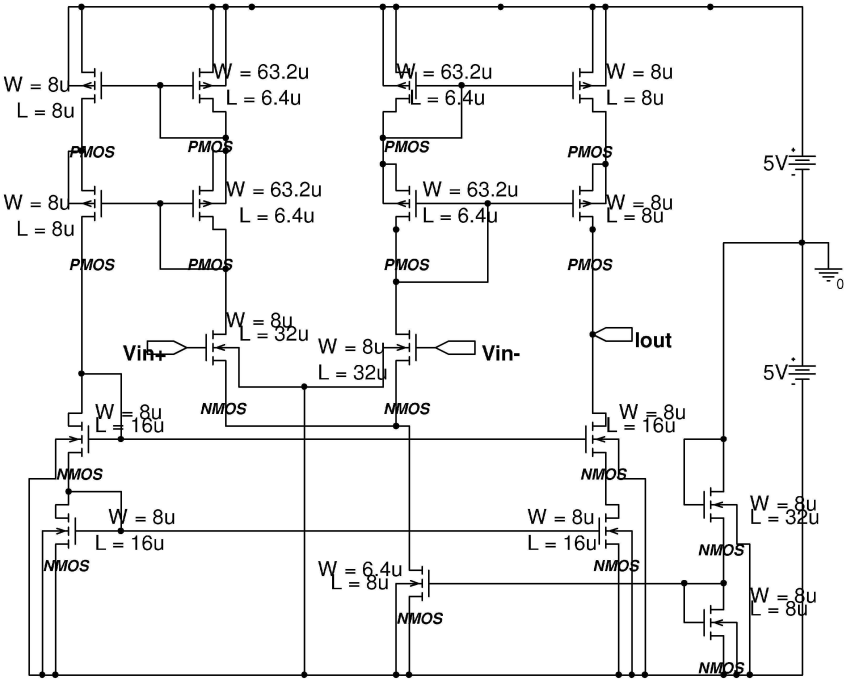

Transconductor for Is

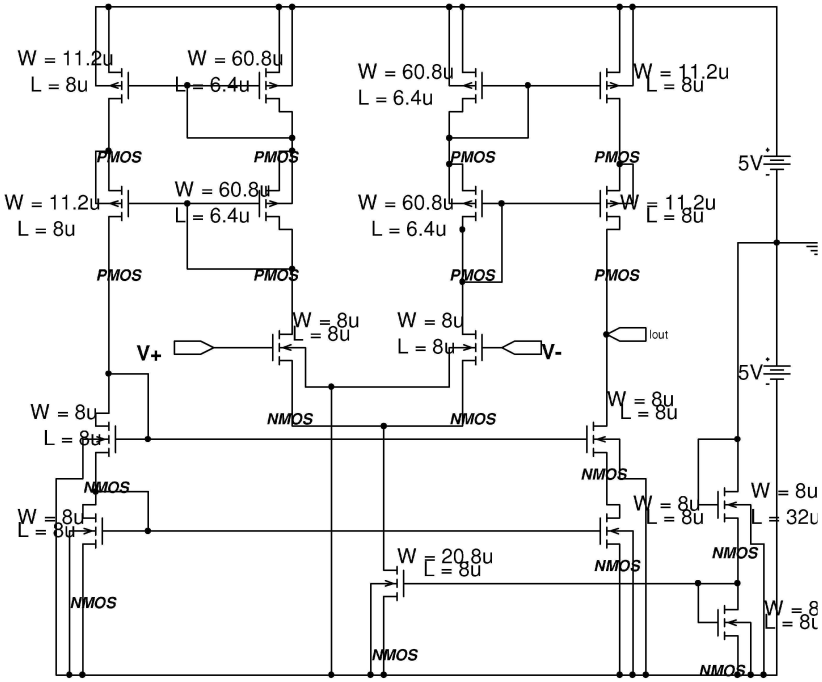

Transconductor for [Ca]i

Category	I_s
Description	Transconductors
Equation	(3.128), (3.130)

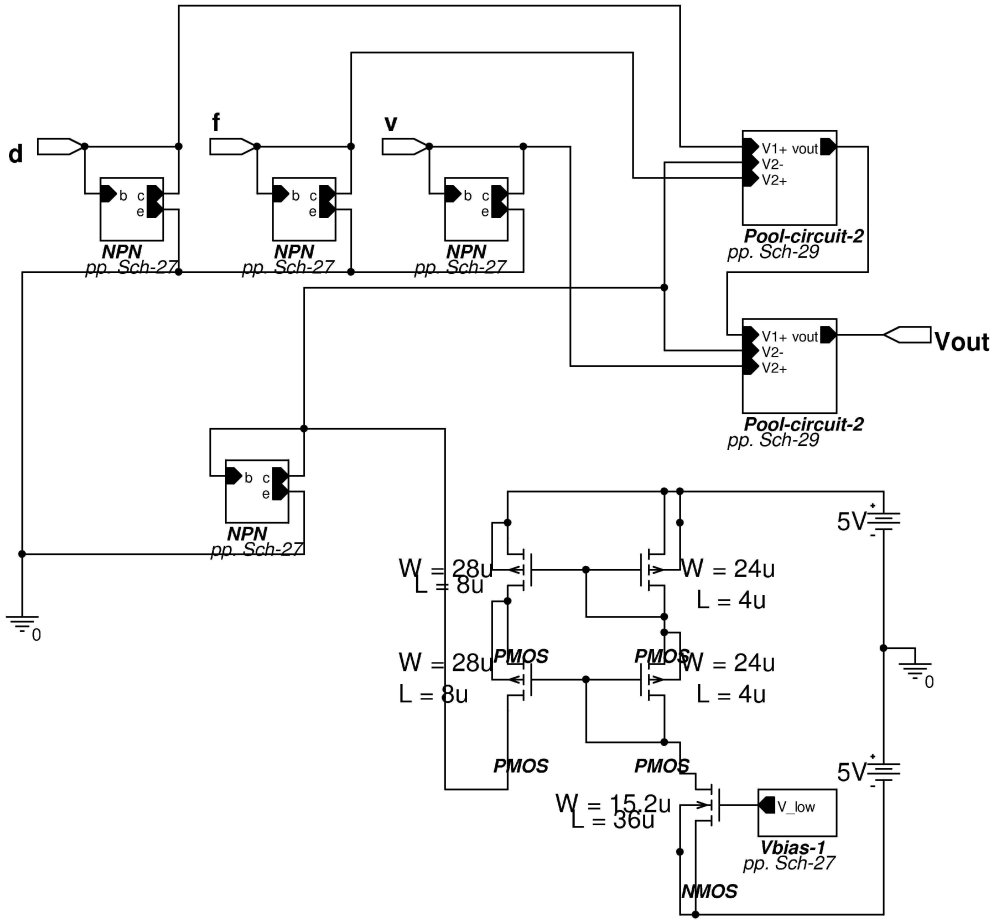

Category	I_S
Description	Multiplier for I_S
Equation	(3.128)

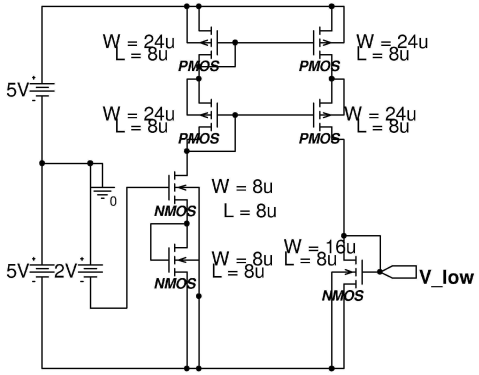

Vbias-1

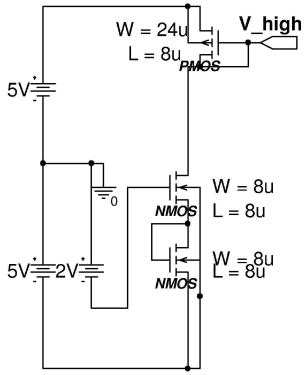

Vbias-2

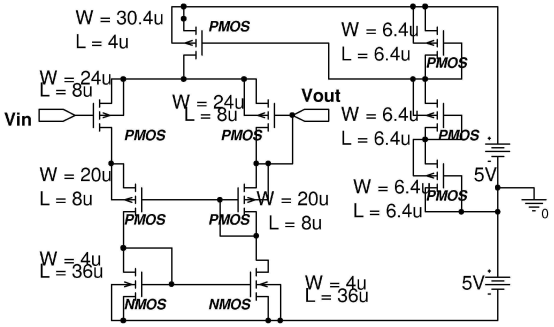

V-Buffer

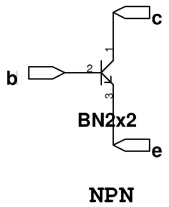

NPN

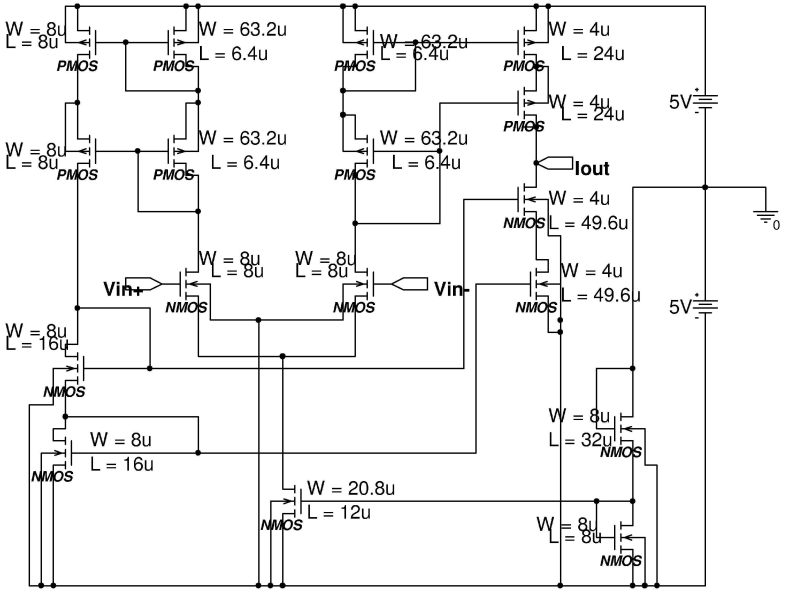

G1

Category	Miscellaneous
Description	Vbias1, Vbias2, V-buffer, NPN, G1

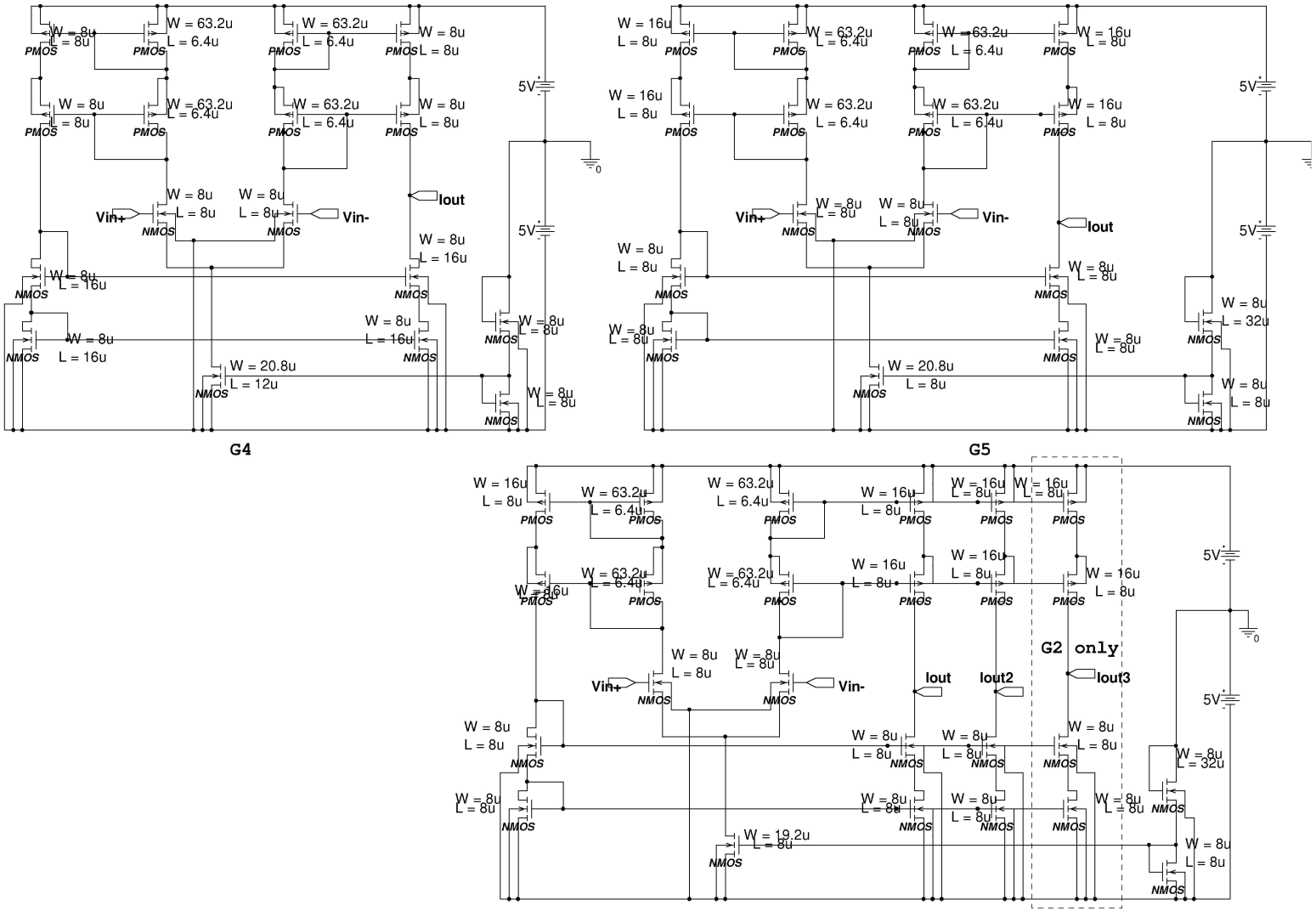

Transconductors: G2 and G3 (Iout3 is for G2 only)

Category	Miscellaneous
Description	G2, G3, G4, G5.

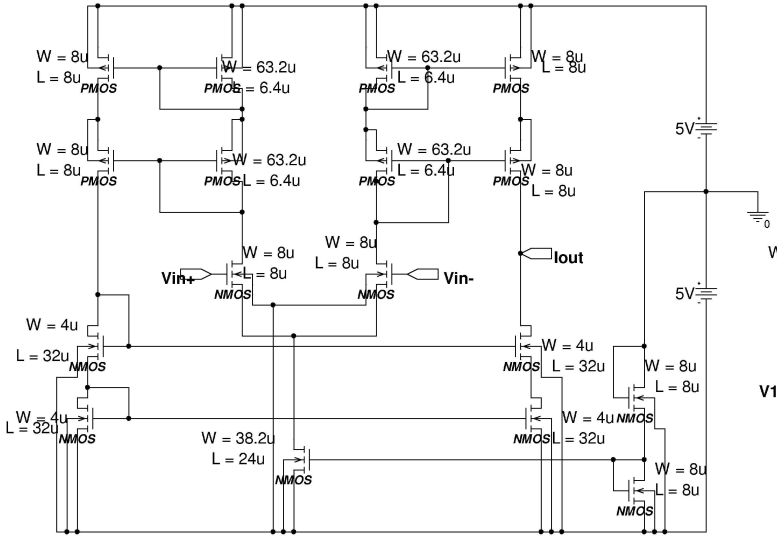

G6

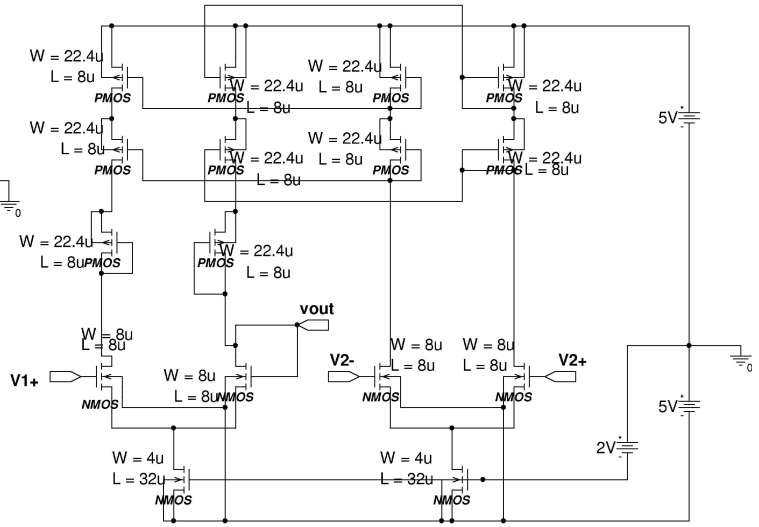

Pool circuit 2

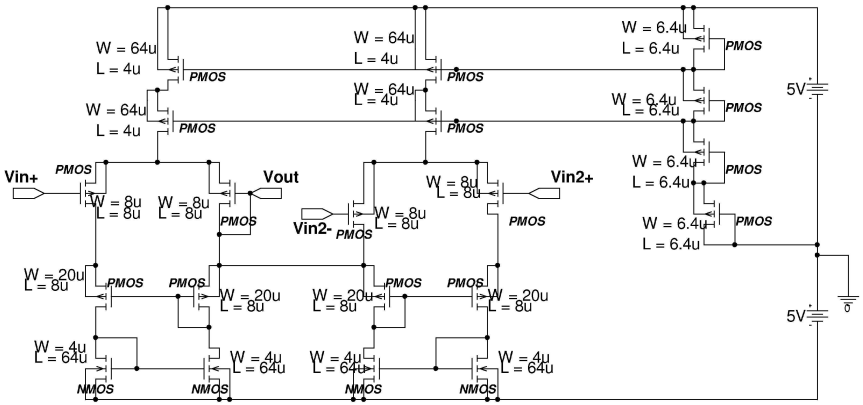

Pool circuit 1

Page Sch-29

Category	Miscellaneous
Description	G6, pool circuit 1 & 2.

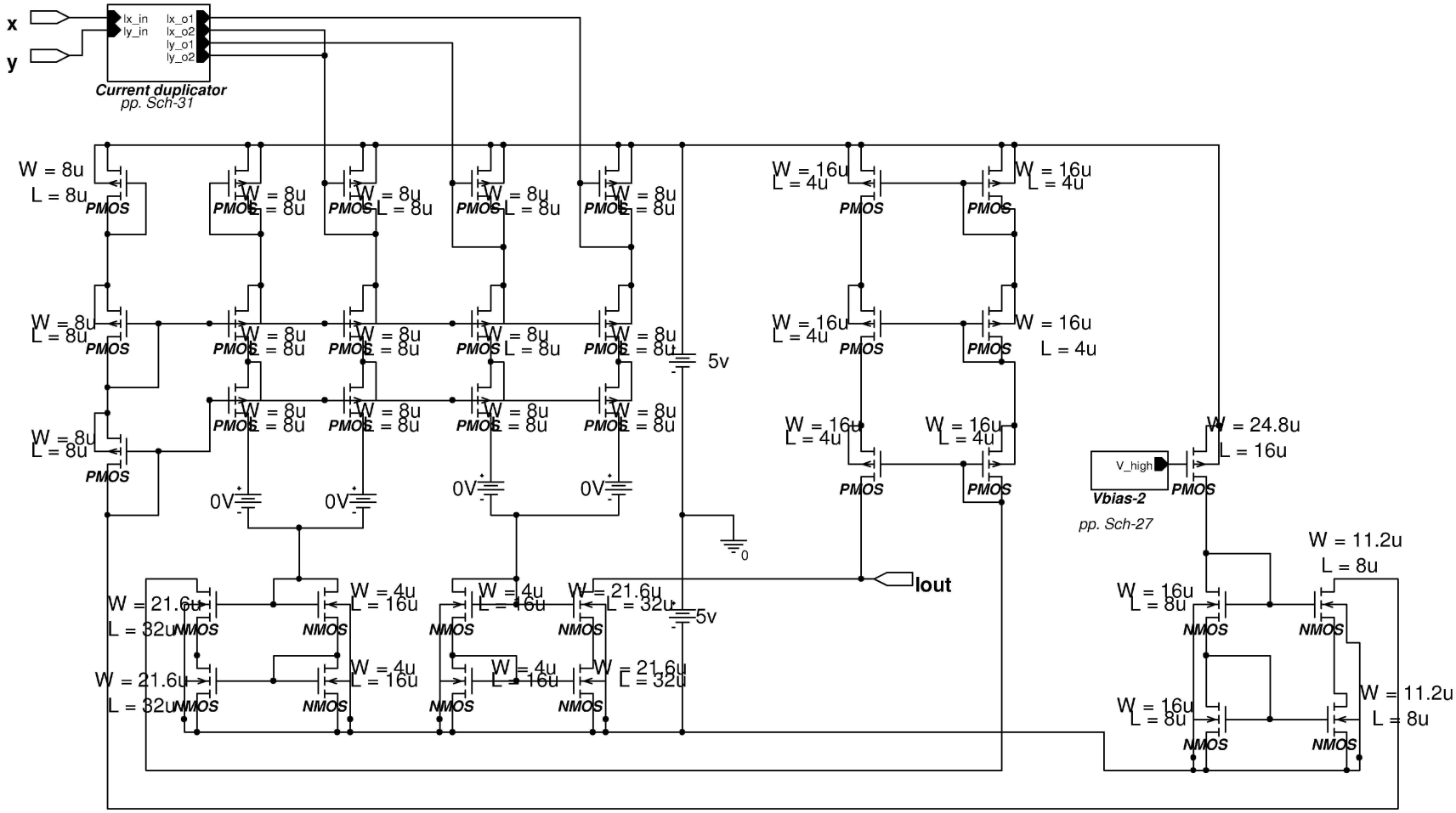

Category	Miscellaneous
Description	Multiplier 1

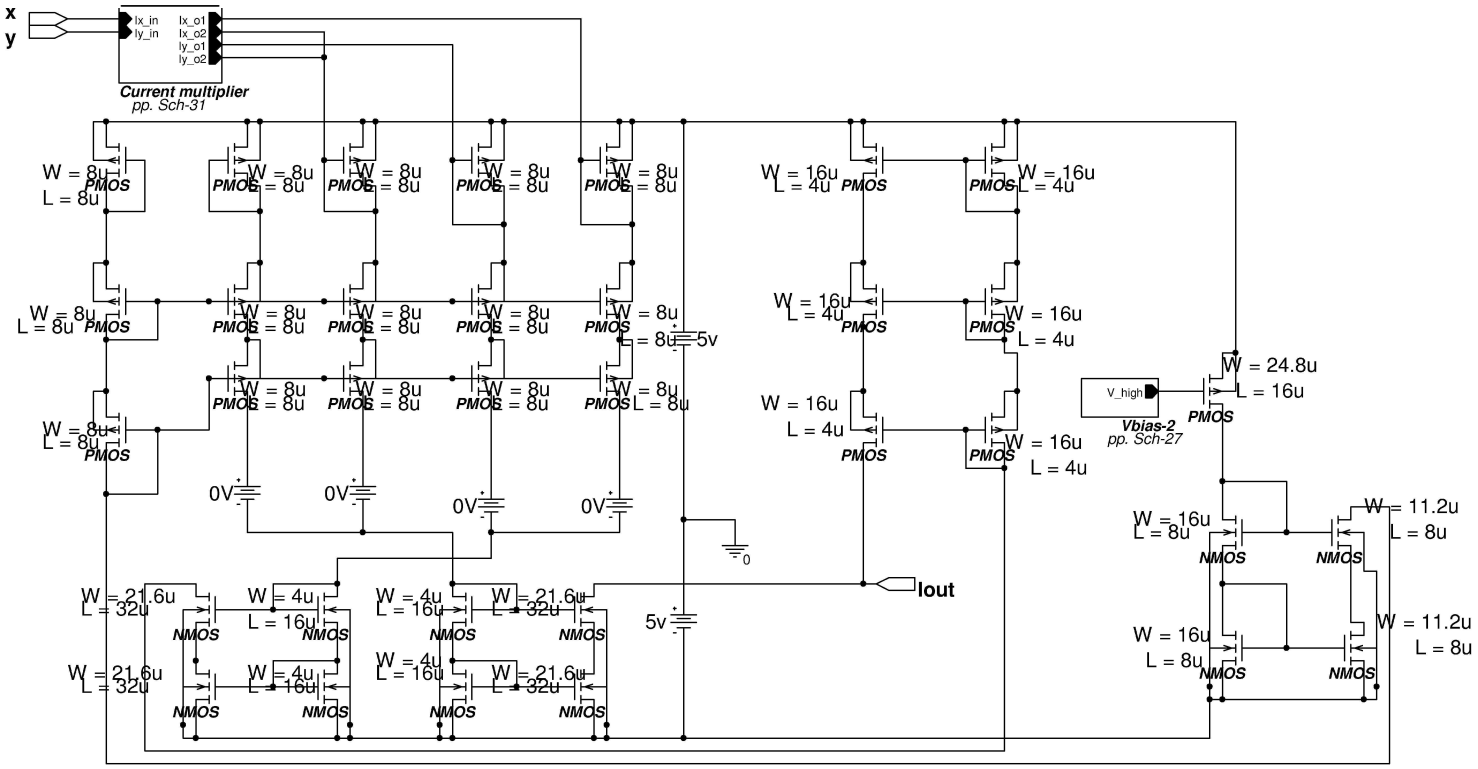

Multiplier 2

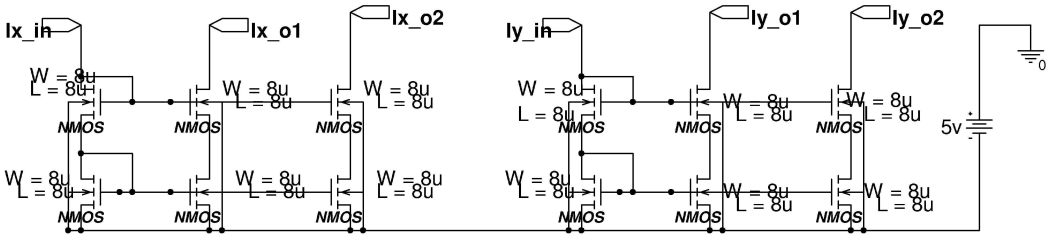

Current duplicator

Category	Miscellaneous
Description	Multiplier 2, current duplicator.

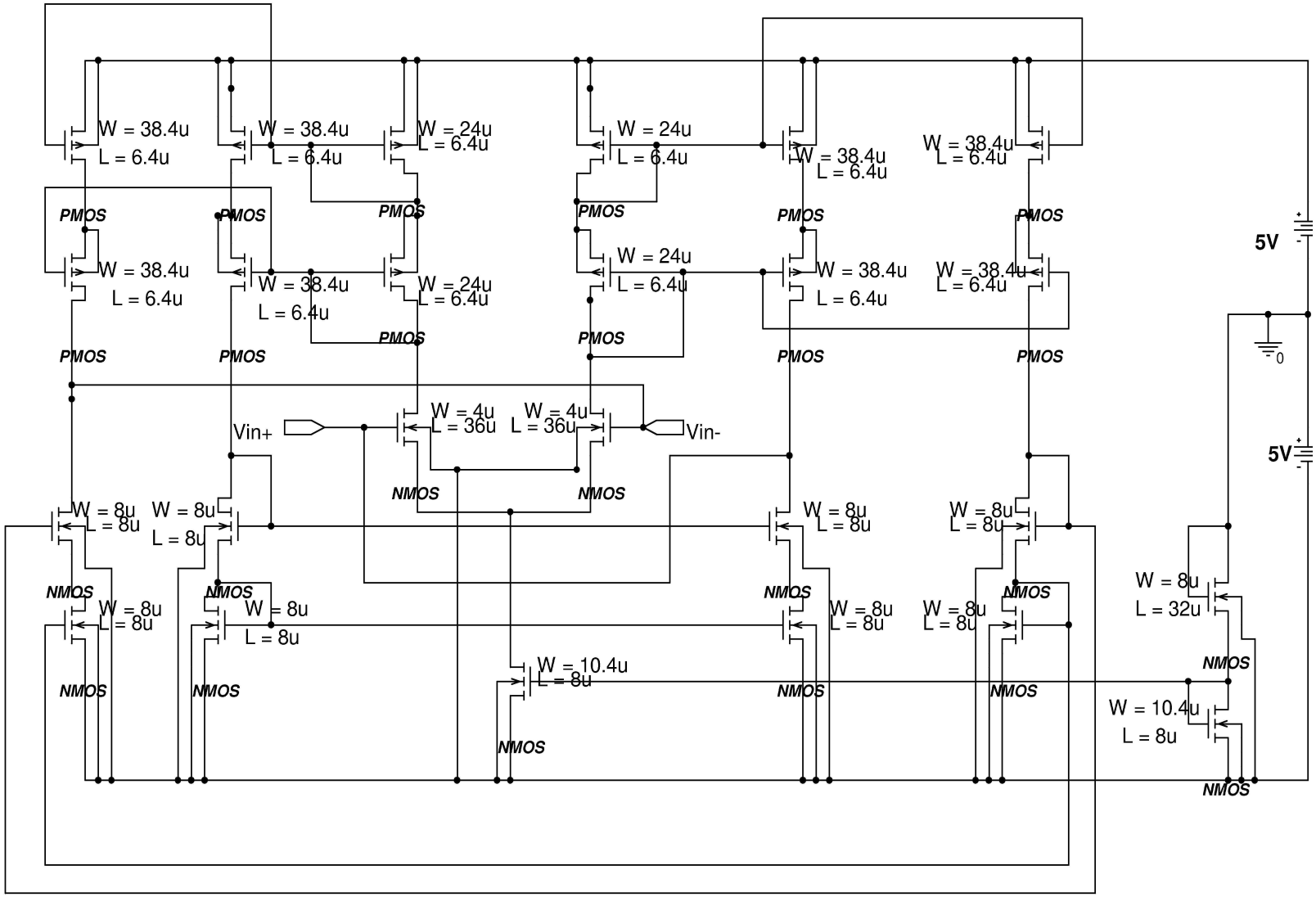

Category	Miscellaneous
Description	Resistor

Appendix B

PSpice Simulation of Anatomical Reentry Using Unidirectional Block

In Appendix B, we present a 1-dimensional circuit that simulates the anatomical reentry phenomena presented in section 4.3.3. The triangular structure of the reentry cardiac tissues, shown in Figure 4.8, is to be modeled by a circuit ring, which is similar to that in Figure 4.5, except the first node and the last node is connected with a special resistor that models a unidirectional block. The simplified diagram of the circuit is illustrated in Figure B.1, where the ring represents a 1-dimensional RC circuit (refer to Figure 4.5) composed of 120 nodes, starting from node #1 at $x = 0, y = 1$, with the node ID number arranged in the increasing order in the direction of anti-clockwise, and #1, #31, #61, and #91 are the four nodes that are on the x or y axis. There is a unidirectional block between node #1 and #120, which blocks the electrical propagation from node #1 to #120 and only allows the passage of signals in the opposite direction. We have presented

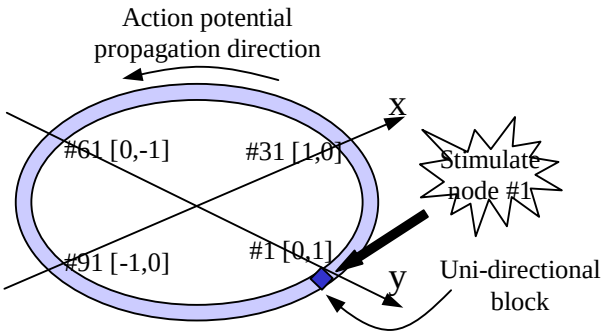

Figure B.1: A circuit ring composed of 120 node for modeling anatomical reentry.

in detail in section 4.3.2 the construction of an RC circuit to model the reaction-diffusion system of the cardiac propagation, and all circuit parameters in the ring circuit follow section 4.3.2, and, thus, we will not repeat the circuit configuration here. In the following discussion, we focus on the introduction of implementing the unidirectional block and show the simulation results of the anatomical reentry.

Constant resistors can be realized with VLSI devices using the differential pair circuit shown in Figure 3.5(b), as introduced in section 3.3.1. On the top of Figure B.2, (a1) depicts a simplified version of the transistor-implemented resistor presented in section 3.3.1, where R_+ and R_- are the two terminals of the equivalent resistor. The block is the differential pair circuit, whose voltage inputs V_+ and V_- and current outputs I_+ and I_- are connected like in Figure B.2 (and Figure 3.5(b)) for a normal resistor. The relation of the resistor currents vs. the difference of the input voltages of the resistor (we call it a *symmetric resistor*) is shown in Figure B.2(a2).

There are two candidate circuits for implementing the unidirectional block, and both are based on a differential circuit. The first candidate is shown in Figure B.2(b1), in which the terminal I_- does not connect to R_- and hence there is no

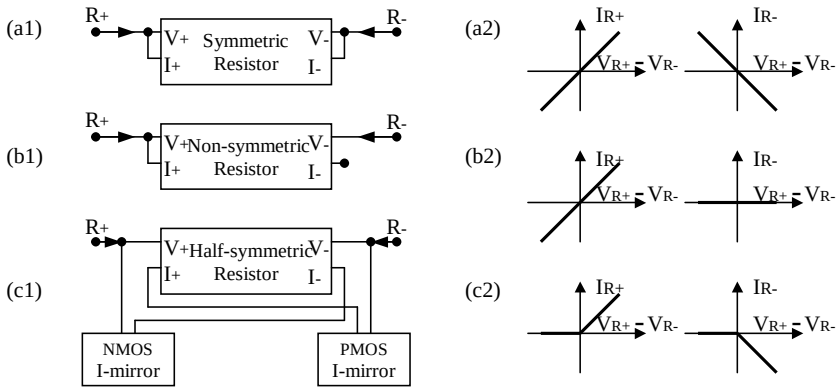

Figure B.2: Implementation of bidirectional and unidirectional resistors using a modified differential pair circuit.

current allowed at the R_- terminal, while the R_+ terminal remains the same as for (a1). Since the I-V properties of the resistor implementation in (b1) is different in two terminals, we call it a *non-symmetric resistor*. This *non-symmetric resistor* does not influence the external circuit connected with R_-, but affects the circuit connected to R_+. Therefore, a signal can pass from R_- to R_+, but not from R_+ to R_-. Figure B.2(c1) shows the second circuit that realizes the unidirectional block, where the currents sourced from I_+ and I_- are "cut" to leave a half of the I-V branch by adding a NMOS and a PMOS current mirror; and this is shown in its I-V curves in Figure B.2(c2). Due to the "halved" I-V properties of this resistor, we call the resister a *half-symmetric resistor*. A *half-symmetric resistor* operates like a normal resistor when $V_+ > V_-$, and when $V_+ < V_-$ it shows no conductivity.

If a *non-symmetric resistor* is employed in our ring circuit, it leads to large re-polarizing current (caused by big voltage difference across the resistor) that rapidly discharges the membrane and distorts the action potential when the cardiac node at one side of the resistor is activated and the node at the other side can not be due to the isolation effect of the *non-symmetric resistor*. Therefore, in

the simulation of the anatomic reentry, we adopt the *half-symmetric resistor* to implement the unidirectional block. Since an excited membrane potential is higher than the resting potential, the properties of the *half-symmetric resistor* necessitate the propagation of the active potential in one direction but not the other. An external stimulus is applied to excite the ring of the 1-dimensional cardiac tissue. It sends a square pulse of current to node #1 at time $t = 10\ ms$, with 2 mA in the amplitude, and 0.1 ms of duration. Ideal components are used to construct all the nodes for saving the longitude simulation time. The simulation results are provided in Figure B.3. At $t = 11\ ms$, shown in Figure B.3(a), the first node is just activated by the stimulus. In (b), at $t = 180\ ms$, the action potential is propagated over about a half of the circle. Note that the propagation is anti-clockwise due to the existence of the unidirectional block between #1 and #120. At $t = 380\ ms$, all nodes on the ring have been activated at lease once, and the action potential is transmitted back to node #1 and creates a reentry wave around there; this is shown in Figure B.3(c). Figure B.3(d) and (e) show that the reentry wave is passed further down to other nodes. The big notch on the voltage potential contour at the positive x and y quarter is due to the shorter duration of the newly reentered action potential (at nodes number ≥ 1) compared to the first action potential of the same node. This results from the not-fully-recovered refractory state of the nodes when the second action potential is activated. This can be seen clearly in Figure B.4, which we will discuss shortly. In Figure B.3(f), at $t = 780\ ms$, a third circulation of the action potential starts. The reentry wave will turn around and around and never stop, and it is responsible for many clinical arrhythmias (disturbances of cardiac rhythm) [26].

Figure B.4 illustrates the membrane potential of node #1 changed by time.

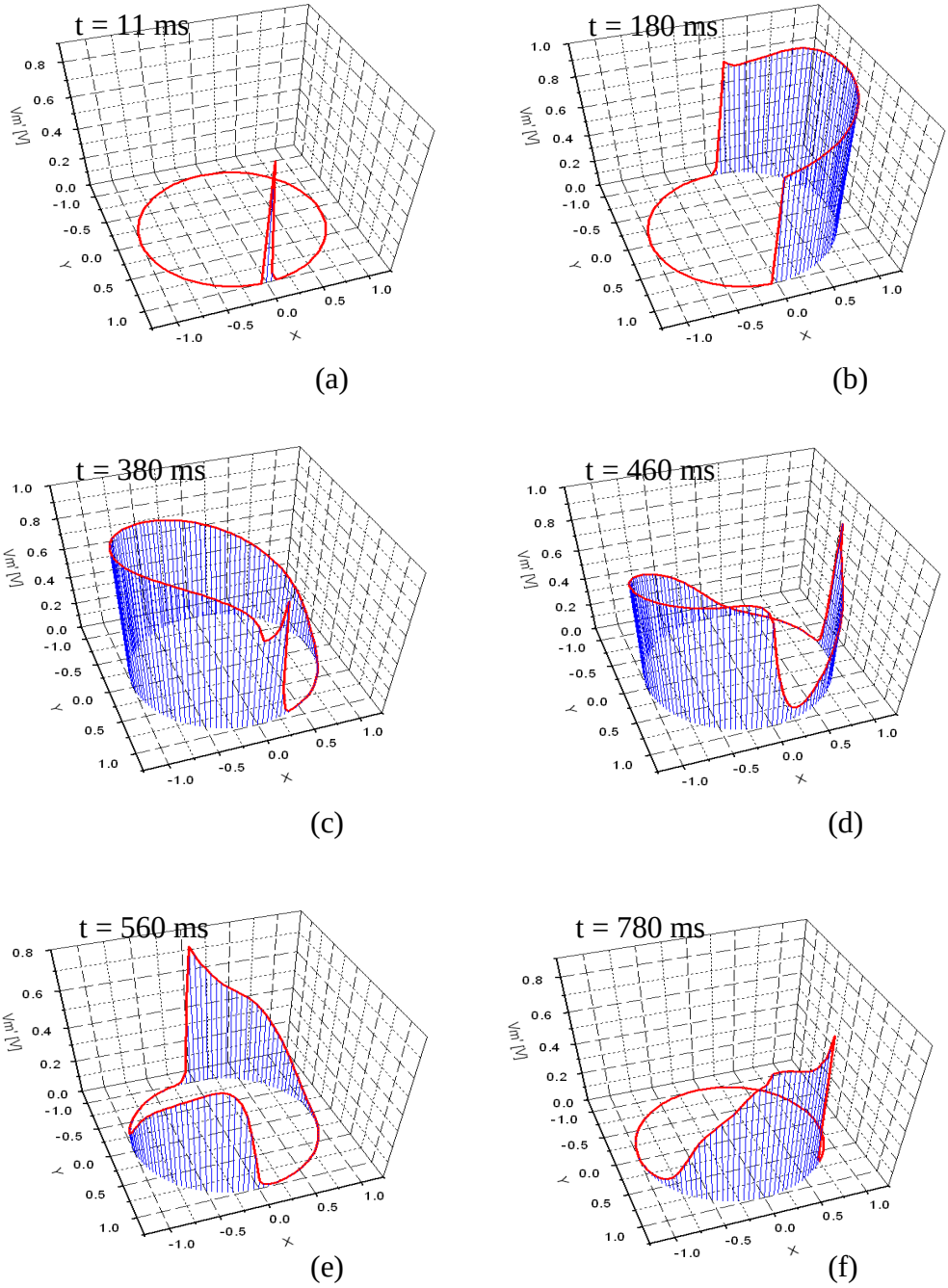

Figure B.3: Reentry wave caused by unidirectional block in 1-dimensional model.

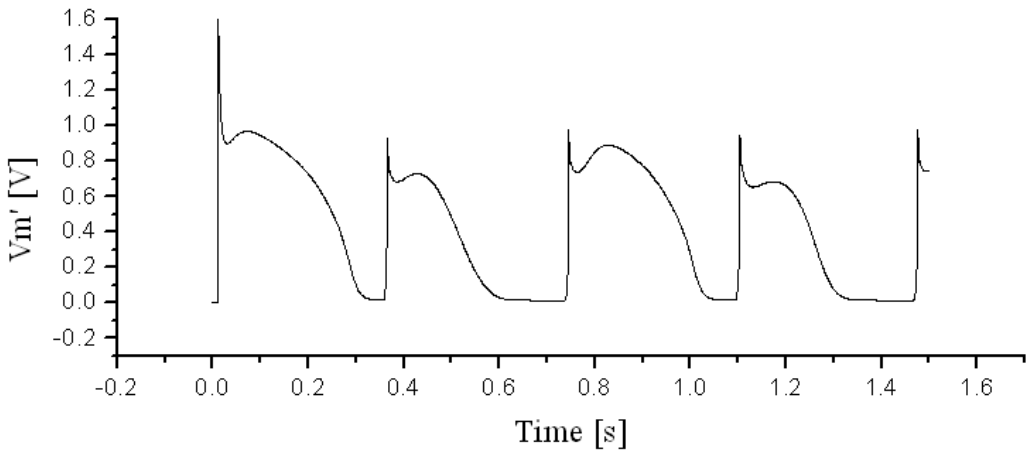

Figure B.4: The time-course of the membrane potential of node #1.

A full action potential is generated at $t = 10\ ms$ when the stimulus sends a current impulse to the node. The second action potential, occurring at about $t = 360\ ms$, is much smaller than the first one due to its activation being too close to the repolarization stage of the first action potential, and consequently its magnitude is degraded by the refractory period of the first action potential. The third action potential is a full action potential again, and it happens at $t = 730\ ms$. The excitation of node #1 will continue on and on, and the shape of each action potential depends on how well the node is recovered from the previous action potential.

BIBLIOGRAPHY

BIBLIOGRAPHY

[1] "Causes of Deaths", $http://www.deardeath.com/causes\_of\_death.htm$.

[2] A. C. Guyton, *Textbook of Medical Physiology*, W. B. Saunders Company, Harcourt Brace Jovanovich, Inc., 8th edition, 1991.

[3] "Heart", $http://www.answers.com/topic/heart-4$.

[4] U.S. Department of Health, Education, and Welfare, *A Handbook of Heart Terms*, U.S. Government Printing Office, May 1964, pp. 42.

[5] F. B. Sachse, *Computational Cardiology: Modeling of Anatomy, Electrophysiology, and Mechanics*, Springer Berlin/Heidelberg, 2004.

[6] J. W. Cain and D. G. Schaeffer, "Two-Term Asymptotic Approximation of a Cardiac Restitution Curve", *SIAM Review*, Vol. 48, No. 3, March 2006, pp. 537-546.

[7] A. L. Hodgkin and A. F. Huxley, "A Quantitative Description of Membrane Current and its Application to Conduction and Excitation in Nerve", *Journal of Physiology*, Vol. 117, No. 4, August 1952, pp. 500-544.

[8] R. A. FitzHugh, "Impulses And Physiological States In Theoretical Models Of Nerve Membrane", *Biophysical Journal*, Vol. 1, No. 4, July 1961, pp. 445-466.

[9] J. Nagumo, S. Animoto, and S. Yoshizawa, "An Active Pulse Transmission Line Simulating Nerve Axon", *Proceedings of the Institute of Radio Engineers*, Vol. 50, No. 10, October 1962, pp. 2061-2070.

[10] B. van der Pol, "On Relaxation Oscillations", *Philosophical Magazine*, Vol. 2, No. 11, July 1926, pp. 978-992.

[11] H. Glaze, "Mathematical Models for Heart Rate Responses to Vagel Nerve Simulation", *Ph.D. Dissertation*, Electrical Engineering Department, Stanford University, 1971.

[12] R. H. Clayton, "Computational Models of Normal and Abnormal Action Potential Propagation in Cardiac Tissue: Linking Experimental and Clinical Cardiology", *Physiological Measurement*, Vol. 22, No. 3, August 2001, pp. 15-34.

[13] D. Noble, "A Modification of the Hodgkin-Huxley Equations Applicable to Purkinje Fibre Action and Pace-maker Potentials", *Journal of Physiology*, Vol. 160, No. 2, February 1962, pp. 317-352.

[14] R. E. McAllister, D. Noble, and R. W. Tsien, "Reconstruction of the Electrical Activity of Cardiac Purkinje Fibres", *Journal of Physiology*, Vol. 251, No. 1, September 1975, pp. 1-59.

[15] G. W. Beeler and H. Reuter, "Reconstruction of the Action Potential of Ventricular Myocardial Fibres", *Journal of Physiology*, Vol. 268, No. 1, June 1977, pp. 177-210.

[16] L. Ebihara and E. A. Johnson, "Fast Sodium Current in Cardiac Muscle: A Quantitative Description", *Biophysical Journal*, Vol. 32, No. 2, November 1980, pp. 779-790.

[17] C. Luo and Y. Rudy, "A Model of the Ventricular Cardiac Action Potential - Depolarisation, Repolarisation and Their Interaction", *Circulation Research*, Vol. 68, No. 6, June 1991, pp. 1501-1526.

[18] C. Luo and Y. Rudy, "A Dynamic Model of the Cardiac Ventricular Action Potential - Simulations of Ionic Currents and Concentration Changes", *Circulation Research*, Vol. 74, No. 6, June 1994, pp. 1071-1097.

[19] D. Noble and Y. Rudy, "Models of Cardiac Ventricular Action Potentials: Iterative Interaction Between Experiment and Simulation", *The Royal Society of London Philosophical Transactions. Series A*, Vol. 359, No. 1783, June 2001, pp. 1127-1142.

[20] O. V. Aslanidi, V. N. Biktashev, M. Chen, R. H. Clayton, A. V. Holden, J. V. Tucker, and H. Zhang, "Computational Biology of Cardiac Arrhythmias: from Basic Science to Clinical Application", *Proceedings of UK e-Science All Hands Meeting*, Nottingham UK, September 2003, pp. 889-896.

[21] L. F. Pavarino and P. C. Franzone, "Parallel Solution of Cardiac Reaction-Diffusion Models", *Proceedings of the 15th International Conference on Domain Decomposition Methods*, Berlin, Germany, July 2003, pp. 669-776.

[22] J. B. Pormann, C. S. Henriquez, J. A. Board (Jr), D. J. Rose, D. M. Harrild, and A. P Henriquez, "Computer Simulations of Cardiac Electrophysiology",

Proceedings of the 2000 ACM/IEEE Conference on Supercomputing, Dallas Texas USA, November 2000, pp. 24.

[23] R. Sarpeshkar, "Analog Versus Digital: Extrapolating from Electronics to Neurobiology", *Neural Computation*, Vol. 10, No. 7, October 1998, pp. 1601-1638.

[24] M. R. Boyett, A. Clough, J. Dekanski, and A. V. Holden, "Modelling Cardiac Excitation and Excitability", *Computational Biology of the Heart*, John Wiley & Sons, chapter 1, March 1997, pp. 1-46.

[25] S. P. Ellner and J. Guckenheimer, "Membrane Channels and Action Potentials", *Dynamic Models in Biology*, Princeton University Press, chapter 3, March 2006, pp. 71-106.

[26] R. M. Berne, M. N. Levy, B. M. Koeppen, and B. A. Stanton, *Physiology*, Mosby, Inc., 4th edition, 1998.

[27] "Ventricular Action Potential", $http://www.answer.com/topic/ventricular-action-potential$.

[28] F. Bezanilla, "The Voltage Sensor in Voltage-Dependent Ion Channels", *Physiological Reviews*, Vol. 80, No. 2, April 2000, pp. 555-592.

[29] E. C. Cooper and L. Y. Jan, "Ion Channel Genes and Human Neurological Disease: Recent Progress, Prospects, and Challenges", *Proceedings of the National Academy of Sciences*, Vol. 96, No. 9, April 1999, pp. 4759-4766.

[30] "Ion Channel", $http://en.wikipedia.org/wiki/Ion\_channel$.

[31] J. Malmivuo and R. Plonsey, "The Heart", *Bioelectromagnetism*, Oxford University Press, New York, 1995, pp. 119-130.

[32] D. DiFrancesco and D. Noble, "A Model of Cardiac Electrical Activity Incorporating Ionic Pumps and Concentration Changes", *The Royal Society of London Philosophical Transactions. Series B*, Vol. 307, No. 1133, January 1985, pp. 353-398.

[33] R. J. Ramirez, S. Nattel, and M. Courtemanche, "Mathematical Analysis of Canine Atrial Action Potentials: Rate, Regional Factors, and Electrical Remodeling", *American Journal of Physiology - Heart and Circulatory Physiology*, Vol. 279, No. 4, October 2000, pp. 1767-1785.

[34] H. Zhang, A. V. Holden, I. Kodama, H. Honjo, M. Lei, T. Varghese, and M. R. Boyett, "Mathematical Models of Action Potentials in the Periphery and Center of the Rabbit Sinoatrial Node", *American Journal of Physiology - Heart and Circulatory Physiology*, Vol. 279, No. 1, July 2000, pp. 397-421.

[35] K. H. W. J. ten Tusscher, D. Noble, P. J. Noble, and A. V. Panfilov, "A Model for Human Ventricular Tissue", *American Journal of Physiology - Heart and Circulatory Physiology*, Vol. 286, No. 4, 2004, pp. 1573-1589.

[36] C. S. Henriquez and A. A. Papazoglou, "Using Computer Models to Understand the Roles of Tissue Structure and Membrane Dynamics in Arrhythmogenesis", *Proceedings of the IEEE*, Vol. 84, No. 3, March 1996, pp. 334-354.

[37] N. F. Otani, "Computer Modeling in Cardiac Electrophysiology", *Journal of Computational Physics*, Vol. 161, No. 1, June 2000, pp. 21-34.

[38] O. Blanc, "A Computer Model of Human Atrial Arrhythmial", *http* : *//ltswww.epfl.ch/pub_files/blanc/thesis_*2537*.pdf*, 2002.

[39] H. Lodish, A. Berk, S. L. Zipursky, P. Matsudaira, D. Baltimore, and J. Darnell, "Transport Across Cell Membranes", *Molecular Cell Biology* W.H. Freeman & Company; 4th edition, October 1999.

[40] A. Hernndez-Cruz, M. Daz-Muoz, M. Gmez-Chavarn, R. Canedo-Merino, D. A. Protti, A. L. Escobar, J. Sierralta, and B. A. Surez-Isla, "Properties of the Ryanodine-sensitive Release Channels that Underlie Caffeine-induced Ca2+ Mobilization from Intracellular Stores in Mammalian Sympathetic Neurons", *European Journal of Neuroscience* , Vol. 7, No. 8, August 1995, pp. 1684-1699.

[41] M. R. Guevara, "Dynamics of excitable cells", *Nonlinear Dynamics in Physiology and Medicine*, Springer-Verlag, New York, chapter 4, January 2003, pp. 87-121.

[42] A. L. Hodgkin and A. F. Huxley, "Currents Carried by Sodium and Potassium Ions through the Membrane of the Giant Axon of Loligo", *Journal of Physiology*, Vol. 116, No. 4, April 1952, pp. 449-472.

[43] M. J. Ackermann and D. E. Clapham, "Ion Channels - Basic Science and Clinical Disease", *New England Journal of Medicine*, Vol. 336, No. 22, May 1997, pp. 1562-1567.

[44] S. S. Demir, J. W. Clark, C. R. Murphey, and W. R. Giles, "A Mathematical Model of a Rabbit Sinoatrial Node Cell", *American Journal of Physiology*, Vol. 266, No. 3, March 1994, pp. 832-852.

[45] L. Priebe and D. J. Beuckelmann, "Simulation Study of Cellular Electric Properties in Heart Failure", *Circulation Research*, Vol. 82, No. 11, June 1998, pp. 1206-1223.

[46] A. F. Strassberg and L. J. DeFelice, "Limitations of the Hodgkin-Huxley Formalism: Effects of Single Channel Kinetics on Transmembrane Voltage Dynamics", *Neural Computation*, Vol. 5, No. 6, November 1993, pp. 843-855.

[47] H. Reuter, "Divalent Cations as Charge Carriers in Excitable Membranes", *Progress in biophysics & Molecular Biology*, Vol.26, 1973, pp. 1-43.

[48] H. Reuter and H. Scholz, "A Study of the Ion Selectivity and the Kinetic Properties of the Calcium-Dependent Slow Inward Current in Mammalian Cardiac Muscle", *Journal of Physiology*, Vol.264, No. 1, January 1977, pp. 17-47.

[49] J. B. Bassingthwaighte and H. Reuter, "Calcium Movements and Excitation Contraction Coupling in Cardiac Cells", *Electrical Phenomena in the Heart*, Academic Press New York NY, 1972, pp. 353-395.

[50] "Numerical Analysis", $http://en.wikipedia.org/wiki/Numerical\_analysis$.

[51] K. Ravindran, K. Ramarao, E. Vidal, and M. Ismail, "Compact Low Voltage Four Quadrant CMOS Current Multiplier", *Electronics Letter*, Vol. 37, No. 24, November 2001, pp. 1428-1429.

[52] O. Oliaei and P. Loumeau, "Four-quadrant class AB CMOS current multiplier", *Electronics Letter*, Vol. 32, No. 25, December 1996, pp. 2327-2329.

[53] R. J. Wiegerink, "A CMOS Four-Quadrant Analog Current Multiplier", *1991 IEEE International Symposium on Circuits and Systems*, Vol. 4, Singapore, June 1991, pp. 2244-2247.

[54] K. Tanno, O. Ishizuka, and Z. Tang, "Four-quadrant CMOS Current-mode Multiplier Independent of Device Parameters", *Circuits and Systems II: Analog and Digital Signal Processing, IEEE Transactions on*, Vol. 47, No. 5, May 2000, pp. 473-477.

[55] B. Maundy and M. Maini, "A Comparison of Three Multipliers Based on the V_{gs}^2 Technique for Low-voltage Applications", *IEEE Transactions on Circuits and Systems I: Fundamental Theory and Applications*, Vol. 50, No. 7, July 2003, pp. 937-940.

[56] G. Han and E. Sanchez-Sinencio, "CMOS Transconductance Multipliers: a Tutorial", *Circuits and Systems II: Analog and Digital Signal Processing, IEEE Transactions on*, Vol. 45, No. 12, December 1998, pp. 1550-1563.

[57] S. Liu and C. Chang, "CMOS Analog Divider and Four-Quadrant Multiplier Using Pool Circuits", *Solid-State Circuits, IEEE Journal of*, Vol. 30, No. 9, September 1995, pp. 1025-1029.

[58] W. Gai, H. Chen, and E. Seevinck, "Quadratic-Translinear CMOS Multiplier-Divider Circuit", *Electronics Letters*, Vol. 33, No. 10, May 1997, pp. 860-861.

[59] A. Cichocki and R. Unbehauen, "New Analogue Four-Quadrant Voltage Divider", *Electronics Letters*, Vol. 26, No. 19, September 1990, pp. 1580-1582.

[60] A. Motamed, C. Hwang, and M. Ismail, "CMOS Exponential Current-to-Voltage Converter", *Electronics Letters*, Vol. 33, No. 12, June 1997, pp. 998-1000.

[61] Q. Duong, T. K. Nguyen, and S. Lee, "CMOS Exponential Current-to-Voltage Circuit Based on Newly Proposed Approximation Method", *Proceedings of the 2004 International Symposium on Circuits and Systems*, Vol. 2, May 2004, pp. 865-868.

[62] "Curve Fitting Toolbox", *http : //www.mathworks.com/access/helpdesk/help/toolbox/curvefit/index.html?/access/helpdesk/help/toolbox/curvefit/cftool.html*.

[63] L. Wang, Y. Jiang, and R. W. Newcomb, "A Current Based VLSI Degree-Two Chaos Generator", *Chaos in Circuits and Systems*, World Scientific Series on Nonlinear Science, Series B, Vol. 11, 2002.

[64] C. Wang and J. Wang, "Design of Linear Transimpedance Amplifiers", *Proceedings. 4th International Conference on ASIC 2001*, Shanghai, China, October 2001, pp. 232-235.

[65] I. Mucha, "Low-output-impedance CMOS Voltage Buffer", *Electronics Letters*, Vol. 28, No. 22, October, 1992.

[66] M. Neag and O. McCarthy, "Low-output-impedance CMOS Voltage Buffer", *Semiconductor Conference, 1998. CAS '98 Proceedings. 1998 International*, Vol. 1, Sinaia, Romania, October, 1998, pp. 175-180.

[67] S. W. Tsay and R. W. Newcomb, "A Neuro-type Pool Arithmetic Unit", *Proceedings of IEEE ISCAS 1991*, 1991, Singapore, pp. 2518-2521.

[68] R. Lee, "Measures of Correlation for Waveform Data in Clinical Research", *http : //biomech.brighton.ac.uk/help/cmc/*.

[69] R. E. McAllister and D. Noble, "The Time and Voltage Dependence of the Slow Outward Current in Cardiac Purkinje Fibres", *Journal of Physiology*, Vol. 186, No. 3, October 1966, pp. 632-662.

[70] G. W. Beeler and H. Reuter, "Membrane Calcium Current in Ventricular Myocardium Fibres", *Journal of Physiology*, Vol.207, No. 1, March 1970, pp. 191-209.

[71] H. Reuter, "Localization of Beta Adrenergic Receptors and Effects of Noradrenaline and Cyclic Nucleotides on Action Potentials, Ionic Currents and Tension in Mammalian Cardiac Muscle.", *Journal of Physiology*, Vol. 242, No. 2, October 1974, pp. 429-451.

[72] L. S. Gettes and H. Reuter, "Slow Recovery from Inactivation of Inward Currents in Mammalian Myocardial Fibres", *Journal of Physiology*, Vol. 240, No. 3, Augest 1974, pp. 703-724.

[73] W. Trautwein, T. F. Mcdonald, and O. Tripathi, "Calcium Conductance and Tension in Mammalian Ventricular Muscle.", *Pflgers Archiv European Journal of Physiology*, Vol. 354, No. 1, March 1975, pp. 55-74.

[74] G. A. Rincon-Mora, "Active Capacitor Multiplier in Miller-Compensated Circuits", *IEEE Transactions on Solid-State Circuits*, Vol. 35, No. 1, January 2000, pp. 26-32.

[75] Y. Tang, M. Ismil, and S. Bibyk, "Active Miller Capacitor Multiplier for Compact On-chip PLL Filter", *IEEE Electronics Letters*, Vol. 39, No. 1, January 2003, pp. 43-45.

[76] C. J. Chang and K. H. Chen, "Bidirectional Current-Mode Capacitor Multiplier in DC-DC Converter Compensation", *Proceedings of the Fifth International Workshop on System-on-Chip for Real-Time Applications*, Alberta Canada, July 2005, pp. 111-116.

[77] Y. Tsividis, *Operation and Modeling of the MOS Transistor*, 2nd edition, McGraw-Hill, 1999.

[78] Q. Zhang, J. J. Liou, J. R. McMacken, J. Thomson, and P. Layman, "SPICE Modeling and Quick Estimation of MOSFET Mismatch Based on BSIM3 Model and Parametric Tests", *IEEE Journal of Solid-State Circuits*, Vol. 36, No. 10, October 2001, pp. 1592-1595.

[79] O. S. Unsal, J. W. Tschanz, K. Bowman, V. De, X. Vera, A. Gonzalez, and O. Ergin, "Impact of Parameter Variations on Circuits and Microarchitecture", *IEEE Micro*, Vol. 26, No. 6, November/December 2006, pp. 30-39.

[80] H. Onodera, "Variability: Modeling and Its Impact on Design ", *IEIE Transactions on Electronics*, Vol. E89-C, No. 3, March 2006, pp. 342-348.

[81] "Wafer Electrical Test Data and SPICE Model Parameters AMIS ABN (1.50 micron)", $http://www.mosis.com/Technical/Testdata/ami-abn-prm.html$.

[82] L. Clerc, "Directional Difference of Impulse Spread in Trabecular Muscle from Mammalian Heart", *Journal of Physiology*, vol. 255, No. 2, February 1976, pp. 335-346.

[83] A. V. Holden and A. V. Panfilov, "Modelling Propagation in Excitable Media", *Computational Biology of the Heart*, John Wiley & Sons, chapter 3, March 1997, pp. 65-100.

[84] A. N. Kolmogorov, I. G. Petrovskii, and N. S. Piskunov, "A Study of the Diffusion Equation with Increase in the Amount of Substance, and Its Application to a Biological Problem", *Selected Works of A. N. Kolmogorov*, Kluwer Academic Publishers, 1991, pp. 242-270.

[85] C. V. Pao, "Nonlinear Parabolic and Elliptic Equations", *Plenum Press*, New York, 1992, pp. 214-219.

[86] A. M. Turing, "The Chemical Basis of Morphogenesis", *The Royal Society of London Philosophical Transactions. Series B*, Vol. 237, No. 641, August 1952, pp. 37-72.

[87] Y. B. Pesin and A. A. Yurchenko, "Some Physical Models of the Reaction-Diffusion Equation, and Coupled Map Lattices", *Russian Mathematical Surveys*, Vol. 59, No. 3, 2004, pp. 481-513.

[88] I. R. Epstein and J. A. Pojman, "An Introduction to Nonlinear Chemical Dynamics", *Oxford University Press*, 1998, pp. 347-348.

[89] R. C. Barr, R. Plonsey, and C. R. Johnson, "Membrane Current from Transmembrane Potentials in Complex Core-conductor Models", *IEEE Transactions on Biomedical Engineering*, Vol. 50, No. 4, April 2003, pp. 405-411.

[90] M. S. Spach, "The Discontinuous Nature of Electrical Propagation in Cardiac Muscle", *Journal Annals of Biomedical Engineering*, Vol. 11, No. 3, May 1984, pp. 208-261.

[91] W. Thomson (Lord Kelvin), "On the Theory of the electric Telegraph", *The Proceeding of the Royal Society of London*, Vol. 7, 1854/1855, pp. 382-399.

[92] J. Clark and R. Plonsey, "A Mathematical Evaluation of the Core Conductor Model", *Biophysical Journal*, Vol. 6, No. 1, January 1966, pp. 95-112.

[93] B. Chen, "Mathematical Models of Motion Detection in the Fly's Visual Cortex", *http : //etd.lib.ttu.edu/theses/available/etd − 11152005 − 114857/unrestricted/Chen_Baili_diss.pdf*, Mathematical Department, Texas Tech University, December 2005.

[94] I. R. Efimov, "Cardiac Bioelectricity: Imaging and Electrotherapy", *http* : *//efimov.wustl.edu/class/BME*140/*handout.pdf*, Department of Biomedical Engineering, Washington University, September 2005.

[95] A. G. Kleber and Y. Rudy, "Basic Mechanisms of Cardiac Impulse Propagation and Associated Arrhythmias", *Physiological Reviews*, Vol. 84, No. 2, April 2004, pp. 431-488.

[96] N. F. Hooke, "Efficient Simulation of Action Potential Propagation in a Bidomain", Department of Computer Science, Duke University, September 1992.

[97] N. Sperelakis and L. Ramasamy, "Modeling Electric Field Transfer of Excitation at Cell Junctions", *IEEE Engineering in Medicine and Biology*, Vol. 21, No. 6, November-December 2002, pp. 130-143.

[98] E. Entcheva and F. J. Claydon, "A Discrete Model of the Dynamic Behavior of the Cardiac Muscle", *Computers in Cardiology (1996 IEEE Conference on Computers in Cardiology)*, Indianapolis USA, September 1996, pp. 609-612s.

[99] A. P. Henriquez, R. Vogel, B. J. Muller-Borer, C. S. Henriquez, R. Weingart, and W. E. Cascio, "Influence of Dynamic Gap Junction Resistance on Impulse Propagation in Ventricular Myocardium: A Computer Simulation Study", *Biophysical Journal*, Vol. 81, No. 4, October 2001, pp. 2112-2121.

[100] J. Wu and D. P. Zipes, "Effects Of Spatial Segmentation In The Continuous Model Of Excitation Propagation In Cardiac Muscle", *Journal of Cardiovascular Electrophysiology*, vol. 10, No. 7, 1999, pp. 965-972.

[101] A. M. Pertsov, "Three-Dimensional Organization of Reentry in Fibrillating Ventricular Wall", *Computer Simulation and Experimental Assessment of Cardiac Electrophysiology*, Blackwell Publishing, 1st edition, New York, July 2001, pp. 63-68.

[102] M. C. Trudel, R. M. Gulrajani, and L. J. Leon, "Simulation of Propagation in a Realistic-Geometry Computer Heart Model with Parallel Processing", *IEEE 2001 Proceedings of the 23rd Annual EMBS International Conference, October 25-28, Istanbul, Turkey*, October 2001, pp. 359-362.

[103] P. C. Franzone, P. Deuflhard, B. Erdmann, J. Lang, and L. F. Pavarino, "Adaptivity in Space and Time for Reaction-Diffusion Systems in Electrocardiology", *SIAM Journal on Scientific Computing* , Vol. 28, No. 3, March 2006, pp. 942-962.

[104] O. H. Schmitt, "An electrical theory of nerve impulse propagation", *The American Journal of Physiology*, Vol. 119, No. 2, June 1937, pp. 399-400.

[105] J. Nagumo, S. Yoshizawa, and S. Arimoto, "Bistable Transmission Lines", *IEEE Transactions on Circuit Theory*, Vol. CT-12, No. 3, September 1965, pp. 400-412.

[106] M. R. Roussel, "Reaction Diffusion Equations", $http://people.uleth.ca/\sim roussel/nld/Turing.pdf$.

[107] S. P. Ellner and J. Guckenheimer, "Spatial Patterns in Biology", *Dynamic Models in Biology*, Princeton University Press, chapter 7, March 2006, pp. 217-242.

[108] M. A. Bray and J. P. Wikswo, "Examination of Optical Depth Effects on Fluorescence Imaging of Cardiac Propagation", *Biophysical Journal*, Vol. 85, No. 6, December 2003, pp. 4134-4145.

[109] F. H. Fenton, A. Karma, H. M. Hastings, and S. J. Evans, "Transition from Ventricular Tachycardia to Ventricular Fibrillation as Function of Tissue Characteristics in a Computer Model", *Proceedings of the 22nd Annual EMBS International Conference*, July 23-28, 2000, Chicago U.S.A., pp. 391-394.

[110] R. Groningen, "Molecular Adaptations in Human Atrial Fibrillation: Mechanisms of Protein Remodeling", $http://disertations.ub.rug.nl/FILES/faculties/medicine/2000/b.j.j.m.brundel\ /titlecon.pdf$, 2000.

[111] S. Sinha and D. J. Christini "Termination of Reentry in an Inhomogeneous Ring of Model Cardiac Cells", *Physical Review E*, Vol. 66, No. 6, December 2002, pp. 061903.1-061903.7.

[112] M. Courtemanche, "Complex Spiral Wave Dynamics in a Spatially Distributed Ionic Model of Cardiac Electrical Activity", *Chaos*, Vol. 6, No. 4, July 1996, pp. 579-600.

[113] A. Xu and M. R. Guevara, "Two Forms of Spiral-Wave Reentry in an Ionic Model of Ischemic Ventricular Myocardium", *Chaos*, Vol. 8, No. 1, November 1997, pp. 157-174.

[114] C. R. Johnson and R. C. Barr, "Termination of Reentrant Propagation by a Single Extracellular Stimulus in an Atrial Ring Model", *Proceedings of the 23rd Annual EMBS International Conference*, October 25-28, 2001, Istanbul Turkey, pp. 398-401.

[115] F. Xie, Z. Qu, A. Garfinkel, and J. N. Weiss, "Electrical Refractory Period Restitution and Spiral Wave Reentry in Simulated Cardiac Tissue", *American Journal of Physiology - Heart and Circulatory Physiology*, Vol. 283, No. 5, November 2002, pp. 448-460.

[116] M. Philip, "Mathematical Modelling of Cardiac Arrhythmias", *http* : *//www.f.kth.se/ ∼ f97 − mph/rapport/rapport.html*.

[117] P. R. Gray and R. G. Meyer, "Analysis and Design of Analog Integrated Circuits", *John Wiley & Sons, Inc.*, 3rd edition, 1993.

[118] P. Zavracky, M. Zavracky, D-P Vu, and B. Dingle, "Three-Dimensional Processor Using Transferred Thin Film Circuits", *US patent 5,656,548*, Patent and Trademark Office, Washington, D.C., August 1997.

[119] D. Bartholomew, "Winning Technologies: Flexible Transistors", *http* : *//www.industryweek.com/ReadArticle.aspx?ArticleID* = 771&*Section ID* = 38, December 2000.

[120] J. Ferrero (Jr), V. Torres, F. Montilla, and E. Cplpmar, "Simulation of Reentry during Acute Myocardial Ischemia: Role of ATP-Sensitive Potassium Current and Acidosis", *Computers in Cardiology (2000 IEEE Conference on Computers in Cardiology)*, Cambridge MA USA, September 2000, pp. 239-242.

[121] N. V. Thakor, J. Ferrero (Jr), J. Salz, B. I. Gramatikov, and J. Ferrero (Sr), "Electrophysiologic Models of Heart Cells and Cell Networks", *Engineering in Medicine and Biology Magazine, IEEE*, Vol. 17, No. 5, September/October 1998, pp. 73-83.

[122] R. M. Shaw and Y. Rudy, "Electrophysiologic Effects of Acute Myocardial Ischemia : a Theoretical Study of Altered Cell Excitability and Action Potential Duration", *Cardiovascular Research*, Vol. 35, No. 2, 1997, pp. 256-272.

[123] S. Seven, S. Vecchietti, I. Rivolta, C. Napolitano, S. G. Priori, and S. Cavalcanti, "Action Potential Changes Due to Y1795H Mutation in Brugada Syndrome Patients: A Simulation Study", *Computers in Cardiology (2003 IEEE Conference on Computers in Cardiology)*, Thessaloniki Greece, September 2003, pp. 437-440.

[124] R. Vogel and R. Weingart, "Mathematical Model of Vertebrate Gap Junctions Derived from Electrical Measurements on Homotypic and Heterotypic Channels", *Journal of Physiology*, Vol. 510, No. 1, 1998, pp. 177-189.

[125] F. J. Jaeger, "Cardiac Arrhythmias", *http* : *//www.clevelandclinicmeded .com/DISEASEMANAGEMENT/cardiology/arrhythmias/arrhythmias .htm*.

[126] J. Saiz, J. M. Ferrero, L. M. Roa, and N. V. Thakor, "Simulation of triggered Activity and Abnormal Automaticity Inventricular Myocytes", *Computers*

in Cardiology (1995 IEEE Conference on Computers in Cardiology), Vienna Austria, September 1995, pp. 345-348.

[127] C. H. Luo and Y. Rudy, "A Dynamic Model of the Cardiac Ventricular Action Potential. II. Afterdepolarizations, Triggered Activity, and Potentiation", *Circulation Research*, Vol. 74, No. 6, June 1994, pp. 1097-1113.

[128] J. Zeng and Y. Rudy, "Early Afterdepolarizations in Cardiac Myocytes: Mechanism and Rate Dependence", *Biophysical journal*, Vol. 68, No. 3, March 1995, pp. 949-964.

[129] "Anti-arrhythmic Drugs", $http://www.anaesthetist.com/icu/organs/heart/rhythm/Findex.htm\#arhythm.htm$.

[130] C. F. Starmer, "How Antiarrhythmic Drugs Increase the Rate of Sudden Cardiac Death", *International Journal of Bifurcation and Chaos*, vol. 12, No. 9, 2002, pp. 1953-1968.

[131] C. F. Starmer, A. O. Grant, and T. J. Colatsky, "What Happens When Cardiac Na Channel Function is Compromised? 2: Numerical Studies of the Vulnerable Period in Tissue Altered by Drugs", *Cardiovascular Research*, vol. 57, No. 4, March 2003, pp. 1062-1071.

[132] O. Bernus, B. V. Eyck, H. Verschelde, and A. V. Panfilov, "Transition From Ventricular Fibrillation to Ventricular Tachycardia: a Simulation Study on the Role of Ca^{2+}-channel Blockers in Human Ventricular Tissue", *Physics in Medicine and Biology*, Vol. 47, No. 23, December 2002, pp. 4167-4173.

[133] A. Cimponeriu, C. F. Starmer, and A. Bezerianos, "A Theoretical Analysis of Acute Ischemia and Infarction Using ECG Reconstruction on a 2-D Model of Myocardium", *IEEE Transactions on Biomedical Engineering*, Vol. 48, No. 1, 2001, Janurary 2001, pp. 41-54.

[134] R. H. Clayton and A. V. Holden, "Computational Framework for Simulating the Mechanisms and ECG of Re-entrant Ventricular Fibrillation", *Physiological Measurement*, Vol. 23, No. 4, November 2002, pp. 707-726.

[135] H. W. Chiu and T. Kao, "A Mathematical Model for Autonomic Control of Heart Rate Variation", *IEEE Engineering in Medicine and Biology Magazine*, Vol. 20, No. 2, March/April 2001, pp. 69-76.

[136] H. R. Warner and A. Cox, "A Mathematical Model of Heart Rate Control by Sympathetic and Vagus Efferent Information", *Journal of Applied Physiology*, Vol. 17, No. 2, March 1962, pp. 349-355.

[137] A. C. Sanderson, "Input-output Analysis of an IPFM Neural Model: Effects of Spike Regularity and Record Length", *IEEE Transactions on Biomedical Engineering*, Vol. 27, No. 3, March 1980, pp. 120-131.

[138] P. J. Hunter, A. D. McCulloch, and H. E. D. J. ter Keurs, "Modelling the Mechanical Properties of Cardiac Muscle", *Progress in Biophysics and Molecular Biology*, Vol. 69, No. 2, March 1998, pp. 289-331.

[139] J. J. Rice, R. L. Winslow, and W. C. Hunter, "Comparison of Putative Cooperative Mechanisms in Cardiac Muscle: Length Dependence and Dynamic Responses", *American Journal of Physiology - Heart and Circulatory Physiology*, Vol. 276, No. 5, May 1999, pp. H1734-H1754.